Development of Structural Steel Components Partially Strengthened by Induction Heating

Liu Yuan

2023

Contents

Research paper and award

A. Peer-reviewed paper related to this thesis

A.1 **Liu, Y.**, Iwata, K., Sanda, S., & Nishiyama, M. (2022). Utilization of motion capture systems for low cycle fatigue tests on induction-hardened steel. Journal of Constructional Steel Research, 190, 107166. https://doi.org/10.1016/j.jcsr.2022.107166 (related to Chapter 6)
The final publication is available at Elsevier via https://doi.org/10.1016/j.jcsr.2022.107166

A.2 **Liu, Y.**, Iwata, K., Sanda, S., Nishiyama, M., & Tani, M. (2021). Development of curved braces partially strengthened by induction heating. Engineering Structures, 233, 111754. https://doi.org/10.1016/j.engstruct.2020.111754 (related to Chapters 2, 3 and 4)
The final publication is available at Elsevier via https://doi.org/10.1016/j.engstruct.2020.111754

B. Other peer-reviewed paper

B.1 **Liu, Y.**, Nishiyama, M., Tani, M., Kurata, M., & Iwata, K. (2021). Steel beam with web opening reinforced by induction heating. Journal of Constructional Steel Research, 176, 106399. https://doi.org/10.1016/j.jcsr.2020.106399

B.2 **Liu, Y.**, Tani, M., Kurata, M., Watase, C., & Nishiyama, M. (2020). Study on I-shaped section steel braces partially strengthened by induction heating. Engineering Structures, 210, 110341. https://doi.org/10.1016/j.engstruct.2020.110341

B.3 **Liu, Y.**, Yasui, A., Nishiyama, M., Tani, M. (2020). Buckling-restrained damper partially strengthened by induction heating. Japan Prestressed Concrete Institute, Proceedings of The 29th Symposium on Developments in Prestressed Concrete, 187-192.

B.4 長屋翔悟，**劉媛**，西山峰広，谷昌典 (2019). 熱処理鋼棒ダンパーのアンボンド PCaPC 耐震壁への適用．プレストレストコンクリート工学会，第 28 回シンポジウム論文集，209-214.

B.5 **Liu, Y.**, Sanda, S., & Nishiyama, M. Development of Induction-Heated Buckling-Restrained Brace using PT bar (Part 1: Design, Production, and Material Investigation). Journal of Structural Engineering. (to be submitted)

B.6 Sanda, S., **Liu, Y.**, & Nishiyama, M. Development of Induction-Heated Buckling-Restrained Brace using PT bar (Part 2: Experiment and Numerical Analysis). Journal of Structural Engineering. (to be submitted)

B.7 Iwata, K., Tian, Z., **Liu, Y.**, & Nishiyama, M. Development of Induction-Heated Eccentric Braces. Engineering Structures. (to be submitted)

C. International conference

C.1 **Liu, Y.**, Sanda, S., Iwata, K., Nishiyama, M., Tani, M. (2021). Analytical investigation into seismic performance of induction-heated curved brace. The 22nd Taiwan-Japan-Korea Joint Seminar on Earthquake Engineering for Building Structures (SEEBUS 2021), 163-172, Oct. 15, Suwon, Korea.

C.2 **Liu, Y.**, Nagaya, S., Tani, M., Nishiyama, M. (2019). Cyclic behavior of partially strengthened hysteretic damper treated by induction heating. The 21st Japan-Korea-Taiwan Joint Seminar on Earthquake Engineering for Building Structures (SEEBUS 2019), 212-222, Dec. 6-7, Hsinchu, Taiwan.

C.3 **Liu, Y.**, Bedrinana, L., Tani, M., Kono, S., Nishiyama, M. (2018). Seismic performance of unbonded post-tensioned precast concrete walls with internal and external dampers. The 20th Taiwan-Korea-Japan Joint Seminar on Earthquake Engineering for Building Structures (SEEBUS 2018), 103-112, Nov. 2-3, Kyoto, Japan.

C.4 Wang, B., Nishiyama, M., Tani, M., Wang, S., **Liu, Y.**, Nagaya, S. (2021). Development of a novel self-centering steel coupling beam with SMA bolts and energy dissipation devices. 17th World Conference on Earthquake Engineering (17WCEE), Paper No. C002231, Sep. 27 - Oct. 2, Sendai, Japan.

D. Domestic conference

D.1 劉媛，三田沙也乃，西山峰広，田中典男，秋元健嗣. (2022). PC 鋼棒の高サイクル疲労試験（その 1：試験概要）（その 2：試験結果）．日本建築学会大会学術講演梗概集構造 IV，689-692，9 月 5 日-8 日，北海道.

D.2 劉媛，岩田佳歩，三田沙也乃，西山峰広，谷昌典，田中典男，秋元健嗣. (2021). 誘導加熱により高強度化された H 形鋼から切り出した試験片に対する低サイクル疲労試験：モーションキャプチャーによるひずみ制御（その 1：試験概要）（その 2：試験結果）．日本建築学会大会学術講演梗概集構造 III，677-680，9 月 7 日-10 日，名古屋.

D.3 三田沙也乃，劉媛，岩田佳歩，西山峰広，谷昌典，田中典男，秋元健嗣. (2021). 誘導加熱により部分高強度化した湾曲ブレースの解析的検討．日本建築学会大会学術講演梗概集構造 III，1025-1026，9 月 7 日-10 日，名古屋.

D.4 長屋翔悟，劉媛，岩田佳歩，西山峰広，谷昌典 (2020). 誘導加熱により部分高強度化した座屈拘束鋼棒ダンパーの開発（その 1：実験概要）（その 2：載荷方法，試験体耐力および荷重—軸平均ひずみ関係）（その 3：破断状況および履歴エネルギー吸収性能）．日本建築学会大会学術講演梗概集構造 IV，753-758，9 月 8 日-10 日，千葉.

D.5 **Liu, Y.**, Nagaya, S., Nishiyama, M., Tani, M. (2019). Development of partially strengthened hysteretic damper treated by induction heating (Part 1: Outlines of experiment and analysis) (Part 2: Results of experiment and analysis). Architectural Institute of Japan, Summaries of Technical Papers of Annual Meeting Structure IV, 797-800, Sep. 3-6, Kanazawa.

D.6 **Liu, Y.**, Bedrinana, L., Tani, M., Kono, S., Nishiyama, M. (2018). Seismic performance of unbonded post-tensioned precast concrete walls with internal and external dampers (Part 1: Outline of experiment) (Part 2: Test results). Architectural Institute of Japan, Summaries of Technical Papers of Annual Meeting Structure IV, 787-790, Sep. 4-6, Sendai.

E. Award

E.1 2020 年度京大建築会優秀修士論文賞

E.2 2018 年大会（東北）日本建築学会大会プレストレストコンクリート構造部門若手優秀発表

Acknowledgement

1 Introduction

1.1 Research background

Conventional buckling steel braces (CBBs) have been widely used as seismic components in steel and concrete structures. CBB is mainly designed to resist the axial tensile load and provide lateral stiffness to the frame. However, once it yields under tension, the stiffness it can provide dramatically reduces, which is inconsistent with its design intention. Additionally, the buckling behavior under compression at small deformation strongly affects the stability of CBB, which not only decreases the compressive load capacity but also leads to the large plastic strain concentration in the limited region, especially at the brace middle. The concentrated damage is unbeneficial to exerting the strength and ductility capacity in the rest of the brace [1.1), 1.2)].

To improve the aforementioned disadvantages, many efforts have been made in the past few decades. One of the most common solutions is buckling-restrained braces (BRBs) [1.3)-1.5)]. The buckling restraint makes the core steel behave the same under compression as under tension, which guarantees stable compressive performance without overall buckling. Besides, the core steel with the low-strength and high-strength steel plates [1.6)], or with various cross-sections along the length and lockup system [1.7)] has been proposed. These designs differentiate the timing of yielding at different regions of the core steel, which effectively heightens the post-yield stiffness. Other than BRBs, the braces with improved joint connections are also proved to show improved post-yield and post-buckling behaviors [1.8)-1.11)].

Though the aforementioned braces exhibit modified structural performances, there is no denying that their steel and other material consumptions are large, and the mechanisms are complicated. To reduce the resource consumption and simplify the mechanism, the brace made by connecting low-strength and high-strength steels with initial eccentricity was proposed [1.12)], as depicted in Figure 1-1. Unlike the mentioned BRBs, the initial eccentricity, which is calculated as the distance between the loading axis and the center of gravity of the brace, is employed here for stabilizing the compressive behavior instead of the buckling restraint. Owing to the initial eccentricity, the sudden drop of the compressive load after buckling is avoided and replaced by a smooth transition into the flexural behavior. The parallel arrangement of low-strength and high-strength steels triggers the multistage yielding response of the brace thanks to their different yield strengths. It is beneficial to improve the post-yield stiffness of the brace. This difference in the timing of yielding is further amplified by the initial eccentricity.
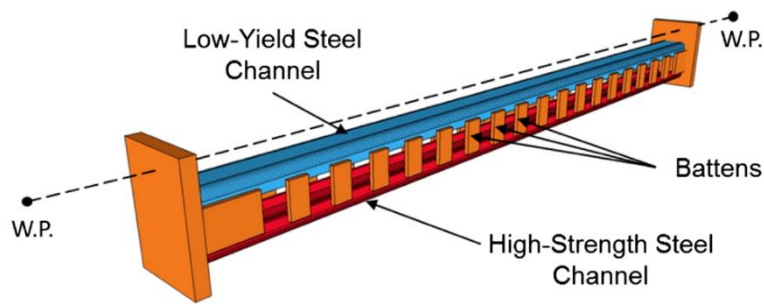
Figure 1-1 Eccentric brace fabricated by welding different steel materials [1.12)]

Despite that the mechanism of the eccentric brace with low and high-strength steels is simple, the fabrication, which includes the welding of the high and low-strength steels by battens, is complex. For the sake of easier fabrication, induction heating (IH) treatment is innovatively applied for partial strengthening. IH technology is an extensively used heat treatment to raise the strength of carbon steel, and it has been applied for fabricating mechanical parts as gears and construction materials as PT bars for several decades. Compared to other heating methods, IH has a distinguishing feature that it only affects a selected region of steel without affecting the other regions.

Owing to this feature, the large-scale hollow round section steel brace partially strengthened by IH treatment, IH-BIE was proposed [1.13)]. Figure 1-2 depicts the specimen image. Half of the section is IH-treated, and the brace with the normal-strength region at the inner side, which is near the loading axis, and the IH-treated high-strength region at the outer side, which locates far away from the loading axis, is eccentrically loaded. The test results comparing CBB and BIE (the brace with the initial eccentricity only) indicate that the eccentricity smoothens the hysteresis loop of the brace. The test results comparing BIE and IH-BIE prove that partial strengthening improves the post-yield stiffness while increasing the load capacity.
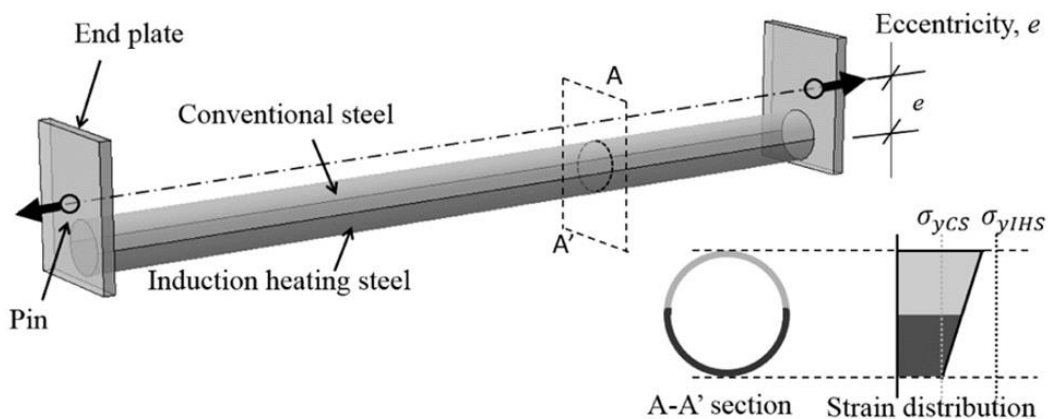
Figure 1-2 Eccentric brace fabricated by induction heating treatment [1.13)]

Above all, the eccentricity and partial strengthening in a brace are proven to be effective to overcome the weakness of CBB. However, the IH-BIE specimen eventually fractured at the brace end unexpectedly. Based on the joint fabrication method, which connected the brace and the end plates by welding eccentrically, two possible reasons are given here. First, during the welding process, the IH-treated high-strength region was reheated. It might have caused a decrease in the strength and ductility of the high-strength region. Second, the sudden inducement of eccentricity resulted in the stress concentration at the brace end, which might have accelerated the fracture at the brace end.

To solve the first problem, the solution of replacing the hollow round section with an I-shaped section was proposed. For the I-shaped section, the bolted connection can be adopted instead of the welding, which greatly reduces the risk of reheating the IH-treated region. Moreover, compared to the hollow round section, the different function between the flange and web of the I-shaped section in resisting the bending moment and shear force respectively increases the flexibility of the IH patterns. The differentiation of the major and minor axes renders the I-shaped section steel brace work more effectively in the selected direction. Although the complex cross-section of the I-shaped section poses a challenge to the IH treatment, especially at the intersection of the flange and the web, it is still worth giving a try since the I-shaped section is one of the most-commonly-used shapes of large-scale braces.

In terms of the second problem, the idea of replacing sudden eccentricity with a smooth curve shape was proposed. Figure 1-3 presents the braces with the curve or crescent shapes. Zhou, et al. [1.14] proposed the curved knee brace with a built-up I-shaped section. Hsu and Halim [1.15], [1.16] developed the curved tabular damper. Palermo, et al. [1.17]-[1.19] invented the crescent-shaped braces, which were like bilinear shapes, with tabular or round sections. They were fabricated by laser-cutting a steel plate or bending a round bar. These special geometrical shapes avoid the sudden inducement of eccentricity, therefore the early fracture at the brace end becomes evitable. Furthermore, these shapes work the same as eccentricity, which can enhance the adjustability of the yield displacement and the initial stiffness. They increase the ductility by preventing the overall buckling and stabilizing the compressive behavior. The double effect of the intrinsic non-linear material property and the modified non-straight geometrical shape achieves the final hardening under tension and moderate softening under compression.

(a) Curved knee brace [1.14]   (b) Crescent shaped brace [1.17]
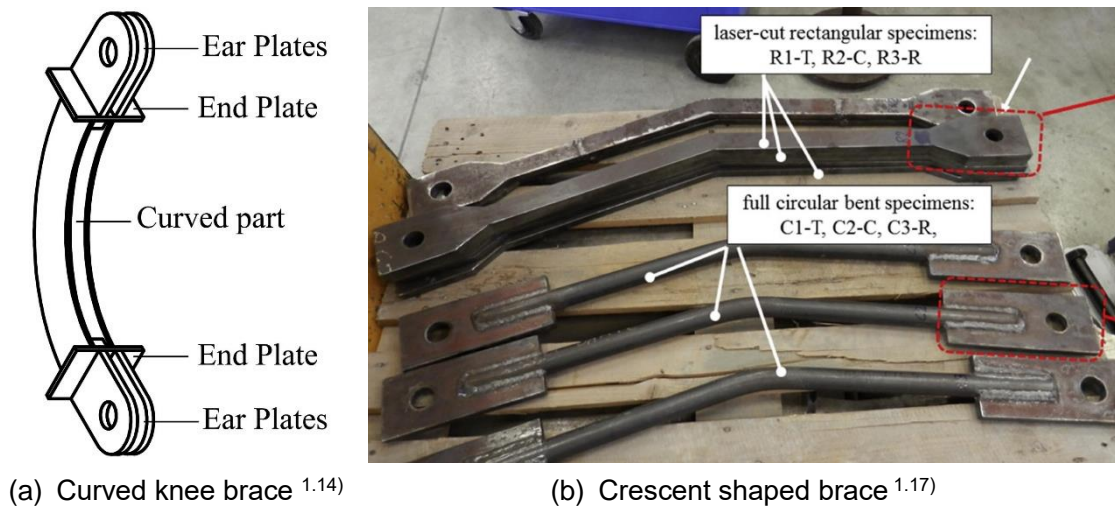
Figure 1-3 Braces with curve or crescent shape

By combining these two solutions, a new kind of curved brace partially strengthened by IH treatment called induction-heated curved brace (IHCB) is proposed in this study [1.20]. The concept of the brace is shown in Figure 1-4. The proposed brace is parallel treated by IH technology along the brace length, thus, the untreated normal-strength region and the IH-treated high-strength region are coexisting in the same cross-section. Besides, this uneven IH treatment bends the brace as an arc where the high-strength region is at the inner side, due to the shrinkage of the high-strength region. Considering that the brace is axially tensioned, while the normal-strength region yields, the high-strength region can remain elastic under large deformation. It is beneficial to increase the post-yield stiffness of the brace. The initial curve shape along the brace length is helpful to stabilize the compressive behavior and delay the first yielding behavior. Furthermore, the brace joint weakened by the bolt holes can also be strengthened by IH treatment.

(a) 3D view of IHCB   (c) Schematic figure of load-axial strain curve
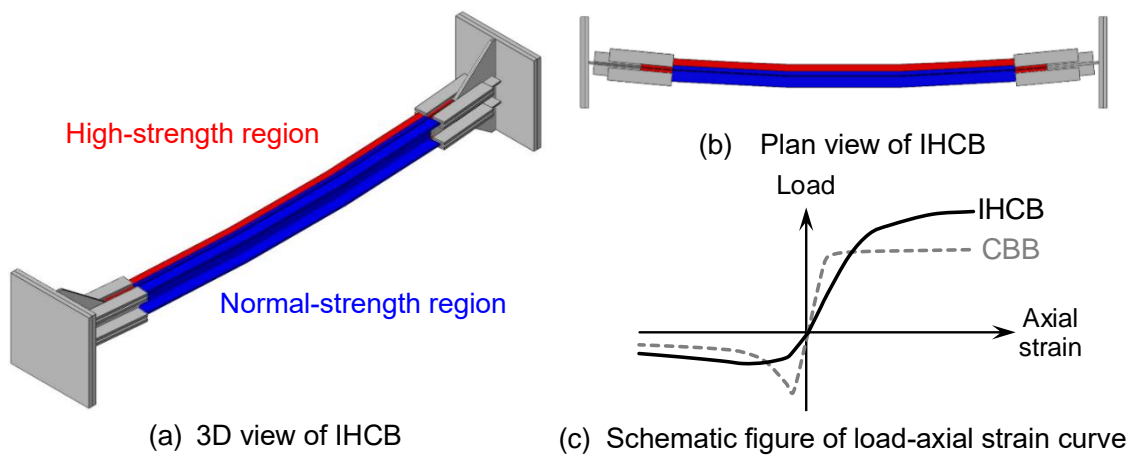
Figure 1-4 Concept of IHCB

As the first trial of partial strengthening on I-shaped section steel, the brace with partial strengthening only was manufactured [1.21]. Note that the curve shape owing to uneven heating was straightened by a universal testing machine to keep the partial strengthening as the unique variable. The tensile coupon tests showed that the yield and tensile strengths were improved to 1.23-1.40 times after IH treatment. The cyclic loading tests proved that the partial strengthening triggered the multistage yielding response and mitigated the local buckling behavior at the final condition. IHCB proposed in this thesis is the second generation of the partially strengthened I-shaped section steel brace. Note that the curve shape was regarded as a shortcoming of heat treatment in the first trial but surprisingly turned into an advantage.

IHCB is expected to work as a novel brace that can provide lower initial stiffness but higher post-yield stiffness with great ductility, which makes it particularly suitable for seismic retrofit of existing buildings. Its lower initial stiffness decreases the influence on the acceleration response and the initial stiffness of the building. The larger displacement demand for yielding helps the brace remain elastic during medium earthquakes. When it faces severe earthquakes, the larger post-yield stiffness of the brace can significantly reduce the story drift and the residual damage to the building.
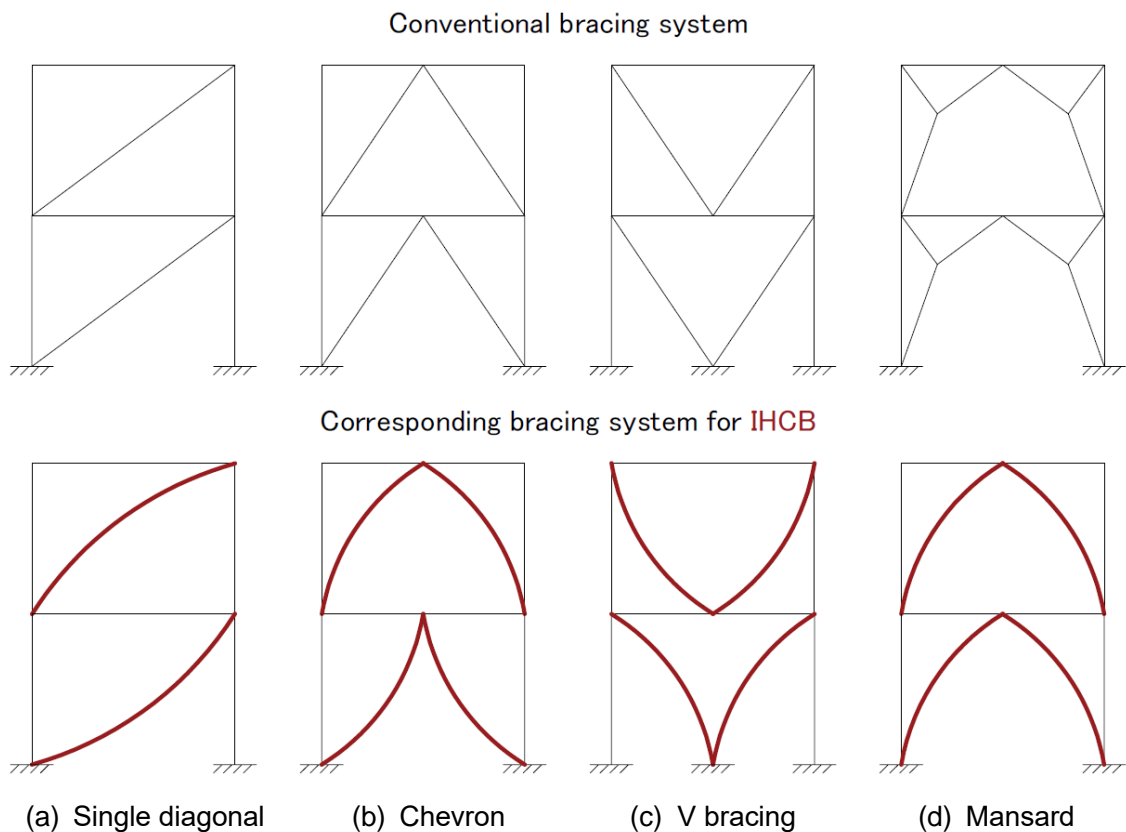
Figure 1-5 IHCB Bracing system

Figure 1-5 shows several bracing systems for the conventional brace and the corresponding ones for IHCB in red. Owing to the curve shape, various and original bracing systems can be easily achieved by changing the installation ways and directions. The design proposal of Mansard bracing, which is to provide larger headroom, can be realized by IHCB with decreased steel consumption and a simplified construction process, as Figure 1-5(d) shows.

1.2 Research objectives and contents

This thesis focuses on creating a new and high-performance brace with the feature of partial strengthening and curve shape. It aims to overcome the weakness of the conventional buckling brace (CBB) whose compressive behavior is unstable, and the post-yield stiffness is low. To achieve this goal, an advanced heat treatment, induction heating (IH) technology is flexibly employed. The research objectives and contents of each chapter are shown as follows.

Chapter 2 presents the cyclic loading tests on the induction-heated curved braces (IHCBs). This chapter aims to investigate the cyclic behavior of IHCBs and confirm whether their performances satisfy the expected goal. First, the target performance level of IHCB is presented. Then, the outline of the specimens, such as the brace design, fabrication method, and dimension, are introduced. Next, the material properties obtained from the tensile coupon test as well as the Vickers hardness test, and the experimental outlines, including the loading setup, and joint design are presented. As one of the most significant parts, the experimental results on four specimens, one CBB, and three IHCBs, are introduced based on the load, deformation, strain, and energy dissipation. Last, the test performances are evaluated and the deficiencies of this study are discussed.

Chapter 3 introduces the numerical analysis of IHCBs. The objective of this chapter is to discuss the cyclic behavior of IHCBs in more detail and analyze the effect brought by IH treatment. First, the numerical model is built by ABAQUS 6.14, and the model accuracy is verified by comparing the numerical analysis results to the experimental results. Then, the individual effect of the curve shape is discussed, and the expected curvedness to meet the target performance of IHCB is evaluated. The individual effect of partial strengthening and the target strength ratio are investigated as well. Last, the synthetic effect of the curve shape and the partial strengthening are concluded.

Chapter 4 proposes the design formulas for IHCBs. This chapter aims to clarify the mechanism and build the design method. The design methods considering the initial stiffness, post-yield stiffness, yield load, maximum tensile load, and post-buckling strength are proposed. The accuracies of the proposed equations are last verified by comparing them to the experimental and numerical analysis results.

Chapter 5 presents the numerical analysis of frames using IHCBs. It is to evaluate the brace behaviors in the frame and confirm whether they still meet the target performances. First, a frame from previous research is reproduced by ABAQUS and its accuracy is verified. Next, the frame using CBB or IHCB is cyclically loaded. The structural performances of the braced frames are evaluated in the aspects of load capacities and critical behaviors.

Chapter 6 presents the fatigue performances of IH-treated steel. It aims to understand the material fatigue performance of the IH-treated steel and accumulate the fatigue data, which is helpful for future investigation into the IH-treated steel in any other field. First, the low cycle fatigue performance of the normal-strength and high-strength coupons cut out from IHCBs are presented. Next, the high cycle fatigue performance of the PT bars is demonstrated. Last, an innovative strain control method proposed for the low cycle fatigue tests is presented.

Chapter 7 concludes this study and discusses the limitation.

The relationship of each chapter and the research contents are briefly illustrated in Figure 1-6.
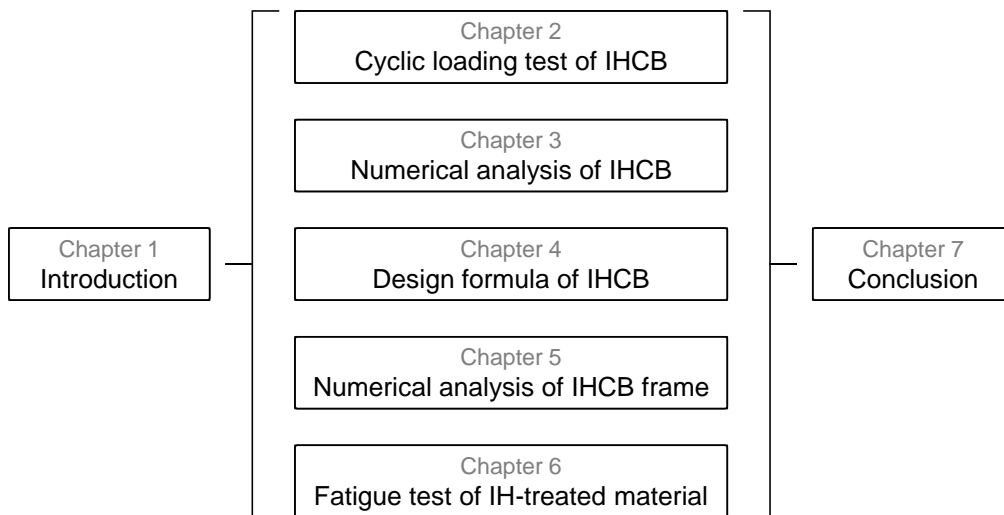
Figure 1-6 Research contents

1.3 Induction heating technology

Induction heating (IH) is a method that can increase the hardness and strength of carbon steel using heating and rapid quenching processes [1.22], [1.23]. As shown in Figure 1-7, when the carbon steel is heated, it undergoes a phase transition from (1) body-centered cubic (BCC), which is called ferrite form, to (2) face-centered cubic (FCC) called austenite form. When it is rapidly cooled, FCC transits into (3) body-centered tetragonal (BCT) called martensite form, which is supersaturated with carbon. The phase transition from BCC to BCT enhances the hardness and strength of the carbon steel. After IH treatment, the material strength can commonly be improved 2-4 times.
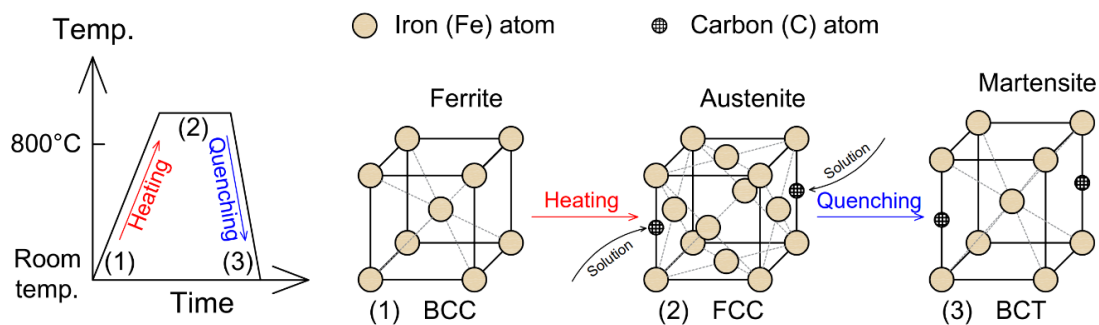
Figure 1-7 Phase transition during IH process

IH treatment is an environmental-friendly and high-efficiency heating method. As presented in Section 1.1, IH treatment can only work on the selected region of the steel, making it possible for the partial strengthening of the steel component. Recently, with the development of technology, IH treatment becomes available for large-scale structural steel components for civil engineering applications.

Based on the application cases, the treatment patterns can be divided into three types, parallel treatment, tandem treatment, and partial treatment. IHCB proposed in this thesis is a representative of the component treated in parallel. As for the component treated in tandem, when it is gradually loaded in the axial direction, all materials keep elastic at the beginning. With the increase of the load, the normal-strength region yields, but the high-strength region remains elastic. If the strength difference between the normal-strength and high-strength regions is large enough, the high-strength region can always maintain elastic. It is helpful to deliberately induce damage to the selected location and trigger energy dissipation. This design concept has been used for the development of the steel bar in the concrete beam-column joint [1.24]-[1.38], and small-scale damper used for the unbonded post-tensioned precast concrete joint [1.39], [1.40]. In terms of the component treated in part, the significant region with higher strength after IH treatment can be protected from being damaged. This concept has been applied for the reinforcement of the steel beam with web opening [1.41].

1.4 Conclusion

This chapter introduces the research background, objectives, and contents of this thesis.

Section 1.1 presents the research background. To overcome the weakness of the conventional buckling brace (CBB) whose compressive behavior is unstable and the post-yield stiffness is low, a new kind of curved brace partially strengthened by IH treatment called induction-heated curved brace (IHCB) is proposed in this study. It is parallel treated by IH technology along the brace length, thus, the untreated normal-strength region and the IH-treated high-strength region are coexisting in the same cross-section. Besides, this uneven IH treatment bends the brace as an arc. While the normal-strength region yields, the high-strength region can remain elastic under large deformation, which is beneficial to increase the post-yield stiffness of the brace. The initial curve shape along the brace length is helpful to stabilize the compressive behavior and delay the first yielding.

Section 1.2 mainly introduces the research contents. Chapter 2 presents the cyclic loading tests of IHCBs, Chapter 3 introduces the numerical analysis of IHCB, Chapter 4 proposes the design methods, Chapter 5 presents the numerical analysis of frames using IHCB, and Chapter 6 presents the fatigue performances of IH-treated steel.

Section 1.3 briefly explains the mechanism and the recent application cases of induction heating (IH) technology. IH treatment is effective to raise the steel material strength at the selected region, and the treating patterns are divided into three types, parallel treatment, tandem treatment, and partial treatment. The recent research on applying IH technology to partially strengthen the steel components in the architecture field become increasingly more. It can be said that IH treatment opens the door for new research exploration in creating new structural components with different strengths.

References

1.1) Takeuchi, T., Nishimaki, M., Matsui, R., & Imamura, A. (2012). Cumulative deformation capacity of braces under various cyclic loading histories. Journal of Structural and Construction Engineering (Transactions of AIJ), 77(677), 1131–1140. https://doi.org/10.3130/aijs.77.1131

1.2) Tremblay, R. (2002). Inelastic seismic response of steel bracing members. Journal of Constructional Steel Research, 58(5–8), 665–701. https://doi.org/10.1016/s0143-974x(01)00104-3

1.3) Takeuchi, T., & Wada, A. (2017). Buckling-restrained Braces and Applications. Japan Society of Seismic Isolation.

1.4) Uang, C., Nakashima, M., & Tsai, K. (2004). Research and application of buckling-restrained braced frames. International Journal of Steel Structures, 4(4), 301–313. https://www.auric.or.kr/User/Rdoc/DocRdoc.aspx?returnVal=RD_R&dn=164939

1.5) Della Corte, G., D'Aniello, M., Landolfo, R., & Mazzolani, F. (2011). Review of steel buckling-restrained braces. Steel Construction, 4(2), 85–93. https://doi.org/10.1002/stco.201110012

1.6) Sitler, B., Takeuchi, T., Matsui, R., Terashima, M., & Terazawa, Y. (2020). Experimental investigation of a multistage buckling-restrained brace. Engineering Structures, 213, 110482. https://doi.org/10.1016/j.engstruct.2020.110482

1.7) Sun, J., Pan, P., & Wang, H. (2018). Development and experimental validation of an assembled steel double-stage yield buckling restrained brace. Journal of Constructional Steel Research, 145, 330–340. https://doi.org/10.1016/j.jcsr.2018.03.003

1.8) Baiguera, M., Vasdravellis, G., & Karavasilis, T. L. (2016). Dual seismic-resistant steel frame with high post-yield stiffness energy-dissipative braces for residual drift reduction. Journal of Constructional Steel Research, 122, 198–212. https://doi.org/10.1016/j.jcsr.2016.03.019

1.9) Lehman, D., Roeder, C., Herman, D., Johnson, S., & Kotulka, B. (2008). Improved seismic performance of gusset plate connections. Journal of Structural Engineering-Asce, 134(6), 890–901. https://doi.org/10.1061/(asce)0733-9445(2008)134:6(890)

1.10) Yoo, J. H., Lehman, D. E., & Roeder, C. W. (2008). Influence of connection design parameters on the seismic performance of braced frames. Journal of Constructional Steel Research, 64(6), 607–623. https://doi.org/10.1016/j.jcsr.2007.11.005

1.11) Haddad, M., & Tremblay, R. (2017). Influence of connection design on the inelastic seismic response of HSS steel bracing members. Tubular Structures XI, 639–646. https://doi.org/10.1201/9780203734964-78

1.12) Hsiao, P., Hayashi, K., Inamasu, H., Luo, Y., & Nakashima, M. (2016). Development and testing of naturally buckling steel braces. Journal of Structural Engineering, 142(1), 04015077. https://doi.org/10.1061/(asce)st.1943-541x.0001319

1.13) Skalomenos, K. A., Kurata, M., Shimada, H., & Nishiyama, M. (2018). Use of induction-heating in steel structures: Material properties and novel brace design. Journal of Constructional Steel Research, 148, 112–123. https://doi.org/10.1016/j.jcsr.2018.05.016

1.14) Zhou, Z., Ye, B., & Chen, Y. (2019). Experimental investigation of curved steel knee braces with adjustable yield displacements. Journal of Constructional Steel Research, 161, 17–30. https://doi.org/10.1016/j.jcsr.2019.06.011

1.15) Hsu, H. L., & Halim, H. (2018). Brace performance with steel curved dampers and amplified deformation mechanisms. Engineering Structures, 175, 628–644. https://doi.org/10.1016/j.engstruct.2018.08.052

1.16) Hsu, H. L., & Halim, H. (2017). Improving seismic performance of framed structures with steel curved dampers. Engineering Structures, 130, 99–111. https://doi.org/10.1016/j.engstruct.2016.09.063

1.17) Palermo, M., Pieraccini, L., Dib, A., Silvestri, S., & Trombetti, T. (2017). Experimental tests on Crescent Shaped Braces hysteretic devices. Engineering Structures, 144, 185–200. https://doi.org/10.1016/j.engstruct.2017.04.034

1.18) Palermo, M., Silvestri, S., Gasparini, G., & Trombetti, T. (2014). Crescent shaped braces for the seismic design of building structures. Materials and Structures, 48(5), 1485–1502. https://doi.org/10.1617/s11527-014-0249-z

1.19) Kammouh, O., Silvestri, S., Palermo, M., & Cimellaro, G. P. (2017). Performance-based seismic design of multistory frame structures equipped with crescent-shaped brace. Structural Control and Health Monitoring, 25(2), e2079. https://doi.org/10.1002/stc.2079

1.20) Liu, Y., Iwata, K., Sanda, S., Nishiyama, M., & Tani, M. (2021). Development of curved braces partially strengthened by induction heating. Engineering Structures, 233, 111754. https://doi.org/10.1016/j.engstruct.2020.111754

1.21) Liu, Y., Tani, M., Kurata, M., Watase, C., & Nishiyama, M. (2020). Study on I-shaped section steel braces partially strengthened by induction heating. Engineering Structures, 210, 110341. https://doi.org/10.1016/j.engstruct.2020.110341

1.22) Lucia, O., Maussion, P., Dede, E., & Burdio, J. (2014). Induction heating technology and its applications: past developments, current technology, and future challenges. IEEE Transactions on Industrial Electronics, 61(5), 2509–2520. https://doi.org/10.1109/tie.2013.2281162

1.23) Neturen Co., Ltd. (2022). Neturen Co., Ltd. Retrieved April 11, 2022, from https://www.k-neturen.co.jp/

1.24) 村田義行，服部修三，岸田慎司，伊藤宏亮，福山拓真.(2014).部分的に高強度化した鉄筋を用いた鉄筋コンクリート造柱梁接合部の力学的挙動に関する実験研究（その１：付着が良い梁曲げ降伏後接合部せん断破壊型に対する検討）（その２：付着が良い梁

曲げ降伏型に対する検討）（その 3：付着が良い場合の鋼板補強が柱梁接合部に与える影響）．日本建築学会大会学術講演梗概集，425-430，9 月 12 日-14 日，神戸．

1.25) 村田義行，福山拓真，岸田慎司. (2015).部分的に高強度化した鉄筋を用いた鉄筋コンクリート造柱梁接合部の力学的挙動に関する実験研究（その 4：部分的に高強度化した鉄筋を柱主筋に用いた試験体）（その 5：部分的に高強度化した鉄筋を梁主筋に用いた試験体）．日本建築学会大会学術講演梗概集，147-150，9 月 4 日-6 日，平塚．

1.26) 村田義行，岸田慎司. (2016).部分的に高強度化した鉄筋を用いた鉄筋コンクリート造柱梁接合部の力学的挙動に関する実験研究（その 6：柱梁曲げ強度比に対する検討）．日本建築学会大会学術講演梗概集，381-382，8 月 24 日-26 日，福岡．

1.27) 北山和宏，村上研，岸田慎司，村田義行，小田稔.(2018). 部分的に高強度化した鉄筋を用いた鉄筋コンクリート柱梁部分架構の耐震性能評価（その 1：実験概要）（その 2：十字形柱梁部分架構の実験結果）（その 3：ト形柱梁部分架構の実験結果）．日本建築学会大会学術講演梗概集，639-644，9 月 4 日-6 日，仙台．

1.28) 村上研，石川巧真，山谷裕介，岸田慎司，北山和宏，村田義行，小田稔. (2019). 部分的に高強度化した鉄筋を用いた鉄筋コンクリート柱梁部分架構の耐震性能評価（その 4：実験概要）（その 5：十字形柱梁部分架構の実験結果）（その 6：ト形柱梁部分架構の実験結果）．日本建築学会大会学術講演梗概集，135-140，9 月 3 日-6 日，金沢．

1.29) 村田義行，道正壮晴，山谷裕介，岸田慎司，北山和宏，村上研，蛭田駿，小田稔.(2020). 部分的に高強度化した鉄筋を用いた鉄筋コンクリート柱梁部分架構の耐震性能評価（その 7：実験概要）（その 8：十字形柱梁部分架構の実験結果）（その 9：ト形柱梁部分架構の実験結果）．日本建築学会大会学術講演梗概集，391-396，9 月 8 日-10 日，千葉．

1.30) 並川元気，中条貴大，寺嶋峻正，山上雄平，佐藤裕一，村田義行，金子佳生.(2015). 高周波熱処理により部分高強度化した鉄筋を用いた RC 梁の曲げせん断性状（その 1：実験目的と計画）（その 2，3，4：実験結果(1), (2), (3)）．日本建築学会大会学術講演梗概集，487-494，9 月 4 日-6 日，平塚．

1.31) 山上雄平，寺嶋峻正，中条貴大，佐藤裕一，村田義行，金子佳生.(2016). 高周波熱処理により部分高強度化した主筋を用いた RC 柱と有孔梁の曲げせん断挙動（その 1：実験概要）（その 2：実験結果）．日本建築学会大会学術講演梗概集，115-118，8 月 24 日-26 日，福岡．

1.32) 多久和大海，岸田慎司，村田義行. (2015).部分的に高強度化した鉄筋を用いた鉄筋コンクリート有孔梁に関する実験研究．日本建築学会大会学術講演梗概集，479-480，9 月 4 日-6 日，平塚．

1.33) 多久和大海，岸田慎司，村田義行.(2016). 部分的に高強度化した鉄筋を用いた鉄筋コンクリート有孔梁に関する実験研究（その 2：開孔部上下の補強に対する検討）．日本建築学会大会学術講演梗概集，109-110，8 月 24 日-26 日，福岡．

1.34) 村田義行，岸田慎司，高桑遼. (2017). 部分的に高強度化した鉄筋を用いた鉄筋コンクリート有孔梁に関する実験研究（その 3：補強筋形状に対する検討—実験概要—）（その 4：補強筋形状に対する検討—実験結果—）．日本建築学会大会学術講演梗概集，61-64，8 月 31 日-9 月 3 日，広島.

1.35) 村田義行，岸田慎司. (2018). 部分的に高強度化した鉄筋を用いた鉄筋コンクリート有孔梁に関する実験研究（その 5：開孔部周りの補強方法に関する検討）．日本建築学会大会学術講演梗概集，179-180，9 月 4 日-6 日，仙台.

1.36) 眞田健伍，岸田慎司，村田義行. (2019). 部分的に高強度化した鉄筋を用いた鉄筋コンクリート有孔梁に関する実験研究（その 6：入力せん断力による影響の検討）．日本建築学会大会学術講演梗概集，453-454，9 月 3 日-6 日，金沢.

1.37) 安藤諒，眞田健伍，岸田慎司，村田義行. (2020). 部分的に高強度化した鉄筋を用いた鉄筋コンクリート有孔梁に関する実験研究（その 7：開孔部周りの補強方法に関する検討—実験概要—）（その 8：開孔部周りの補強方法に関する検討—実験結果—）．日本建築学会大会学術講演梗概集，209-212，9 月 8 日-10 日，千葉.

1.38) 眞田健伍，岸田慎司，村田義行. (2021). 部分的に高強度化した鉄筋を用いた鉄筋コンクリート有孔梁に関する実験研究（その 9：孔周囲補強筋量による破壊性状への影響）．日本建築学会大会学術講演梗概集，307-308，9 月 7 日-10 日，名古屋.

1.39) Liu, Y., Yasui, A., Nishiyama, M., & Tani, M. (2020). Buckling-restrained damper partially strengthened by induction heating. Japan Prestressed Concrete Institute, Proceedings of The 29th Symposium on Developments in Prestressed Concrete, 187-192.

1.40) 長屋翔悟，劉媛，西山峰広，谷昌典 (2019). 熱処理鋼棒ダンパーのアンボンド PCaPC 耐震壁への適用．プレストレストコンクリート工学会，第 28 回シンポジウム論文集，209-214.

1.41) Liu, Y., Nishiyama, M., Tani, M., Kurata, M., & Iwata, K. (2021). Steel beam with web opening reinforced by induction heating. Journal of Constructional Steel Research, 176, 106399. https://doi.org/10.1016/j.jcsr.2020.106399

2   Cyclic loading test on induction-heated curved braces

This chapter presents the experimental study on induction-heated curved braces (IHCBs). First, the target performance is illustrated. Then, the outline of the specimens, such as the brace design and dimension, are introduced. The material properties obtained from the tensile coupon test as well as the Vickers hardness test, and the experimental outlines, including the loading setup, and joint design are presented. Next, experimental results on four specimens, one conventional buckling brace (CBB), and three IHCBs, are introduced based on the load, strength degradation, deformation, strain, and energy dissipation. Last, the test performances are evaluated and the deficiencies of this study are discussed.

2.1   Target performance level

As presented in Section 1.1, IHCB has the feature of partial strengthening and curve shape. It overcomes the weakness of CBB by differentiating the timing of yielding of two materials and triggering the smooth compressive behavior. The following structural performances are required for IHCB: low initial stiffness, large post-yield stiffness, stable compressive behavior, and sufficient load capacity at the brace end. The explanation for each target is as follows.

1.   Low initial stiffness

Commonly, the elastic design of the braced frame requires that when the major structural component yields, the base shear coefficient (= Shear load at the base floor / gross weight of the building) must be no less than 0.2, and the story drift ratio no larger than 1/200 [2.1), 2.2)]. Considering the case when the brace is singly placed diagonally in a frame with an angle of 45°, CBB generally yields under tension at the story drift ratio of about 1/500, while the frame yields at about 1/100. Thus, the yielding of CBB dominates the elastic design of the CBB frame. In short, for the CBB frame, at the story drift ratio of about 1/500, the base shear coefficient should be no less than 0.2.

To satisfy the requirement on the base shear coefficient, the braced frame should exert sufficient load capacity at the story drift ratio of about 1/500. However, the load provided by the frame is very limited at this story drift ratio, which eventually requires a large amount of the brace or the large cross-sectional area of the beam and column. If the yielding of the brace can be delayed from the story drift ratio of 1/500 to a larger value, such as 1/250, the elastic design of the braced frame can be mitigated. At this story drift ratio, the load carried by the frame becomes large. Therefore, both the brace and the frame can exert the load capacity together to meet the requirement of the base shear coefficient. It finally mitigates the amount of the brace or the size of the frame, thereby reducing the total steel consumption.

Given that, the yield displacement of IHCB is expected to be twice that of CBB, corresponding to the story drift ratio of about 1/250-1/200. The aforementioned requirement can be briefly rewritten as follows: for the IHCB frame, at the story drift ratio of about 1/250, the base shear coefficient should be no less than 0.2. Therefore, the target initial stiffness of IHCB, $K_{e,IHCB}$, is set at approximately 50% of that of CBB, $K_{e,CBB}$: $K_{e,IHCB} \approx 0.5 K_{e,CBB}$.

2. Large post-yield stiffness

The post-yield stiffness of CBB, $K_{p,CBB}$, is commonly 1% of its initial stiffness. Once CBB yields, the sudden drop of the stiffness may result in the displacement concentration at the corresponding floor, eventually causing the story to collapse. Therefore, higher post-yield stiffness is essential. However, extremely high post-yield stiffness in turn decreases the energy dissipation of the brace and brings difficulty to the joint design. Therefore, the target post-yield stiffness of IHCB, $K_{p,IHCB}$, is set approximately 10 times that of CBB, $K_{p,CBB}$, in other words, 0.1 times the initial stiffness of CBB, $K_{e,CBB}$: $K_{p,IHCB} \approx 10 K_{p,CBB} \approx 0.1 K_{e,CBB}$.

Besides, the plastic design of the braced frame commonly requires that the base shear coefficient should be no less than 0.25 at the story drift ratio no larger than 1/100 [2.1), 2.2)]. If the proposed brace can keep providing the large post-yield stiffness until the story drift ratio of 1/100, the design requirement on the frame load capacity can be lowered. Therefore, IHCB is expected to exert its target post-yield stiffness from the yield strain, $\varepsilon_{y,IHCB}$, until 3 times the yield strain, $3\varepsilon_{y,IHCB}$. It approximately corresponds to the story drift ratio from 1/250 to 1/80.

3. Stable compressive behavior

The compressive load of CBB dramatically drops once it buckles. Its compressive load at the -0.5% axial strain, which is called post-buckling load according to AIJ Recommendation, is usually 1/3 of the buckling load [2.3)]. Given that, the compressive load of CBB is usually simplified as the post-buckling load, and the buckling load is additionally calculated during practical engineering design [2.4)]. If the proposed brace shows a stable compressive behavior without buckling, not only the design can be simplified without considering the buckling load, but also the deficiencies, such as strain concentration at the limited region, brought by buckling can be solved. Therefore, the post-buckling load of IHCB, $P_{s,IHCB}$, is expected to be similar to its maximum compressive load, $P_{c,IHCB}$: $P_{s,IHCB} \approx P_{c,IHCB}$.

4. Sufficient load capacity at the brace end

To ensure that the brace can exert its structural performance as planned, the brace end is required not to fracture until the main part of the brace enters the plastic stage. For the material SS400 which is used as the raw material of the brace in this thesis, the maximum tensile load of the brace end, $P_{u,end}$, should be 1.25-1.30 times larger than the yield load of the main part, P_y [2.5]. This value is called the connection coefficient and is mainly affected by strain hardening and deviation of the material property. Note that the strain hardening of the IH-treated high-strength region is about 1.1 times from experience, which is commonly smaller than the strain hardening of the untreated normal-strength region. For the proposed brace, the high post-yield stiffness may increase the load capacity by 40%, and the strain hardening keeps working on the second post-yield stiffness. Given that, the connection coefficient is set as 1.6 in this study. Therefore, $P_{u,IHCB-end} \geq 1.6 P_{y,IHCB}$.

Figure 2-1 Target performance of IHCB

Figure 2-1 summarizes the target performances. This chapter later conducts the pilot tests on one CBB and three IHCBs to confirm whether IHCBs satisfy the requirements. Note that the post-yield stiffness is the abbreviation of the first post-yield stiffness. The stiffness after that is the second post-yield stiffness and is hardly discussed since it usually agrees with the material's post-yield stiffness.

2.2 Outlines of specimen

2.2.1 Specimen design

Four kinds of I-shaped 100 × 100 × 6 × 8 mm section steel braces, CBB, IHCB-F40, IHCB-2F60, IHCB-F40W60 with material SS400 (nominal yield strength = 235 MPa, nominal tensile strength = 400 MPa) in Japan are designed as shown in Figure 2-2. The specimen length is 1783 mm. The supported length, including the specimen length and the joints, in other words, the distance between the two ends of gusset plates, is 2241 mm. It is approximately 50% scale of the typical brace. The slenderness ratio is 90. It is in the recommended slenderness ratio range of conventional buckling brace, which is 20-250 according to AIJ standard [2.3]. Brace ends of all specimens, which are connected to gusset plates by high-strength bolts, are IH-treated for a length of 140 mm along the axial direction at the whole cross-section, shown in the red diagonal line, to compensate for the section loss due to bolt holes.

Table 2-1 outlines the features and the test purposes of the four braces. The IHCB series is designed to investigate the dual effect of the partial strengthening and the initial curve deformation on the structural performance compared with CBB. The differences among the three IHCBs are aimed at investigating the effect of different IH-treated locations and widths.

Table 2-1 Brace design

Specimen	Feature	Purpose
CBB	Untreated (except for the brace ends)	To simulate the cyclic behavior of the conventional buckling brace
IHCB-F40	Treated at one side of the flange (F) along the brace length for the width of 40 mm	To investigate the cyclic behavior of the brace treated at one side of the flange
IHCB-2F60	Treated averagely at two sides of the flange (2F) along the brace length for a total width of 60 mm	To investigate the cyclic behavior of the brace treated at two sides of the flange
IHCB-F40W60	Treated at one side of the flange (F) for 40 mm, and the web (W) for 60 mm	To investigate the cyclic behavior of the brace treated both at the flange and web

Supported length: 2241

Specimen length: 1783

400

0-0

High strength bolt (F10TM16)
Gusset plate (t=12)
End plate (t=24)

Specimen

40x7=280

Plan view of CBB

100

100

6

8

1-1

CBB

40

2-2

IHCB-F40

30 40 30

3-3

IHCB-2F60

40

60

4-4

IHCB-F40W60
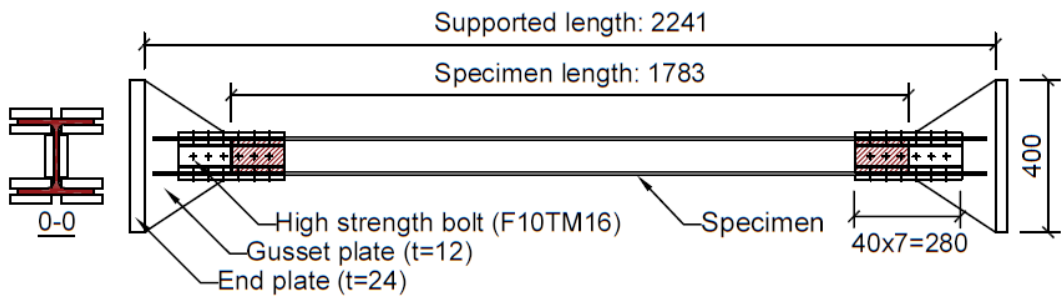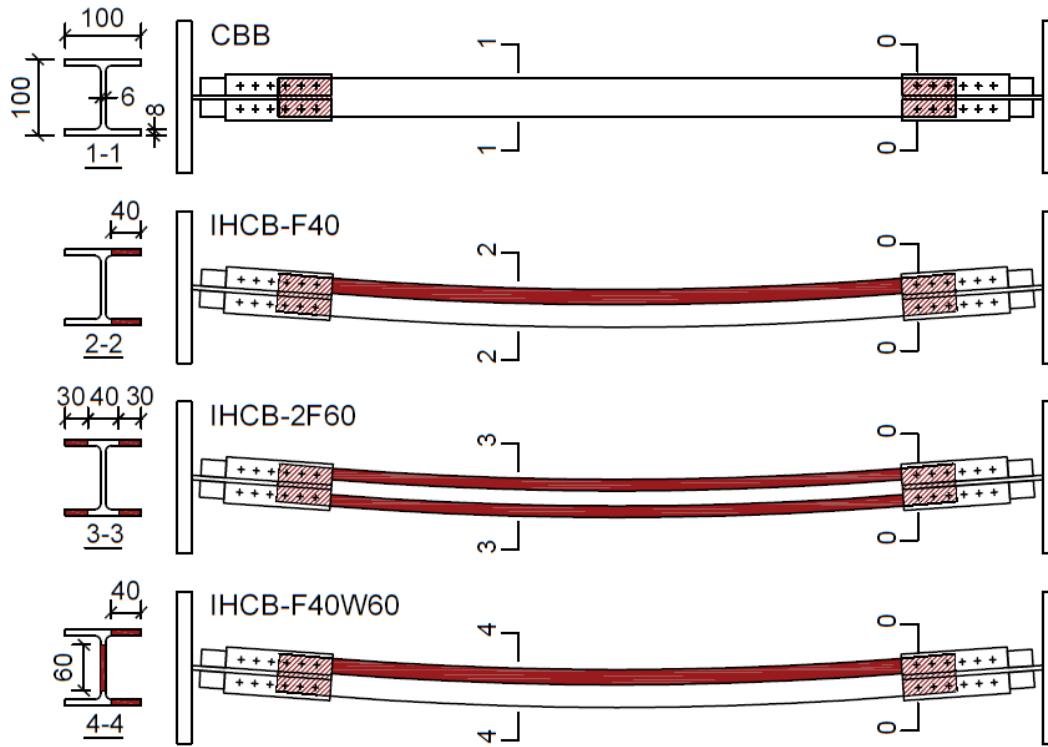
Top view

Normal-strength region   High-strength region

Figure 2-2 Brace design (Unit: mm)

2.2.2   Fabrication method

Figure 2-3 shows the specimen IHCB-F40 under IH treatment. The images of the cross-section being heated and cooled are also presented. The devices comprised the coils and the water pipes. The IH process is as follows. First, an I-shaped section steel was hung vertically by a crane and placed on a metal foundation. Note that the metal foundation sandwiched the brace, which constrained the brace end movement parallel to the major axis. Then, coils moved smoothly from the bottom of the brace to the top while heating was performed at a temperature not lower than the A3 transformation point about 800 degrees Celsius [2.6)]. Last, the heated regions were rapidly cooled by water. Note that although the partial strengthening and the curve shape can be given to the brace simultaneously by IH treatment, the correlation between the strength improvement ratio and the curvature is yet unclear in this study.

The IH treatment was conducted by Neturen Co., Ltd. The coils were custom-built for the I-shaped section and set close to the flange or web surfaces. It is known that for surface hardening, such as the fabrication of gear, the current frequency is about ten to several hundred kHz. In this case, uniform heat treatment not only on the surface but also on the interior was necessary. Therefore, the current frequency was set as a lower value, within the range of one to ten kHz. The control of the temperature was visually judged from the color of the brace surface which was shown as orange. Further confidential information is unavailable.
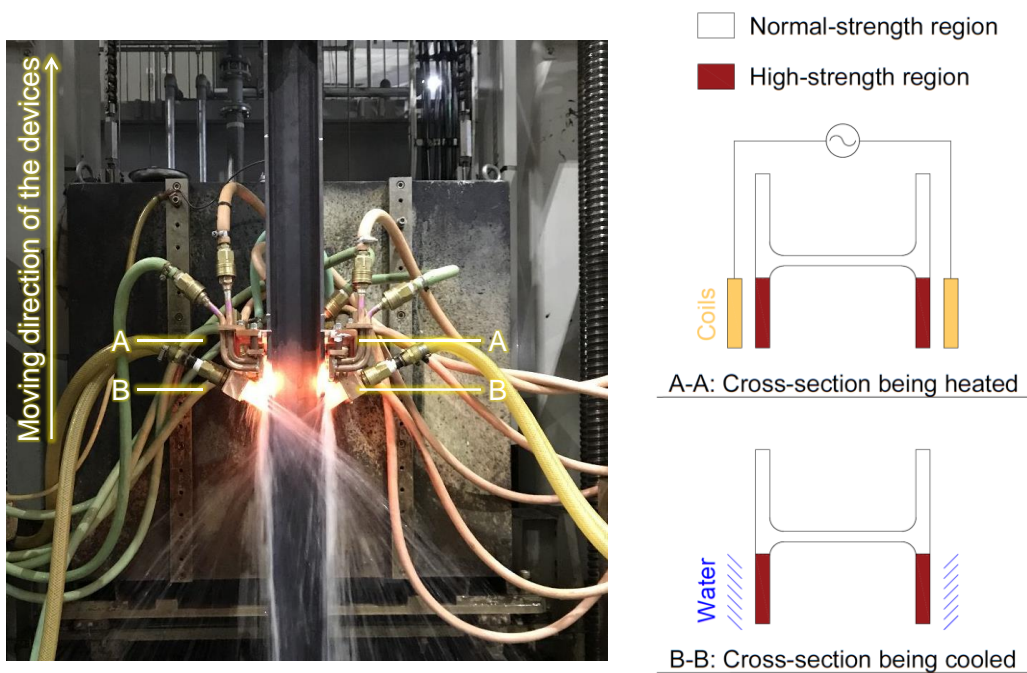
Figure 2-3 Specimen under IH treatment

2.2.3　Longitudinal dimension

IHCB would bend as a circular arc during IH treatment due to uneven heating. To quantify the initial bending deformation, the longitudinal dimensions of five IHCB-F40s, five IHCB-2F60s, and five IHCB-F40W60s were measured. Figure 2-4(a) shows the overall photo of IHCB, which was placed on the floor. The initial bending along the minor axis is observed, and it is idealized in Figure 2-4(b) and summarized in Table 2-2. L_1, L_2, L_3 are defined as the linear length between the brace ends at the inner, middle, and outer sides of the arc, respectively. e is defined as the initial transverse deformation, which is the distance from the floor to the edge of the inner side of the flange at the brace middle. θ is defined as the central angle, under the assumption that the brace is a part of a circle.
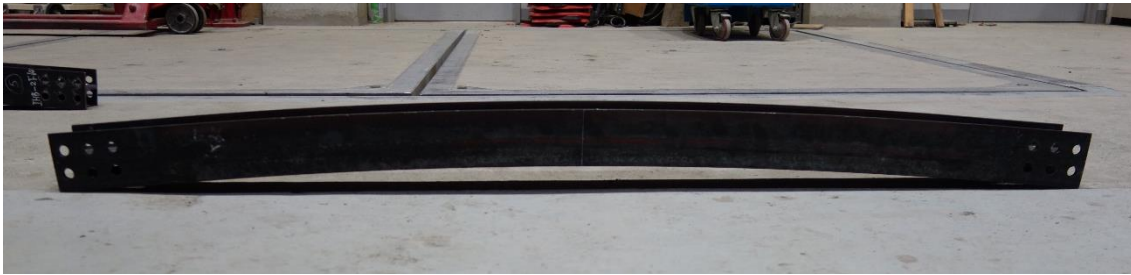
(a) Brace on the floor
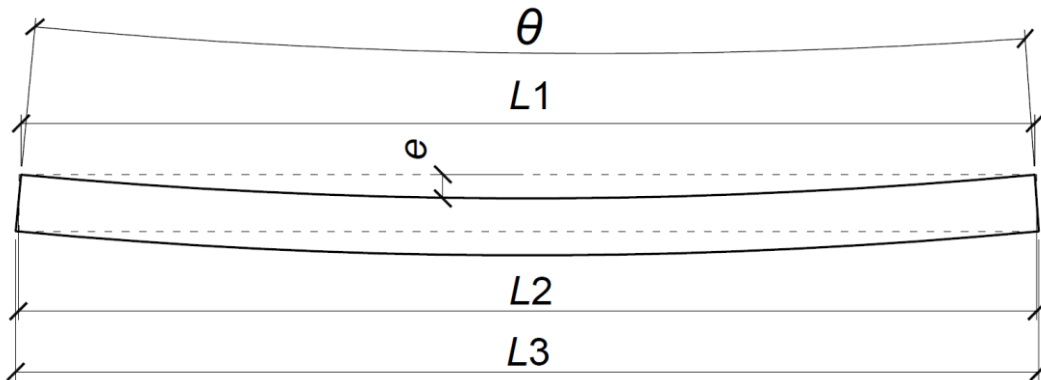
(b) Measurement of the brace in length direction

Figure 2-4 Longitudinal dimension

The shrinkage of the heated region occurred, which made the specimens bent as an arc where the high-strength region was at the inner side. The average linear length at the middle L_2 was 1785 mm for IHCB-F40, 1784 mm for IHCB-2F60, and 1784 mm for IHCB-F40W60, which generally satisfied the designed specimen length of 1783 mm. The initial transverse deformation e ranged from 39.9 mm to 47.1 mm, which was 2.2%-2.6% of the specimen length, and the angle θ ranged from 6.4° to 8.9° with the average from 7.1° to 8.0°.

Surprisingly, the different IH-treated patterns did not bring about obvious changes in the longitudinal dimension. Although it is not clarified yet, one possible reason is that there were temperature differences in the same cross-section during IH treatment. Therefore, the fiber which reached the transformation temperature first, usually the fiber on the surface which was close to the heating devices, was the first one to reach the high strength and also the first one to shrink, thereby, inducing the bending of the whole brace. Once the bending occurred, the change in the deformation became irreversible. Because the treating devices and conditions were the same for all IHCBs, their shape distortions became similar. Note that although there were five specimens for each type of brace, the cyclic loading test to be introduced later was only conducted on one specimen of each type. The remaining specimens were used as the third generation of the I-shaped section steel braces, or the coupons of the fatigue test presented in Chapter 6.

Table 2-2 Measurement of longitudinal dimension of IHCB series

Specimen		Linear length (mm)			Init. transverse def.		Angle (°)
		Inner L_1	Middle L_2	Outer L_3	e (mm)	e/L_2 (%)	θ
IHCB-F40	1	1776	1783	1790	41.5	2.3	8.1
	2	1779	1784	1790	42.9	2.4	6.4
	3	1779	1785	1792	46.2	2.6	7.5
	4	1778	1785	1790	39.9	2.2	6.9
	5*	1780	1786	1791	41.0	2.3	6.6
	Ave.	1778	1785	1791	42.3	2.4	7.1
IHCB-2F60	1*	1777	1783	1790	41.4	2.3	7.2
	2	1776	1783	1790	43.3	2.4	8.3
	3	1776	1784	1791	46.8	2.6	8.9
	4	1777	1785	1791	47.1	2.6	7.8
	5	1776	1784	1790	43.5	2.4	8.0
	Ave.	1776	1784	1790	44.4	2.5	8.0
IHCB-F40W60	1	1777	1785	1791	42.7	2.4	7.8
	2	1777	1784	1790	40.7	2.3	7.2
	3	1777	1785	1791	45.9	2.6	8.1
	4	1776	1784	1790	46.0	2.6	8.1
	5*	1777	1784	1790	40.7	2.3	7.2
	Ave.	1777	1784	1790	43.2	2.4	7.7
All	Ave.	1777	1784	1790	43.3	2.4	7.6

* The tested specimens presented in Section 2.4

2.2.4 Sectional dimension

The changes in the longitudinal dimension were generally accompanied by the changes in the sectional dimension. Therefore, the sectional sizes of all IHCBs were measured. For comparison, the sectional dimensions of five CBBs were measured as well. Figure 2-5(a) shows the photo of the deformed cross-section of IHCB. Figure 2-5(b) and (c) present the definition of the factor in cross-section and the measuring position, respectively. A, B, and C are the cross-sections of one brace end, middle, and the other brace end, respectively. H_1, H_2, and H_3 are the heights, and W_1 and W_2 are the cross-section widths. t_{f1}-t_{f4} are the thicknesses of the flanges at different positions, and t_w is the thickness of the web. The measured data are summarized in Table 2-3, and it was confirmed that the differences among the five specimens of the same kind were minor. Based on the average value of the measured data, the deformed cross-sections of each type of specimen are described in Figure 2-6.

(a) Deformed cross-section   (b) Measurement of the brace in cross-section

(c) Measuring position
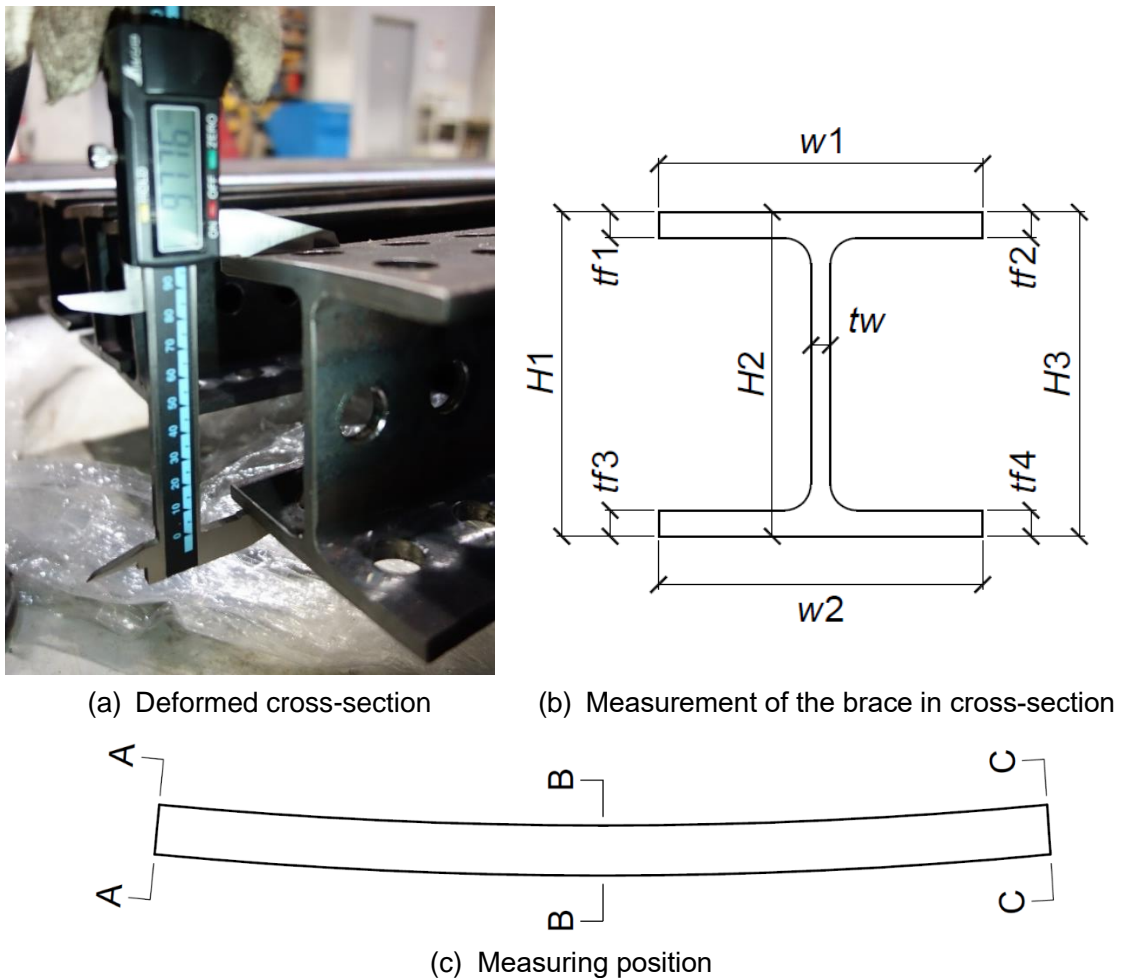
Figure 2-5 Sectional dimension

Table 2-3 Measurement of sectional dimension

Specimen			Height direction (mm)							Width direction (mm)		
			H_1	H_2	H_3	t_{f1}	t_{f2}	t_{f3}	t_{f4}	W_1	W_2	t_w
CBB	1*	A	100.37	100.10	100.17	7.54	7.94	7.81	7.77	99.11	99.61	6.02
		B	100.60	/	100.50	8.18	7.99	7.73	7.74	99.87	99.53	/
		C	97.25	99.70	99.82	7.74	7.84	7.82	8.43	99.82	99.68	6.05
	2	A	100.01	100.49	98.86	7.34	7.46	7.49	7.59	99.62	99.67	6.20
		B	101.05	/	101.16	7.70	8.32	7.59	8.10	99.84	99.91	/
		C	98.20	99.63	98.49	7.63	7.68	7.89	8.34	99.65	99.96	5.77
	3	A	99.45	99.70	98.95	7.39	7.37	7.57	7.64	99.46	99.60	6.04
		B	100.90	/	101.22	7.59	7.94	7.76	7.82	100.03	100.05	/
		C	97.29	99.60	98.10	7.91	7.47	8.05	7.74	99.93	100.10	5.77
	4	A	99.43	100.17	99.25	7.48	7.84	7.28	7.43	99.69	99.78	6.05
		B	100.62	/	101.14	7.72	7.94	8.09	7.68	99.60	100.16	/
		C	97.45	99.64	98.61	7.79	8.15	7.41	7.97	100.02	100.09	5.98
	5	A	99.39	100.52	98.98	7.42	7.30	7.77	7.62	99.60	99.53	6.00
		B	100.80	/	101.34	8.02	7.72	8.12	7.77	98.89	100.06	/
		C	97.92	99.51	98.70	7.85	7.36	7.83	7.79	99.73	99.92	5.85
	Ave.	A	99.73	100.20	99.24	7.43	7.58	7.58	7.61	99.50	99.64	6.06
		B	100.79	/	101.07	7.84	7.98	7.86	7.82	99.65	99.94	/
		C	97.62	99.62	98.74	7.78	7.70	7.80	8.05	99.83	99.95	5.88
IHCB-F40	1	A	99.67	100.11	98.33	7.55	7.34	7.76	7.38	99.55	99.63	6.09
		B	103.34	/	100.91	8.05	7.87	7.95	8.06	99.61	99.5	/
		C	97.44	99.8	96.75	8.23	7.52	8.01	7.63	99.82	99.45	6.18
	2	A	100.63	100.18	100.15	7.83	7.94	7.58	7.33	99.6	99.66	6.15
		B	104.25	/	99.17	7.77	8.35	8.01	7.55	99.6	98.95	/
		C	97.28	99.52	97.45	7.7	7.66	8.04	7.57	99.97	98.88	6.1
	3	A	99.40	100.17	98.33	7.39	7.70	7.28	7.77	99.35	99.84	6.19
		B	103.56	/	100.85	7.83	7.97	7.79	7.64	99.58	99.47	/
		C	98.21	99.47	96.73	7.73	8.07	7.44	7.91	99.93	99.99	5.73
	4	A	99.11	100.74	97.92	7.62	7.32	7.68	7.56	99.66	99.85	5.98
		B	103.57	/	101.61	7.80	7.73	7.83	7.92	99.18	99.16	/
		C	98.78	99.50	99.20	7.96	7.76	8.08	7.54	99.53	100.33	5.85
	5*	A	99.84	100.13	98.83	7.55	7.31	7.78	7.57	99.72	99.54	5.84
		B	103.92	/	100.48	7.76	7.78	8.27	8.21	99.82	99.30	/

Specimen			Height direction (mm)							Width direction (mm)		
			H_1	H_2	H_3	t_{f1}	t_{f2}	t_{f3}	t_{f4}	W_1	W_2	t_w
		C	97.92	99.46	97.58	7.55	7.39	7.93	7.81	99.85	99.81	5.84
	Ave.	A	99.73	100.27	98.71	7.59	7.52	7.62	7.52	99.58	99.70	6.05
		B	103.73		100.60	7.84	7.94	7.97	7.88	99.56	99.28	
		C	97.93	99.55	97.54	7.83	7.68	7.90	7.69	99.82	99.69	5.94
IHCB-2F60	1*	A	99.27	99.99	99.14	7.59	7.37	7.65	7.51	99.63	99.09	5.85
		B	100.10		100.71	7.86	7.73	7.77	7.67	99.73	99.78	
		C	97.92	99.62	98.58	7.94	7.62	7.91	7.66	100.21	99.73	5.75
	2	A	99.61	100.01	98.57	7.46	7.25	7.76	7.63	99.70	99.65	5.85
		B	100.67		100.56	7.64	7.69	7.94	7.85	99.86	100.02	
		C	98.71	99.84	98.27	7.75	7.66	7.85	7.78	100.08	99.60	5.86
	3	A	99.14	100.04	99.16	7.56	7.26	7.66	7.52	100.17	99.00	5.78
		B	101.26		100.59	7.92	7.79	7.81	7.72	99.95	99.79	
		C	98.52	99.91	98.69	7.74	7.69	7.92	7.78	99.91	100.00	5.94
	4	A	99.95	100.10	99.20	7.60	7.38	7.70	7.49	99.58	99.56	5.81
		B	100.86		100.50	7.95	7.69	7.90	7.81	99.82	99.76	
		C	98.75	99.59	98.44	7.95	7.57	8.03	7.88	99.91	99.74	6.05
	5	A	99.34	99.95	98.67	7.42	7.25	7.83	7.54	99.66	99.14	5.75
		B	100.84		100.76	8.06	7.70	7.83	7.77	100.05	99.87	
		C	99.01	99.76	97.94	7.68	7.71	7.71	7.82	99.81	99.66	5.79
	Ave.	A	99.46	100.02	98.95	7.53	7.30	7.72	7.54	99.75	99.29	5.81
		B	100.75		100.62	7.89	7.72	7.85	7.76	99.88	99.84	
		C	98.58	99.74	98.38	7.81	7.65	7.88	7.78	99.98	99.75	5.88
IHCB-F40W60	1	A	97.56	99.33	97.83	7.56	7.28	8.03	7.50	99.58	99.40	5.83
		B	101.06		99.88	7.68	7.70	8.09	7.79	99.80	99.52	
		C	96.46	99.08	98.84	7.62	7.40	7.95	7.88	100.19	99.85	5.80
	2	A	99.03	100.06	98.24	7.47	7.37	7.55	7.33	99.65	99.20	6.10
		B	101.22		99.75	7.65	7.75	7.85	7.60	99.10	99.23	
		C	96.71	99.48	98.51	7.96	7.45	7.95	7.61	99.89	99.87	5.88
	3	A	99.03	100.34	98.27	7.32	7.62	7.32	7.64	99.29	99.92	6.02
		B	104.37		97.93	7.71	7.84	7.82	7.77	99.37	99.19	
		C	99.21	99.68	95.95	7.65	7.72	7.55	7.79	99.79	99.91	5.83
	4	A	98.50	100.08	98.45	7.36	7.53	7.30	7.44	99.19	99.80	6.00
		B	104.34		99.24	7.84	8.07	7.96	7.66	99.41	99.75	

Specimen			Height direction (mm)							Width direction (mm)		
			H_1	H_2	H_3	t_{f1}	t_{f2}	t_{f3}	t_{f4}	W_1	W_2	t_w
		C	99.46	99.74	96.19	7.65	7.70	7.56	7.73	99.87	99.95	5.72
	5*	A	95.40	99.82	95.98	7.84	8.13	7.66	7.78	100.05	99.90	5.78
		B	100.39	/	101.14	7.80	7.80	7.68	7.72	99.47	99.59	/
		C	98.16	100.15	98.98	7.44	7.63	7.28	7.79	99.67	99.56	5.84
	Ave.	A	97.90	99.93	97.75	7.51	7.59	7.57	7.54	99.55	99.64	5.95
		B	102.28	/	99.59	7.74	7.83	7.88	7.71	99.43	99.46	/
		C	98.00	99.63	97.69	7.66	7.58	7.66	7.76	99.88	99.83	5.81
All IHCBs	Ave.	A	99.03	100.07	98.47	7.54	7.47	7.64	7.53	99.63	99.55	5.93
		B	102.25	/	100.27	7.82	7.83	7.90	7.78	99.62	99.53	/
		C	98.17	99.64	97.87	7.77	7.64	7.81	7.75	99.90	99.76	5.88

* The tested specimens presented in Section 2.4

The center lines are shown in grey dashed lines in Figure 2-6. Since all specimens were treated at the brace ends, the deformed cross-sections of A and C for all specimens were similar. The upper and bottom flanges tended to get closer to each other under the constraint of the web, which finally led the edges of the flanges to bend inwards. The cross-section of B for CBB was normal since it was untreated. For IHCB-F40 and IHCB-F40W60, due to the uneven treatment at the cross-section, the treated edges of the flanges bent inwards, while the untreated ones bent outwards. The height difference between the treated and untreated sides was about 3 mm. For IHCB-2F60, no obvious deformation was observed, which might be attributed to the symmetrical IH treatment. Though the slight torsion along the length was seen in IHCBs, mainly due to the different deformed cross-sections of the same specimen, this imperfection was difficult to evaluate. Since the effect of the torsional imperfection was minor, which will be proved later in the analytical research in Chapter 3, this study neglected the torsional imperfection.

Note that the unmeasurable data were manually corrected based on measured data and the actual shape of the specimens. For example, the value of H_2 at the cross-section of B was unmeasurable for all specimens. Thus, this value was calculated as the average value of H_2 at the cross-sections of A and C. Besides, to simplify the shape of the cross-section, the measured points were connected by a straight line instead of a curve line. The specimens CBB-1, IHCB-F40-5, IHCB-2F60-1, and IHCB-F40W60-5, were used for the loading tests, and their names were simplified as CBB, IHCB-F40, IHCB-2F60, and IHCB-F40W60 in the following discussions.

CBB

IHCB-F40

IHCB-2F60

IHCB-F40W60

A   B   C
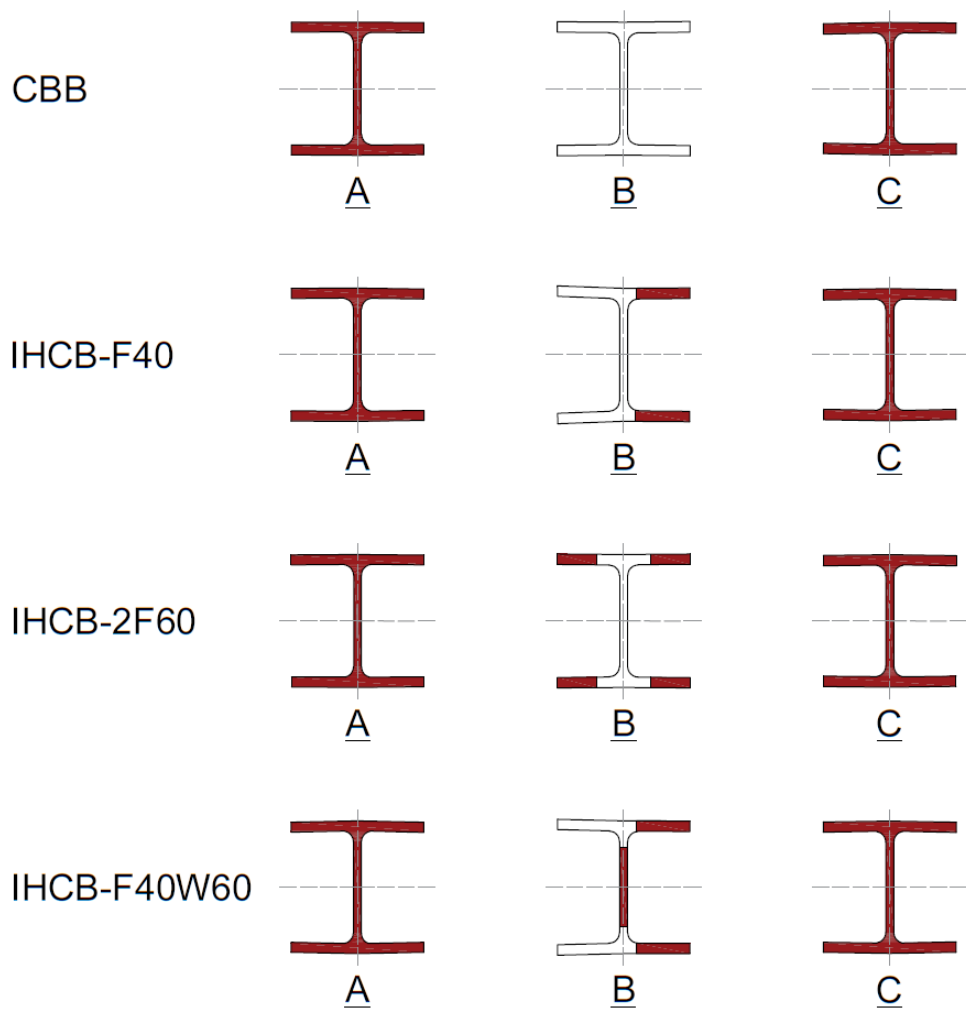
Figure 2-6 Deformed cross-sections

2.3　Outlines of material

2.3.1　Chemical composition

As mentioned in Section 1.3, IH treatment involves a solid solution of carbon. Therefore, the higher the carbon content is, the better the IH effect will be. The chemical composition of the material used is shown in Table 2-4. The carbon content of SS400 was at a lower level about 0.13%. The carbon equivalent content ($= C + Mn/6 + Si/24 + Ni/40 + Cr/5 + Mo/4 + V/14$) was 0.23%. Note that there is not a clear limit on the carbon content for the material SS400. The reason why this study used SS400 as the brace material was that the most of I-shaped section steels were produced from SS400 steel.

Table 2-4 Chemical composition*

C (%)	Si (%)	Mn (%)	P (%)	S (%)
0.13	0.19	0.54	0.018	0.015

* According to the inspection certificate

2.3.2　Tensile coupon tests

Six normal-strength coupons (three from the flange and three from the web) and six IH-treated high-strength coupons (three from the flange and three from the web) were tested by a universal testing machine. The coupon regions from the specimen IHCB-F40W60 are shown in Figure 2-7. Take the high-strength coupon from the flange as an example. First, the plate with the size of $660 \times 41 \times 8$ mm (= length × width × thickness) was obtained by gas cutting. Note that due to the curve shape of the brace, the width of 0 mm - 1 mm from the flange edge was removed. The remaining fillet which connected the flange and web was also removed. Next, the plate was processed to a similar shape as the designed coupon dimension by wet cutting. Note that the wet cutting was adopted here to avoid re-heat treating the high-strength coupon. Last, the parallel part of the test region with 220 mm length was made by electrical discharge machining (EDM). The gauge length was 200 mm.
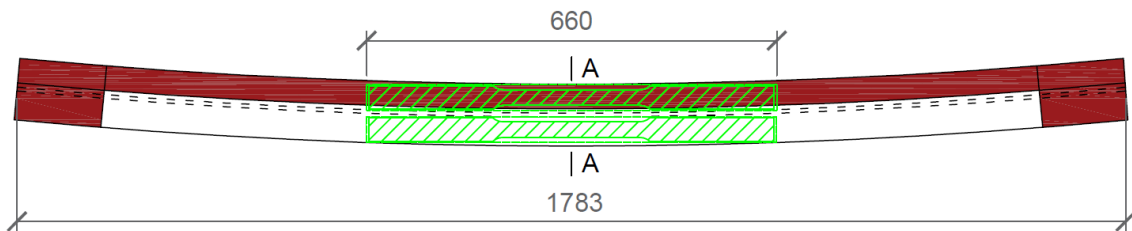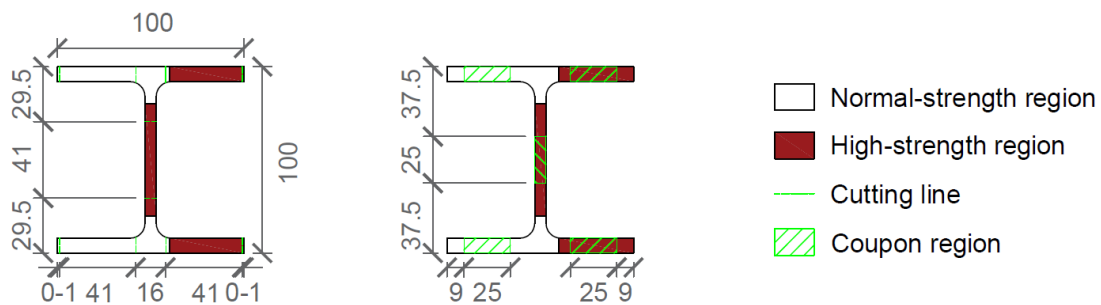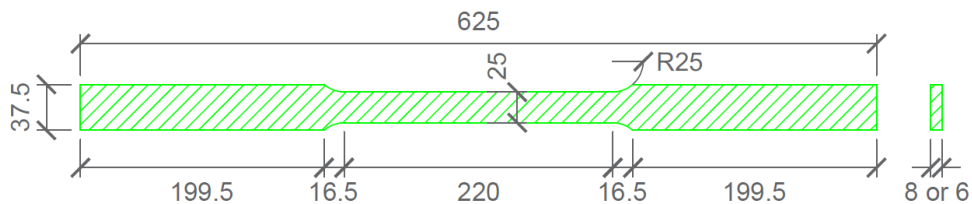
Figure 2-7 Tensile coupon designs (Unit: mm)

The stress-strain relationships are shown in Figure 2-8. The differences among three coupons of the same kind were negligible, and the apparent improvement in the strength of the IH-treated coupons was observed.

(a) Coupons from the flange   (b) Coupons from the web
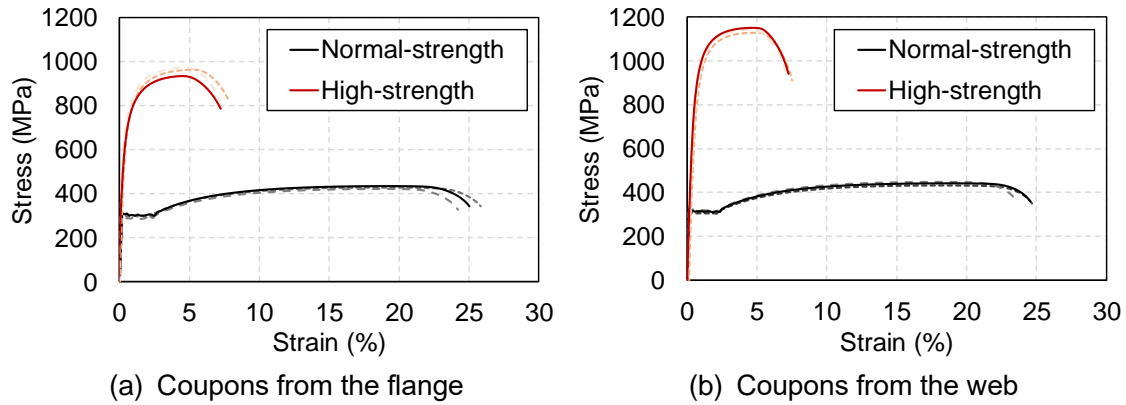
Figure 2-8 Tensile coupon test results

The average values are summarized in Table 2-5. Young's modulus remained unchanged after IH treatment. The ratios of the yield and tensile strengths of the high-strength coupon to those of the normal-strength coupon were approximately 2.2 at the flange and 2.6 at the web. The slightly different IH effect between the flange and web was mainly attributed to the different thicknesses, where the control of the quenching rate at the web, which was thinner, was much easier. On the other hand, the elongation of the high-strength coupon decreased to one-third of the normal-strength coupon. It is confirmed that IH technology can work as an effective way to raise the strength of structural steel even if the carbon content was not so high, but the lower ductility induced by IH treatment should be paid attention to.

Table 2-5 Material properties

Coupon		Young's modulus (GPa)	Yield		Tensile strength (MPa)	Elongation (%)
			Strength (MPa)	Strain (%)		
Normal-strength	Flange	194	304.4	0.16	425.3	25.8
	Web	203	326.5	0.16	438.5	24.7
High-strength (High / normal)	Flange	195 (1.0)	678.1* (2.2)	0.35 (2.2)	952.3 (2.2)	7.8 (0.3)
	Web	196 (1.0)	846.5* (2.6)	0.43 (2.6)	1134.7 (2.6)	7.8 (0.3)

* 0.2% proof stress

2.3.3 Vickers hardness tests

Vickers hardness tests were conducted to investigate the hardness and range of the IH-treated region of all specimens. There were six points measured in the I-shaped cross-section. Points 1, 2, and 3 were for the flange, and points 4, 5, and 6 were for the web. Points 1, 3, 4, and 6 were 1 mm from the surface, and Points 2 and 5 were at the mid-depth of the flange and web, respectively. The measurement was conducted at every 5 mm in the total length of 100 mm at the brace end of CBB and the brace middle of IHCB-2F60, and 50 mm at the brace middle of IHCB-F40. The Vickers hardness test results were converted to the tensile strength based on the hardness conversion table. Generally, the ratio of the Vickers hardness to the tensile strength was about 3/10.

The Vickers hardness test results and the converted tensile strength for CBB at the flange and web are shown in Figure 2-9(a) and (b), respectively. The results for IHCB-F40 and IHCB-2F60 at the flange are shown in Figure 2-10(a) and (b), respectively. For the Vickers hardness test results, the measured locations are shown at the bottom of each figure. The converted results are shown with t in the legend. The tensile strengths obtained from the tensile coupon tests are shown as horizontal dashed lines for comparison.

First of all, the hardness deviations at different points at the same location were observed. The ones near the heating devices, which were Point 1 for the flange and Point 4 for the web, tended to show the largest hardness. While, the ones far from the heating devices, which were Point 3 for the flange and Point 6 for the web, showed the lowest. It is because the effect of IH treatment depends on the heating and quenching conditions, and those close to the IH-treated surfaces were treated more effectively. The position relation of the devices and the IH-treated surfaces is referred to as Figure 2-3. For easy understanding, the following discussions on hardness are based on the converted tensile strength.

At the brace end of CBB, see Figure 2-9, the results at the flange and web showed different features. The flange was more uniformly treated than the web, but the converted tensile strength was lower than the tensile strength of the high-strength coupon overall. It was mainly because the high-strength coupons were cut out from the flange of the brace middle of the IHCB series, where the IH-treated widths were smaller than those of the brace end. Thus, the larger IH-treated regions at the brace end increased the quenching difficulty, and it eventually led to lower tensile strength. By comparison, the converted tensile strength of the web at Point 6 was consistent with the tensile strength of the high-strength coupon for a width of about 40 mm. The converted tensile strength of the web was higher than that of the flange mainly due to the smaller thickness of the web.
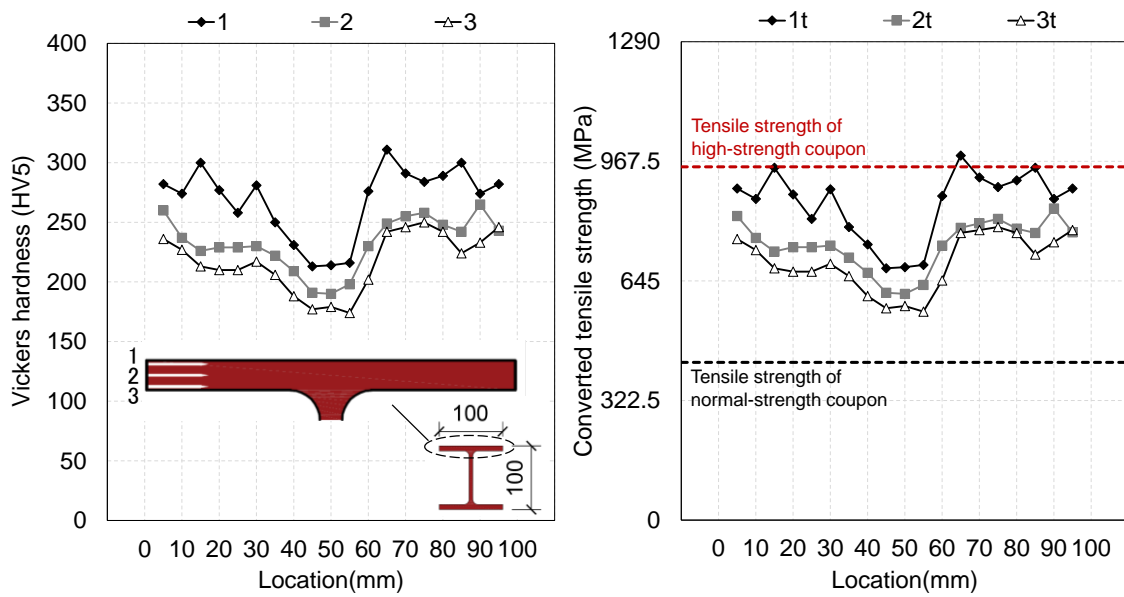
(a) Brace end of CBB (flange)
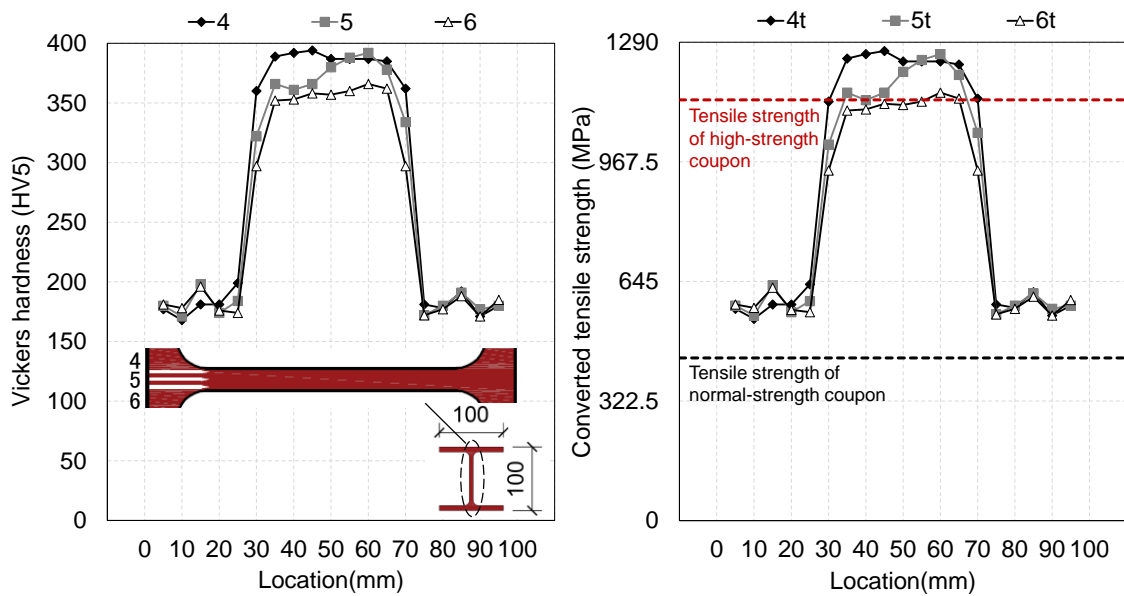
(b) Brace end of CBB (web)

Figure 2-9 Vickers hardness test results at the brace end

The load capacity at the brace end was inferred based on the converted tensile strengths. By multiplying the converted tensile strength and the area of the corresponding region, the maximum tensile load at the brace end was calculated as 1060 kN at the cross-section without bolt holes, and 702 kN with bolt holes. The calculated value of 702 kN was lower than the designed value of 1180 kN which will be presented in Section 2.4.4, since the junctions between the web and flanges, which were designed to be IH-treated, were nearly untreated due to the limitation of the coil size.

Though the calculated maximum tensile load was not high enough to meet the designed value, this value might not be real due to the errors in the hardness conversion and IH-treated regions. A higher fracture load of the brace end was obtained from the experiment, which will be explained in Section 2.6. Therefore, 702 kN was for reference only.
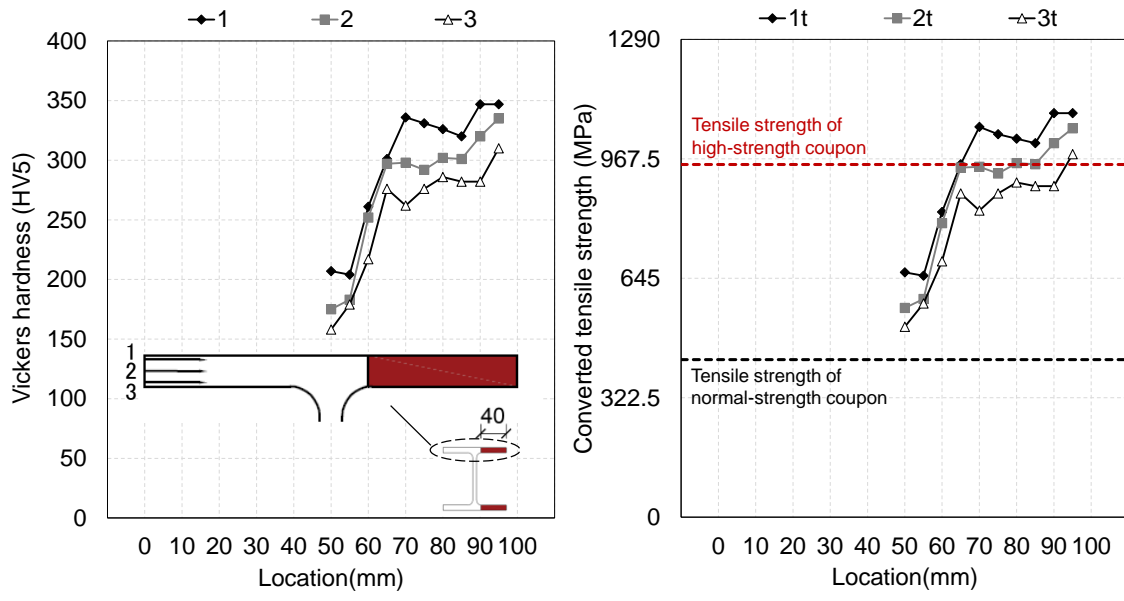
(a) Brace middle of IHCB-F40 (flange)
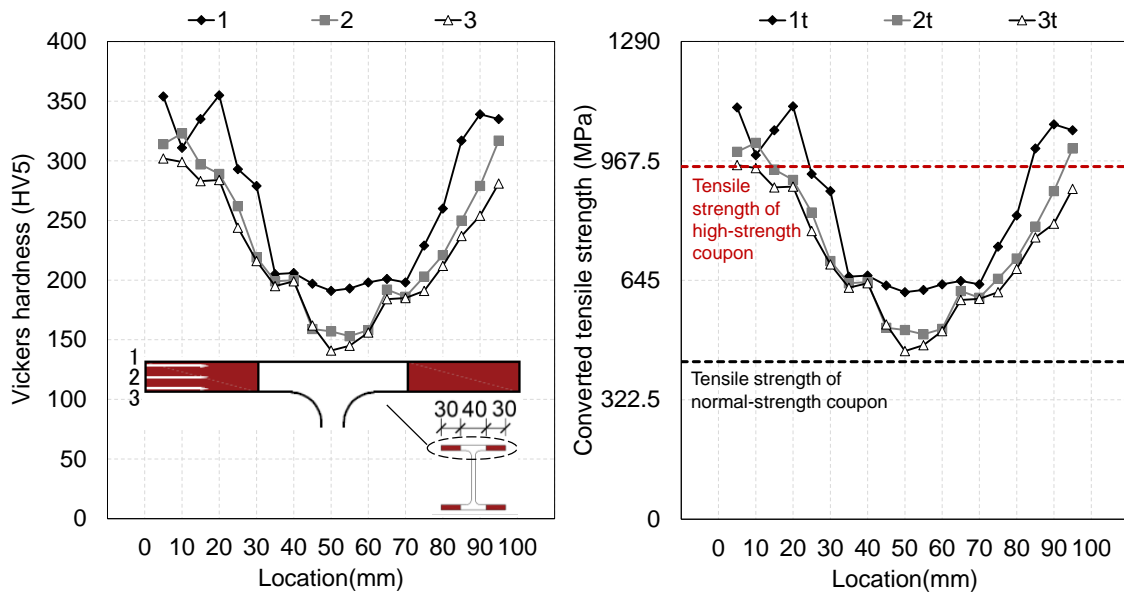
(b) Brace middle of IHCB-2F60 (flange)

Figure 2-10 Vickers hardness test results at the brace middle

For IHCB-F40, see Figure 2-10, the converted tensile strength was approximately 950 MPa at the flange edge, agreeing with the tensile strength of the high-strength coupon, for a width of about 35 mm. Then, the converted tensile strength gradually decreased to about 500 MPa towards the web. For IHCB-2F60, the converted tensile strength remained no less than 950 MPa for 15 mm - 20 mm from two flange edges, and then gradually reduced with the decrease of the distance to the web. Thus, compared to the designed IH-treated widths, the measured IH-treated widths were 5 mm - 15 mm shorter. The converted tensile strength of the designed untreated region was higher than the tensile strength of the normal-strength coupon for both specimens. It was pointed out by a previous study that the precision of the converted tensile strength decreased when the value was lower than 700 MPa, and the deviation within 100 MPa might exist [2.7]. In all, it is confirmed that IH technology is a controllable way to raise the material strength in the designed region although the deviation in the IH range of about 15 mm should be allowed in this case.

2.4　Outlines of experiment

2.4.1　Loading setup

The loading setup is shown in Figure 2-11. One boundary of the specimen was connected to a concrete block fixed to the reaction floor, and the other boundary was connected to a jack through a channel guide. The channel guide ensured that the brace was pushed or pulled only in the axial direction, and the details are demonstrated in Figure 2-12.

(a)　Front view of loading setup

(b)　Top view of loading setup

(c)　Back view of loading setup
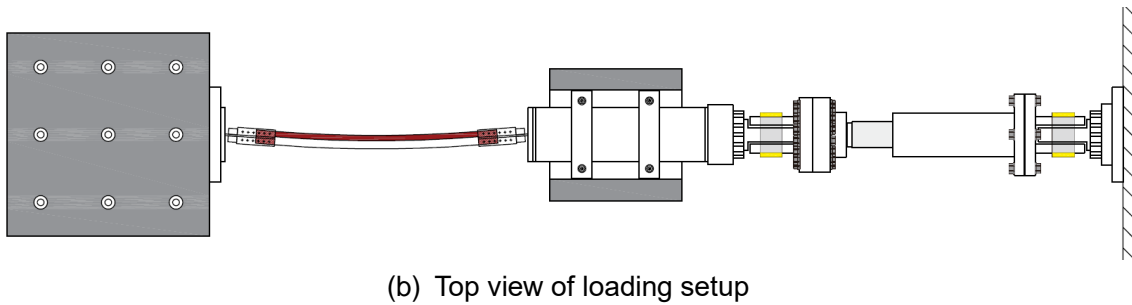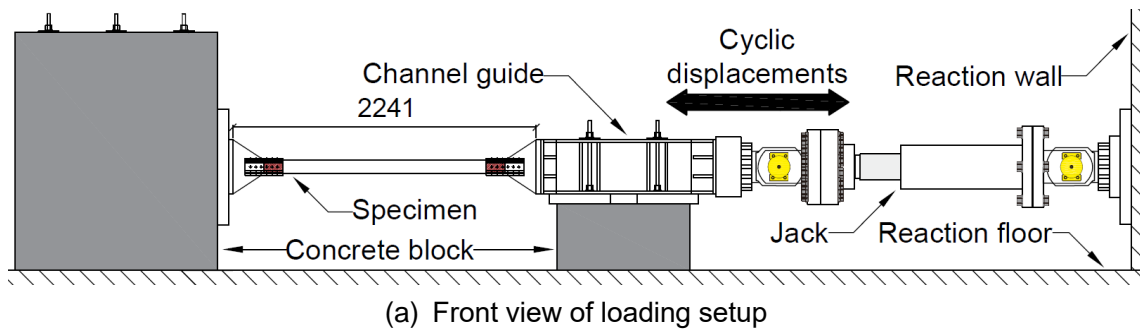
Figure 2-11 Loading setup: example of IHCB-F40 (Unit: mm)

One foundation, two channels with vertical stiffeners, and two cover plates were integrated and fixed to the floor by four vertical PT bars called channel guide. In the channel guide, an I-shaped $400 \times 400 \times 13 \times 21$ mm section steel with longitudinal stiffeners was employed to transfer the axial force. Two steel plates were welded at the ends of the I-shaped section steel for the bolt joint, and it was wrapped with Teflon sheets on four faces along the axial direction to ensure it was slidable with reduced friction. The measured friction force was about 3.0 kN while pushed or pulled, which was neglected in the test.
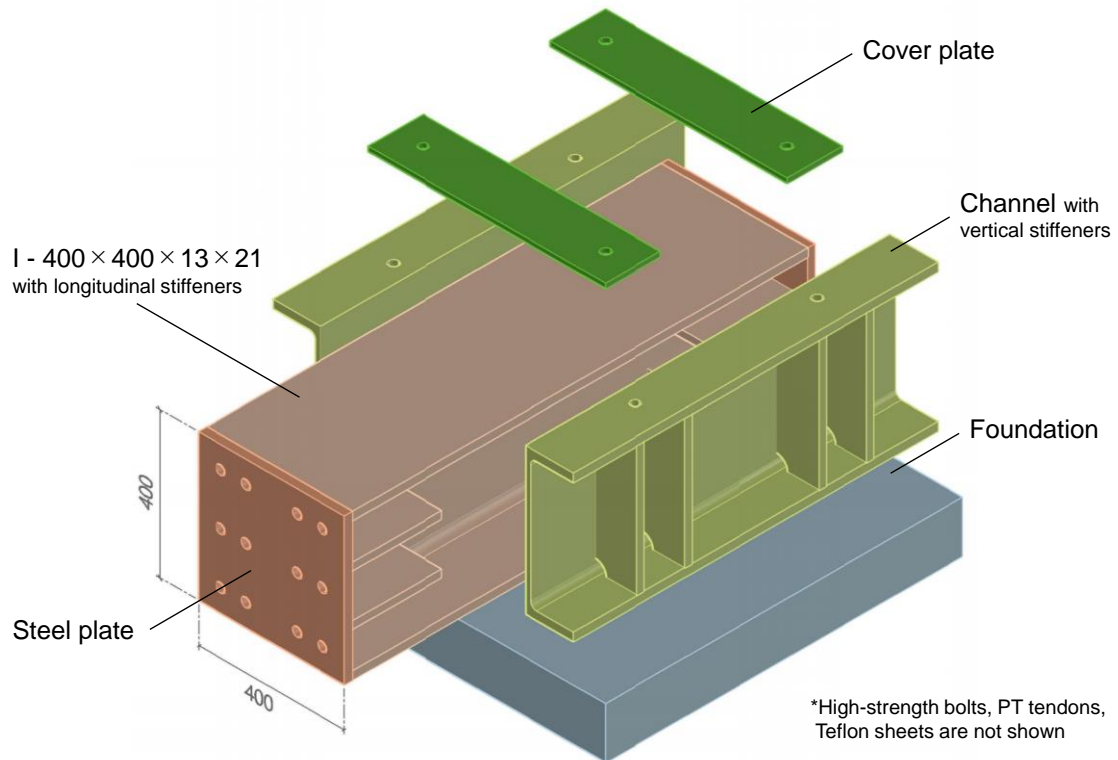
(a) Detail of channel guide

(b) Channel guide

Figure 2-12 Channel guide (Unit: mm)

2.4.2 Loading protocol

Cyclic axial displacements were applied to the specimen from 0.1% peak axial strain, via 0.15%, 0.3%, 0.45%, 0.6%, 0.9%, to 1.2% peak axial strain. Two full cycles were applied at each peak axial strain, and the first quarter-cycle was under compression, summarized in Table 2-6 and Figure 2-13. The axial strain was defined as the ratio of the axial deformation to the supported length of 2241 mm. The story drift ratio was calculated when the brace was placed in a single diagonal bracing system with an angle of 45°.

Table 2-6 Loading protocol

Axial strain (%)	Story drift ratio (%)	Number of cycles
0.10	0.20	2
0.15	0.30	2
0.30	0.60	2
0.45	0.90	2
0.60	1.20	2
0.90	1.80	2
1.20	2.40	2
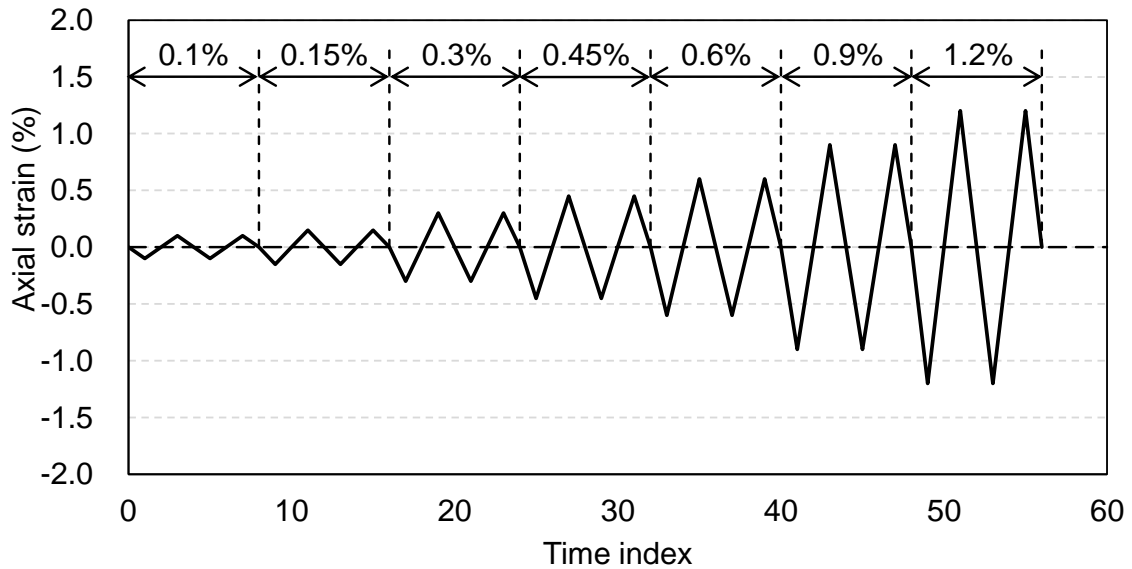
Figure 2-13 Loading protocol

2.4.3 Measurement setup

Figure 2-14 demonstrates the measurement setup. Figure 2-14(a) shows the locations of the displacement transducers. Wire-type displacement transducers were attached at seven cross-sections. For each cross-section, there were three displacement transducers. To measure the transverse deformation, which was the deformation around the minor axis, as well as the torsion along the brace length, fourteen displacement transducers, seven at the upper flange and seven at the bottom flange were used. They were horizontally connected to the specimen by studs welded at the mid-depth of the upper and bottom flanges. Seven displacement transducers were vertically connected to the upper flange for the deformation around the major axis. Besides, the baseline connecting the center of the two end plates was used to evaluate the curve level, where the transverse deformation is defined as 0. Beyond those presented in the figure, four contact-type displacement transducers were attached in the axial direction for the strain control, and another three contact-type displacement transducers were attached to the end plates for measuring the rotation of the brace ends.

Figure 2-14(b) presents the locations of the strain gauges at the flanges and the web. Strain gauges were attached to five cross-sections. For each cross-section, two strain gauges were attached at the upper flange, two at the web, and two at the bottom flange.
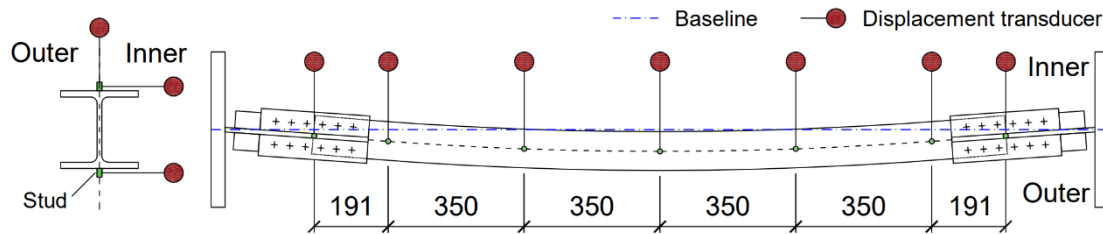
(a) Location of wire-type displacement transducer
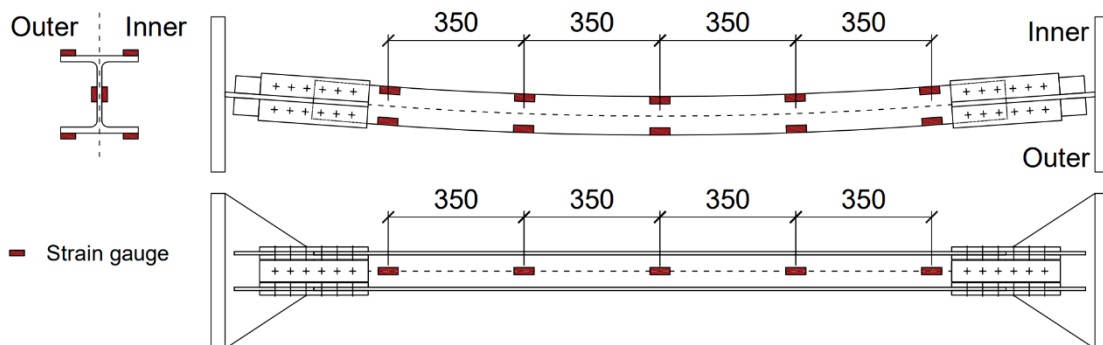
(b) Location of strain gauge
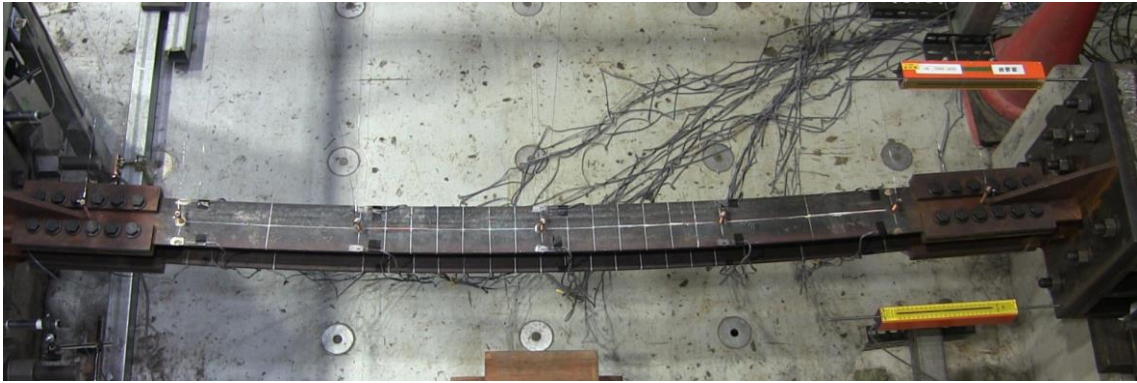
(c) Top view of measurement setup
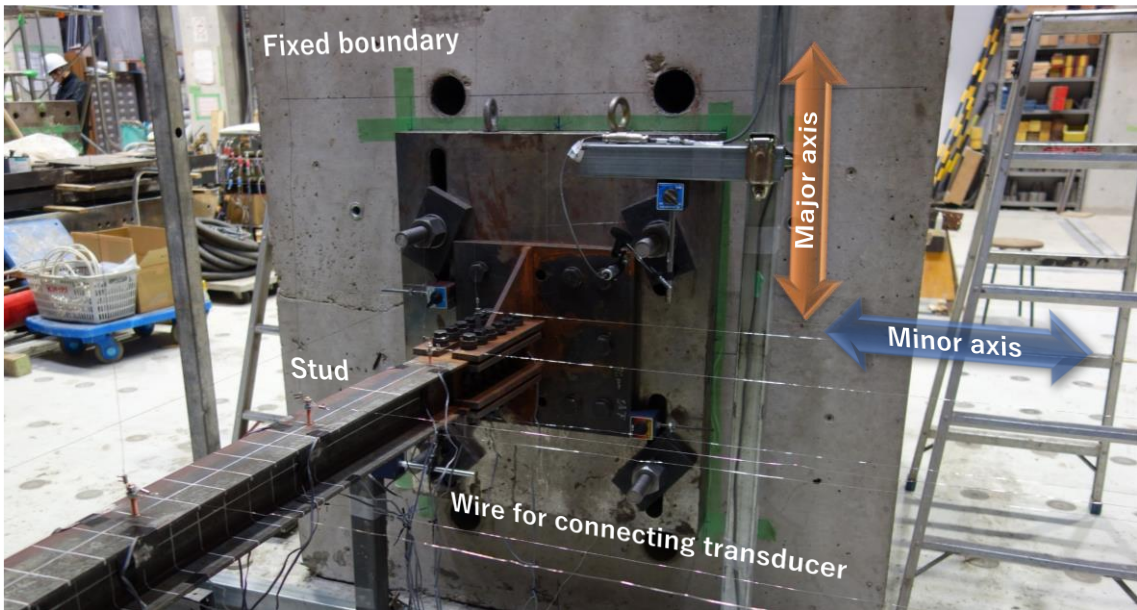
(d) Detail of measurement setup

Figure 2-14 Measurement setup (Unit: mm)

2.4.4 Joint detail

The designed joint composition is shown in Figure 2-15.
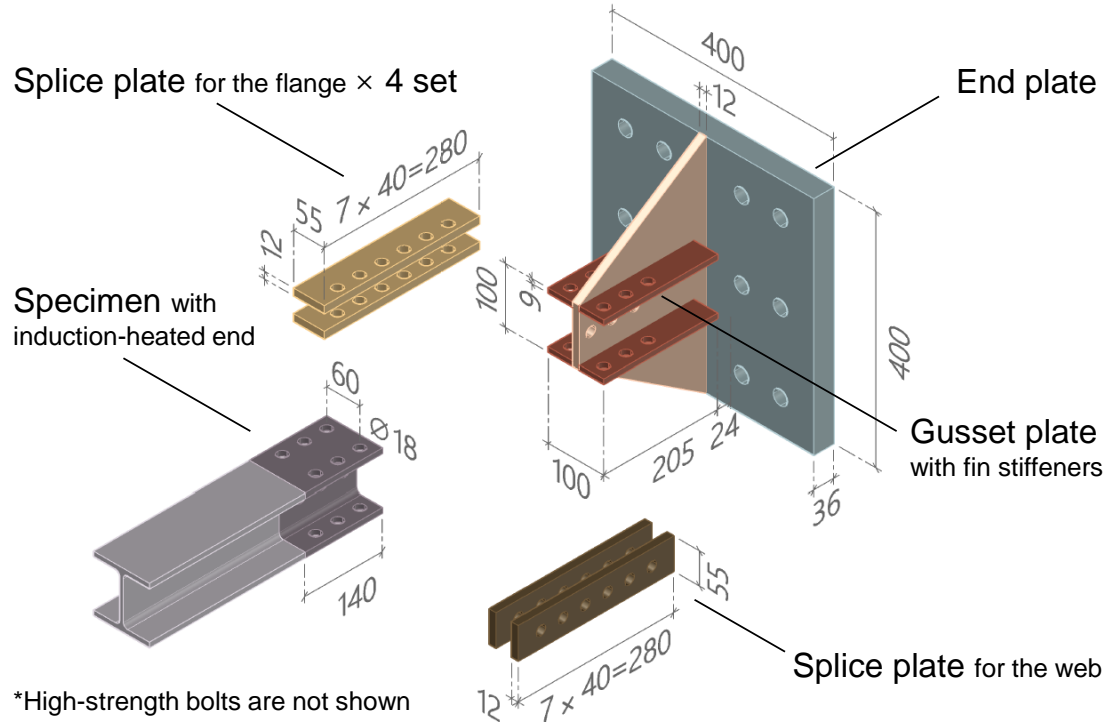
Figure 2-15 Joint detail (Unit: mm)

Material SS400 (nominal yield strength = 235 MPa, nominal tensile strength = 400 MPa) was used for the brace as presented in Section 2.2.1, and material SM490 (nominal yield strength = 325 MPa, nominal tensile strength = 490 MPa) was used for the joint. It is confirmed that the strength ratio of the high-strength region to the normal-strength region was 1.2-1.4 from the study on the first generation of the I-shaped section steel brace [2.8]. Therefore, the strength ratio, K, was assumed as 2 in this study since a higher strength ratio was hard to expect. The yield load, P_y, of IHCB-F40W60, which ignored the curve shape was 742 kN as written in Eq. 2-1.

$$P_y = A_{high} \times 235 \times K + A_{normal} \times 235 = 742 \text{ kN} \qquad \text{Eq. 2-1}$$

Where,

$A_{high} = 40 \times 2 \times 8 + 60 \times 6 = 1000$ mm². It is the cross-sectional area of the high-strength region. The specimen IHCB-F40W60 is considered here since it has the largest cross-sectional area of the high-strength region among the four braces.

$A_{normal} = A - A_{high} = 1159$ mm². It is the cross-sectional area of the normal-strength region.

$A = 2159$ mm². It is the cross-sectional area of the I-shaped $100 \times 100 \times 6 \times 8$ mm section.

The brace ends were IH-treated for a length of 140 mm to compensate for the load capacity loss due to the bolt holes. There were five bolt holes at one cross-section, one at the web and four at the flanges with a diameter of 18 mm. Note that the shear failure of the bolts or the tear failure of the brace end required relatively large loads. Therefore, the maximum tensile load at the brace end was decided by the tension failure at the cross-section weakened by the bolt holes. The maximum tensile load at the brace end, $P_{u,end}$, was calculated as 1180 kN as demonstrated in Eq. 2-2. This value satisfied the required performance of the brace end as presented in Section 2.1.

$$P_{u,end} = A_{end} \times 400 \times K = 1180 \text{ kN}$$

$$\frac{P_{u,end}}{P_y} = \frac{1180}{742} = 1.6, \text{ satisfies the target performance}$$

Eq. 2-2

Where,

$A_{end} = A - 4 \times 18 \times 8 - 18 \times 6 = 1475$ mm².

The brace end was connected to the gusset plate at the web and fin stiffeners at the flanges by 15 high-strength bolts F10TM16 (tensile strength ≥ 1000 MPa, diameter = 16 mm for one bolt) at each side. The slip load of the joint, P_{slip}, was 1431 kN as calculated in Eq. 2-3. The safety factor for preventing slippage, which was the ratio of the slip load to the maximum tensile load at the brace end, was 1.2.

$$P_{slip} = nm\mu_s N_{b0} = 15 \times 2 \times 0.45 \times 106 = 1431 \text{ kN}$$

$$\frac{P_{slip}}{P_{u,end}} = \frac{1431}{1180} = 1.2$$

Eq. 2-3

Where,

$n =$ Number of bolts.

$m =$ Number of friction surfaces.

$\mu_s =$ Friction coefficient.

$N_{b0} = \frac{N_{bi}}{1.1} =$ Designed tensile force of one bolt.

$N_{bi} = 117$ kN. It is the initial tensile force of one bolt.

The torque control method was used for the bolted connection. Five sets of the splice plates, one for the web and four for the flanges, were used to ensure the friction joint. For each bolt, the torque T was 318 N·m as written in Eq. 2-4.

$$T = kd_sN_{bi} = 0.17 \times 16 \times 117 = 318 \text{ N·m} \qquad \text{Eq. 2-4}$$

Where,

$k =$ Torque coefficient.

$d_s =$ Diameter of the bolt.

The calculation of the minimum thickness of the gusset plate is shown in Eq. 2-5. Because the value should be larger than 10.8 mm, a 12-mm-thick steel plate was used as the gusset plate. The clearance was designed as the length of $2t = 24$ mm. The clearance region was expected to yield and rotate around the minor axis, which ensured the pin-supported condition of the brace.

$$b_e = H + 2 \times \tan 30 \times L_{stiffness} = 100 + 2 \times \tan 30 \times 205 = 337 \text{ mm}$$

$$t_{gusset} \geq \frac{P_{u,end}}{b_e \times 325} = \frac{1180}{337 \times 325} = 10.8 \text{ mm} \qquad \text{Eq. 2-5}$$

Where,

$b_e =$ Effective width of the gusset plate. It assumes that the axial load of the brace is transmitted to the clearance region of the gusset plate within an angle of 30° from the horizontal axis.

$H =$ Height of I-shaped section.

$L_{stiffener} =$ Length of the stiffener.

$t_{gusset} =$ Thickness of gusset plate.

Four fin stiffeners with 9 mm thick were welded to the gusset plate. Because of the thickness difference between the 12 mm-thick gusset plate and the 6 mm-thick web, thin steel plates were used to compensate for the gap. The gusset plates were welded at the end plate. The end plate was connected to the I-shaped 400 × 400 × 13 × 21 mm section steel shown in Figure 2-12(a) by no less than 6 high-strength bolts F14TM22 (tensile strength ≥ 1400 MPa, diameter = 22 mm for one bolt). The maximum tensile load to keep them tightened, $P_{tightness}$, was 1614 kN, as presented in Eq. 2-6. The safety factor for preventing the separation of the end plate and the loading device was 1.4.

$$P_{tightness} = nN_{bt} = 6 \times 269 = 1614 \text{ kN}$$

$$\frac{P_{tightness}}{P_{u,end}} = \frac{1614}{1180} = 1.4 \qquad \text{Eq. 2-6}$$

Where,

$N_{bt} =$ The force to keep the bolt tightened.

Last, to connect the joint to IHCB which was curved, the gusset plates at two ends were slightly bent around the minor axis by a universal testing machine. The eccentricity of the joint was approximately 7 mm after bending, based on the curvature of IHCBs.

2.5   Experiment results

2.5.1   Load-axial strain relationships

Cyclic loading tests on CBB, IHCB-F40, IHCB-2F60, and IHCB-F40W60 were conducted. The load-axial strain relationships and the skeleton curve are illustrated in Figure 2-16. The tensile and compressive load capacities are shown in Table 2-7 and Table 2-8, respectively. The value in bracket ( ) shows the ratio of the corresponding value to that of CBB. Tension is positive.

The definitions of each parameter are shown below.
- Axial strain (%): the ratio of the axial deformation to the supported length of 2241 mm.

Under tension:
- Initial stiffness (GPa): the slope between the yield point and the origin when considered in the graph of the stress-strain relationship.
- First post-yield stiffness (GPa): the slope between two points, one is at the 1st cycle of +0.3% peak axial strain, and the other is at the 1st cycle of +0.9% peak axial strain. Note that the 1st cycle of +0.3% axial strain is the assumed yield cycle, and the 1st cycle of +0.9% axial strain is regarded as 3 times the yield cycle of the IHCB series. It is corresponding to the definition of the strain range of the target post-yield stiffness presented in Section 2.1. Besides, the first post-yield stiffness is abbreviated as the post-yield stiffness in this study.
- Second post-yield stiffness (GPa): the slope after the 1st cycle of +0.9% peak axial strain. Note that this value is consistent with the post-yield stiffness of the material property. Thus, this study does not discuss this issue in detail.
- Yield load (kN): there are two conditions for the definition of the yield point. First, the point when the stiffness starts to be lower than 95% of the elastic stiffness. Second, the stiffness in the following loading step does not increase anymore. Since it is hard to predict the elastic behavior of the IHCB series for their curve shapes, the elastic stiffness is defined as the stiffness at the 1st cycle of +0.1% peak axial strain.
- Maximum tensile load (kN): the maximum load under tension.

Under compression:
- Buckling load (kN): the load while it suddenly decreases with the increase of the axial strain on the compressive side. It is the start point of the convex curve in the load-displacement relationship.
- Maximum compressive load (kN): the maximum load under compression.
- Post-buckling load (kN): the load at the 1st cycle of -0.5% peak axial strain, regarded as the designed compressive load of a brace according to AIJ Recommendation [2.3]. Though IHCB is not expected to buckle, the behavior under the large compressive axial strain is simply called post-buckling behavior in this study.

(a) CBB

(b) IHCB-F40

(c) IHCB-2F60

(d) IHCB-F40W60

(e) Skeleton curve

○ Yield load
● Maximum tensile load
▲ Buckling / Maximum compressive load
□ Post-buckling load
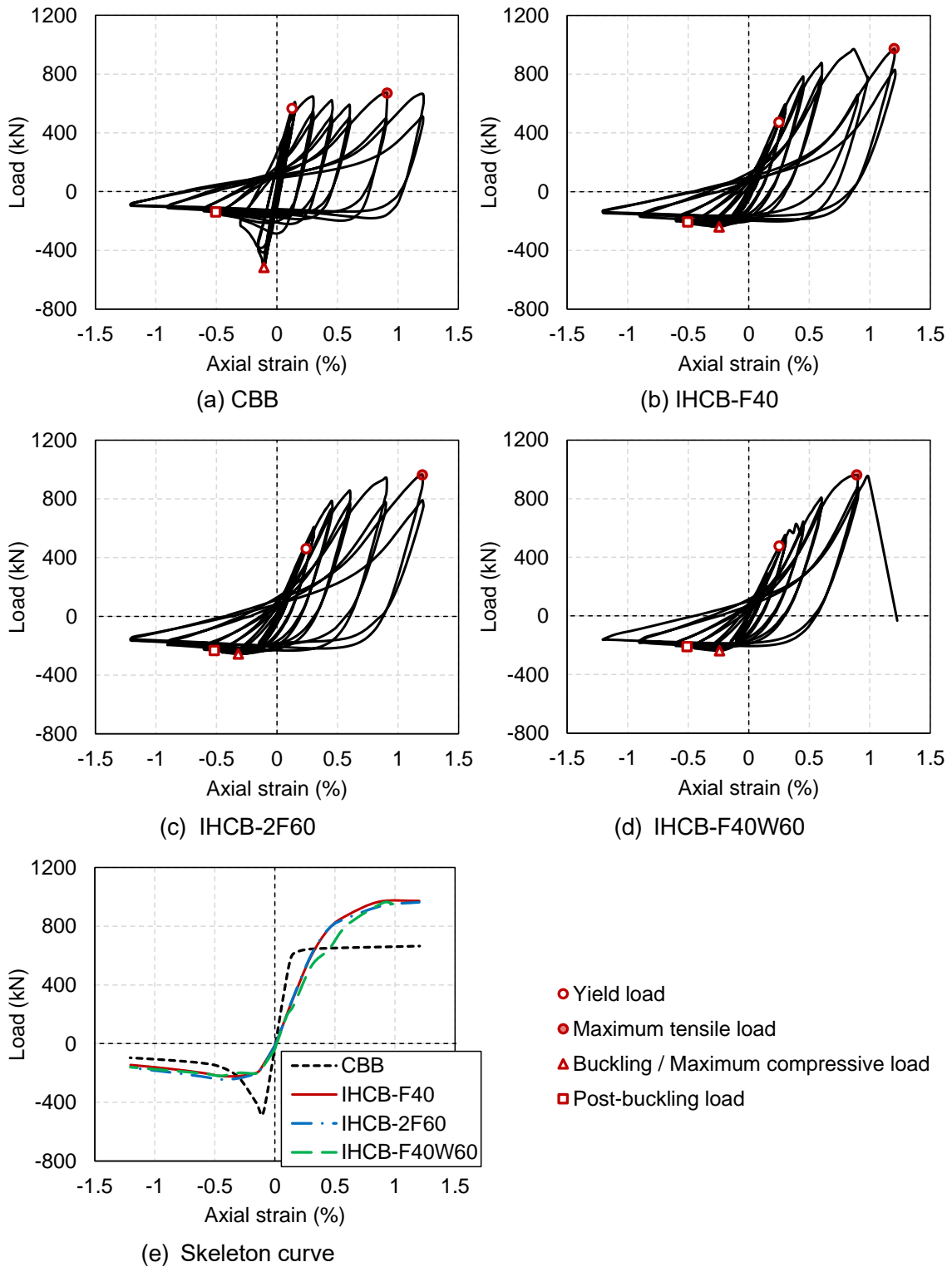
Figure 2-16 Load-axial strain relationships

Figure 2-16 demonstrates that all specimens were loaded as planned except for IHCB-F40W60. IHCB-F40W60 fractured at the 1st cycle of +1.2% axial strain, which will be discussed later. Note that the slippage of the joint occurred once at the 1st cycle of +0.9% axial strain for IHCB-F40 and twice at the 1st cycle of +0.45% axial strain for IHCB-F40W60, rendering the tensile load loss shown in Figure 2-16(b), and Figure 2-16(d), respectively. Apart from the aforementioned factors, the skeleton curve presented that all IHCBs succeeded in expressing stable structural behaviors without sharp turning points. Besides, the differences in the skeleton curve among the three IHCBs were insignificant.

Table 2-7 Tensile load capacities

| Specimen | Stiffness | | | Tensile load | | | | | |
| | | | | Yield load | | | Maximum load | | |
	Initial (GPa)	Post-yield (GPa)	Post-yield/ initial	Value (kN)	Strain (%)	Cycle	Value (kN)	Strain (%)	Cycle
CBB	207.7	1.88	0.009	565.1	0.13	1st of +0.15%	670.0	0.91	1st of +0.90%
IHCB-F40	87.3 (0.42)	30.2 (16.06)	0.35	471.0 (0.83)	0.25	2nd of +0.30%	972.6 (1.45)	1.20	1st of +1.20%
IHCB-2F60	88.2 (0.42)	25.8 (13.72)	0.29	460.7 (0.82)	0.24	2nd of +0.30%	963.7 (1.44)	1.20	1st of +1.20%
IHCB-F40W60	87.6 (0.42)	34.0 (18.09)	0.39	474.8 (0.84)	0.25	1st of +0.30%	960.5 (1.43)	0.89	1st of +0.90%

For the tensile performance, IHCBs showed approximately 58% lower initial stiffnesses about 88 GPa than about 208 GPa, of CBB, which was due to the initial curve shape. Owing to the lower initial stiffness, the IHCB series reached the yield loads at larger axial strains, which were 0.24%-0.25% at the 1st or 2nd cycles of +0.30% axial strains (about 1/150 story drift), compared to that of CBB at 0.13% axial strain during the 1st cycle of +0.15% axial strain (about 1/300 story drift). It indicated that the IHCB series could remain elastic during small earthquakes while CBB was already plastic.

After yielding, the stiffness of CBB dramatically dropped to 1.88 GPa, whose ratio to the initial stiffness was 0.9%. By comparison, the IHCB series succeeded in maintaining higher post-yield stiffnesses, which were 30.2 GPa for IHCB-F40, 25.8 GPa for IHCB-2F60, and 34.0 GPa for IHCB-F40W60. The ratios of the post-yield stiffness to the initial stiffness were 35%, 29%, and 39% for IHCB-F40, IHCB-2F60, and IHCB-F40W60, respectively. The post-yield stiffness ratio of the IHCB series to CBB was approximately 13-18. The large post-yield stiffness of IHCB achieved the goal of providing a larger lateral stiffness to the frame during severe earthquakes. Owing to the partial strengthening, the maximum tensile loads of the IHCB series during the loading were 1.43-1.45 times larger than that of CBB.

Table 2-8 Compressive load capacities

Specimen	Compressive load									Post-buckling/maximum
	Buckling			Maximum			Post-buckling			
	Value (kN)	Strain (%)	Cycle	Value (kN)	Strain (%)	Cycle	Value (kN)	Strain (%)	Cycle	
CBB	-515.8	-0.11	1st of -0.15%	-515.8	-0.11	1st of -0.15%	-139.5			0.27
IHCB-F40				-239.9 (0.47)	-0.25	2nd of -0.30%	-208.0 (1.49)	-0.5	1st of -0.60%	0.87
IHCB-2F60				-256.3 (0.50)	-0.32	1st of -0.45%	-233.5 (1.67)			0.91
IHCB-F40W60				-237.8 (0.46)	-0.24	2nd of -0.30%	-210.6 (1.51)			0.89

Regarding the compressive performance, owing to the initial curve shape, the apparent and typical buckling behaviors were not observed in the IHCB series. CBB buckled at the 1st cycle of -0.15% axial strain (about 1/300 story drift) with the sudden and sharp drop of the compressive load capacity, which strongly affected the plastic strain concentration at the brace middle. IHCB-F40, IHCB-2F60, and IHCB-F40W60 reached the maximum compressive loads at the 2nd cycle of -0.3% axial strain, the 1st cycle of -0.45% axial strain, and the 2nd cycle of -0.3% axial strain, respectively, with an overall smooth flexural behavior. Moreover, the post-buckling load of IHCB-F40, IHCB-2F60, and IHCB-F40W60, respectively, became 1.49 times, 1.67 times, and 1.51 times larger than that of CBB. The ratios of the post-buckling load to the maximum compressive load were 0.27, 0.87, 0.91, and 0.89 for CBB, IHCB-F40, IHCB-2F60, and IHCB-F40W60, respectively. The stabilized compressive capacity of the IHCB series softened the design conditions for braces. Their behaviors were similar to the IH-treated eccentric brace [2.9], showing that the curve shape of a brace could be considered an alternative to eccentricity. The idea of avoiding buckling behavior by employing the initial curve shape could be fully and flexibly used in further research.

2.5.2 Strength degradation

The strength degradation between the 2nd and 1st cycles for the same peak axial strain occurred in all specimens, see Figure 2-16(a) to Figure 2-16(d). Here, the ratio of the load at the 2nd cycle to that at the 1st cycle for the same peak axial strain is defined as the strength degradation ratio. Figure 2-17 presents the strength degradation ratio under compression and tension. Table 2-9 summarizes the values. Note that IHCB-F40W60 fractured during the 1st cycle of +1.2% axial strain.

Under compression, a great decrease in the strength degradation ratio was found at the 0.3% cycle for CBB, which resulted from the unstable post-buckling behavior. Different from CBB, the strength degradation ratio was larger than 1.0 at the 0.3% cycle in turn for all IHCBs. It might be contributed to their smooth bending behaviors. After the 0.3% cycle, the strength degradation ratios of all specimens were similar, and the values were slightly smaller than 1.0.

Under tension, with the increase of the peak axial strain, the strength degradation ratio gradually decreased. It was mainly because a larger axial strain was necessary for straightening the brace at the 2nd cycle under tension than required at the 1st cycle, which resulted in a lower peak load value at the 2nd cycle. For CBB, it needed the largest axial strain to straighten the brace because of the dramatic buckling behavior and the strain concentration at the limited region, especially at the brace middle. Thus, CBB showed the largest strength degradation, except for the joint slippage of IHCB-F40 at the 0.9% peak axial strain.

(a) Under compression   (b) Under tension
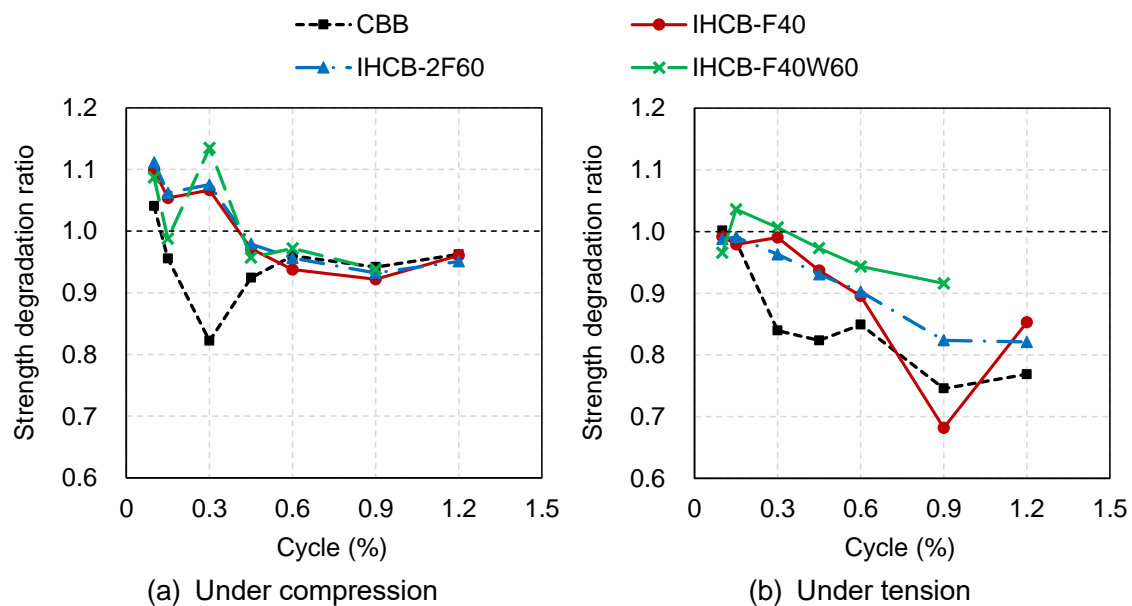
Figure 2-17 Strength degradation ratio (the 2nd cycle VS. the 1st cycle)

Table 2-9 Strength degradation ratio (the 2nd cycle VS. the 1st cycle)

Cycle	Specimen	CBB	IHCB-F40	IHCB-2F60	IHCB-F40W60
0.1%	Compression	1.04	1.10	1.11	1.09
0.1%	Tension	1.00	0.99	0.99	0.97
0.15%	Compression	0.96	1.05	1.06	0.99
0.15%	Tension	0.98	0.98	0.99	1.04
0.3%	Compression	0.82	1.07	1.08	1.13
0.3%	Tension	0.84	0.99	0.96	1.01
0.45%	Compression	0.92	0.97	0.98	0.96
0.45%	Tension	0.82	0.94	0.93	0.97
0.6%	Compression	0.96	0.94	0.96	0.97
0.6%	Tension	0.85	0.90	0.90	0.94
0.9%	Compression	0.94	0.92	0.93	0.94
0.9%	Tension	0.75	0.68	0.82	0.92
1.2%	Compression	0.96	0.96	0.95	
1.2%	Tension	0.77	0.85	0.82	

2.5.3 Residual strains

The residual strain is defined as the strain when the unloading is finished, which is the value on the horizontal axis when load = 0 kN in the load-axial strain relationship. If the data when load = 0 kN was not captured during the test, linear interpolation was used to calculate the residual strain. Figure 2-18(a) demonstrates the residual strain of each specimen, and Figure 2-18(b) and (c) demonstrate the residual strain ratio of IHCB to that of CBB under compression and tension, respectively. Table 2-10 summarizes the values. For easy understanding, the unloading stiffness at the final cycle, which is the second cycle of 1.2% peak axial strain, is presented in Table 2-11. Note that the unloading stiffnesses of the same specimen were similar after yielding on the tensile side, and the initial and post-yield stiffnesses are also demonstrated for comparison. Besides, IHCB-F40W60 fractured during the 1st cycle of +1.2% axial strain.

(a) Residual strain of each specimen

(b) Residual strain ratio under compression   (c) Residual strain ratio under tension
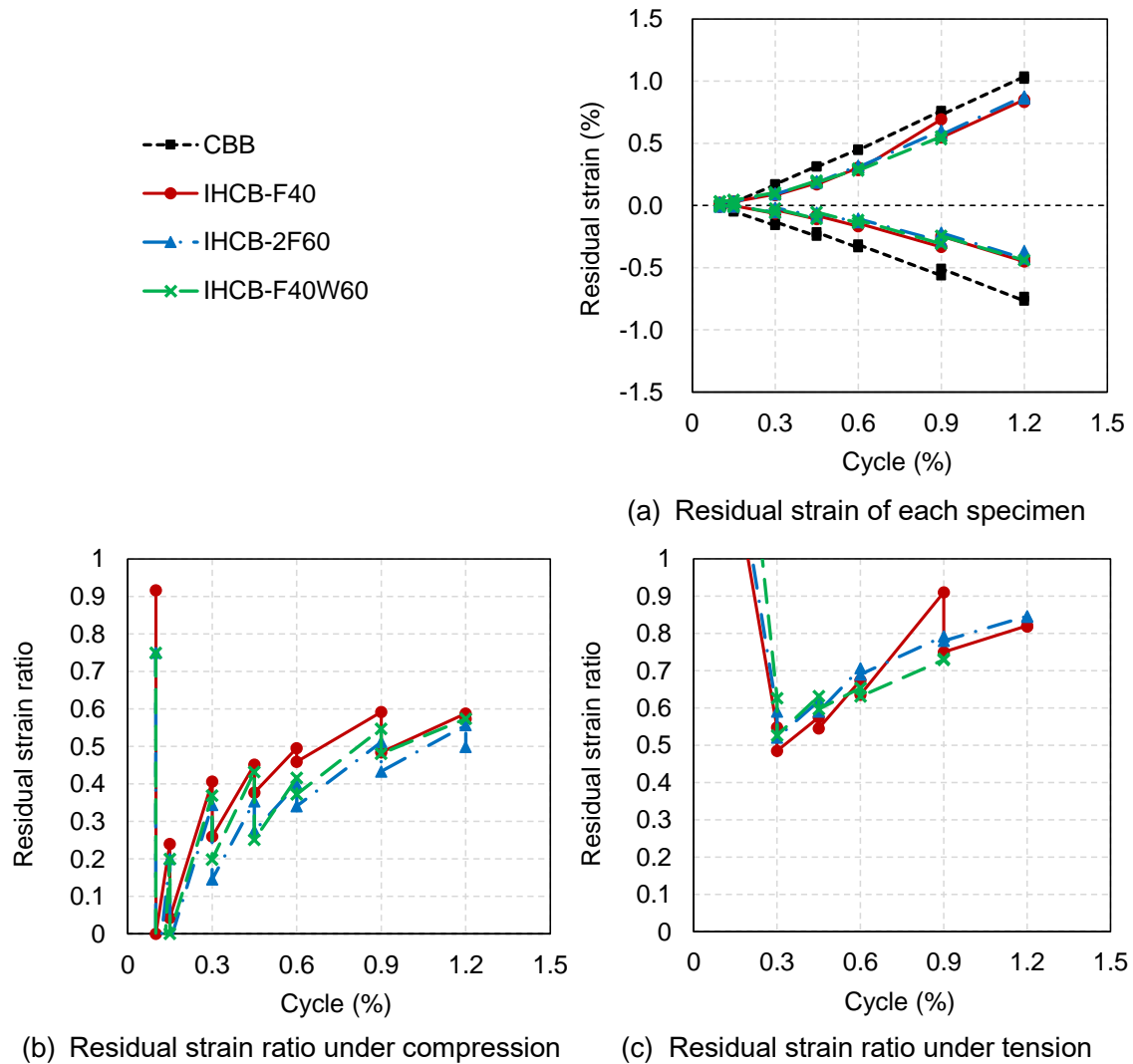
Figure 2-18 Residual strains

It can be known from Figure 2-18(a) that the residual strain increased almost linearly with the increase of the axial strain for all specimens, and the residual strain was slightly higher at the 1st cycle than that at the 2nd cycle when the peak axial strains were the same. Except that the slippage of the joint occurred on IHCB-F40 at the 1st cycle of +0.9% axial strain, the differences among the IHCB series were small. Considering that the yield cycles were different between CBB and IHCB series, and the residual strains before yielding were too small to evaluate, only the residual strains after the 0.3% cycle are discussed here. Under compression, see Figure 2-18(b), the residual strain ratios of the IHCB series were always smaller than 0.6 times those of CBB.

Under tension, see Figure 2-18(c), except for IHCB-F40, the residual strain ratios of the IHCB series were always smaller than 0.9 times those of CBB. The unloading stiffness of CBB under tension was slightly larger than that of IHCBs, and the relatively large load capacity of IHCBs at the same peak axial strain required more elastic deformations during the unloading, which eventually reduced the residual strains of the IHCB series. What is interesting is that the unloading stiffnesses of IHCBs under tension were similar to their initial stiffnesses, indicating that their curve shape did not change greatly during the initial loading and unloading.

Table 2-10 Residual strain at each cycle

Cycle		Specimen	CBB	IHCB-F40		IHCB-2F60		IHCB-F40W60	
			Value (%)	Value (%)	Ratio	Value (%)	Ratio	Value (%)	Ratio
0.1%	1st	Compression	-0.012	-0.011	0.92	-0.009	0.75	-0.009	0.75
		Tension	0.012	0.020	1.67	0.023	1.92	0.031	2.58
	2nd	Compression	-0.007	0.000	0.00	0.001	-0.14	0.003	-0.43
		Tension	0.012	0.021	1.75	0.022	1.83	0.032	2.67
0.15%	1st	Compression	-0.050	-0.012	0.24	-0.010	0.20	-0.010	0.20
		Tension	0.026	0.031	1.19	0.034	1.32	0.043	1.65
	2nd	Compression	-0.047	-0.002	0.04	0.001	-0.02	0.000	0.00
		Tension	0.025	0.030	1.20	0.032	1.28	0.042	1.68
0.3%	1st	Compression	-0.160	-0.065	0.41	-0.055	0.34	-0.059	0.37
		Tension	0.166	0.091	0.55	0.098	0.59	0.104	0.63
	2nd	Compression	-0.131	-0.034	0.26	-0.019	0.15	-0.026	0.20
		Tension	0.171	0.083	0.49	0.089	0.52	0.090	0.53
0.45%	1st	Compression	-0.246	-0.111	0.45	-0.087	0.35	-0.106	0.43
		Tension	0.315	0.181	0.57	0.195	0.62	0.199	0.63

Cycle		Specimen	CBB Value (%)	IHCB-F40 Value (%)	Ratio	IHCB-2F60 Value (%)	Ratio	IHCB-F40W60 Value (%)	Ratio
	2nd	Compression	-0.215	-0.081	0.38	-0.059	0.27	-0.054	0.25
		Tension	0.310	0.169	0.55	0.183	0.59	0.185	0.60
0.6%	1st	Compression	-0.339	-0.168	0.50	-0.135	0.40	-0.141	0.42
		Tension	0.451	0.304	0.67	0.319	0.71	0.295	0.65
	2nd	Compression	-0.314	-0.144	0.46	-0.107	0.34	-0.117	0.37
		Tension	0.445	0.283	0.64	0.307	0.69	0.281	0.63
0.9%	1st	Compression	-0.563	-0.333	0.59	-0.288	0.51	-0.308	0.55
		Tension	0.761	0.693	0.91	0.603	0.79	0.555	0.73
	2nd	Compression	-0.508	-0.246	0.48	-0.220	0.43	-0.244	0.48
		Tension	0.728	0.546	0.75	0.568	0.78	0.533	0.73
1.2%	1st	Compression	-0.767	-0.451	0.59	-0.427	0.56	-0.440	0.57
		Tension	1.037	0.851	0.82	0.878	0.85		
	2nd	Compression	-0.734	-0.421	0.57	-0.366	0.50		
		Tension	1.016	0.832	0.82	0.858	0.84		

Table 2-11 Unloading stiffness at the 1.2% cycle (Unit: GPa)

	Initial stiffness	Post-yield stiffness	Unloading stiffness	
			Under compression	Under tension
CBB	207.7	1.88	8.58	122.3
IHCB-F40	87.3	30.2	8.02	104.7
IHCB-2F60	88.2	25.8	8.25	107.3
IHCB-F40W60	87.6	34.0	9.50	104.7*

* Unloading stiffness at the 0.9% cycle

2.5.4　Transverse deformations

The braces hardly deformed around the major axis and twisted along the brace length. The end plates did not rotate either. Therefore, only the transverse deformation (= deformation around the minor axis) is presented below. The transverse deformation was nearly symmetric about the brace middle in the axial direction for all specimens. The maximum value of transverse deformation at the 1st cycle of 0.1%, 0.3%, 0.45%, 0.9%, and 1.2% peak axial strains are summarized in Table 2-12. The value in bracket ( ) shows the ratio of the corresponding value to that of CBB. Note that IHCB-F40W60 fractured during the 1st cycle of +1.2% axial strain.

Table 2-12 Maximum transverse deformation at each cycle

Specimen		Maximum transverse deformation (mm)				
		0.1%	0.3%	0.45%	0.9%	1.2%
CBB	Compression	3.6	69.3	111.1	174.0	210.6
	Tension	-1.2	4.0	11.8	13.3	15.8
IHCB-F40	Compression	60.5 (16.81)	87.2 (1.26)	108.2 (0.97)	162.3 (0.93)	200.3 (0.95)
	Tension	36.6 (-30.50)	22.7 (5.68)	18.4 (1.56)	14.5 (1.09)	13.8 (0.87)
IHCB-2F60	Compression	60.2 (16.72)	86.3 (1.25)	105.7 (0.95)	160.0 (0.92)	196.6 (0.93)
	Tension	36.9 (-30.75)	22.7 (5.68)	17.9 (1.52)	13.8 (1.04)	14.4 (0.91)
IHCB-F40W60	Compression	61.4 (17.06)	88.9 (1.28)	110.1 (0.99)	161.5 (0.93)	194.7 (0.92)
	Tension	37.6 (-31.33)	24.5 (6.13)	24.1 (2.04)	14.7 (1.11)	

Figure 2-19 and Figure 2-20 demonstrate the transverse deformations under compression and tension, respectively. The horizontal axis shows the location of the displacement transducers. The values are -891 mm (near the block), -700 mm, -350 mm, 0 mm (brace middle), 350 mm, 700 mm, and 891 mm (near the jack). The vertical axis shows the average value measured by two displacement transducers attached horizontally at the upper and bottom flanges, respectively at the same cross-section. The coordinate direction corresponds to the actual transverse deformation of the IHCB series. Because the buckling direction of CBB was opposite to the initial curve shape of the IHCB series, the vertical values of CBB were reversed for comparison. The vertical dash-line shows the symmetry axis (sym. axis) at 0 mm. The curved dot-dash-line shows the initial curve shape of the IHCB series, including the value measured in Section 2.2.3 of 41 mm and the joint transverse deformation of 7 mm presented in Section 2.4.4.

As presented in Figure 2-19, the transverse deformation increased with the increase of axial strain under compression. Before the 0.3% cycle, the transverse deformations of the IHCB series were larger than that of CBB due to the initial curve shape. After the 0.45% cycle, the transverse deformation of CBB at the brace middle became similar to these of the IHCB series. The difference was the transverse deformation of CBB concentrating at the brace middle, which led to a triangle transverse deformation-location relationship. However, the transverse deformation of the IHCB series was more dispersed, making the transverse deformation-location relationship a smoother curve. At the 0.9% cycle, the transverse deformation at the brace middle of CBB became the largest, and the value reached 210.6 mm for CBB at the 1.2% cycle. By comparison, the transverse deformation was 200.3 mm for IHCB-F40, 196.6 mm for IHCB-2F60, and 194.7 mm for IHCB-F40W60 at the 1.2% cycle.
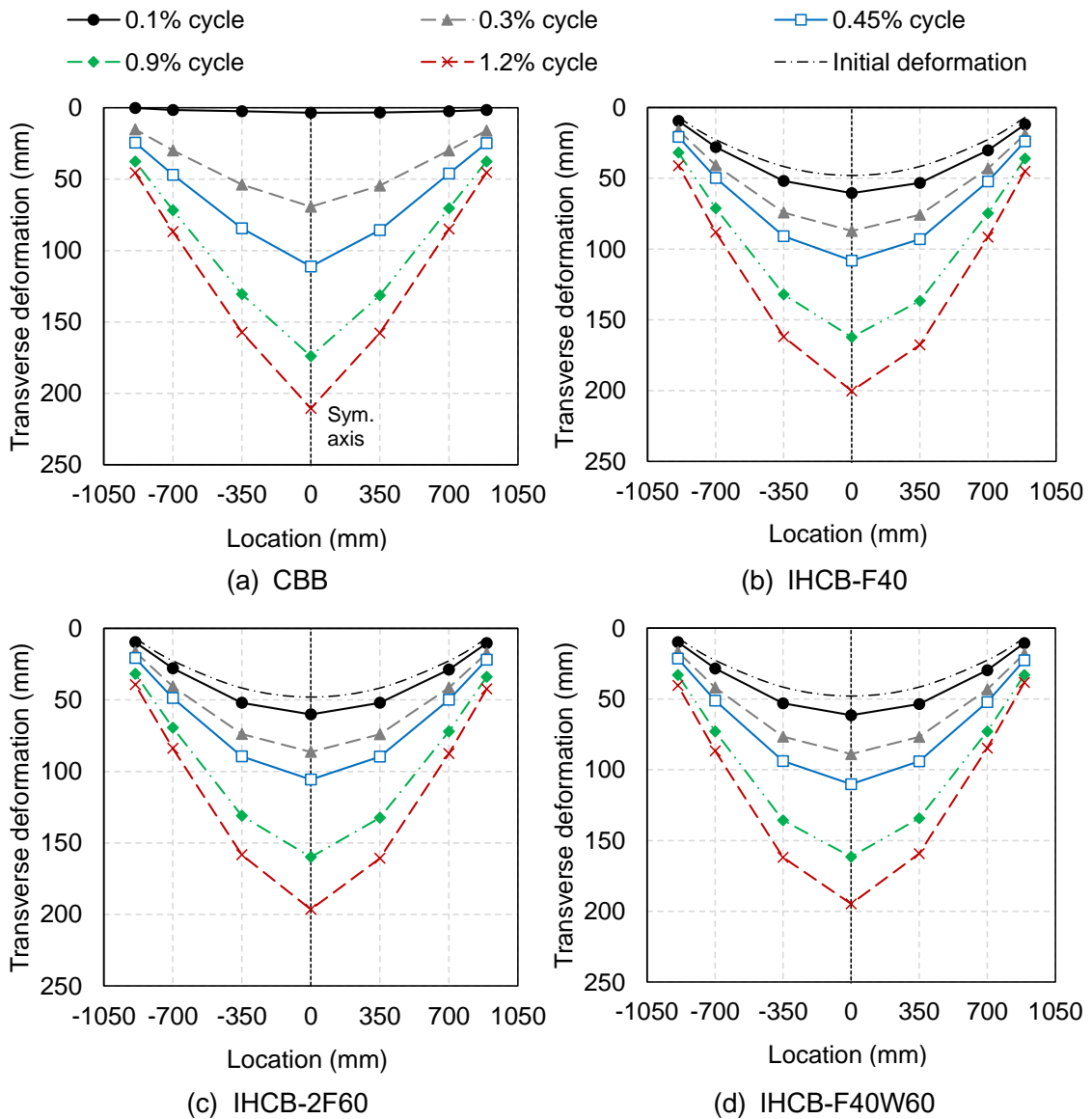
Figure 2-19 Transverse deformations under compression

It can be known from Figure 2-20 that the transverse deformation of CBB increased with the growth of the axial strain under tension while the IHCB series decreased in turn. For CBB, the transverse deformation concentrated at the brace middle after the 0.45% cycle, which was mainly attributed to the buckling, and the deformations at the brace ends were negligible during the whole test. The value reached 13.3 mm at the 0.9% cycle, and 15.8 mm at the 1.2% cycle. For the IHCB series, the transverse deformation gradually decreased until the 0.9% cycle, and rarely varied at the 1.2% cycle. The differences in the value of the maximum transverse deformation among IHCBs were small, and CBB reached the maximum value at the 1.2% cycle among them. Note that the direction of the transverse deformation of IHCBs under tension was the same as the direction of their initial curve shape.
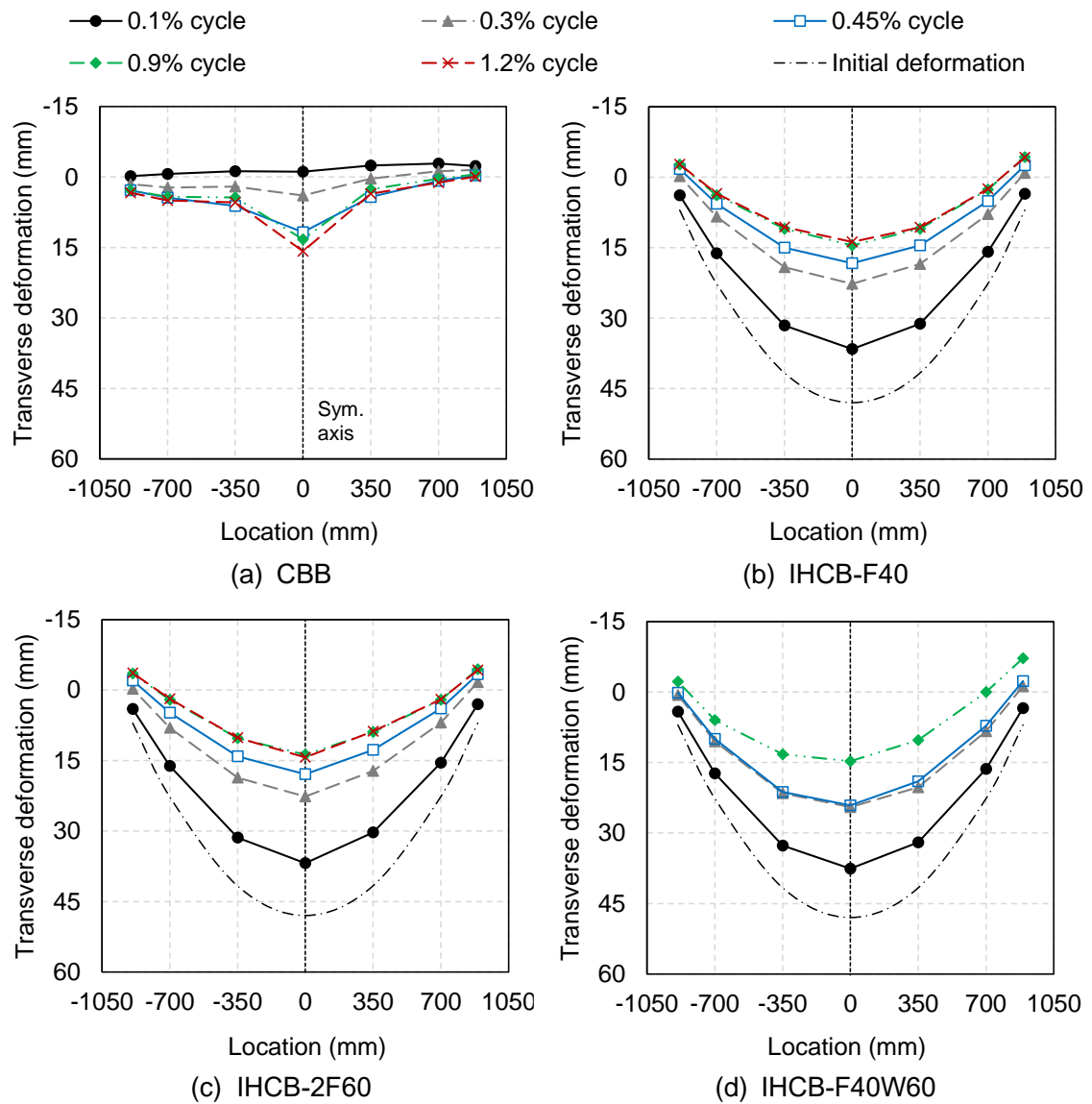
Figure 2-20 Transverse deformations under tension

Figure 2-21 shows the transverse deformation at the 1st cycle of 1.2% axial strain. For IHCB-F40W60, the fracture condition is presented instead of the state at +1.2% peak axial strain. Although the IHCB series had initial deformation, the transverse deformation was more uniformly distributed along the brace length, and the value tended to be smaller than that of CBB both in compression and tension. Hence, the concern about whether the initial curve shape would intensify the transverse deformation of a curved brace or not was resolved.

(a) At the peak axial strain of -1.2%

CBB

IHCB-F40

IHCB-2F60

IHCB-F40W60
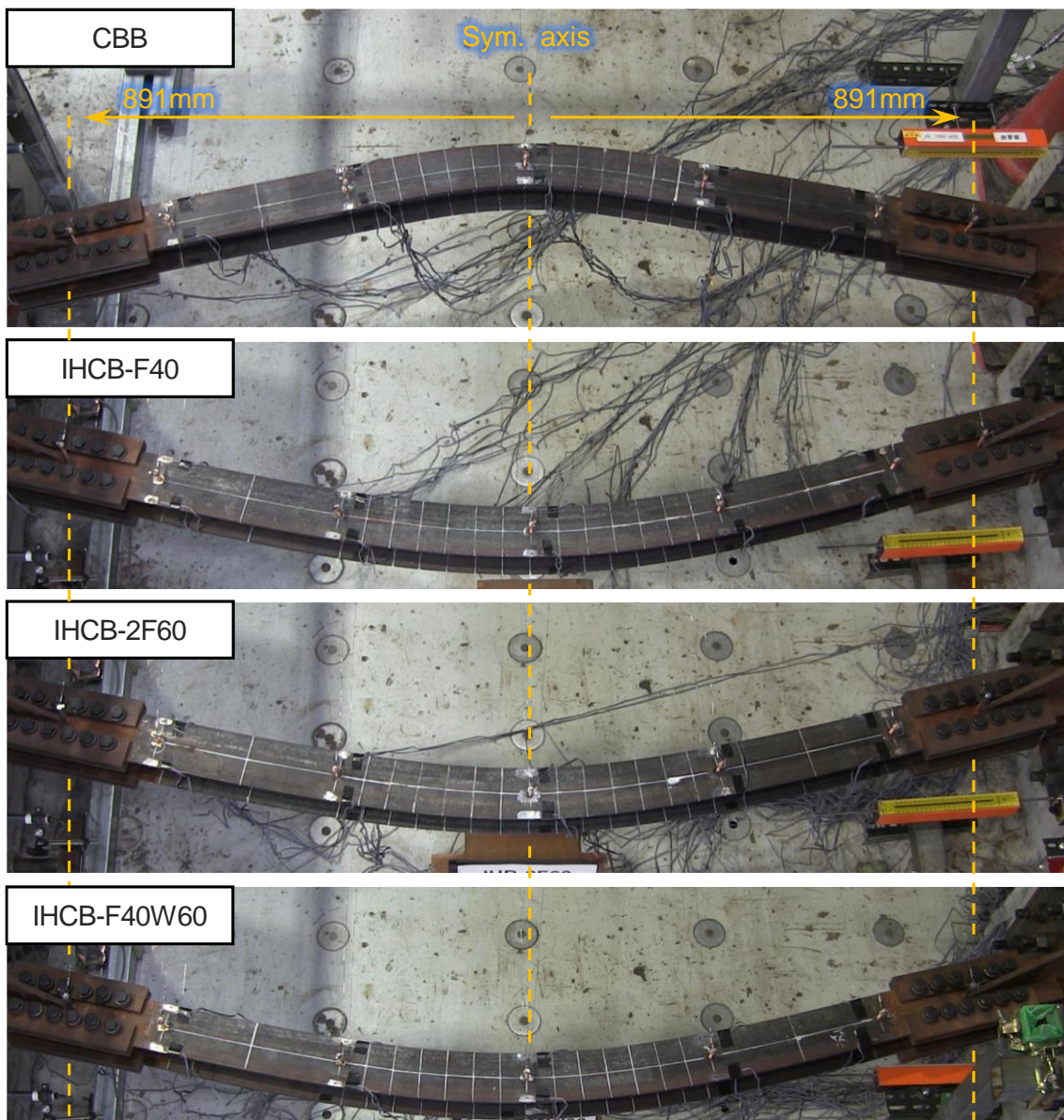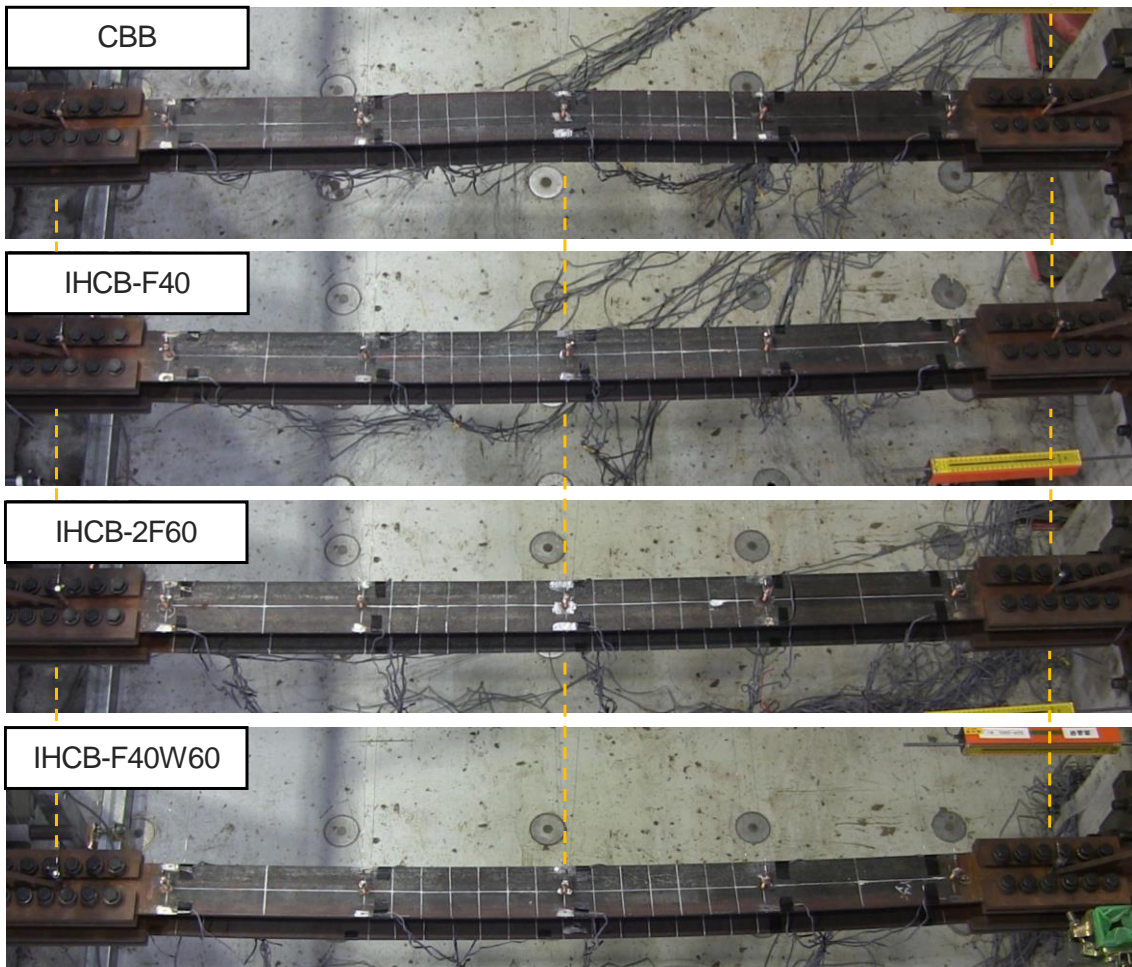
(b) At the peak axial strain of +1.2%

Figure 2-21 Transverse deformations during the 1st cycle of 1.2%

2.5.5 Local strain at yield cycles

The local strains were measured by the strain gauges described in Section 2.4.3. The strain gauges were attached for two purposes, one was to judge whether the specimen yielded or not, and the other was to know the tendency of strain concentration.

Table 2-13 summarizes the occurrence of yielding. It shows the cycle when the local strain first exceeded the corresponding yield strain. From the perspective of overall behavior, it can be inferred that the yielding occurred at the 0.15% cycle for CBB, 0.3% cycle for IHCB-F40, IHCB-2F60, and IHCB-F40W60, which generally matched the cycle of the yield load presented in Section 2.5.1. Note that the underlined values which occurred on CBB were irregular.

Table 2-13 Occurrence of yielding

Specimen		Outer side			Inner side		
		Upper flange	Web	Bottom flange	Upper flange	Web	Bottom flange
CBB	Compression	0.15%	0.1%	0.15%	0.15%	0.1%	0.15%
	Tension	0.15%	0.1%	0.1%	0.1%	0.1%	0.15%
IHCB-F40	Compression	0.1%	0.15%	0.1%	0.3%	0.6%	0.3%
	Tension	0.45%	0.3%	0.3%	0.3%	0.3%	0.3%
IHCB-2F60	Compression	0.3%	0.6%	0.45%	0.3%	0.9%	0.3%
	Tension	0.6%	0.3%	0.6%	0.3%	0.3%	0.3%
IHCB-F40W60	Compression	0.15%	0.9%	0.3%	0.3%	1.2%	0.3%
	Tension	0.3%	0.6%	0.3%	0.3%	0.6%	0.3%

* Underlined values are irregular

To evaluate the irregular values, the strain concentrations of CBB at the 0.1% cycle and the 0.15% cycle are demonstrated in Figure 2-22. The horizontal axis indicates the location of the strain gauge. The values are -700 mm (near the block), -350 mm, 0 mm (brace middle), 350 mm, and 700 mm (near the jack). The cross-section of each specimen and the location of the strain gauges at the cross-section are shown as well. The irregular values are highlighted in red.

Under compression, the strains at the flanges were smaller than the yield strain at the 0.1% cycle and gradually became larger at the 0.15% cycle, which was normal. However, the strains at the web were extremely large at the beginning, which were approximately -0.8% both at the outer and inner sides at the 0.1% cycle at the location of 700 mm. One of the most plausible reasons was that the brace ends of CBB were IH-treated, and the cross-sections deformed as described in Section 2.2.4. Therefore, some residual deformations and residual strains should have remained at the untreated regions of CBB for balancing the internal stress. When CBB was connected to the joint, it might be straightened, which

finally led to the large strain at the beginning. This reason could also explain the similar phenomenon that occurred on CBB under tension at the 0.1% cycle. For the IHCB series, it did not undergo the straightening process, since the joints were bent according to the curve shape in advance, thus, the irregular values of strains were not observed in the IHCB series.
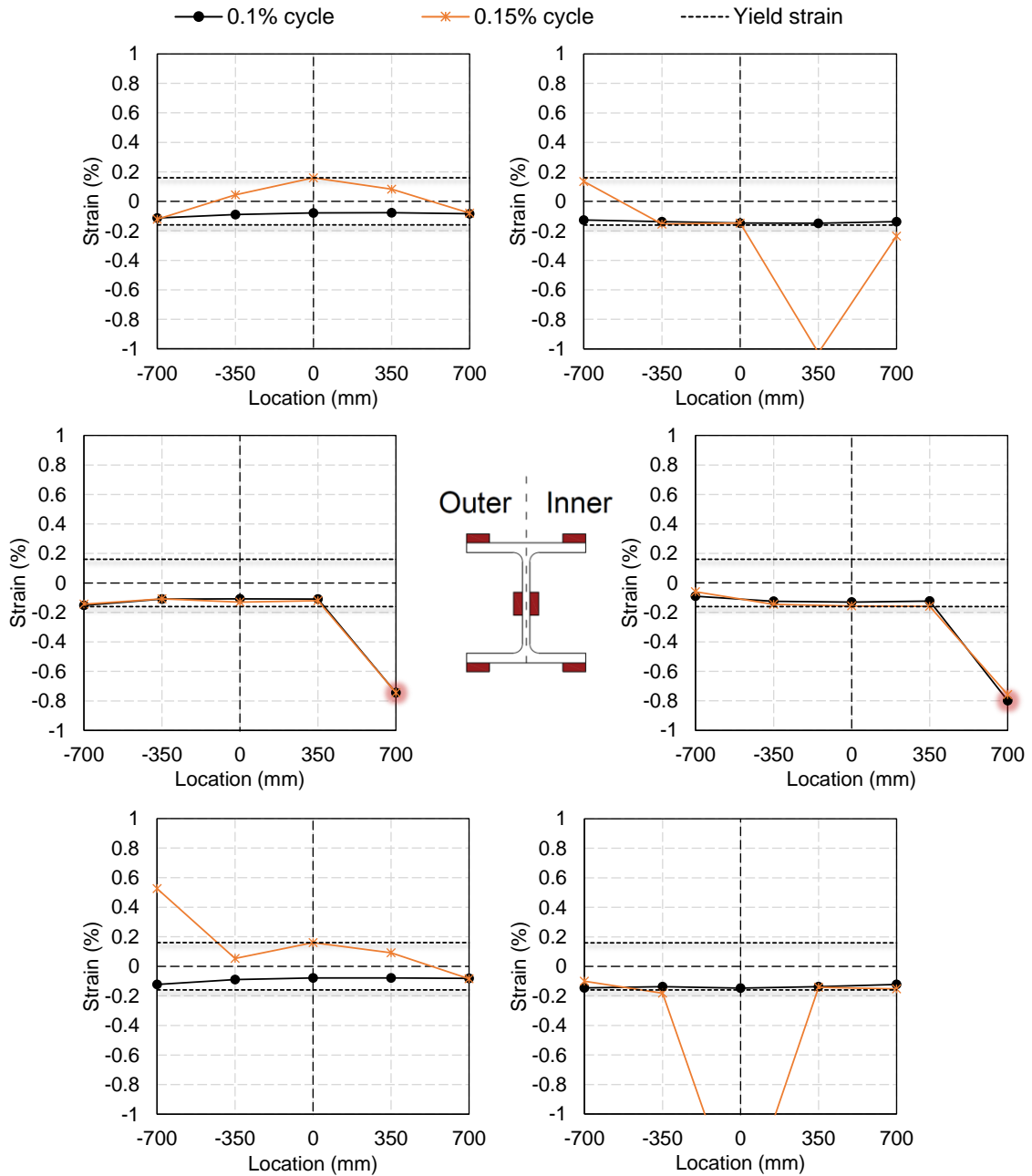
(a) CBB under compression
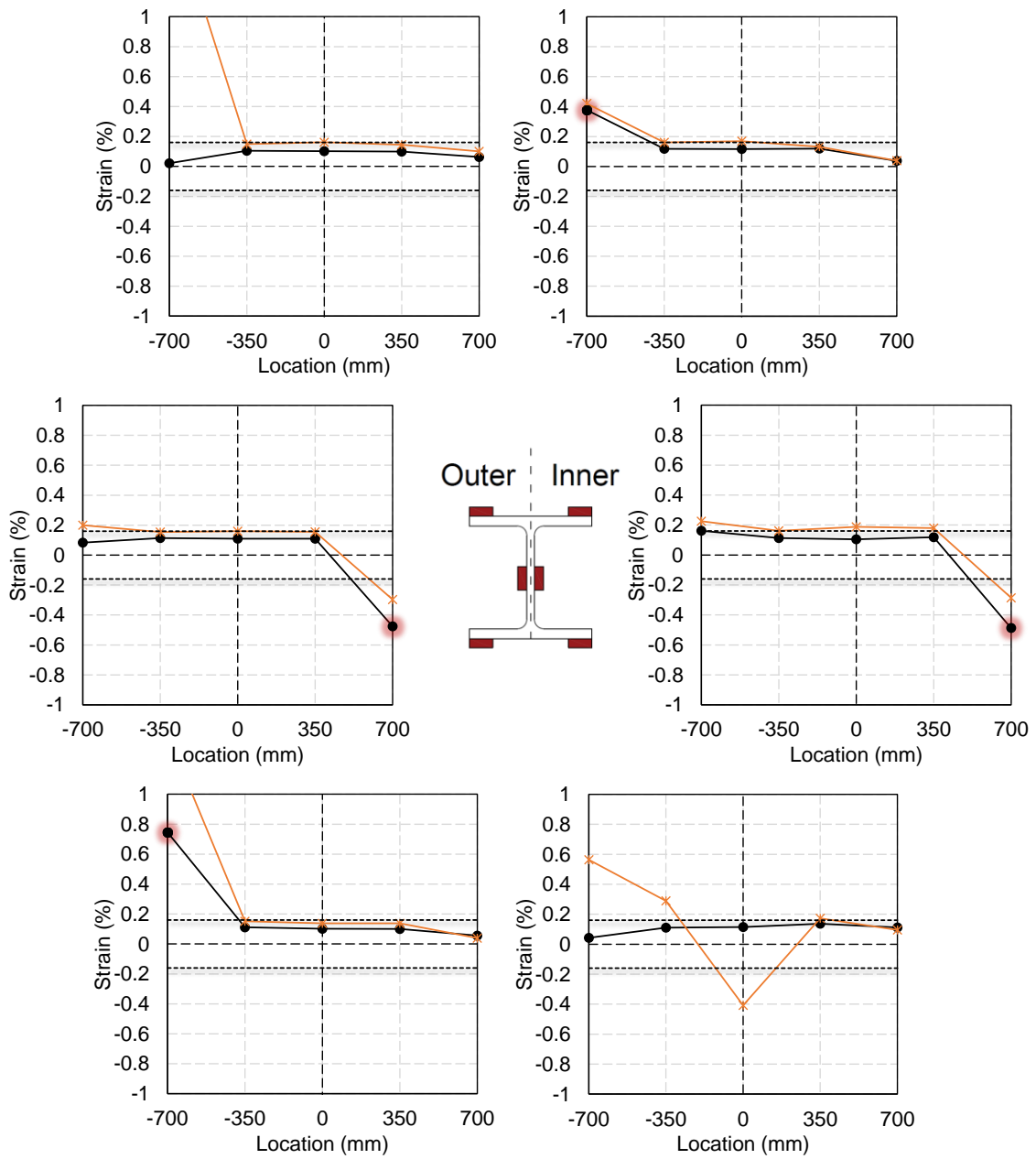
(b) CBB under tension

Figure 2-22 Irregular local strains

2.5.6　Local strain tendencies

To know the tendency of the strain concentration, the local strains at the 1st cycle of each peak axial strain under compression and tension are demonstrated in Figure 2-23 and Figure 2-24, respectively. Overall, rather than distributed dispersedly, the strain tended to spread as a W-shape along the brace length, especially on the flanges. The strain was concentrated at the brace middle and ends with the increase of the cycle.

As presented in Figure 2-23, under compression, for CBB, the strains at the outer side were tensile in general. The strains at the inner side were complicated, of which only the strains on the flanges at the brace middle were compressive, mainly due to the buckling. For IHCB-F40, the strains at the untreated outer side showed a similar tendency as those of CBB. What is different is that the strains on the IH-treated flanges at the inner side were all compressive, and the values remained at a low level. It represented that the initial curve shape helped the strains distribute uniformly instead of concentrating locally as CBB did. The higher strength induced by IH treatment further raised the capacity of resisting deformation. The differences in strain concentrations among the IHCB series were small.

As presented in Figure 2-24, under tension, for CBB, the strains at the outer side were similar to those under compression. Although the strains at the inner side became tensile, the shape was more like a reversed V rather than a W, showing that the strains concentrated at -350 mm to 350 mm. For IHCB-F40 and IHCB-2F60, the variations of the strains were like those of CBB, but the values were low. For IHCB-F40W60, the strains were extremely small. The strain concentrated at the other regions, specifically, the brace end, which fractured at an early stage, rather than the test region, which resulted in such a strain distribution.

In conclusion, the values of CBB were relatively larger than those of the IHCB series during the whole test. The different states of the strain concentration between CBB and IHCB series indicated that the IHCB series performed better in avoiding the strain concentration at the limited region and the sudden change of the strain direction. It ensured that the IHCB series resisted the force evenly along the length, eventually mitigating the local buckling.

(a) CBB

Outer | Inner

(b) IHCB-F40

Outer | Inner
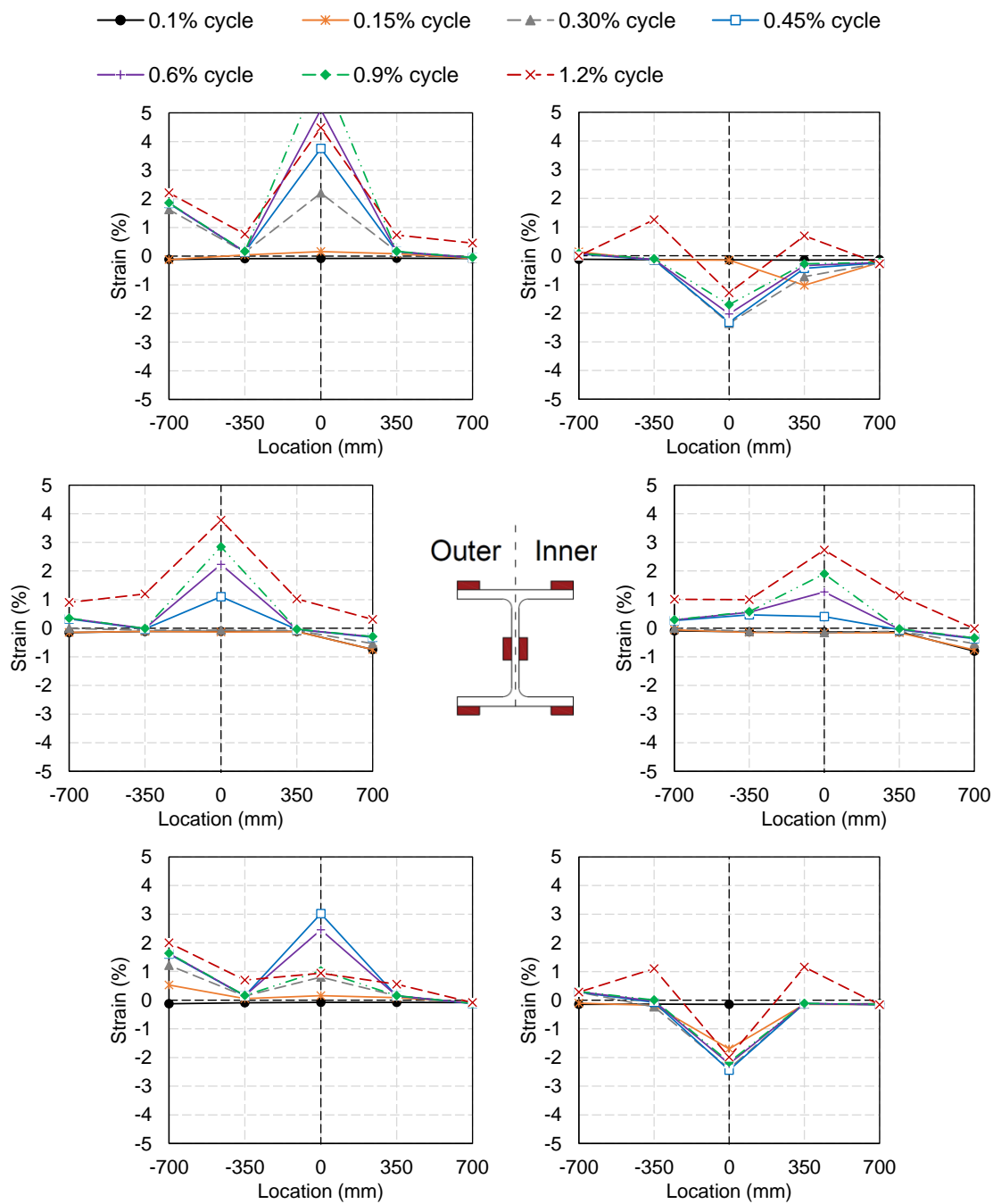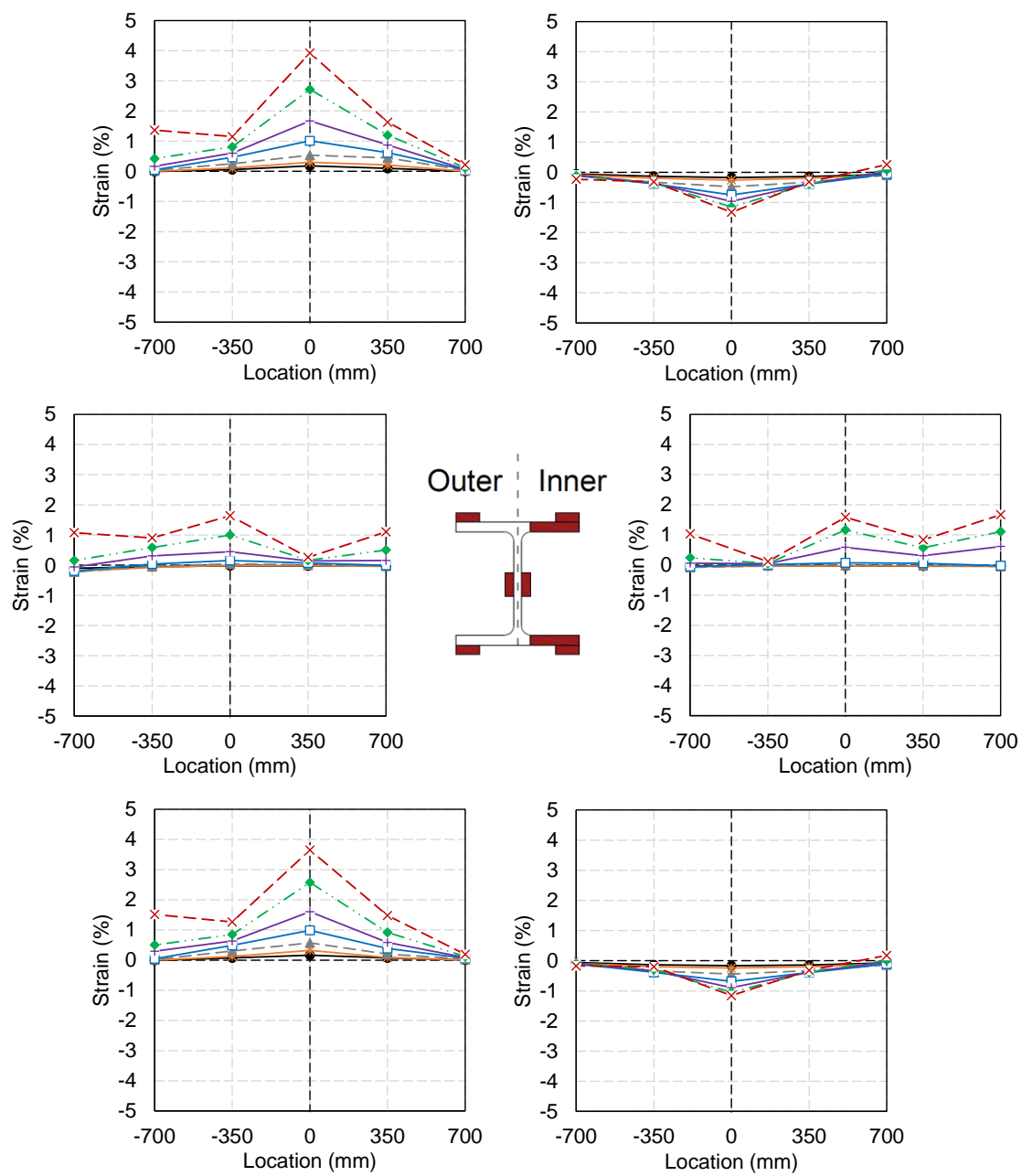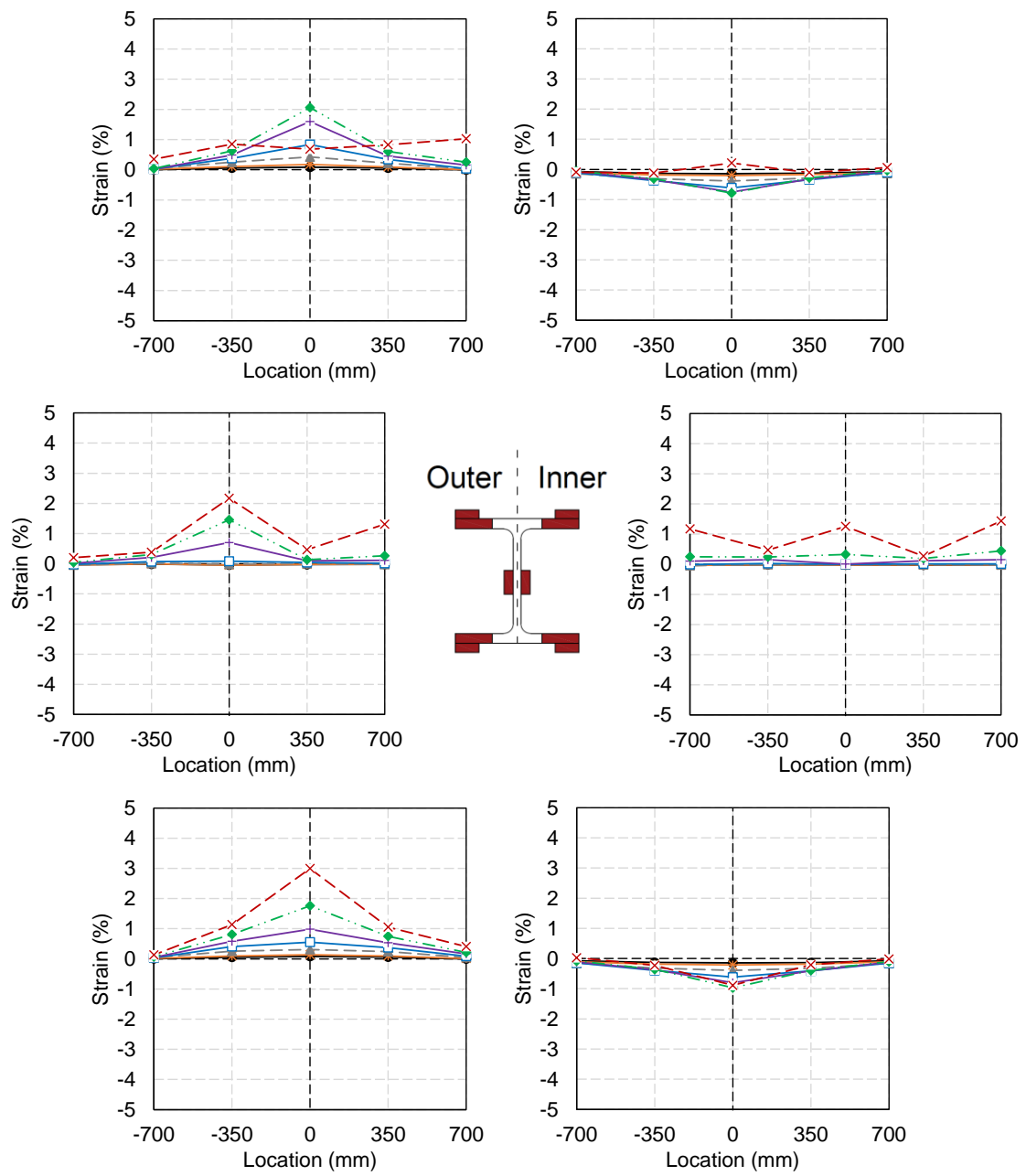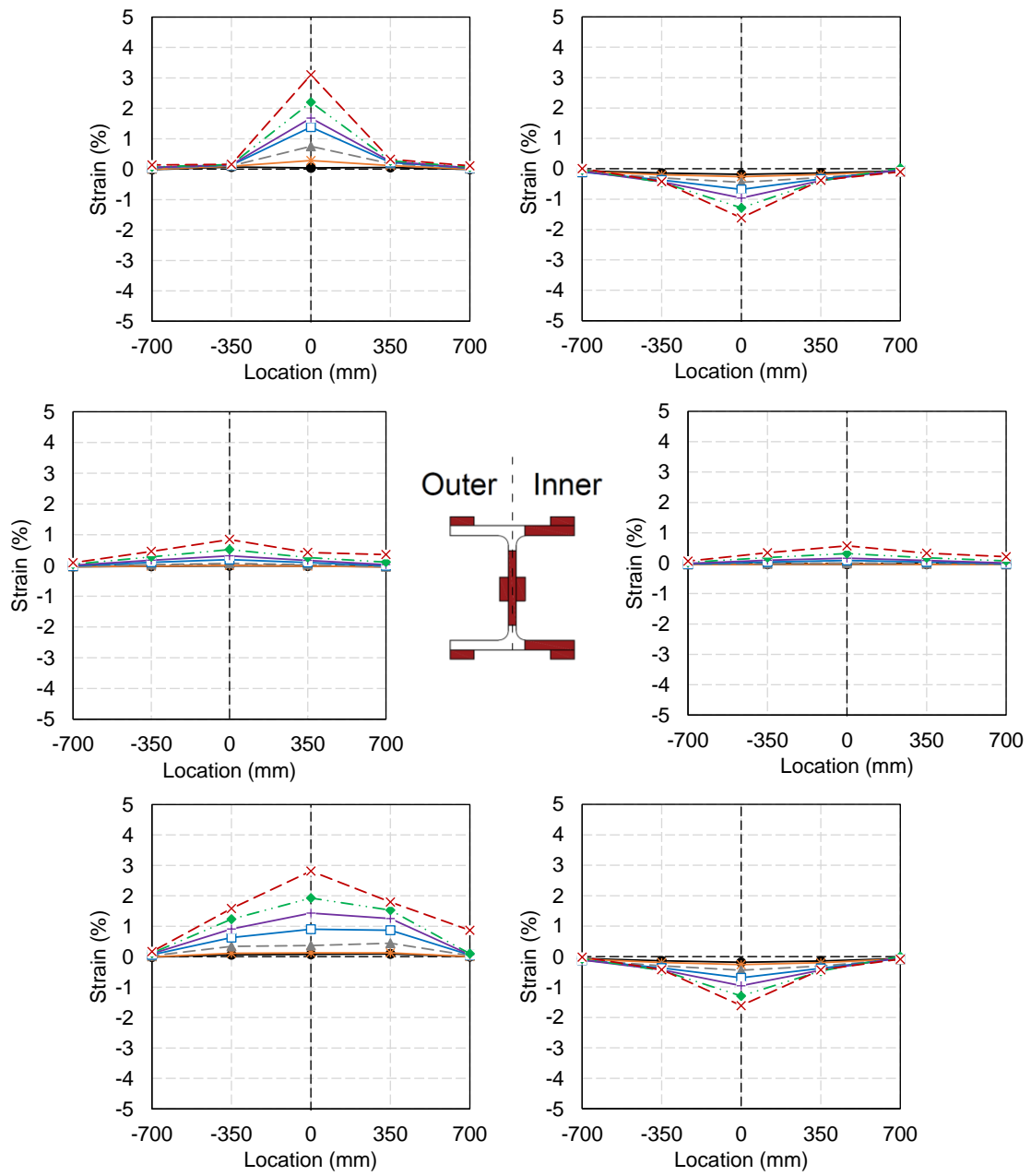
(c) IHCB-2F60

(d) IHCB-F40W60

Figure 2-23 Local strains under compression
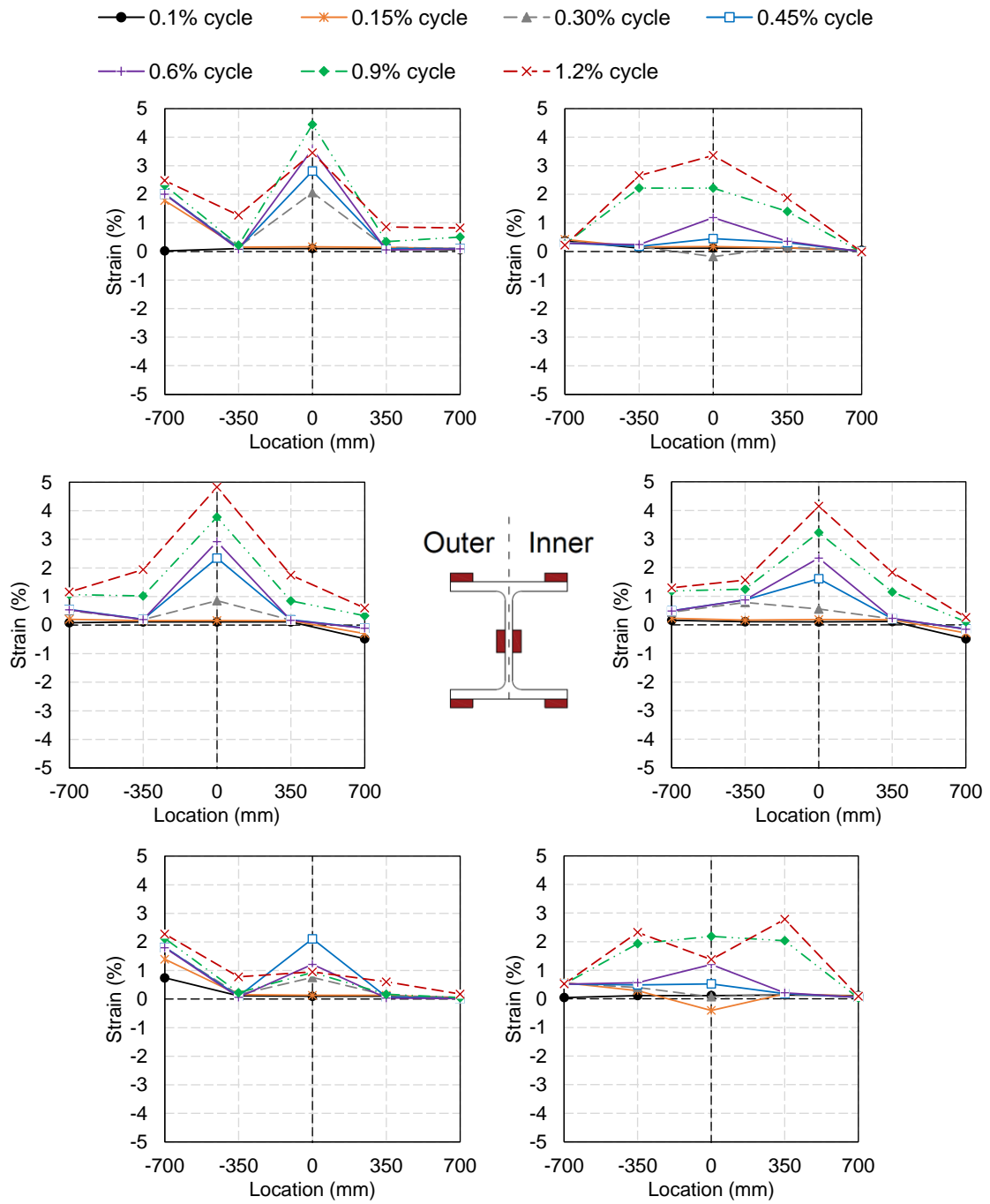
(a) CBB
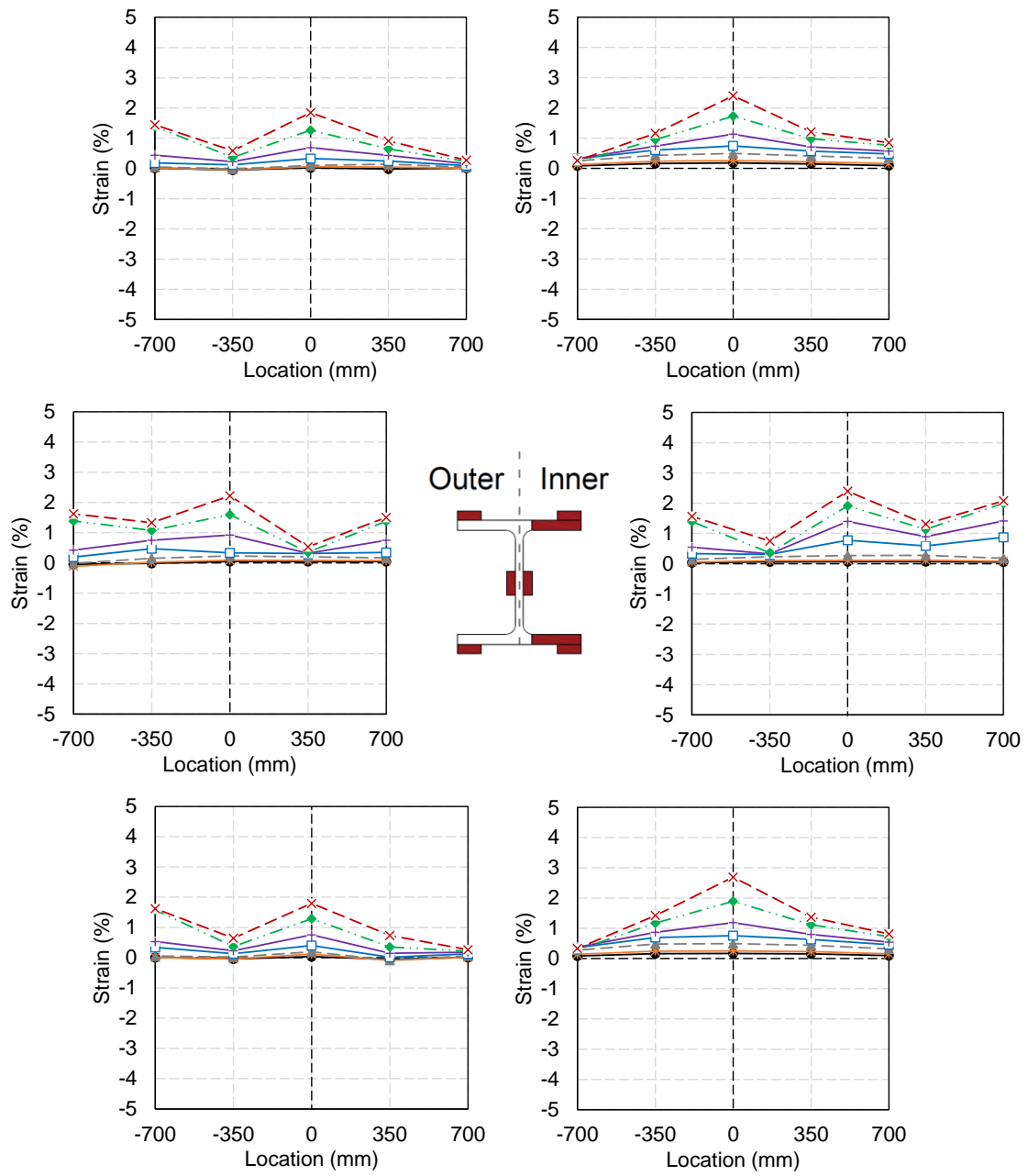
(b) IHCB-F40
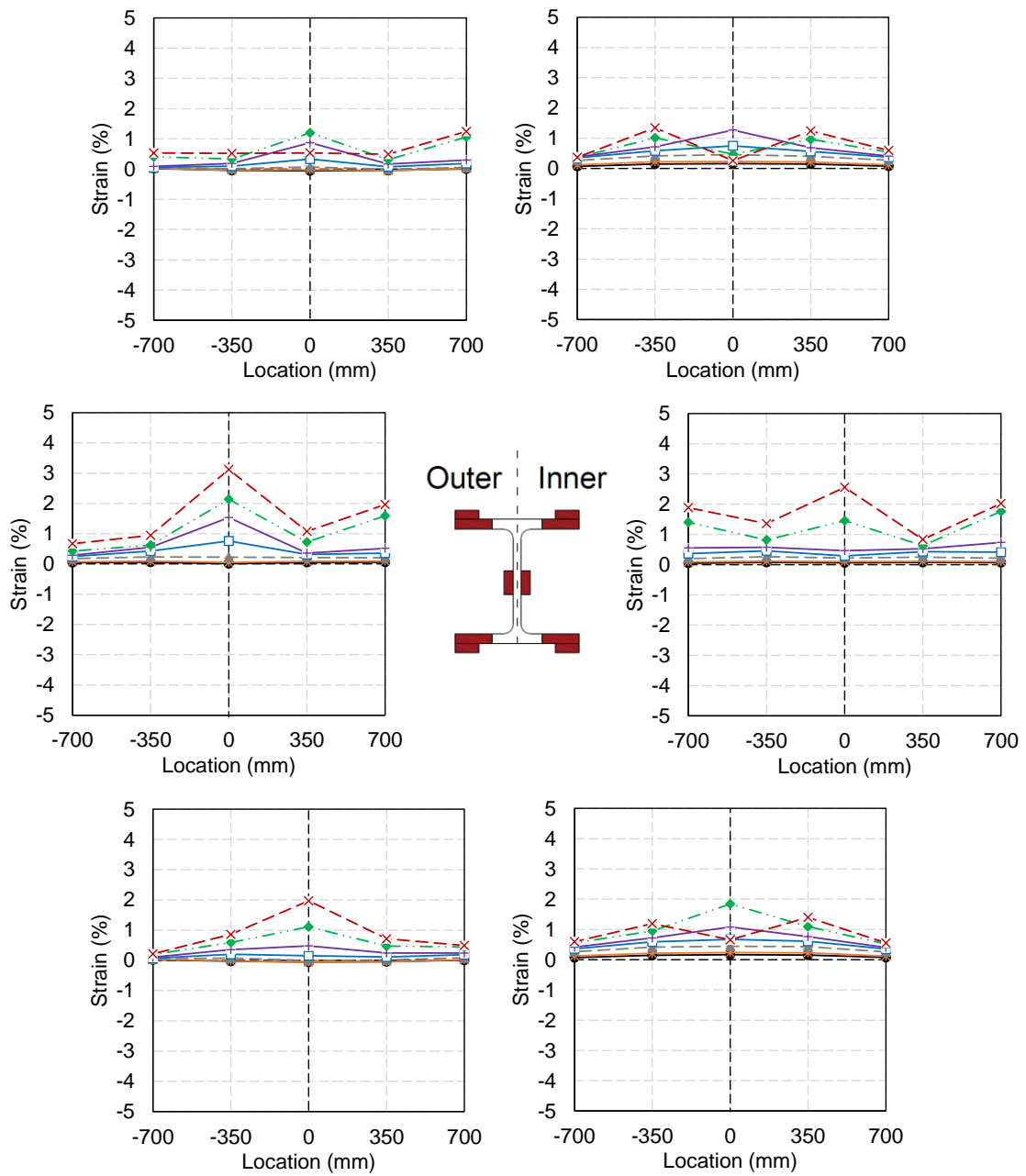
(c) IHCB-2F60
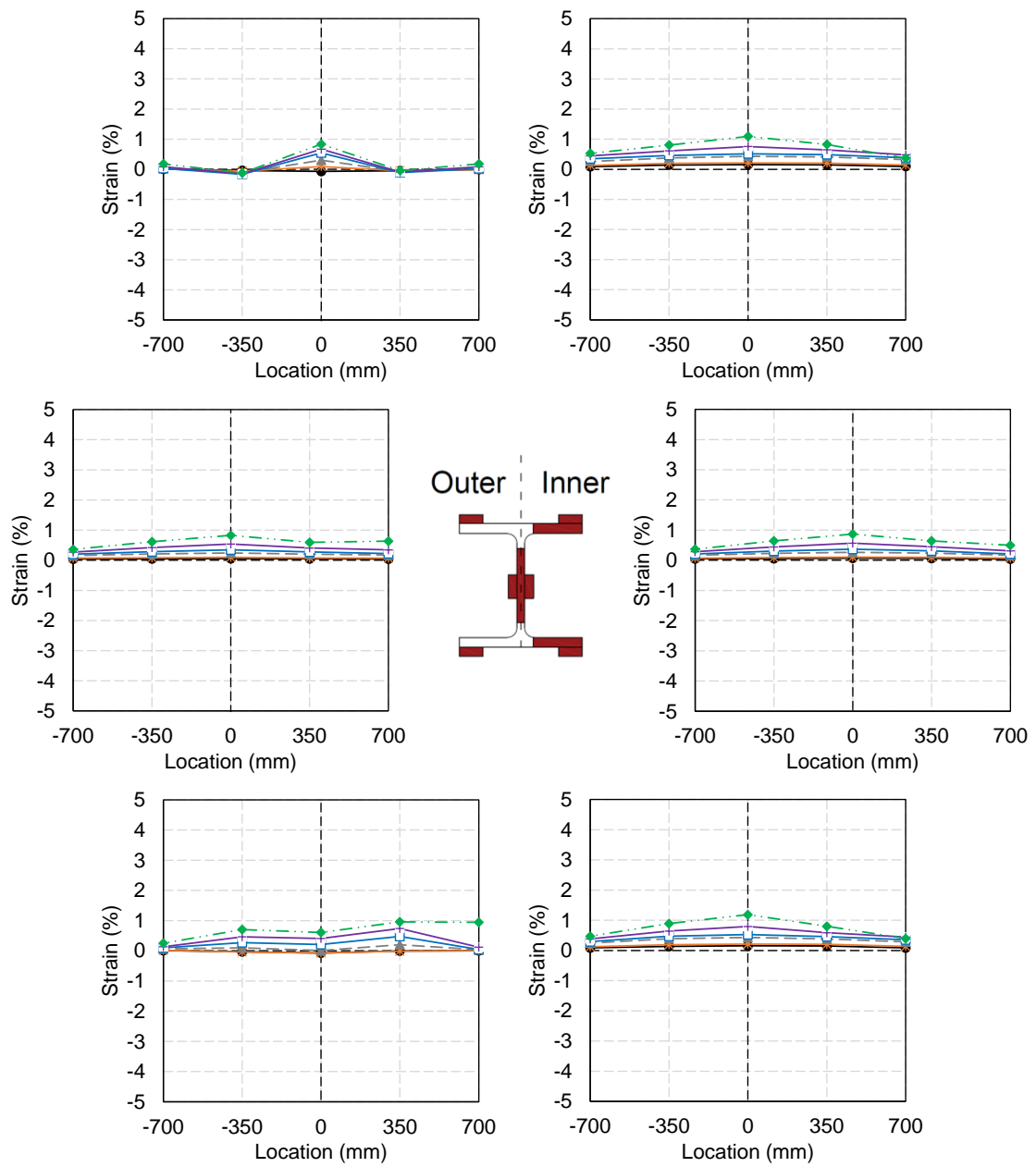
(d) IHCB-F40W60

Figure 2-24 Local strains under tension

2.5.7 Energy dissipation

Two factors evaluate the energy dissipation capacities of the specimens. One is the hysteretic energy dissipation, calculated by force times deformation. The other one is the equivalent viscous damping factor, $h_{eq} = \Delta W / 4\pi W$, where ΔW is the hysteretic energy in one cycle, W is the area of the right triangle comprised of the original point, the peak point, and the horizontal axis in a load-deformation relationship. Figure 2-25(a) demonstrates the hysteretic energy at each cycle (= ΔW), Figure 2-25(b) describes the accumulated hysteretic energy, and Figure 2-25(c) and (d) show h_{eq} at the first and second cycles, respectively. Table 2-14 concludes the energy dissipations.
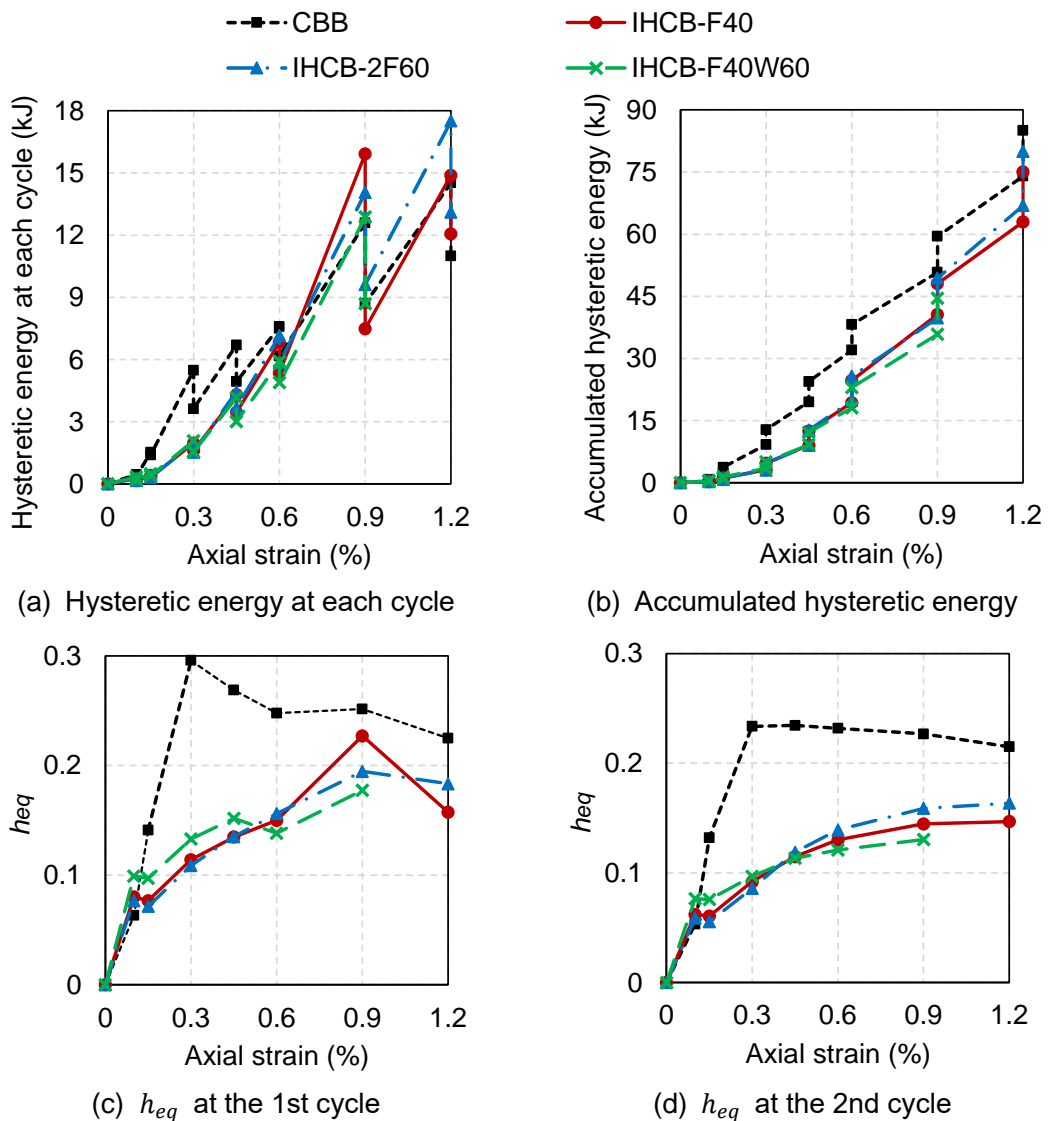
Figure 2-25 Energy dissipations

The hysteretic energy at each cycle and the accumulated hysteretic energy reveal that, due to the early yielding of CBB, it started to dissipate the energy after the 0.15% cycle. By contrast, the IHCB series started to dissipate the energy after the 0.3% cycle. After that, the hysteretic energy at each cycle was similar among all specimens. Despite that, h_{eq} of CBB was much higher than those of the IHCB series. The reason was that the lower load capacity of CBB decreased the denominator in the calculation of h_{eq}. Therefore, h_{eq} might not be proper for the evaluation of the energy dissipation ability of the brace with high load capacity as IHCBs. The differences among IHCBs were small. The total energy dissipations until the 1.2% cycle were similar, which were 85 kJ, 75 kJ, and 80 kJ for CBB, IHCB-F40, and IHCB-2F60, respectively. It was confirmed that the IHCB series possessed almost the same energy dissipation ability as CBB after yielding.

Table 2-14 Energy dissipation

Specimen / Cycle		CBB ΔW (kJ)	h_{eq}	IHCB-F40 ΔW (kJ)	h_{eq}	IHCB-2F60 ΔW (kJ)	h_{eq}	IHCB-F40W60 ΔW (kJ)	h_{eq}
0.1%	1st	0.448	0.063	0.268	0.080	0.259	0.077	0.339	0.099
	2nd	0.360	0.053	0.158	0.062	0.154	0.059	0.196	0.076
0.15%	1st	1.520	0.141	0.411	0.077	0.384	0.071	0.479	0.097
	2nd	1.387	0.132	0.327	0.061	0.305	0.055	0.384	0.076
0.3%	1st	5.474	0.296	1.960	0.114	1.963	0.109	2.073	0.133
	2nd	3.623	0.234	1.611	0.092	1.531	0.086	1.550	0.097
0.45%	1st	6.699	0.269	4.299	0.135	4.445	0.135	4.161	0.152
	2nd	4.929	0.234	3.450	0.115	3.680	0.119	3.009	0.113
0.6%	1st	7.583	0.248	6.837	0.150	7.161	0.156	5.908	0.138
	2nd	6.169	0.232	5.360	0.130	5.845	0.139	4.890	0.121
0.9%	1st	12.589	0.252	15.927	0.227	14.064	0.195	12.878	0.177
	2nd	8.706	0.227	7.478	0.145	9.621	0.159	8.703	0.130
1.2%	1st	14.524	0.225	14.882	0.157	17.509	0.183		
	2nd	11.005	0.215	12.058	0.147	13.103	0.164		
Total		85.0		75.0		80.0			

2.6 Test performance evaluation

This section is to verify whether the test performances of IHCBs satisfy their target performances. Because IHCB-F40W60 fractured at the brace end, see Figure 2-26, at the load of 949.4 kN, the maximum tensile load at the brace end, $P_{u,end}$, was regarded as 949.4 kN for all specimens. By referring to the load and stiffness values presented in Table 2-7 and Table 2-8, the test performance can be compared to the target performance as summarized in Table 2-15.

Figure 2-26 Fracture of IHCB-F40W60 at the brace end

For the initial stiffness, although the obtained ones of IHCBs were 16% lower than the target value, their yield strains were approximately 0.24%-0.25%, corresponding to the story drift ratio of 1/200, when the brace was singly placed diagonally with an angle of 45°. Note that the requirement of low initial stiffness proposed in Section 2.1 aimed to enlarge the elastic range of the brace to the story drift ratio of about 1/200 under tension. Therefore, the test performance met the target performance, and the target range is modified as $0.4K_{e,CBB} \leq K_{e,IHCB} \leq 0.5K_{e,CBB}$.

For the post-yield stiffness, all the IHCBs satisfied the target performances. However, it is noted that extremely high post-yield stiffness brings about other unsafety factors and makes the joint design difficult. Based on the test results, the post-yield stiffness of IHCBs should not be larger than 20 times that of CBB. Therefore, the target range is modified as $10K_{p,CBB} \leq K_{p,IHCB} \leq 20K_{p,CBB}$.

For the post-buckling load, the best condition is that the value of the post-buckling load is the same as the maximum compressive load as proposed in Section 2.1. Although the compressive behavior was stabilized as planned, the obtained post-buckling loads of IHCBs were 87%-91% of their maximum compressive loads. Considering that the load loss under compression was nearly unavoidable for the braces without buckling restraints or other mechanisms, errors about 20% should be allowed.

For the brace end capacity, all the IHCBs satisfied the target performances.

Table 2-15 Test performance VS. Target performance

Initial stiffness		
Target performance	$K_{e,IHCB} \approx 0.5K_{e,CBB}$	
Test performance	IHCB-F40	$K_{e,IHCB} = 0.42K_{e,CBB}$
	IHCB-2F60	$K_{e,IHCB} = 0.42K_{e,CBB}$
	IHCB-F40W60	$K_{e,IHCB} = 0.42K_{e,CBB}$
Evaluation	All the IHCBs satisfied the target performance. Considering the relationship with the story drift ratio, the target range is modified as $0.4K_{e,CBB} \leq K_{e,IHCB} \leq 0.5K_{e,CBB}$.	
Post-yield stiffness		
Target performance	$K_{p,IHCB} \geq 10K_{p,CBB}$	
Test performance	IHCB-F40	$K_{p,IHCB} = 16.06K_{p,CBB}$
	IHCB-2F60	$K_{p,IHCB} = 13.72K_{p,CBB}$
	IHCB-F40W60	$K_{p,IHCB} = 18.09K_{p,CBB}$
Evaluation	All the IHCBs satisfied the target performance. To ensure the sufficient load capacity at the brace end, the target range is modified as $10K_{p,CBB} \leq K_{p,IHCB} \leq 20K_{p,CBB}$.	
Post-buckling load		
Target performance	$P_{s,IHCB} \approx P_{c,IHCB}$	
Test performance	IHCB-F40	$P_{s,IHCB} = 0.87P_{c,IHCB}$
	IHCB-2F60	$P_{s,IHCB} = 0.91P_{c,IHCB}$
	IHCB-F40W60	$P_{s,IHCB} = 0.89P_{c,IHCB}$
Evaluation	IHCBs failed to satisfy the target performance with a slight deviation. Considering the unavoidable load loss under compression, the errors within 20% should be allowed. The target range is modified as $0.8P_{c,IHCB} \leq P_{s,IHCB} \leq 1.2P_{c,IHCB}$.	
Brace end capacity		
Target performance	$P_{u,IHCB-end} \geq 1.6P_{y,IHCB}$	
Test performance	IHCB-F40	$P_{u,IHCB-end} = 2.02P_{y,IHCB}$
	IHCB-2F60	$P_{u,IHCB-end} = 2.06P_{y,IHCB}$
	IHCB-F40W60	$P_{u,IHCB-end} = 2.00P_{y,IHCB}$
Evaluation	All the IHCBs satisfied the target performance.	

Above all, no large deviations were found between the test performance and the target performance, representing that the target performance was practical and realizable. Despite that, there are still some deficiencies in IHCB as follows.

1. The curvature of the specimen resulting from the IH treatment is hard to design intentionally. It is known that uneven heat treatment on steel induces shrinkage of the treated regions, therefore, the formation of the curve shape is inevitable. The differences in curvature among IHCB-F40, IHCB-2F60, and IHCB-F40W60 were small, indicating that the formation of the curve must be regular. However, without enough knowledge and experience, the curvature was yet unpredictable before the heat treatment. Therefore, further investigation combining the knowledge of material science may be necessary in the future to make the curvature designable. Note that in the first generation of I-shaped section steel brace, the curve shape was regarded as a disadvantage of the heat treatment and revised by imposing the transverse deformation through a universal testing machine [2.8]. In the second generation of I-shaped section steel brace presented in this study, the curve shape is surprisingly turned into an advantage.

2. The range of IH-treated regions is hard to control. As mentioned in Section 2.3.3, the measured IH-treated regions were smaller than the designed ones in most cases, since the heating or the quenching of the boundaries was difficult, not only in the width direction but also in the thickness direction. Hence, there is still much progress to be made in the improvement of treating devices and conditions.

3. The strength of IH-treated regions is hard to adjust. SS400 (carbon content of 0.13%) is not the steel for heat treatment essentially. Hence, the strength improvement was not so significant as the one of steel born to be heat-treated, such as S45C (carbon content of 0.45%). Further studies on stabilizing the strength of IH-treated regions in a given range are of great importance to popularize the application of IH technology in strengthening structural steels. Note that in the first generation of the I-shaped section steel brace, the strength ratio of the high-strength region to the normal-strength region was 1.2-1.4 times [2.8]. In the second generation as presented in this study, although the same material SS400 was used, the treating conditions, such as the treating speed, were improved. Therefore, the strength ratio of 2.2-2.6 times became available in this study. However, due to the limit of carbon content, a higher strength ratio is hard to expect.

Further requirements on the curvature and strength ratio between the high-strength and normal-strength regions of IHCBs are investigated in Chapter 3.

2.7 Conclusion

This chapter presents the novel experimental study on induction-heated curved braces (IHCBs) with an I-shaped section.

Section 2.1 proposes the target performance level of IHCBs. Considering the weakness of CBB, and the feature of partial strengthening and initial curve shape, the target performance of IHCBs was built in terms of the initial stiffness, post-yield stiffness, post-buckling load, and the load relationship between the main part of the brace and the brace end.

Section 2.2 presents the basic information about the four braces. CBB was untreated at the test region. IHCB-F40 was treated at one side of the flange (F) along the brace length for the width of 40 mm. IHCB-2F60 was treated averagely at two sides of the flange (2F) along the brace length for a total width of 60 mm. IHCB-F40W60 was treated at one side of the flange (F) for 40 mm, and the web (W) for 60 mm. The IHCB series was designed to investigate the dual effect of the partial strengthening and the initial curve shape on the structural performance compared with CBB. The measured longitudinal dimensions of the braces showed that the IHCB series had the initial transverse deformation ranging from 39.9 mm to 47.1 mm, corresponding to 2.2% to 2.6% of the specimen length, but the differences among the three types were small. The measured sectional dimensions proved that the IH-treated region shrank. For example, the edges of the IH-treated flanges significantly bent inwards.

Section 2.3 mentions the outlines of the material. The tensile coupon tests demonstrated that Young's modulus hardly changed after IH treatment. The yield and tensile strengths were raised to approximately 2.2 times at the flange and 2.6 times at the web, but the elongation was reduced by two-thirds. Vickers hardness tests pointed out the deviations in the designed IH-treated regions and the measured ones were about 5 mm - 15 mm. Besides, the junctions between the web and flanges were hard to treat. IH effect depends on the carbon content, treating conditions, and so on. In this study, the higher IH effect was inaccessible mainly due to the relatively lower carbon content of 0.13%.

Section 2.4 explains the outlines of the experiment. The brace was connected to the joint by bolts and pin-supported by gusset plates. The gusset plate allowed the brace rotation around the minor axis. One brace end was fixed in all directions, and the other brace end was movable only in the axial direction. Cyclic axial displacement was applied to the movable brace end with the peak axial strain of 0.1%, 0.15%, 0.3%, 0.45%, 0.6%, 0.9%, and 1.2%. Several displacement transducers and strain gauges were attached to the brace to measure its deformation and local strains.

Section 2.5 presents the experimental results of four braces. Note that except for IHCB-F40W60, all specimens were loaded as planned. IHCB-F40W60 fractured at the 1st cycle of +1.2% axial strain. For the tensile performance, the IHCB series showed approximately 58% lower initial stiffnesses but two times larger yield cycles compared to these of CBB. After yielding, the stiffness of CBB dramatically dropped to 0.9% of the initial stiffness, but the IHCB series maintained higher post-yield stiffnesses, which were 13-18 times that of CBB. For the compressive performance, the buckling behavior seemed in CBB was replaced by overall smooth flexural behavior for all IHCBs. Moreover, the post-buckling load of the IHCB series became 1.49-1.67 times larger than that of CBB, and it was 87%-91% of the maximum compressive load for IHCBs. Regarding the strength degradation between the 2nd and the 1st cycles for the same peak axial strain and the residual strains, CBB was the largest. Transverse deformations and local strains of the IHCB series were more uniformly distributed along the brace length rather than locally concentrated at the brace middle as CBB. Besides, smaller transverse deformations of the IHCB series than CBB were measured after the 0.9% cycle. Last, the energy dissipation demonstrated that the IHCB series possessed almost the same energy dissipation ability as CBB after yielding. Apart from the early fracture of IHCB-F40W60, and the slippage of the joints of IHCB-F40 and IHCB-F40W60, the differences in cyclic behaviors among the three IHCBs were unobvious.

Section 2.6 compares the test performance with the target performance of IHCBs. All IHCBs succeeded in satisfying the target performances. Their initial stiffness was approximately 42% of that of CBB, and the post-yield stiffness was larger than 10 times that of CBB. They presented stable compressive behavior, and the load loss after the maximum compressive load was controlled within 20%. The load capacity at the brace end was sufficient enough to meet the requirement for the connection coefficient of 1.6. However, several unknowns, such as the curvature of the specimen, the range of IH-treated regions, and the strength improvement ratio of IH-treated regions, are remaining to explore.

In all, the IHCB series is able to remain elastic to a larger axial strain, which lowers the load capacity demands for the frame at the small story drift ratio of about 1/200. Additionally, IHCBs provide relatively large post-yield stiffness, indicating that they can continue supporting the frame at the large story drift ratio of about 1/100. Besides, stable compressive behavior is achieved, which reduces the damage brought by buckling and simplifies the design conditions. The uniform transverse deformation represents the whole brace rather than the limited region involved in resisting the deformation, and the smaller transverse deformation of IHCBs than CBB removes the doubt on whether the initial curve shape will intensify the transverse deformation of a curved brace. Part of the content is published in reference [2.10)].

References

2.1)　建築物の構造関係技術基準解説書. (2020). 全国官報販売協同組合.

2.2)　日本大学. (2020,3). 折返し式ブレースの構造特性に関する研究（博士論文）. 波田雅也

2.3)　AIJ Recommendations for Plastic Design of Steel Structures (3rd ed.). (2017). Architectural Institute of Japan.

2.4)　構造計算適合性判定 判定内容事例集(Ver.090210) 解説編. (2009). 愛知県建築住宅センター.

2.5)　AIJ Recommendations for Design of Connections in Steel Structures (3rd ed.). (2012). Architectural Institute of Japan.

2.6)　全面改訂 熱処理技術入門. (2004). 日本熱処理技術協会, 日本金属熱処理工業会. 大河出版.

2.7)　松岡三郎. (2004). 低炭素オーステナイト系ステンレス鋼 SUS316 の加工硬化材における 0.2%耐力とビッカース硬さの関係. 日本機械学会論文集(A 編), 70(698), 185-191.

2.8)　Liu, Y., Tani, M., Kurata, M., Watase, C., & Nishiyama, M. (2020). Study on I-shaped section steel braces partially strengthened by induction heating. Engineering Structures, 210, 110341. https://doi.org/10.1016/j.engstruct.2020.110341

2.9)　Skalomenos, K. A., Kurata, M., & Nishiyama, M. (2020). Induction-heat treated steel braces with intentional eccentricity. Engineering Structures, 211, 110461. https://doi.org/10.1016/j.engstruct.2020.110461

2.10)　Liu, Y., Iwata, K., Sanda, S., Nishiyama, M., & Tani, M. (2021). Development of curved braces partially strengthened by induction heating. Engineering Structures, 233, 111754. https://doi.org/10.1016/j.engstruct.2020.111754

3 Numerical analysis on induction-heated curved braces

This chapter introduces the numerical analysis of induction-heated curved braces (IHCBs). It aims to investigate the load capacity of the braces at the test region, and the effects of curve shape and partial strengthening brought by IH treatment. First, the numerical model is built by ABAQUS 6.14, and the model accuracy is verified by comparing the numerical analysis results to the experiment results. Then, the individual effect of the curve shape is discussed, and the expected curvedness to meet the target performance of IHCB is evaluated. The individual effect of partial strengthening and the target strength ratio are investigated as well. Last, the synthetic effect of the curve shape and the partial strengthening are concluded.

3.1 Modeling

The numerical investigation was conducted by ABAQUS/implicit [3.1]. The 3D views as well as the plan views of CBB, IHCB-F40, and IHCB-2F60 are respectively shown from Figure 3-1 to Figure 3-3. Note that this chapter focuses on the performance at the test region of the braces. Because the specimen IHCB-F40W60 fractured at the brace end, there is a possibility that its test region did not fully exert the load capacity during the test. Hence, IHCB-F40W60 is not considered here.

The models were built as shell elements S4R (4-node shell element with reduced integration). Shell element was employed in this study since the brace thickness was far less than its length. The mesh size was 10 mm in both the length and width directions. Five section points through the shell thickness were integrated by Gaussian integration. To simulate the buckling behavior, the first buckling mode around the minor axis was employed to CBB. Its initial imperfection at the brace middle was 2.2 mm, which was equal to 0.1% of the supported length of 2241 mm. For the IHCB series, the braces were built in a curve shape around the minor axis. The initial imperfection was 41 mm at the brace middle, corresponding to the average value in the experiment shown in Section 2.2.3.

Other components, including the end plate, gusset plate, fin stiffener, splice plate, and the thin plate, which was for the gap between the web of the brace and the gusset plate, were all built as shell elements based on their sizes presented in Section 2.4.4. All the jointing and welding were simulated by normal tie constraints. Note that the eccentricity of approximately 7 mm was induced to the joint used for IHCBs. Cyclic axial displacements were applied to one end plate, where only the axial deformation was allowed, and the other end plate was fixed in all directions. The static and general type was used for the analysis with the option of NLGEOM (nonlinear geometry) on. Other details, such as specimen designs and loading protocol, are referred to in Chapter 2. Note that the deformed cross-sections, the bolt holes, and the high-strength bolts were not modeled.

(a) 3D view

(b) Plan view
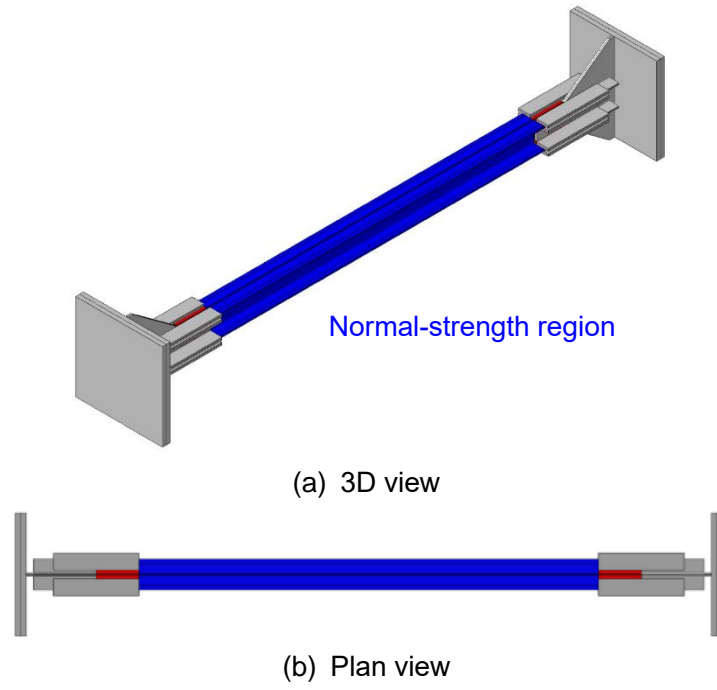
Figure 3-1 Modeling of CBB

(a) 3D view

(b) Plan view
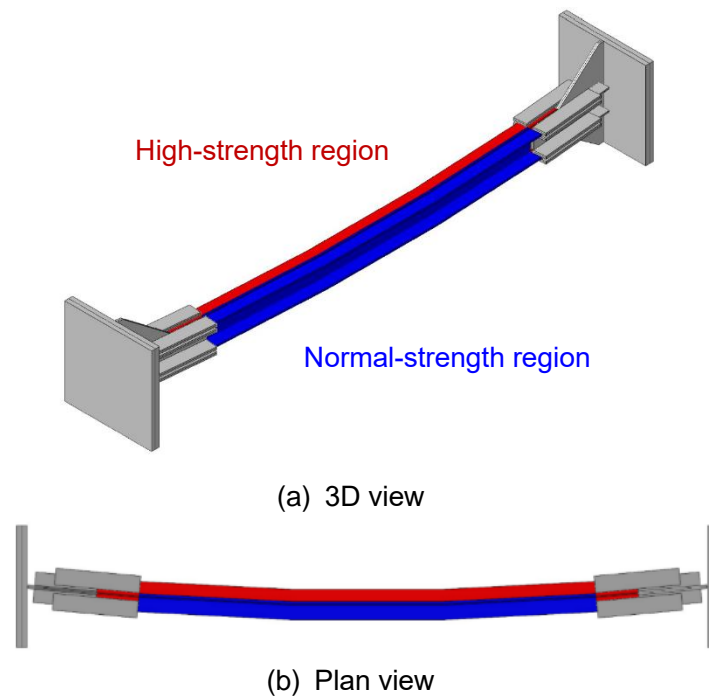
Figure 3-2 Modeling of IHCB-F40

(a) 3D view

(b) Plan view
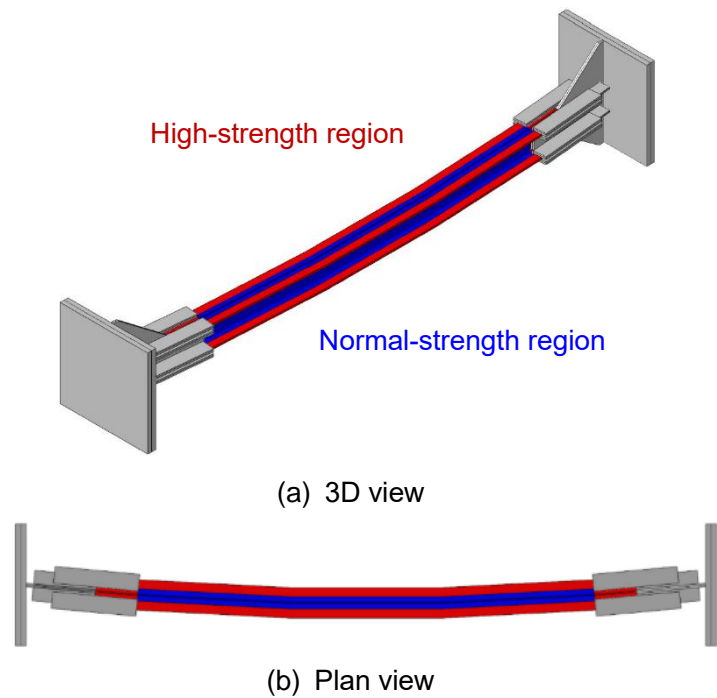
Figure 3-3 Modeling of IHCB-2F60

Figure 3-4 shows the stress-strain relationships of the flange and web for the numerical model. Experiment is the true stress-strain relationship converted from the engineering stress-strain relationship obtained from the tensile coupon test results in Section 2.3.2. Analysis is the stress-strain relationship used for the numerical model. Multi-linear stress-strain relationships based on isotropic hardening were employed.

(a) Flange

(b) Web
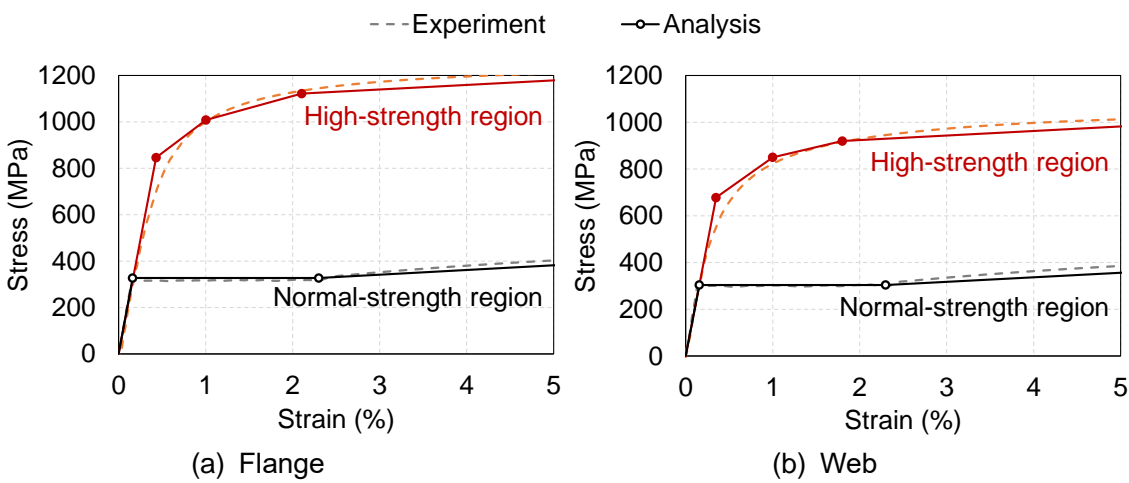
Figure 3-4 Material properties for numerical model

For the elastic range, Young's modulus and yield strength obtained from the experiment were adopted for the numerical analysis. The yield point is shown as the first point of each analysis stress-strain curve. However, for the high-strength region, there are some deviations in the stress-strain curves between the experimental ones and the analysis ones. It is because the high-strength region did not show a typical yield stage in the test, and 0.2% proof stress was regarded as its yield strength. Although adding new points in the analysis stress-strain curve, such as the elastic limit point, can correct this deviation, other problems may arise. For example, the first yield of the fiber in the analysis may be decided by the elastic limit strength rather than the yield strength, thereby, resulting in the error during the judgement of models' yield behaviors. Given that, these deviations were allowed and kept unmodified. Besides, the Poisson ratio was set as 0.3.

For the yield stage, the line connecting the first and the second points represents the yield stage of the normal-strength region, since it was almost linear. While, for the high-strength region, the lines connecting the first, second, and third points represent its yield stage. For the plastic range, the strain hardening equal to 1% of Young's modulus was assigned both for the normal and high-strength regions according to the previous similar study on the IH-treated braces [3.2].

The material SM490 was used for the joint. The yield strength was modeled as 325 MPa and the maximum tensile strength as 490 MPa. Note that the strength transition region between the normal and high-strength regions, the dispersion in the IH-treated ranges, and the residual stress induced by IH treatment were not considered.

3.2 Verification of model

3.2.1 Load-axial strain relationships

The load-axial strain relationships of analysis compared to the test results are shown in Figure 3-5. The values of tensile and compressive load capacities are summarized in Table 3-1 and Table 3-2, respectively. The value in bracket ( ) shows the ratio of the analysis result to the experimental one. The analysis results captured the test results well in shape, except for the slight drift of the load capacity from the tensile side to the compressive side, in other words, the underestimation of the tensile load capacity and the overestimation of the compressive load capacity, at the 1st cycle of 1.2% axial strain for IHCB-2F60. It was because its transverse deformation at -1.2% axial strain in the analysis slightly overestimated the test results, which increased the deformation for straightening the brace at the following cycle to +1.2% axial strain and reduced the axial deformation demand.

(a) CBB

(b) IHCB-F40

(c) IHCB-2F60
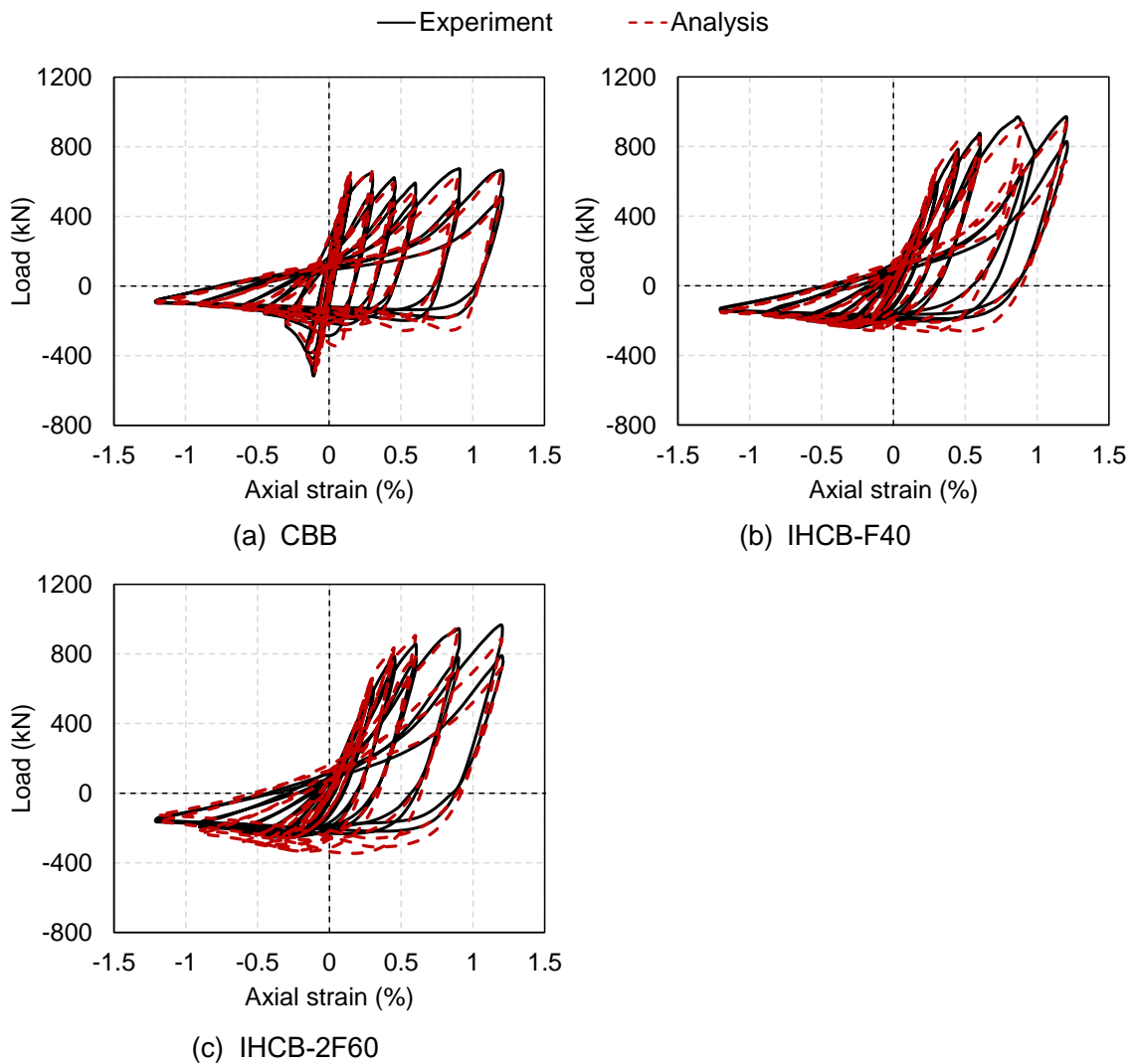
Figure 3-5 Load-axial strain relationships

Table 3-1 Tensile load capacities

Specimen	Initial stiffness (GPa)		Post-yield stiffness (GPa)		Yield load (kN)		Maximum load (kN)	
	Exp.	Ana.	Exp.	Ana.	Exp.	Ana.	Exp.	Ana.
CBB	207.7	230.0 (1.11)	1.88	-1.80 (-0.96)	565.1	595.8 (1.05)	670.0	666.4 (0.99)
IHCB-F40	87.3	101.7 (1.16)	30.2	20.2 (0.67)	471.0	461.1 (0.98)	972.6	936.9 (0.96)
IHCB-2F60	88.2	100.3 (1.14)	25.8	23.4 (0.91)	460.7	454.9 (0.99)	963.7	957.3 (0.99)

For the tensile load capacities, the yield and the maximum loads of the analysis captured the experimental results well, and the errors were within 5%. The errors of the initial and post-yield stiffnesses were within 16%, except for the post-yield stiffness of CBB and IHCB-F40. For CBB, the negative post-yield stiffness was observed in the analysis, though the absolute value was similar to the experimental one. For IHCB-F40, the post-yield stiffness in the analysis was only 67% of that in the experiment. While analyzing the stiffness, the strain was one of the key factors. Because the strain was the denominator, the slight deviation when selecting the critical points also influenced the final answer of the post-yield stiffness.

Table 3-2 Compressive load capacities

Specimen	Buckling load (kN)		Maximum load (kN)		Post-buckling load (kN)	
	Exp.	Ana.	Exp.	Ana.	Exp.	Ana.
CBB	-515.8	-504.7 (0.98)	-515.8	-504.7 (0.98)	-139.5	-141.7 (1.02)
IHCB-F40			-239.9	-262.5 (1.09)	-208.0	-209.4 (1.01)
IHCB-2F60			-256.3	-345.6 (1.35)	-233.5	-292.1 (1.25)

For the compressive load capacities, the experimental results of CBB and IHCB-F40 were generally captured, and the errors were within 9%. For IHCB-2F60, the analysis results overestimated the experimental results by up to 35%. It is assumed that the slight difference in the deformation under compression resulted in these phenomena. In all, the results obtained from the experiment and analysis were in great agreement.

3.2.2 Yield cycles

The contours of all specimens, including the 3D view and plan view, when the yielding was first observed are shown in Figure 3-6. Analysis results revealed that the yielding of CBB first occurred at the 0.15% cycle nearly at the whole cross-section, especially at the inner side of the initial imperfection. The yielding of IHCB-F40 first occurred in the normal-strength region at the outer side, and that of IHCB-2F60 occurred at the boundary between normal and high-strength regions at the inner side, both at the 0.3% cycle. The analyzed first yield cycles were consistent with the experimental results. Further investigation into the first yield fiber is presented in Section 4.2.2.

(a) CBB: at the 0.15% cycle   (b) IHCB-F40: at the 0.3% cycle

■ Yielded region
■ Unyielded region

(c) IHCB-2F60: at the 0.3% cycle
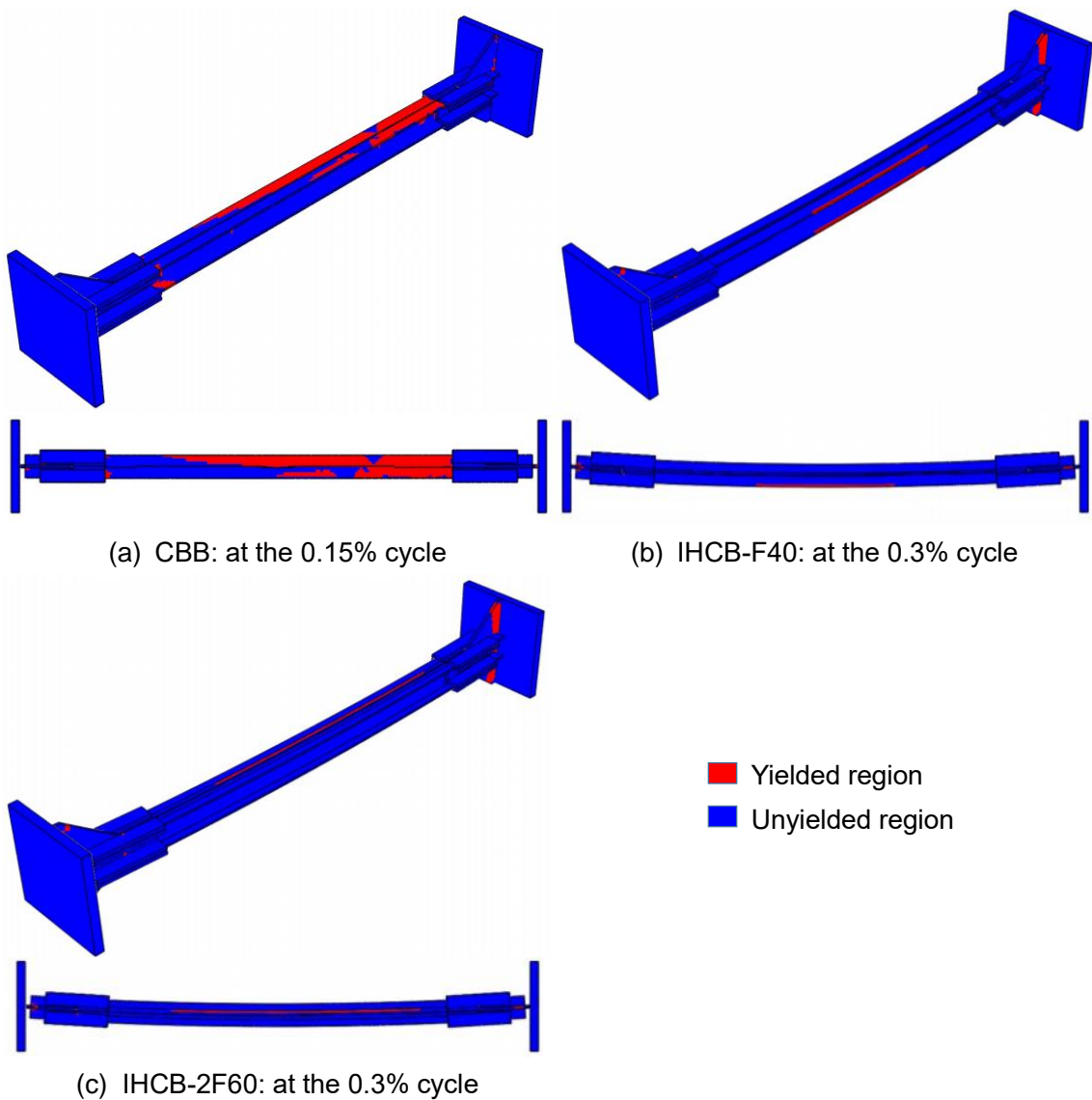
Figure 3-6 First yield cycles

3.2.3 Transverse deformations and local strain distributions

The stress distributions at the first cycle of -1.2% axial strain with the maximum transverse deformations are shown in Figure 3-7, and the data of transverse deformations are summarized in Table 3-3. The stress concentrated at the brace middle of CBB which is shown as the green region, but it was more uniformly distributed along the brace length of the IHCB series shown as the green to red regions. It indicated that for IHCB, the whole brace rather than the limited regions took part in resisting the external load. In terms of transverse deformations, CBB was the largest. The analysis results generally captured the experimental results with the errors controlled within 11%. IHCB series showed a smoother and smaller bending along the length, especially for IHCB-F40, even though they possessed relatively large initial curve shapes.

(a) CBB

(b) IHCB-F40
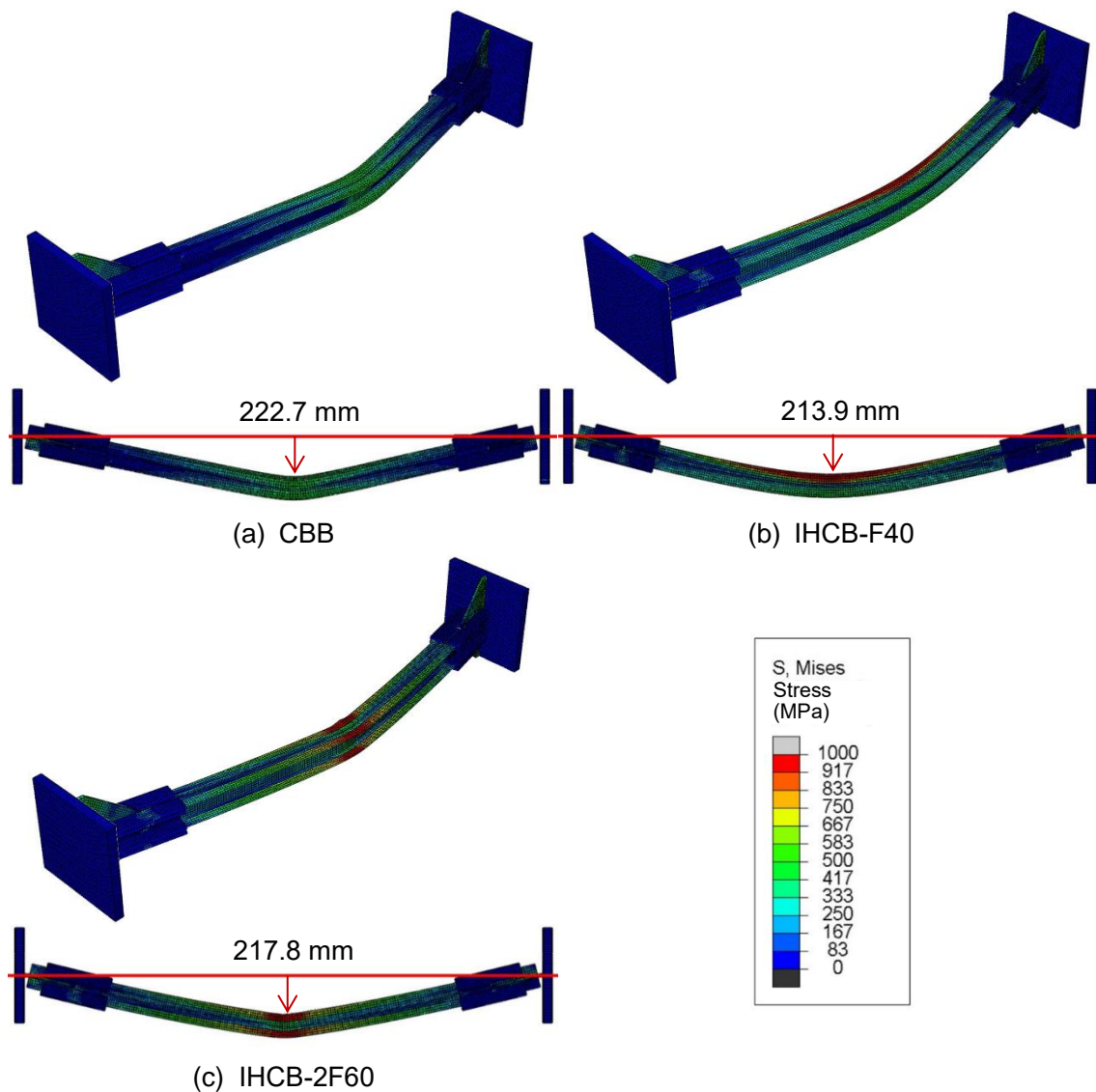
(c) IHCB-2F60

Figure 3-7 Stress distributions and transverse deformations at -1.2% peak axial strain

Table 3-3 Maximum transverse deformation at -1.2% peak axial strain

Specimen	Ana. (mm)	Exp. (mm)	Ana. /Exp.
CBB	222.7	210.6	1.06
IHCB-F40	213.9	200.3	1.07
IHCB-2F60	217.8	196.6	1.11

Although further efforts can be made to evaluate the data more precisely, for example, by combining the isotropic and kinematic hardenings in the material property, which has been done in the investigation into the third generation of induction-heated I-shaped section steel braces [3.3], the accuracy shown here is satisfying. Therefore, the following discussion will be carried on based on these numerical models, and IHCB-F40 is treated as a baseline model for comparison.

3.3 Target curve shape level

3.3.1 Effect of curve shape

To investigate the effect of the curve shape, the curved brace, see Figure 3-8, with the initial transverse deformation of 41 mm at the brace middle, without partial strengthening, was simulated. The only difference between IHCB-F40 and the curved brace is the existence or nonexistence of the partially strengthened region.
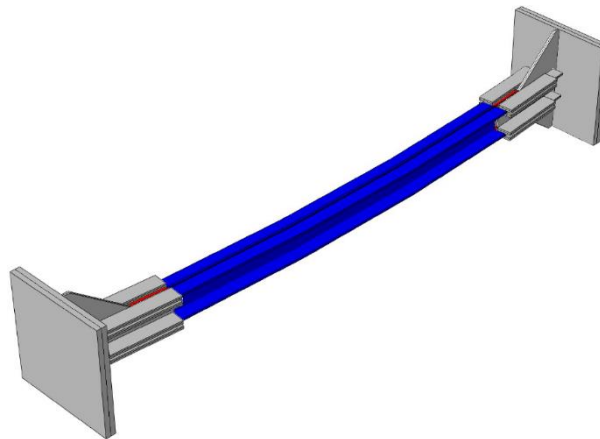
Figure 3-8 3D view of curved brace

Figure 3-9 shows the load-axial strain relationship of the curved brace compared to that of CBB and IHCB-F40. The values of tensile and compressive load capacities are concluded in Table 3-4 and Table 3-5, respectively. The value in bracket ( ) shows the ratio of the corresponding one to that of CBB.

(a) Curved brace VS. CBB   (b) Curved brace VS. IHCB-F40
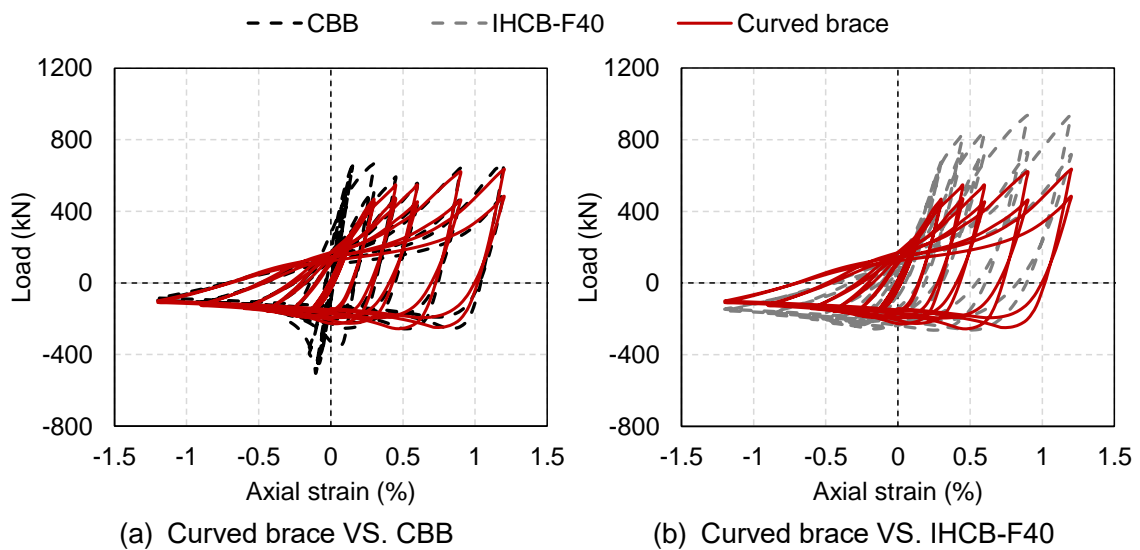
Figure 3-9 Load-axial strain relationship of curved brace

Table 3-4 Effect of curve shape on tensile load capacities

Numerical model	Stiffness (GPa)		Load			
			Yield load		Maximum load	
	Initial	Post-yield	Value (kN)	Cycle	Value (kN)	Cycle
CBB	230.0	-1.80	595.8	1st of +0.15%	666.4	1st of +1.20%
Curved brace	92.0 (0.40)	12.0 (-6.66)	134.1 (0.23)	1st of +0.15%	635.4 (0.95)	1st of +1.20%
IHCB-F40	101.7 (0.44)	20.2 (-11.22)	461.1 (0.77)	1st of +0.30%	936.9 (1.41)	1st of +1.20%

Table 3-5 Effect of curve shape on compressive load capacities

Numerical model	Load					
	Buckling		Maximum		Post-buckling	
	Value (kN)	Cycle	Value (kN)	Cycle	Value (kN)	Cycle
CBB	-504.7	1st of -0.15%	-504.7	1st of -0.15%	-141.7	
Curved brace			-255.3 (0.51)	1st of +0.90%	-149.4 (1.05)	1st of -0.60%
IHCB-F40			-262.5 (0.52)	1st of +0.90%	-209.4 (1.48)	

Overall, the behaviors of the curved brace were almost coincident with those of CBB after the 0.3% cycle both under tension and compression. Under tension, the curved brace showed approximately 60% lower initial stiffness than that of CBB, representing that the curve shape dominated the initial stiffness of the brace. But the yield load of the curved brace was relatively lower than that of CBB and the yield cycle was unvaried, indicating that the curve shape alone was difficult to delay the yield strain. Surprisingly, the negative post-yield stiffness observed in CBB was not observed in the curved brace, and the value was as large as 12.0 GPa. Under compression, the curved brace avoided buckling with a smooth bending behavior. Its ratio of the post-buckling load to the maximum compressive load was 0.59, twice as high as that of CBB, which was 0.28.

In comparison to IHCB-F40, despite the value of the load, the shape of the load-axial strain relationship of the curved brace was as similar to that of IHCB-F40. Under tension, due to the lack of the high-strength region, the post-yield stiffness of the curved brace was approximately 40.6% lower than that of IHCB-F40 with an earlier yield cycle. Under compression, the maximum load capacity was similar, but the post-buckling load was 28.7% lower than that of IHCB-F40.

Different from CBB, the yield deformation of a curved brace not only depends on its material's yield strain but also relies on its shape, to be specific, its eccentricity. However, it seems hard to adjust the yield cycle of a brace only by employing the curve shape. What is meaningful is that the curve shape triggers the flexural behavior under compression, and the compressive behavior is kept the same as the post-buckling behavior of CBB. Therefore, if a curved brace is to be designed, only the post-buckling load should be calculated in the aspect of compression, and the existing equation for CBB [3.4] can be used as well, which greatly simplifies the design process.

3.3.2 Effect of different curvedness

After confirming the effect of curve shape, this section aims to evaluate the brace behaviors with different curvedness. A new evaluation index, curvedness, is adopted here, which is the ratio of the initial transverse deformation to the specimen length. It is 2.2%-2.6% for the measured specimens in Section 2.2.3, and approximately 2.3% (= 41 mm / 1783 mm) for the tested specimens. Note that a similar index, curvature, is mainly used for the evaluation of the central angle of the arc shape of IHCB.

The baseline model IHCB-F40 was modified with different curvedness. The curvedness was changed every 0.5% in a wide range, and every 0.2% in a small range. In all, the curvedness of 1.5%, 2.0%, 2.1%, 2.3% (baseline model), 2.5%, 2.7%, 3.0%, and 3.5% was adopted for the model of IHCB-F40.

(a) Under tension with the curvedness of 1.5%-2.3%

(b) Under tension with the curvedness of 2.3%-2.7%

(c) Under tension with the curvedness of 2.3% and 3.0%-3.5%

(d) Under compression with the curvedness of 1.5%, 2.3%, and 3.5%
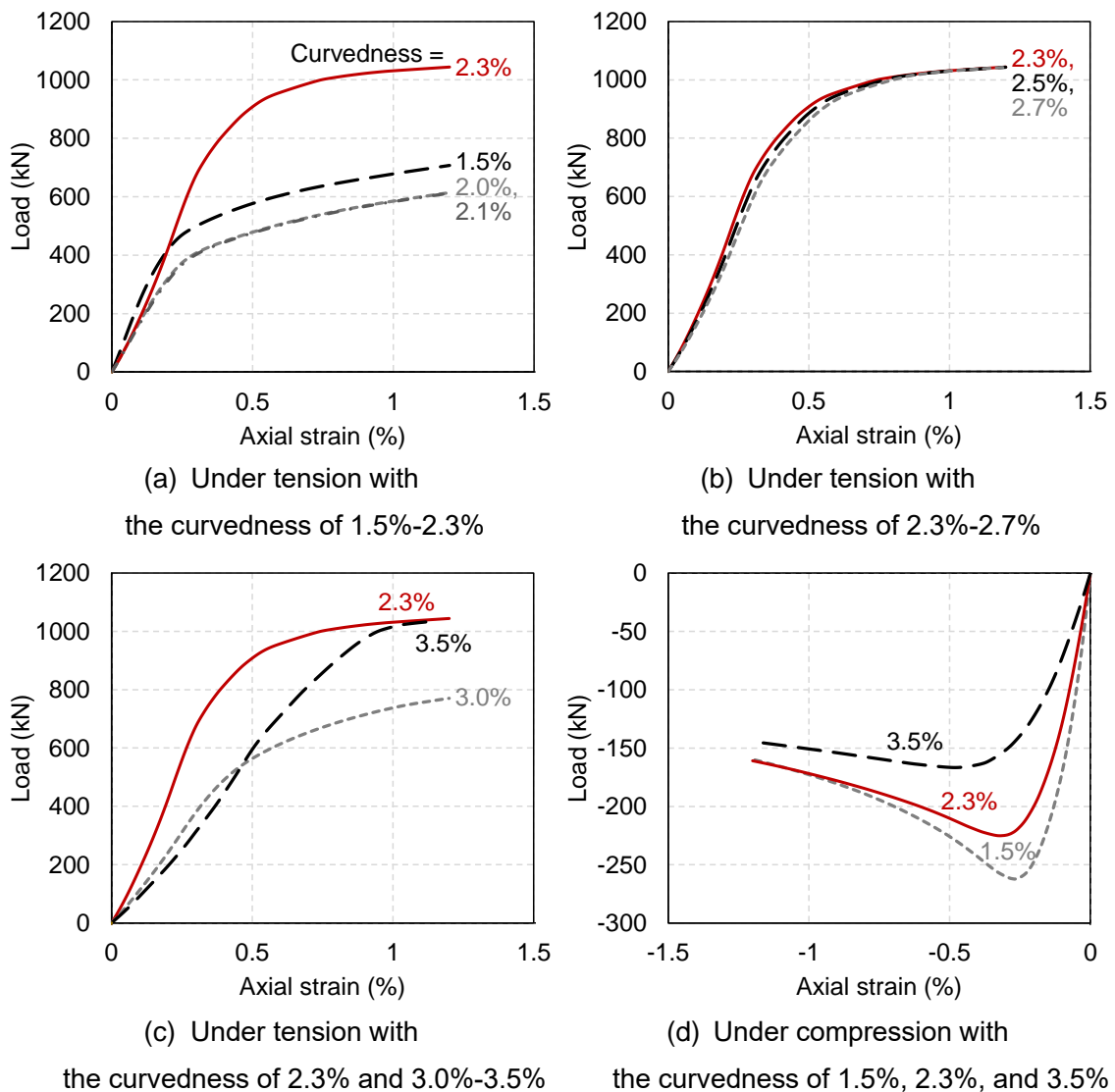
Figure 3-10 Load-axial strain relationship of IHCB-F40 with different curvedness

The monotonic load-axial strain relationships with the axial strain from -1.2% to 1.2% are shown in Figure 3-10(a) to (d). The tensile behaviors are divided into three types, and the behavior of the baseline model with a curvedness of 2.3% is shown in all figures for comparison. To explain different yield behaviors, the yield regions of these three types are also presented in Figure 3-11(a) to (c).

First, when the curvedness ranged from 1.5% to 2.1%, see Figure 3-10(a), the initial stiffness reduced with the increase of the curvedness as predicted. Their first yield regions were at the boundary between the high and normal-strength regions on the inner side, as shown in Figure 3-11(a).

The second type was the braces with the curvedness ranging from 2.3% to 2.7%, see Figure 3-10(b). Increasing the curvedness from 2.1% to 2.3% surprisingly changed the initial behavior and greatly increased the load capacity. One of the most possible reasons is that the first yield region relocated to the high-strength region on the inner side, as demonstrated in Figure 3-11(b). The differences among the ones with the curvedness of 2.3%, 2.5%, and 2.7% were small.

The third type was the braces with the curvedness ranging from 3.0% to 3.5%, as described in Figure 3-10(c). Because of the relatively large curvedness compared to the aforementioned ones, their initial stiffnesses were relatively low, and they yielded first at the normal-strength region on the outer side, as shown in Figure 3-11(c). It is confirmed that the curvedness played a great role in deciding the first yield region, thereby, affecting the tensile behaviors.
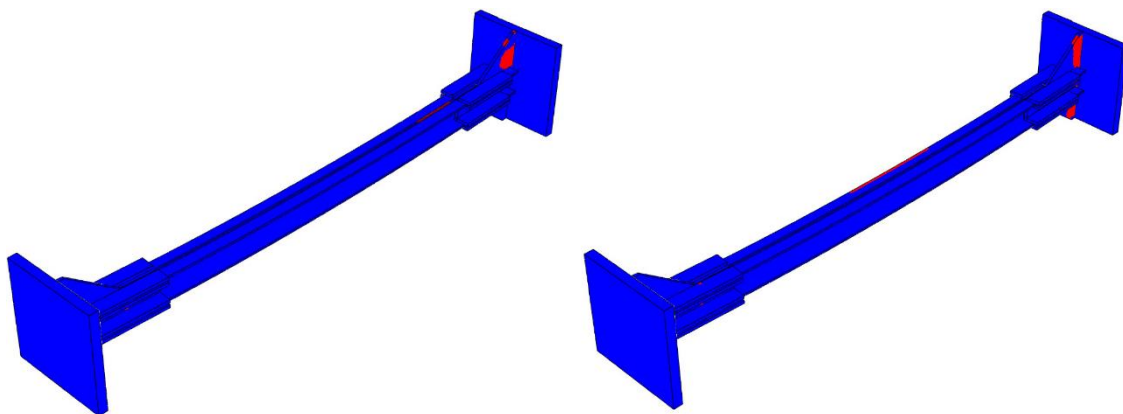
(a) With the curvedness of 1.5%-2.1%   (b) With the curvedness of 2.3%-2.7%
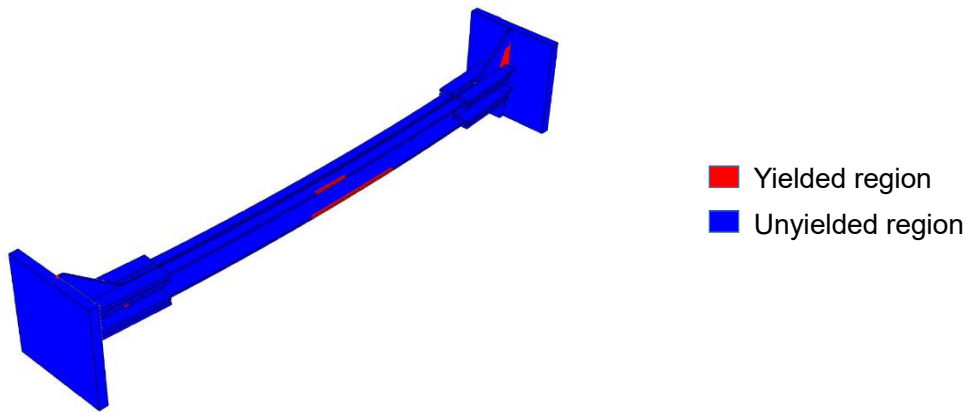
(c) With the curvedness of 3.0%-3.5%

Figure 3-11 Yield regions of IHCB-F40 with different curvedness

In terms of the compressive behavior, since the tendency was similar for all IHCB-F40s, only the representative ones with the curvedness of 1.5%, 2.3%, and 3.5% are presented in Figure 3-10(d). It is proved that the increasing curvedness smoothened the compressive behavior and helped delaying the occurrence of the maximum compressive load.

3.3.3 Target curvedness

Although the curve shape of IHCB is unpredictable yet as presented in Section 2.6, the target curve shape, specifically, the allowable deviation in the curve shape, to meet the target performance of IHCB is worth investigating. The target curvedness can be judged from the investigation into the effect of different curvedness presented in Section 3.3.2.

Figure 3-12(a) to (c) show the initial stiffness ratio $K_e/K_{e,CBB}$-curvedness relationship, the post-yield stiffness ratio $K_p/K_{p,CBB}$-curvedness relationship, and the post-buckling load ratio P_s/P_c-curvedness relationship, respectively. Note that $K_e/K_{e,CBB}$ (or $K_p/K_{p,CBB}$) is the ratio of the initial stiffness (or the post-yield stiffness) of IHCB-F40 model with corresponding curvedness to that of CBB. P_s/P_c is the ratio of the post-buckling load to the maximum compressive load of the same IHCB-F40 model. $K_{e,CBB} = 207.7$ GPa, $K_{p,CBB} = 1.88$ GPa obtained from the test were employed.

(a) Low initial stiffness

(b) Large post-yield stiffness

(c) Stable compressive behavior
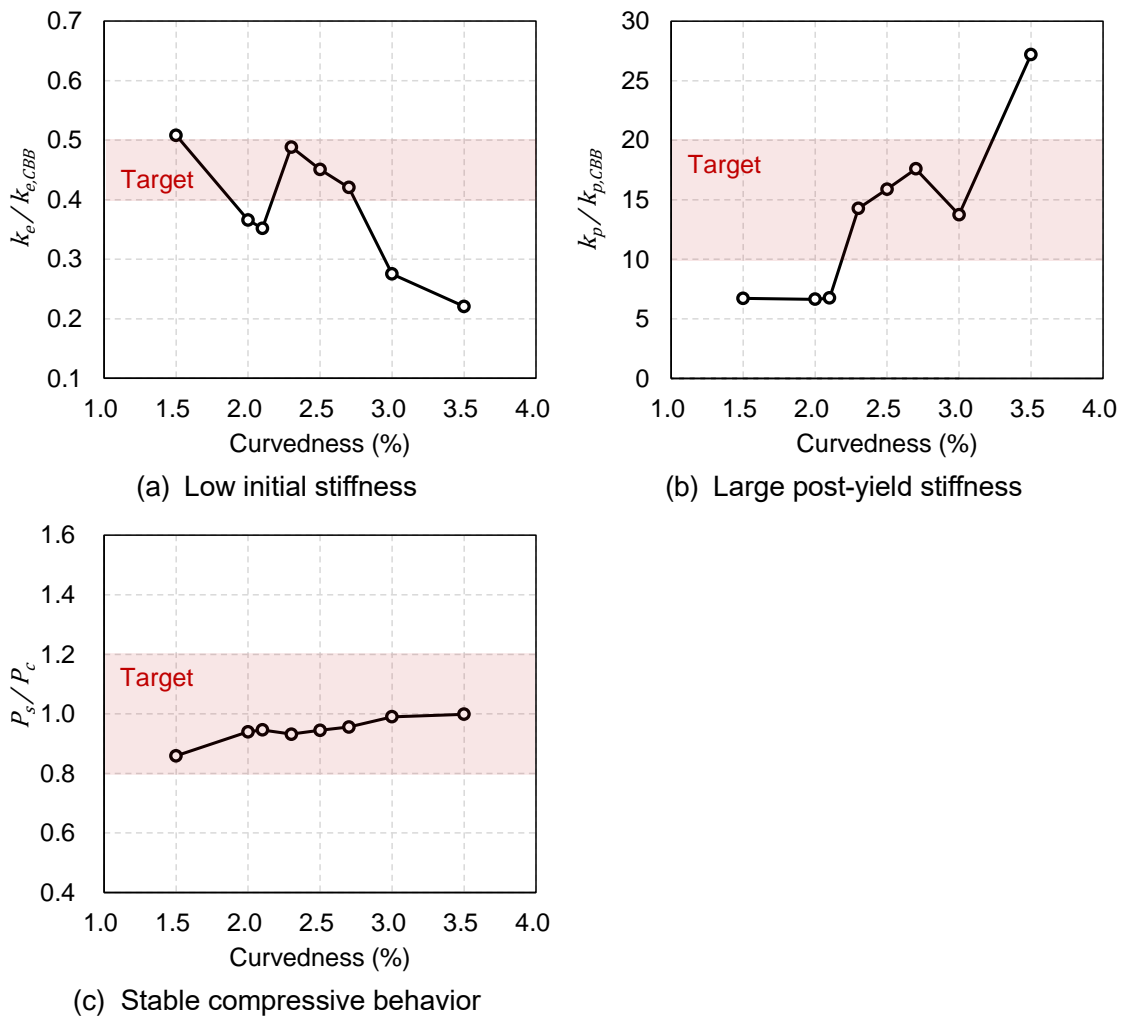
Figure 3-12 Target curvedness

The target value of $K_e/K_{e,CBB}$ is approximately 0.4 to 0.5, of $K_p/K_{p,CBB}$ is 10 to 20, of P_s/P_c is 0.8 to 1.2 according to Sections 2.1 and 2.6, and their ranges are shown in red. It is confirmed that the curvedness of 2.3% to 2.7% satisfied the requirement on the low initial stiffness, of 2.3% to 3.0% met the requirement on the large post-yield stiffness. While the stable compressive behavior was easily achieved by the IHCB-F40 models with the curvedness ranging from 1.5% to 3.5%. Therefore, without regard to the deviation of the partial strengthening, the target curvedness of IHCB-F40 is 2.3% to 2.7%.

3.4 Target partial strengthening level

3.4.1 Effect of partial strengthening

The effect of partial strengthening is investigated in this section. The partially strengthened brace, see Figure 3-13, is treated at one side of the flange for 40 mm without the curve shape. The only difference between the partially strengthened brace and IHCB-F40 is that the partially strengthened brace is straight, which is the same as IHB-W40 in the first generation of the induction-heated brace series [3.5)].
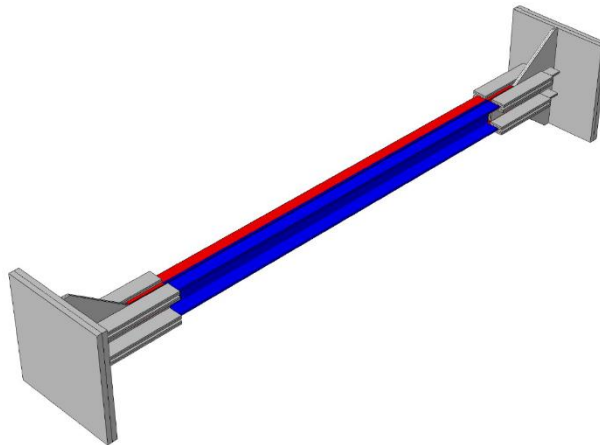
Figure 3-13 3D view of partially strengthened brace

Figure 3-14 shows the load-axial strain relationship of the partially strengthened brace compared to that of CBB and IHCB-F40. The values are summarized in Table 3-6 and Table 3-7.

(a) Partially strengthened brace VS. CBB

(b) Partially strengthened brace VS. IHCB-F40
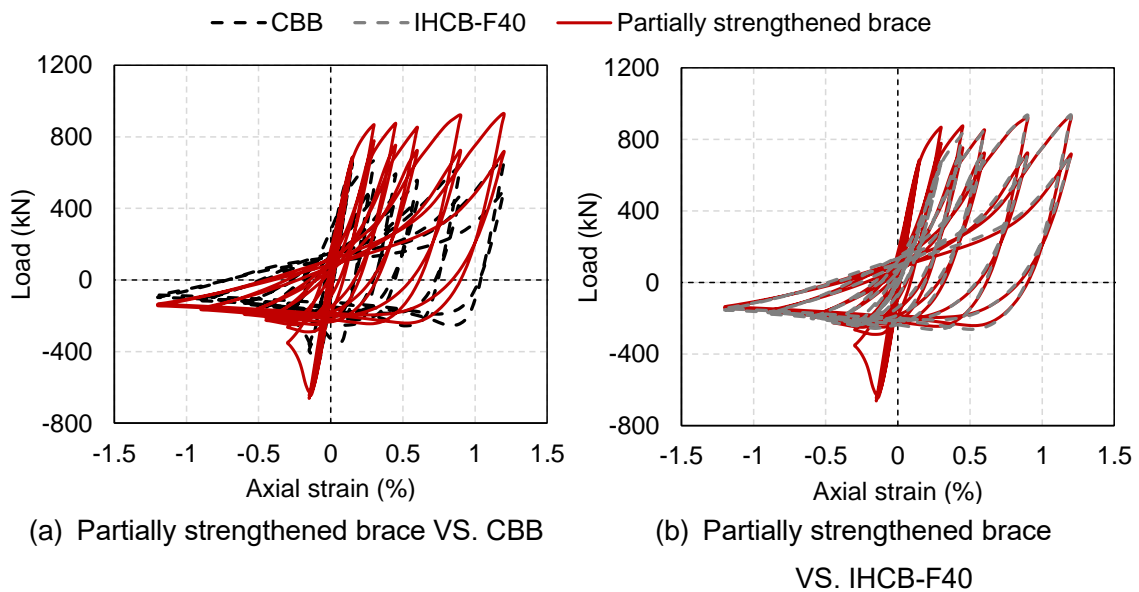
Figure 3-14 Load-axial strain relationship of partially strengthened brace

Table 3-6 Effect of partial strengthening on tensile load capacities

| Numerical model | Stiffness (GPa) | | Load | | | |
| | | | Yield load | | Maximum load | |
	Initial	Post-yield	Value (kN)	Cycle	Value (kN)	Cycle
CBB	230.0	-1.80	595.8	1st of +0.15%	666.4	1st of +1.20%
Partially strengthened brace	231.2 (1.01)	4.15 (-2.31)	599.0 (1.01)	1st of +0.15%	930.5 (1.40)	1st of +1.20%
IHCB-F40	101.7 (0.44)	20.2 (-11.22)	461.1 (0.77)	1st of +0.30%	936.9 (1.41)	1st of +1.20%

Table 3-7 Effect of partial strengthening on compressive load capacities

| Numerical model | Load | | | | | |
| | Buckling | | Maximum | | Post-buckling | |
	Value (kN)	Cycle	Value (kN)	Cycle	Value (kN)	Cycle
CBB	-504.7	1st of -0.15%	-504.7	1st of -0.15%	-141.7	
Partially strengthened brace	-626.4 (1.24)	1st of -0.30%	-662.0 (1.31)	1st of -0.15%	-199.5 (1.41)	1st of -0.60%
IHCB-F40			-262.5 (0.52)	1st of +0.90%	-209.4 (1.48)	

Overall, the load value of the partially strengthened brace was approximately 1.40 times higher than that of CBB after yielding. Under tension, the initial stiffness and the yield load of the partially strengthened brace were kept nearly the same as that of CBB because of the straight shape and the same Young's modulus of the material. For the partially strengthened brace, the multistage yielding behavior was observed. The negative post-yield stiffness observed in CBB was modified in the partially strengthened brace, and the value was as large as 4.15 GPa. Under compression, the buckling behavior was unavoidable, but the post-buckling load was slightly higher than that of CBB. This phenomenon is discussed in detail in Section 4.2.

In comparison to IHCB-F40, despite the initial behaviors before the 0.3% cycle and the buckling behavior, the shape of the load-axial strain relationship of the partially strengthened brace was the same as that of IHCB-F40. Under tension, the straight shape increased the initial stiffness by 2.3 times but reduced the post-yield stiffness to 20.6% of that of IHCB-F40. However, the maximum loads of these two braces were the same, indicating that under a large tensile load, the curve shape of IHCB-F40 was almost straightened. Under compression, similar post-buckling loads were achieved.

It is confirmed that the greatest effects brought by partial strengthening are high load capacity and multistage yielding behavior. Despite the partial strengthening works on increasing the compressive load capacity, its influence on compressive stability seems small.

3.4.2 Effect of different strength ratio

This section aims to evaluate the brace behaviors with different strength ratios. The strength ratio, K, is the abbreviation of the strength ratio of the high-strength region to the normal-strength region. It is 2.2 for the flange and 2.6 for the web as tested in Section 2.3.2. Note that the material of the normal strength region is SS400.

The IHCB-F40 model was modified with different materials. For the normal-strength flange and normal-strength web, although their material properties for numerical analysis were slightly different as Section 3.1 describes, the material properties of the web were set as those of the flange for easy comparison. The strength ratio was changed every 0.5. Considering that the IH treatment commonly improves the strength of the carbon steel by 2-4 times, the strength ratio of 1.5, 2.0, 2.2 (baseline model), 2.5, 3.0, 3.5, and 4.0 was adopted. Figure 3-15 shows the material properties of the representative ones. The monotonic load-axial strain relationships under tension and compression are shown in Figure 3-16(a) and (b), respectively. To explain different yield behaviors, the yield regions are also presented in Figure 3-17(a) and (b).
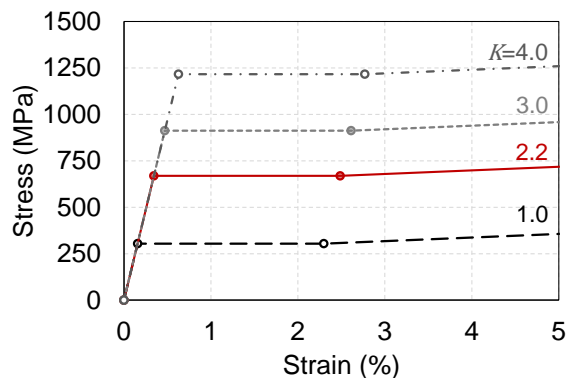
Figure 3-15 Material properties for numerical model

Because the tendency was similar, the load-axial strain relationships when the strength ratio is 1.5, 2.2, 3.0, and 4.0 are presented. Before reaching the turning points, their load-axial strain relationships were almost consistent. After that, the ones with the larger strength ratio showed larger load capacities both under tension and compression. The larger strength ratio also delayed the occurrence of the critical loads, for example, the maximum compressive load. The obvious difference in the tensile behaviors is that the ones with the strength ratio from 1.5 to 2.2 first yielded at the high-strength region on the inner side as Figure 3-17(a) describes. While those with a strength ratio larger than 2.5 first yielded at the boundary between the high and normal-strength regions at the inner side as shown in Figure 3-17(b). Therefore, the strength ratio played a great role in deciding the first yield region of the brace.

(a) Under tension   (b) Under compression
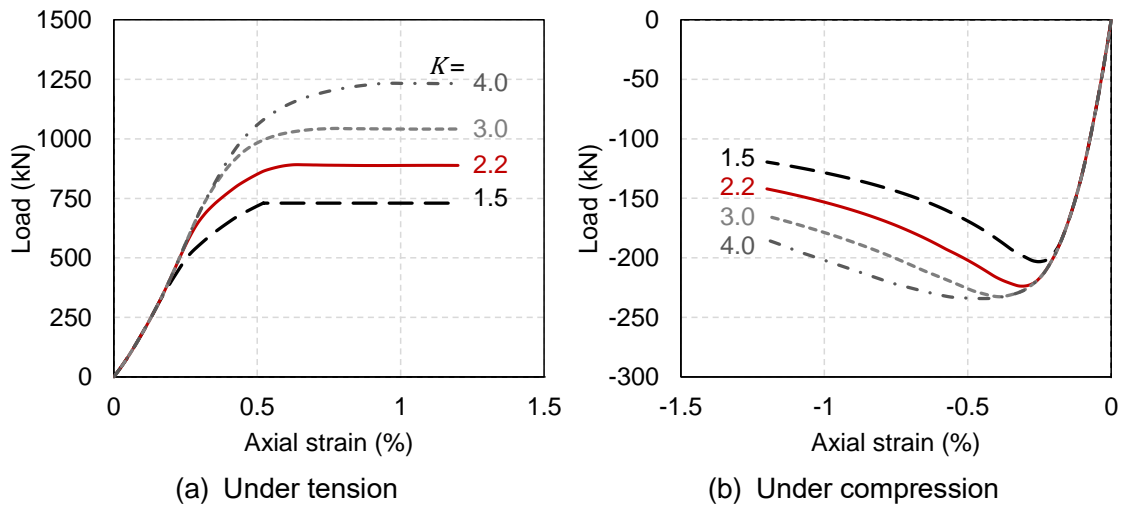
Figure 3-16 Load-axial strain relationship of IHCB-F40 with different strength ratios

(a) With the strength ratio of 1.5-2.2   (b) With the strength ratio of 2.5-4.0
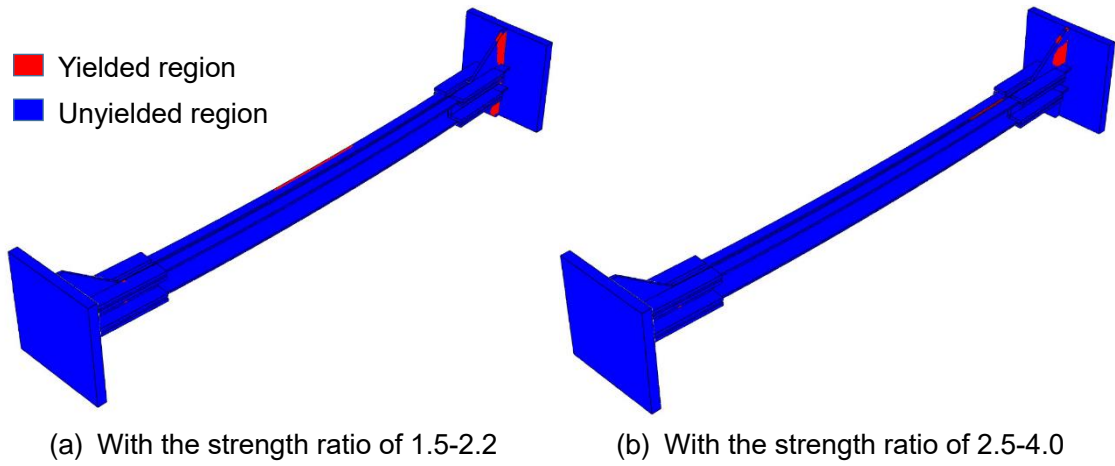
Figure 3-17 Yield regions of IHCB-F40 with different strength ratios

3.4.3 Target strength ratio

Although the strength ratio is hard to control yet as presented in Section 2.6, the allowable deviation in the strength ratio to satisfy the target performance of IHCB is worth evaluating. The target strength ratio can be judged from the investigation into the effect of different strength ratios presented in Section 3.4.2.

Figure 3-18(a) to (c) show the initial stiffness ratio $K_e/K_{e,CBB}$-strength ratio relationship, the post-yield stiffness ratio $K_p/K_{p,CBB}$-strength ratio relationship, and the post-buckling load ratio P_s/P_c-strength ratio relationship, respectively. The target value of $K_e/K_{e,CBB}$ is approximately 0.4 to 0.5, of $K_p/K_{p,CBB}$ is 10 to 20, of P_s/P_c is 0.8 to 1.2 according to Sections 2.1 and 2.6, and their ranges are shown in red.

(a) Low initial stiffness

(b) Large post-yield stiffness

(c) Stable compressive behavior
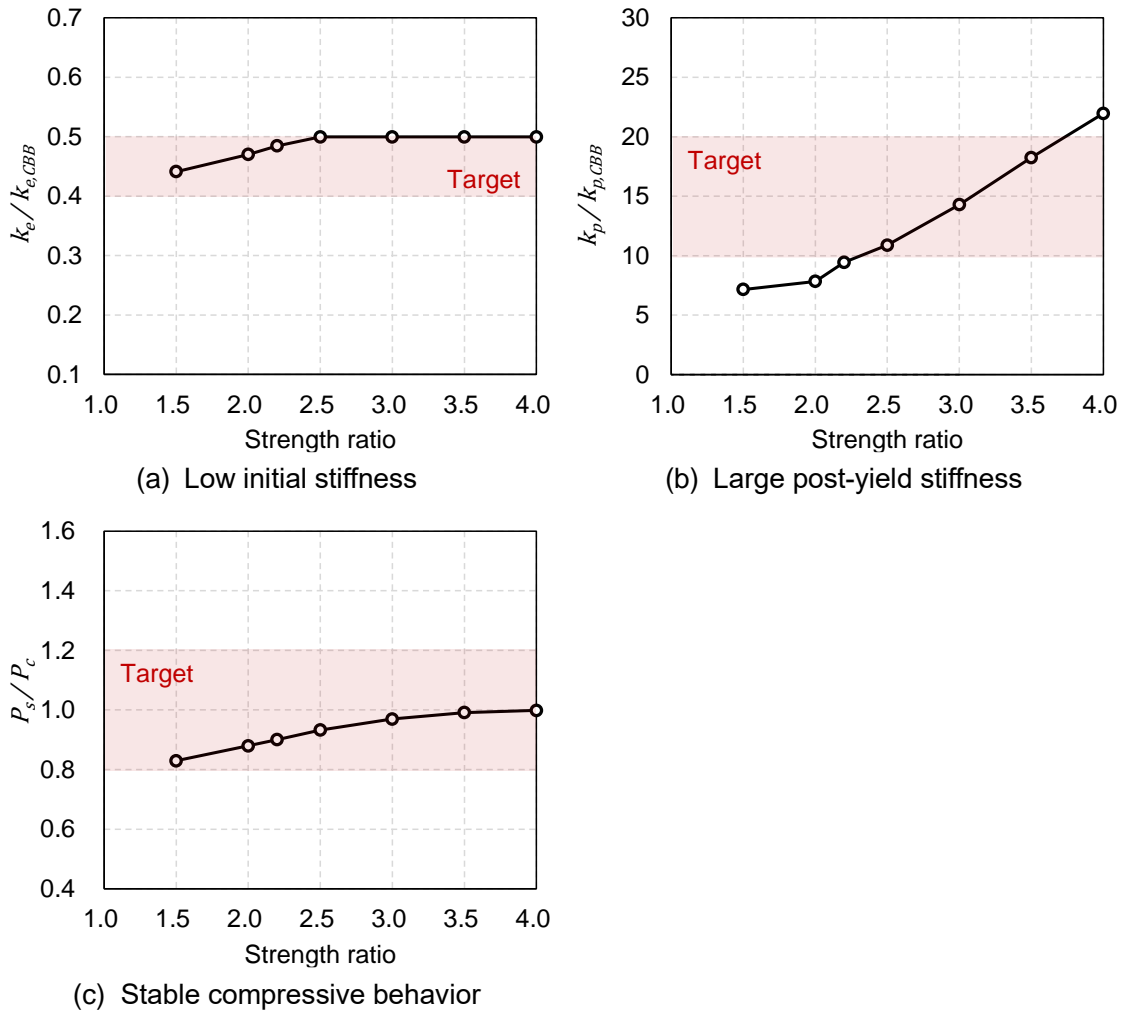
Figure 3-18 Target strength ratio

It is confirmed that the strength ratio of 1.5 to 4.0 satisfied the requirement on the low initial stiffness, of 2.5 to 3.5 met the requirement on the large post-yield stiffness. While the stable compressive behavior was easily achieved by the IHCB-F40 models with the strength ratio ranging from 1.5 to 4.0. Additionally, the post-yield stiffness ratio was 9.4 of the brace with a strength ratio of 2.2. Although the value of 9.4 was lower than the required minimum value of 10, this deviation was allowable. Therefore, the target strength ratio of IHCB-F40 is 2.2 to 3.5.

3.5 Dual effect of curve shape and partial strengthening

The individual effect of each factor was confirmed in the above analyses. The qualitative analysis of the individual effect and the dual effects of the curve shape and the partial strengthening are concluded in Table 3-8.

The curve shape mainly acts on smoothing the load-axial strain relationship and removing the sharp turning points, but hardly affects the maximum tensile load. The partial strengthening mainly works on increasing the load value, but does not work on the initial stiffness and yield load. Both the curve shape and the partial strengthening work on the increase of post-yield stiffness, the improvement of the buckling behavior or the buckling load, and the improvement of the post-buckling load. The data of the maximum compressive load is worth noticing. The curve shape reduces the maximum compressive load, but the partial strengthening increases it, therefore, the variation of the maximum compressive load while employing the curve shape and the partial strengthening doubly should be hard to judge. However, in this study, it is proved that the curve shape was dominant in deciding the maximum compressive load. Therefore, the maximum compressive load of IHCB-F40 decreased eventually.

Table 3-8 Dual effect of curve shape and partial strengthening

Effect	Stiffness		Tensile load		Compressive load		
	Intial	Post-yield	Yield	Max.	Buckling	Max.	Post-buckling
Curve shape	-	+	-	×	+	-	+
Partial strengthening	×	+	×	+	+	+	+
Curve shape + Partial strengthening	-	+	-	+	+	-	+

*+: Increase or modify; -: Decrease; ×: Hardly affect

3.6 Conclusion

This chapter presents the numerical analysis of induction-heated curved braces (IHCBs) with an I-shaped section.

Section 3.1 introduces the modeling of the braces. ABAQUS/implicit was employed to conduct the numerical investigation. The specimen modeling, the boundary condition, and the material properties are presented.

Section 3.2 verifies the accuracy of the models. The load-axial strain relationships, yield cycles, and transverse deformations were well-captured, showing that the models are appropriate for further investigation.

Section 3.3 discusses the effect of the curve shape and the target curvedness. The curve shape alone mainly acted on smoothing the load-axial strain relationship and removing the sharp turning points, specifically, lowering the initial stiffness and stabilizing the compressive behavior. Besides, the degree of the curvedness, which was the ratio of the initial transverse deformation to the specimen length, affected the first yield region. To meet IHCB's target performance, the curvedness should be controlled within the range of 2.3% to 2.7%.

Section 3.4 evaluates the effect of the partial strengthening and the target strength ratio. The partial strengthening alone mainly worked on increasing the value and delaying the occurrence of critical loads. It triggered the multistage yielding behavior under tension, but its effect on compressive stability was not confirmed. In addition, the degree of the strength ratio of the high-strength region to the normal-strength one played a great role in deciding the first yield region of the brace. It is proved that the strength ratio from 2.2 to 3.5 fulfilled the target demand of IHCB.

Section 3.5 concludes the synthetic effect of the curve shape and the partial strengthening. They worked together on the increase of the post-yield stiffness, improvement of the buckling behavior or the buckling load, and improvement of the post-buckling load. Note that the stabilization of the compressive behavior due to the curve shape prevailed over the increase of the compressive load brought by the partial strengthening. Therefore, the maximum compressive load of IHCB was lower than CBB.

Above all, it is meaningful to use the curve shape and partial strengthening doubly for IHCB to meet the target performance. The curvedness should be controlled within the range from 2.3% to 2.7%, and the strength ratio within the range from 2.2 to 3.5. By controlling these two factors, IHCB is expected to provide lower initial stiffness but higher post-yield stiffness. The lower initial stiffness decreases its influence on the initial stiffness of a building, and the larger yield displacement makes the brace remain elastic during moderate earthquakes. Under severe earthquakes, the larger post-yield stiffness of IHCB reduces the story drift response and the residual damage of the building, making it particularly suitable for seismic retrofit of existing buildings. Part of the content is published in reference [3.6].

References

3.1)   ABAQUS Learning Edition. 3DEXPERIENCE EDU. Retrieved December 16, 2022, from https://edu.3ds.com/en/software/abaqus-learning-edition

3.2)   Skalomenos, K. A., Kurata, M., & Nishiyama, M. (2020). Induction-heat treated steel braces with intentional eccentricity. Engineering Structures, 211, 110461. https://doi.org/10.1016/j.engstruct.2020.110461

3.3)   京都大学. (2022,3). 誘導加熱により部分高強度化した偏心 H 形鋼ブレースの開発（修士論文）. 岩田佳歩

3.4)   AIJ Recommendations for Plastic Design of Steel Structures (3rd ed.). (2017). Architectural Institute of Japan.

3.5)   Liu, Y., Tani, M., Kurata, M., Watase, C., & Nishiyama, M. (2020). Study on I-shaped section steel braces partially strengthened by induction heating. Engineering Structures, 210, 110341. https://doi.org/10.1016/j.engstruct.2020.110341

3.6)   Liu, Y., Iwata, K., Sanda, S., Nishiyama, M., & Tani, M. (2021). Development of curved braces partially strengthened by induction heating. Engineering Structures, 233, 111754. https://doi.org/10.1016/j.engstruct.2020.111754

4 Design formula of induction-heated curved braces

This chapter proposes several new equations for evaluating the structural behavior of induction-heated curved braces (IHCBs). First, the assumption of transverse deformation is introduced. Then, the equations of initial stiffness, yield load, post-yield stiffness, maximum tensile load, and post-buckling strength are proposed. The accuracies of the proposed equations are last verified by comparing them to the experimental and numerical analysis results.

4.1 Precondition of deformation

4.1.1 Assumption of curve shape

As presented in Chapters 2 and 3, the curve shape of IHCB is regarded as an arc around the minor axis. Figure 4-1 compares the initial transverse deformation when considering the curve shape as an arc curve and as a sine curve.
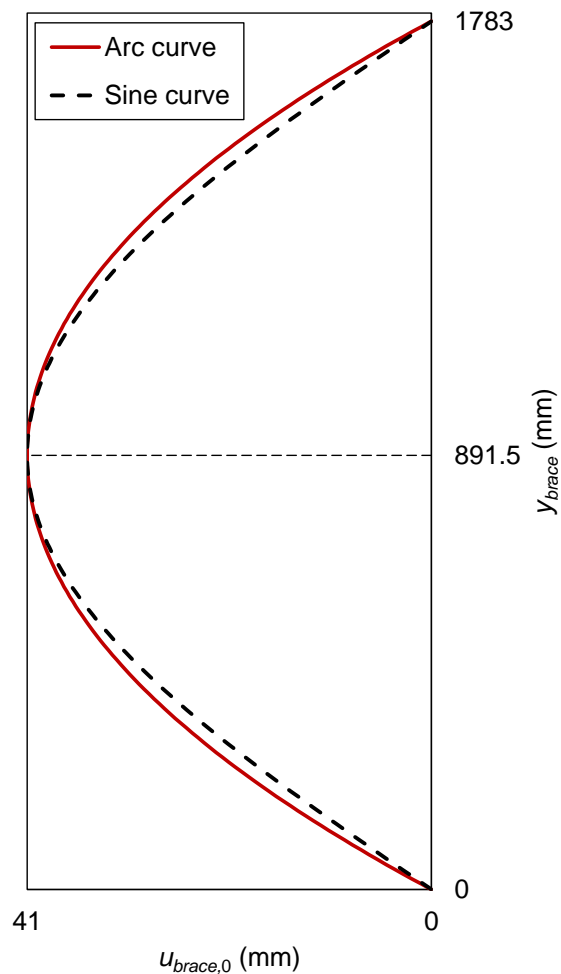
Figure 4-1 Assumption of initial transverse deformation

It is confirmed that the sine curve is well consistent with the arc curve. The correlation coefficient, R^2, between the two curves, is 0.99959, which satisfies the commonly recommended value of no less than 0.99. Therefore, the curve shape of IHCB can also be regarded as a sine curve. Their equations are respectively shown as Eq. 4-1 and Eq. 4-2. Note that they all satisfy the conditions when $y_{brace} = 0$ mm or 1783 mm, $u_{brace,0} = 0$ mm, and when $y_{brace} = 891.5$ mm, $u_{brace,0} = 41$ mm. The symbols with the subscript of "brace" focus on the geometric shape within the brace length.

For the arc curve:

$$[u_{brace,0} - (d_{brace,0} - R_{brace})]^2 + \left(y_{brace} - \frac{L_{brace}}{2}\right)^2 = R_{brace}^2 \qquad \text{Eq. 4-1}$$

$$\left(u_{brace,0} + 9671.8\right)^2 + (y_{brace} - 891.5)^2 = 9712.8^2$$

Where,

$y_{brace} = $ Axial direction of the brace. 0 mm $\leq y_{brace} \leq 1783$ mm.

$u_{brace,0} = $ Initial transverse deformation along the brace length. 0 mm $\leq u_{brace,0} \leq 41$ mm.

$d_{brace,0} = $ Initial transverse deformation at the brace middle within the brace length. It is 41 mm.

$L_{brace} = $ Brace length. It is 1783 mm for all braces.

$R_{brace} = $ Radius of the curvature. Because $\left(R_{brace} - d_{brace,0}\right)^2 + \left(\frac{L_{brace}}{2}\right)^2 = R_{brace}^2$, $R_{brace} = 9712.8$ mm.

For the sine curve:

$$u_{brace,0} = d_{brace,0} \sin \frac{\pi y_{brace}}{L_{brace}}$$

$$\qquad \text{Eq. 4-2}$$

$$u_{brace,0} = 41 \sin \frac{\pi y_{brace}}{1783}$$

4.1.2 Calculation of transverse deformation

Based on the assumption of the curve shape presented in Section 4.1.1, the curve shape is simply regarded as a sine curve for the calculation of the critical load. In this section, the calculation equations for the flexural buckling considering the initial imperfection [4.1)] are referred to. The relationship between the changing transverse deformation along the supported length and the bending moment can be written as Eq. 4-3. Note that for the calculation of the stiffness, the curve shape is still regarded as an arc curve.

$$M = Pu \hspace{4cm} \text{Eq. 4-3}$$

Where,

$M = $ Bending moment.

$P = $ Axial load.

$u = $ Transverse deformation along the supported length.

The bending moment can also be written as Eq. 4-4.

$$M = -EI\emptyset = -EI\frac{d^2(u - u_0)}{dy^2} \hspace{3cm} \text{Eq. 4-4}$$

Where,

$\emptyset = $ Section curvature.

$E = $ Young's modulus of the material.

$I = $ Cross-sectional moment of inertia around the minor axis.

$u_0 = $ Initial transverse deformation along the supported length. $u_0 = d_0 \sin\frac{\pi y}{L}$ as assumed in Section 4.1.1.

$y = $ Axial direction.

$d_0 = $ Initial transverse deformation at the brace middle within the supported length.

$L = $ Supported length.

By correlating Eq. 4-3 and Eq. 4-4, Eq. 4-5 can be obtained as follows.

$$\frac{d^2(u - u_0)}{dy^2} = -n^2 u \hspace{3cm} \text{Eq. 4-5}$$

Where,

$$n^2 = \frac{P}{EI} = \frac{P}{P_{cr}} \left(\frac{\pi}{L}\right)^2.$$

$$P_{cr} = \frac{\pi^2 EI}{L^2} = \text{Euler buckling load.}$$

Thus, the general solution is presented as Eq. 4-6.

$$u = A \sin ny + B \cos ny + Cu_0 \qquad \text{Eq. 4-6}$$

The boundary conditions are presented as Eq. 4-7.

When $y = 0$, $u = 0$ Therefore, $B = 0$

When $y = L$, $u = 0$ Therefore, $A \sin nL = 0$

Eq. 4-7

For $A \sin nL = 0$, there are two possibilities. First, $\sin nL = 0$. In this case, $nL = 0,\ \pi,\ 2\pi,\ ....$ By substituting $nL = \pi$ to $n^2 = \frac{P}{EI}$, the Euler buckling load P_{cr} can be obtained. Second, $A = 0$. In this case, $u = Cu_0$. By substituting $u = Cu_0$ to Eq. 4-5, C can be obtained as Eq. 4-8.

$$C = \frac{1}{1 - \dfrac{P}{P_{cr}}} \qquad \text{Eq. 4-8}$$

Thus, u can be expressed as Eq. 4-9, which is the particular integral.

$$u = \frac{d_0}{1 - \dfrac{P}{P_{cr}}} \sin \frac{\pi y}{L} \qquad \text{Eq. 4-9}$$

When $y = L/2$, the relationship between the transverse deformation at the brace middle and the axial load can be presented as Eq. 4-10. Eq. 4-10 is flexibly used for the calculation of the critical load.

$$d = \frac{d_0}{1 - \dfrac{P}{P_{cr}}} \qquad \text{Eq. 4-10}$$

Where,

$d =$ Transverse deformation at the brace middle within the supported length. It is a function of the axial load.

4.2 Proposal of design formula

4.2.1 Initial stiffness

As presented in Table 3-8, the curve shape strongly affects the initial stiffness, but the partial strengthening does not. Therefore, only the initial curve shape is considered here. The calculation equations for the normal curved brace [4.2)] are referred to.

(a) Axial load distribution   (b) Bending moment distribution
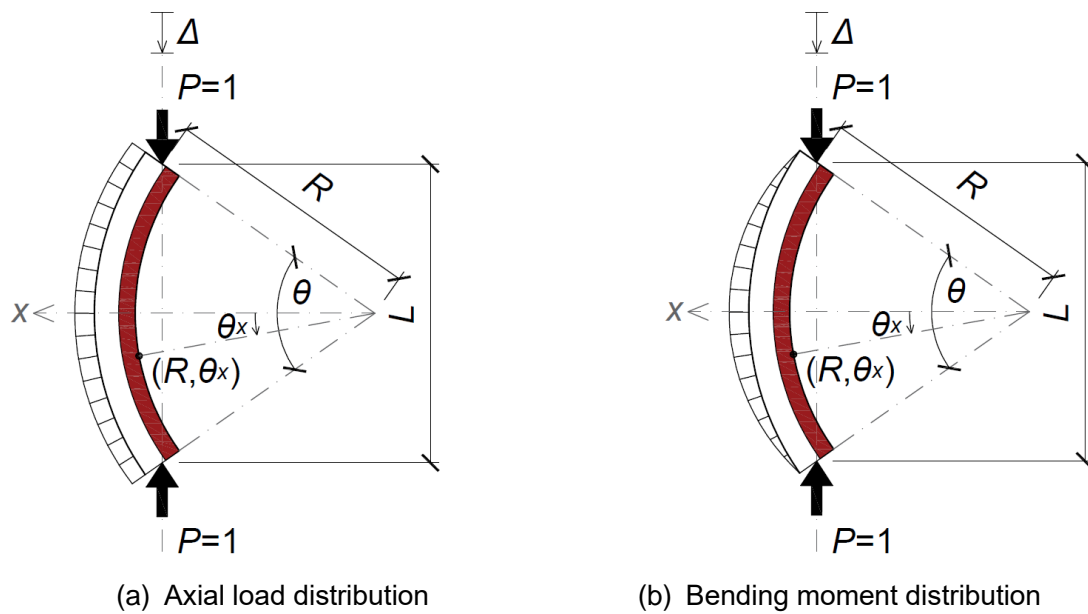
Figure 4-2 Stress distribution under unit axial load

$$R = \frac{L}{2 \sin \frac{\theta}{2}}$$

Eq. 4-11

Where,

$R =$ Radius of the curvature within the supported length.

$\theta =$ Central angle.

$L =$ Supported length.

The initial stiffness is affected by the dual action of axial load and bending moment. As described in Figure 4-2, the distribution of the unit axial load N_{unit} and the unit bending moment M_{unit} can be calculated as Eq. 4-12 and Eq. 4-13, respectively.

$$N_{unit} = \cos \theta_x, \quad -\frac{\theta}{2} \leq \theta_x \leq \frac{\theta}{2}$$

Eq. 4-12

$$M_{unit} = R\left(\cos\theta_x - \cos\frac{\theta}{2}\right), \quad -\frac{\theta}{2} \leq \theta_x \leq \frac{\theta}{2}$$

Eq. 4-13

The axial deformation at the baseline Δ (unit: mm/N), which connects the center of the two end plates, is written as Eq. 4-14.

$$\Delta = \int_{-\frac{\theta}{2}}^{\frac{\theta}{2}} \left(\frac{M_{unit}M_{unit}}{EI} + \frac{N_{unit}N_{unit}}{EA}\right) R d\theta_x$$

$$\Delta = \frac{R^3}{EI}\int_{-\frac{\theta}{2}}^{\frac{\theta}{2}} \left(\cos\theta_x - \cos\frac{\theta}{2}\right)^2 d\theta_x + \frac{R}{EA}\int_{-\frac{\theta}{2}}^{\frac{\theta}{2}} \cos^2\theta_x \, d\theta_x$$

Eq. 4-14

$$\Delta = \frac{L^3}{4EI\sin^3\frac{\theta}{2}}\left(\frac{\theta}{4} - \frac{3}{4}\sin\theta + \frac{\theta}{2}\cos^2\frac{\theta}{2}\right) + \frac{L}{EA\sin\frac{\theta}{2}}\left(\frac{1}{4}\sin\theta + \frac{\theta}{4}\right)$$

Where,

$E =$ Young's modulus of the material.

$A =$ Cross-sectional area.

$I =$ Cross-sectional moment of inertia around the minor axis.

Therefore, the initial stiffness of the IHCB series $K_{e,IHCB}$ (unit: N/mm^2), of which the grade is equal to Young's modulus, can be calculated as Eq. 4-15. IHCBs are supposed to maintain the initial stiffness until the yield cycle of IHCB about the axial strain of 0.3%.

$$K_{e,IHCB} = \frac{\sigma}{\varepsilon} = \frac{L}{\Delta A} = \frac{E}{\frac{L^2 A}{4I\sin^3\frac{\theta}{2}}\left(\frac{\theta}{4} - \frac{3}{4}\sin\theta + \frac{\theta}{2}\cos^2\frac{\theta}{2}\right) + \frac{1}{\sin\frac{\theta}{2}}\left(\frac{1}{4}\sin\theta + \frac{\theta}{4}\right)}$$

Eq. 4-15

The initial stiffness of CBB $K_{e,CBB}$ (unit: N/mm^2), is calculated as Eq. 4-16.

$$K_{e,CBB} = \frac{\sigma}{\varepsilon} = E$$

Eq. 4-16

4.2.2 Yield load

Different from the conventional steel components, two steel materials are existing in one IHCB. Based on the experimental and numerical analysis results presented in Chapters 2 and 3, a concept called the first-yield-fiber concept is proposed in this study. It is assumed that the fiber that yields first determines the yield load of the whole brace. This concept is referred to as the concept for the calculation of the buckling load based on the strength of the edge fiber [4.3)].

The stress distributions of the IHCB series at the brace middle when tensioned are shown in Figure 4-3. The critical fibers A, B, and C for IHCB-F40, and A, B, C, and D for IHCB-2F60 at different locations are considered. Apparently, $|\sigma_A| < |\sigma_B|$ for IHCB-F40. $|\sigma_A| < |\sigma_D|$, and $|\sigma_B| < |\sigma_C|$ for IHCB-2F60. Based on the first-yield-fiber concept, the yield loads $P_{y,IHCB-F}$ and $P_{y,IHCB-2F}$ (unit: kN) can be calculated as Eq. 4-17.
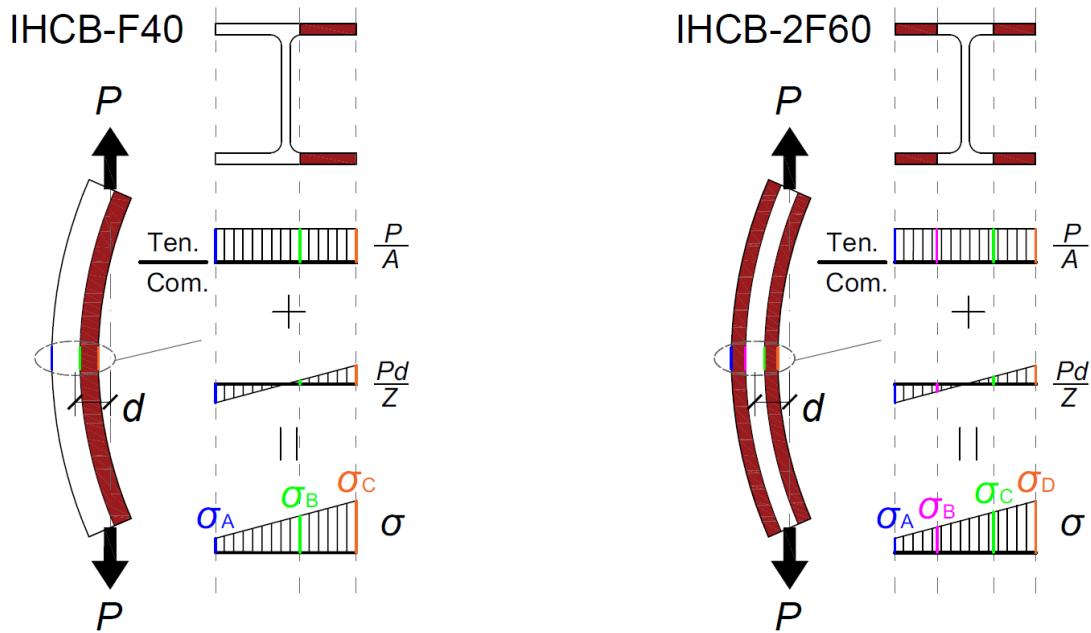
Figure 4-3 Stress distribution for the calculation of the yield load

$$P_{y,IHCB-F} = P_{y,IHCB-2F} = \min\left\{\frac{\sigma_{y,N}}{\frac{d}{Z}\alpha + \frac{1}{A}}, \frac{\sigma_{y,IH}}{\frac{d}{Z} + \frac{1}{A}}\right\}$$

Eq. 4-17

Where,

$\sigma_{y,N}$ = Yield strength of the normal-strength region.

$\sigma_{y,IH}$ = Yield strength of the high-strength region.

$d =$ Transverse deformation at the brace middle within the supported length. It is a variable presented in Section 4.1.2. It gradually decreases with the increase of the tensile load.

$Z =$ Elastic section modulus.

$\alpha =$ Location of the corresponding fiber from the mid-depth of the flange. It is 0.2 (= 10 mm / 50 mm, location of fiber B) for IHCB-F40 and 0.4 (= 20 mm / 50 mm, location of fiber C) for IHCB-2F60.

By substituting d presented as Eq. 4-10 into Eq. 4-17, the yield loads of IHCB-F40 and IHCB-2F60 can be summarized as Eq. 4-18.

$$P_{y,IHCB-F} = P_{y,IHCB-2F} = \min \left\{ \frac{\sigma_{y,N}}{\frac{d_0}{Z\left(1-\frac{P_y}{P_{cr}}\right)}\alpha + \frac{1}{A}}, \frac{\sigma_{y,IH}}{\frac{d_0}{Z\left(1-\frac{P_y}{P_{cr}}\right)} + \frac{1}{A}} \right\} \qquad \text{Eq. 4-18}$$

By substituting initial transverse deformation $d_0 = 0$ into Eq. 4-18, the yield load of CBB $P_{y,CBB}$ (unit: kN) can be calculated as simply as Eq. 4-19.

$$P_{y,CBB} = \sigma_{y,N} A \qquad \text{Eq. 4-19}$$

4.2.3　Post-yield stiffness

The post-yield stiffness is strongly affected by the curve shape and partial strengthening both as described in Table 3-8. The multistage response in yielding due to the partial strengthening and the complex deformation which tends to straighten the initial curve shape makes it hard to precisely calculate the post-yield stiffness. To simplify the calculation, it is assumed that the slope in the graph of the load-axial strain relationship is constant after the first yield load. In this stage, the high-strength region keeps working as an elastic spine. This spine is the main factor in providing post-yield stiffness. Therefore, the post-yield stiffness of the IHCB series $K_{p,IHCB}$ (unit: N/mm²) can be considered as Eq. 4-20.

$$K_{p,IHCB} = \frac{2A_f\beta}{A}K_{e,IHCB}$$

$$K_{p,IHCB} = \frac{2A_f\beta}{A} \times \frac{E}{\dfrac{L^2 A}{4I\sin^3\dfrac{\theta}{2}}\left(\dfrac{\theta}{4} - \dfrac{3}{4}\sin\theta + \dfrac{\theta}{2}\cos^2\dfrac{\theta}{2}\right) + \dfrac{1}{\sin\dfrac{\theta}{2}}\left(\dfrac{1}{4}\sin\theta + \dfrac{\theta}{4}\right)} \qquad \text{Eq. 4-20}$$

Where,

$A_f = $ Cross-sectional area of one flange.

$\beta = $ Ratio of effective spine width to the flange width. It is 0.4 (= 40 mm / 100 mm) for IHCB-F40 and 0.3 (= 30 mm / 100 mm) for IHCB-2F60.

Note that for IHCB-2F60, there are two spines at the inner and outer sides of the arc, respectively, but the spines tend to yield once the adjacent untreated region yields due to the accompanying large deformation. Therefore, in this study, only one spine is taken into consideration for IHCB-2F60. The range of the post-yield stiffness is considered between the axial strains of 0.3% and 0.9% as presented in the experiment and numerical analysis.

The post-yield stiffness of CBB $K_{p,CBB}$ (unit: N/mm²) and the second post-yield stiffness of the IHCB series $K_{2p,IHCB}$ after the 0.9% axial strain are presented as Eq. 4-21.

$$K_{p,CBB} = K_{2p,IHCB} = E' \qquad \text{Eq. 4-21}$$

Where,

$E' = $ Post-yield stiffness of the material. It is generally 1% of Young's modulus.

4.2.4 Maximum tensile load

Table 3-8 demonstrates that the initial curve shape hardly affects the maximum tensile loads because the braces become almost straight at large tensile deformations. Therefore, the maximum tensile load P_u (unit: kN) can be expressed as Eq. 4-22 for CBB and Eq. 4-23 for the IHCB series.

$$P_{u,CBB} = \sigma_{u,N} A \qquad\qquad \text{Eq. 4-22}$$

$$P_{u,IHCB} = \sigma_{u,N}(A - 2A_f\gamma) + \sigma_{u,IH} \times 2A_f\gamma \qquad\qquad \text{Eq. 4-23}$$

Where,

$\sigma_{u,N}$ = Tensile strength of the normal-strength region.

$\sigma_{u,IH}$ = Tensile strength of the high-strength region.

γ = Ratio of the high-strength width to the flange width. It is 0.4 (= 40 mm / 100 mm) for IHCB-F40, and 0.6 (= 60 mm / 100 mm) for IHCB-2F60.

4.2.5 Post-buckling strength

The compressive capacity starts to fall after buckling for CBB or after reaching the maximum compressive load for the IHCB series. This phenomenon is simply called post-buckling behavior in this study. Figure 4-4 shows the brace deformation for the calculation of the post-buckling strength, which is an idealization of a buckled pin-supported brace in compression. The calculation equations for the post-buckling strength of a simple I-shaped section that neglects the web [4.1)] are referred to.
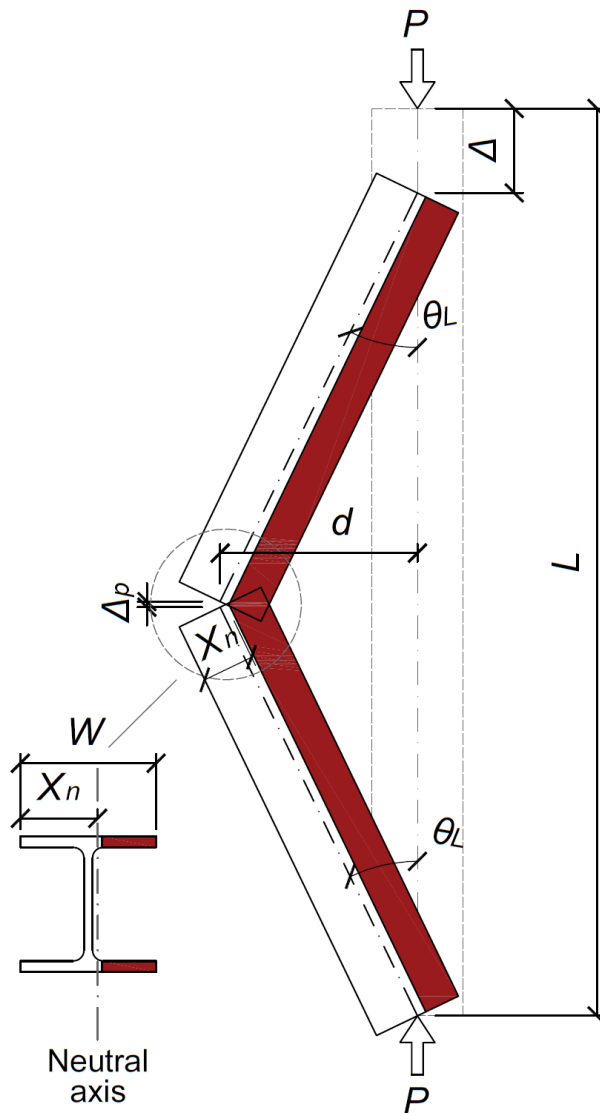
Figure 4-4 Brace deformation for the calculation of the post-buckling strength

The transverse deformation is defined as Eq. 4-24. Note that in this stage, the transverse deformation presented in Section 4.1.2 is unavailable. The sine curve assumption of the curve shape is no longer valid due to the plastic hinge at the brace middle.

- 126 -

$$d = \frac{L \tan \theta_L}{2} = \frac{L\theta_L}{2}$$

<div align="right">Eq. 4-24</div>

Where,

$\theta_L =$ End rotation.

The sum of the axial deformation Δ can be calculated as Eq. 4-25.

$$\Delta_e = \frac{PL}{EA}$$

$$\Delta_b = d \tan \theta_L = d\theta_L = \frac{L\theta_L{}^2}{2}$$

$$\Delta_p = \left(\frac{W}{2} - x_n\right) \tan 2\theta_L = (W - 2x_n)\theta_L$$

$$\Delta = \Delta_e + \Delta_b + \Delta_p = \frac{PL}{EA} + \frac{L\theta_L{}^2}{2} + (W - 2x_n)\theta_L$$

<div align="right">Eq. 4-25</div>

Where,

$\Delta_e =$ Elastic deformation due to the axial load.

$\Delta_b =$ Axial deformation provided by transverse deformation.

$\Delta_p =$ Plastic deformation in the hinge region.

$W =$ Flange width of the cross-section.

$x_n =$ Location of the neutral axis from the tensile edge.

Therefore, the relationship between the axial strain ε and the axial load P at the post-buckling stage can be written as Eq. 4-26. When $\varepsilon = -0.5\%$, the obtained axial load is the post-buckling strength [4.4].

$$\varepsilon = \frac{\Delta}{L} = \frac{P}{EA} + \frac{\theta_L{}^2}{2} + \frac{(W - 2x_n)\theta_L}{L}$$

<div align="right">Eq. 4-26</div>

Here, θ_L and x_n are unknown, but they both can be expressed as the function of the axial load and the bending moment. θ_L can be expressed based on the relationship between the axial load and the bending moment shown as Eq. 4-27. x_n can be obtained from the $P\text{-}M_{pn}$ curve presented in Appendix 1. M_{pn} is the full plastic moment around the minor axis, and it is a function of P.

$$M = Pd = P\frac{L\theta_L}{2}$$

$$\theta_L = \frac{2M}{PL}$$

Eq. 4-27

4.3　Verification of design formula

Table 4-1 and Table 4-2 show the load capacities under tension and compression, respectively. Exp., Ana. and Cal. show the results obtained from the experiment shown in Section 2.5.1, analysis in Section 3.2.1, and calculation, respectively. The ratios of the analysis or calculation results to the experimental results are also shown in the bracket ( ). Note that although the equation for the maximum tensile load is proposed in Section 4.2.4, the maximum tensile load presented here is calculated as the load at the 1.2% axial strain, since it is comparable to the experiment and analysis results.

Table 4-1 Tensile load capacities

Specimen	Initial stiffness (GPa)			Post-yield stiffness (GPa)			Yield load (kN)			Maximum load (kN)		
	Exp.	Ana.	Cal. [1]	Exp.	Ana.	Cal. [2]	Exp.	Ana.	Cal. [3]	Exp.	Ana.	Cal. [4]
CBB	207.7	230.0 (1.11)	194.0 (0.93)	1.88	-1.80 (-0.96)	1.94 (1.03)	565.1	595.8 (1.05)	657.2 (1.16)	670.0	666.4 (0.99)	700.9 (1.05)
IHCB-F40	87.3	101.7 (1.16)	96.7 (1.07)	30.2	20.2 (0.67)	28.7 (0.95)	471.0	461.1 (0.98)	467.7 (0.99)	972.6	936.9 (0.96)	1031.7 (1.06)
IHCB-2F60	88.2	100.3 (1.14)	96.7 (1.10)	25.8	23.4 (0.91)	21.5 (0.83)	460.7	454.9 (0.99)	340.2 (0.74)	963.7	957.3 (0.99)	941.2 (0.98)

1. Eq. 4-16 for CBB, Eq. 4-15 for IHCBs
2. Eq. 4-21 for CBB, Eq. 4-20 for IHCBs
3. Eq. 4-19 for CBB, Eq. 4-18 for IHCBs
4. Load at the 1.2% axial strain

For the tensile load capacities, except for the yield load of IHCB-2F60, the calculation captured the experimental results well, and the errors were within the range of 17%. The calculation result underestimated the yield load of IHCB-2F60 by 26%, which may be attributed to the neglect of the joint bending behaviors in the design formula.

Table 4-2 Compressive load capacities

Specimen	Buckling load (kN)			Post-buckling strength (kN)		
	Exp.	Ana.	Cal. [1]	Exp.	Ana.	Cal. [2]
CBB	-515.8	-504.7 (0.98)	-510.9 (0.99)	-139.5	-141.7 (1.02)	-114.8 (0.82)
IHCB-F40				-208.0	-209.4 (1.01)	-179.5 (0.86)
IHCB-2F60				-233.5	-292.1 (1.25)	-250.6 (1.07)

1. Euler buckling load for CBB
2. Eq. 4-26 for CBB and IHCBs (ε = -0.5%)

For the compressive load capacities, the experimental results were generally captured by the calculation results, and the errors were within 18%. The neglect of strain hardening and joint bending behaviors might result in errors.

Figure 4-5 compares the experimental, numerical analysis, and calculation results in the load-axial strain relationships together with the definitions of each evaluation index. To conclude, the calculation results generally captured the experimental and analysis results in shape for all specimens. It is confirmed that the proposed design formulas are effective enough to evaluate the structural behaviors of the braces.

(a) CBB

(b) IHCB-F40

(c) IHCB-2F60
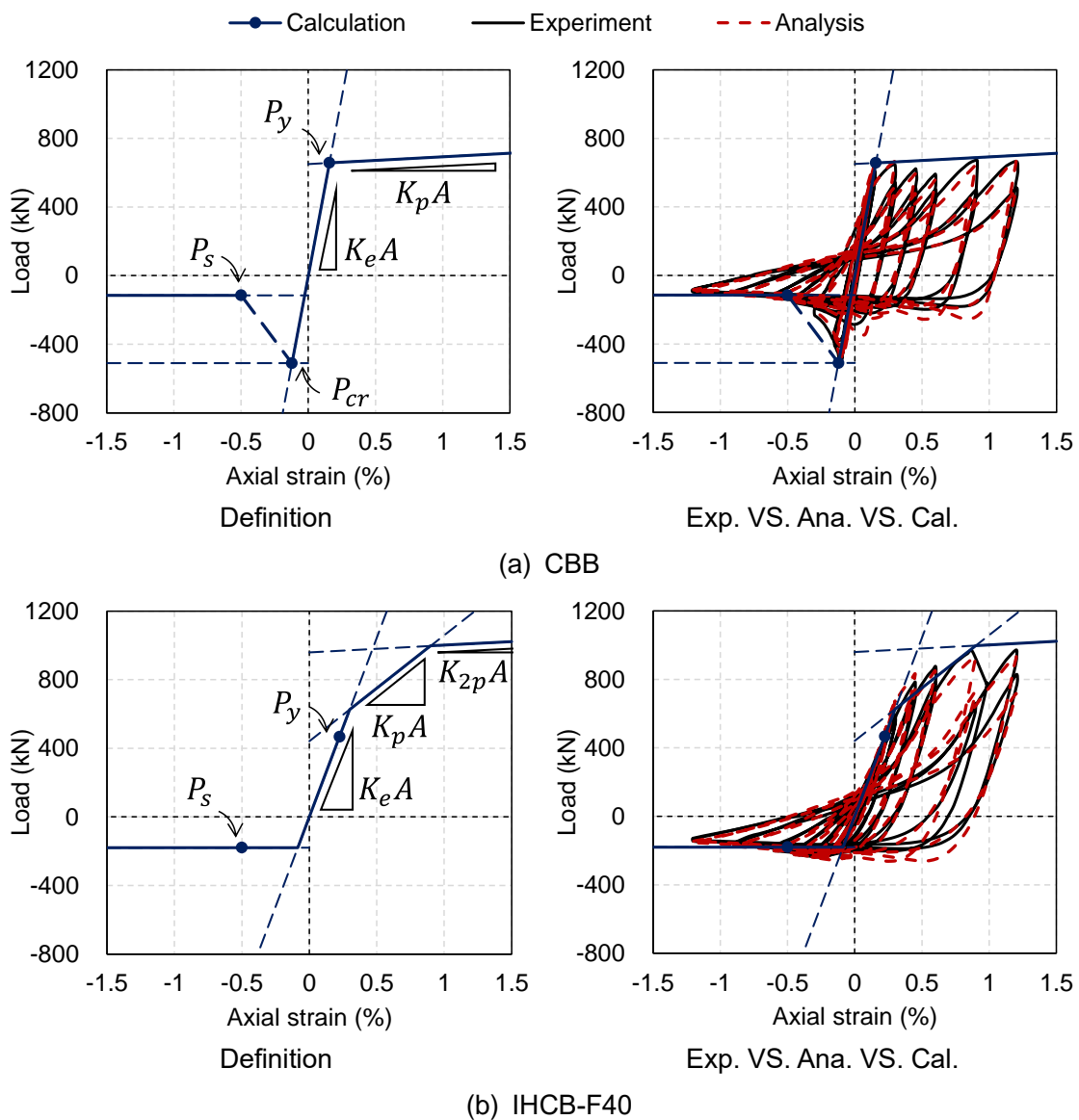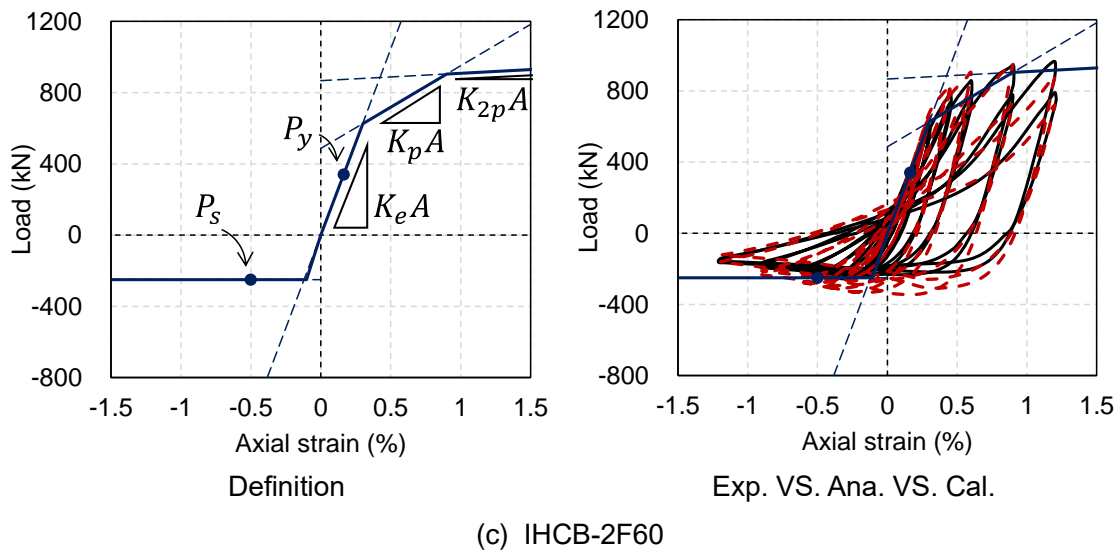
Figure 4-5 Verification of load-axial strain relationships

The values used for the calculation are summarized as follows.

Material parameter:

$E = 194$ GPa, $\sigma_{y,N} = 304.4$ MPa, referring to those of the normal-strength flange from tensile coupon tests in Section 2.3.2.

$\sigma_{y,IH} = 678.1$ MPa, referring to that of the high-strength flange from tensile coupon tests in Section 2.3.2.

$K = 2.23 = 678.1$ MPa / 304.4 MPa.

$E' = 1.94$ GPa $= 1\%E$

Sectional parameter:

$L = 2241$ mm, $A = 2159$ mm², $A_f = 800$ mm², $I = 134$ cm⁴, $Z = 26.7$ cm³, $W = 100$ mm, referring to the specimen design in Section 2.2.1.

$\theta = 7\pi/180$ rad $= 7° = (6.6° + 7.2° + 7.2°) / 3$, referring to the longitudinal dimension in Section 2.2.3.

Others:

$d = 25$ mm and 29 mm for calculating the yield loads of IHCB-F40 and IHCB-2F60, respectively. It is a variable and a function of axial load.

$d_0 = 48$ mm. It includes the initial transverse deformation of IHCBs of 41 mm mentioned in Section 2.2.3 and the deformation of the joint of 7 mm presented in Section 2.4.4.

$\alpha = 0.2$ for IHCB-F40, and 0.4 for IHCB-2F60. It is the location of the corresponding fiber from the

mid-depth of the flange.

$\beta =$ 0.4 for IHCB-F40, and 0.3 for IHCB-2F60. It is the ratio of the effective spine width to the flange width.

$\gamma =$ 0.4 for IHCB-F40, and 0.6 for IHCB-2F60. It is the ratio of the high-strength width to the flange width.

4.4 Conclusion

This chapter presents the design methods of induction-heated curved braces (IHCBs) with an I-shaped section.

Section 4.1 presents the precondition of deformation. Although the initial curve shape is an arc curve, it is also assumable as a sine curve. The transverse deformation which is the function of the axial load is presented as well.

Section 4.2 proposes the calculation equations for CBB and the IHCB series. The initial stiffness, yield load, post-yield stiffness, maximum tensile load, and post-buckling strength are considered based on their material properties, deformations, and IH-treated patterns. Note that the calculation of the post-buckling strength is referred to as the P-M_{pn} curve presented in Appendix 1.

Section 4.3 verifies the accuracy of the proposed equations with the experimental and analysis ones. The design formulas were proven effective to evaluate the behaviors of CBB and the IHCB series, and the deviations of most of the evaluation index were within 20%. The simplification of the equation and the neglect of strain hardening and joint behaviors might attribute to the errors. Part of the content is published in reference [4.5)].

References

4.1) 井上一朗, 吹田啓一郎. (2007). 建築鋼構造—その理論と設計—. 鹿島出版会.

4.2) Zhou, Z., Ye, B., & Chen, Y. (2019). Experimental investigation of curved steel knee braces with adjustable yield displacements. Journal of Constructional Steel Research, 161, 17–30. https://doi.org/10.1016/j.jcsr.2019.06.011

4.3) Fenner, R. T., & Reddy, J. N. (2012). Mechanics of Solids and Structures (Applied and Computational Mechanics) (2nd ed.). CRC Press.

4.4) AIJ Recommendations for Plastic Design of Steel Structures (3rd ed.). (2017). Architectural Institute of Japan.

4.5) Liu, Y., Iwata, K., Sanda, S., Nishiyama, M., & Tani, M. (2021). Development of curved braces partially strengthened by induction heating. Engineering Structures, 233, 111754. https://doi.org/10.1016/j.engstruct.2020.111754

5 Numerical analysis on frames using induction-heated curved braces

This chapter analyzes the frame using induction-heated curved braces (IHCBs) to evaluate the brace behaviors in the frame and confirm whether they still meet the target performances. First, a frame from previous research is introduced. It is reproduced by ABAQUS 6.14 and the numerical model is verified by comparing the analysis results to those presented in the previous research. Next, the frame using CBB or IHCB is cyclically loaded. The structural performances of the braced frames are evaluated in the aspects of load capacities and critical behaviors.

5.1 Outlines of the referenced frame

5.1.1 Introduction

In this study, a frame tested by a shake table was used as a basic frame [5.1]. It was a single-story, single-span frame with chevron brace specimens. The frame dimensions and section details of the beam and columns are shown in Figure 5-1.
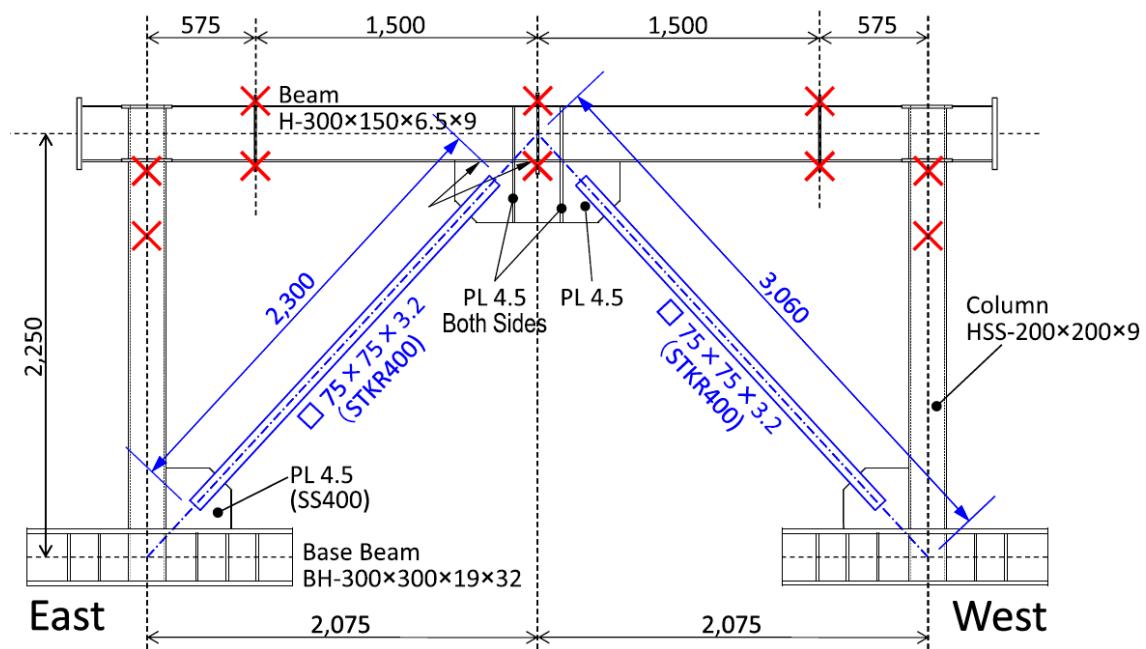
Figure 5-1 Frame specimen details (Unit: mm) [5.1]

The frame was corresponding to 70% scale of typical buildings, representing the bottom story of a 3 to 5-story building in Japan. The ones marked in red are where the out-of-plane deformations were controlled in the test.

Two square HSS 75 × 75 × 3.2 mm steel were used as traditional braces in this frame. They were welded at the gusset plates through the slots in brace ends, with a length of the welding seam of 235 mm for each end. The supported length of the brace was 2300 mm, and the test length was 1830 mm (= 2300 mm – 2 × 235 mm). The clearance of the gusset plates was 8 times their thickness for 36 mm (= 4.5 mm × 8), ensuring the pin-supported conditions of the braces and allowing their out-of-plane rotations.

The material properties for each specimen can be referred to in Table 5-1. Note that, in terms of STKR400 used for the brace, SN400B for the beam, and BCR295 for the column, the yield strengths F_y obtained from the tensile coupon tests were approximately 50% higher than the nominal yield strengths. However, for SS400 used for the gusset plate, its yield strength was 204 MPa, unsatisfying the nominal yield strength of 245 MPa. Since the deficiency of the material, the yield load of the brace, which was 342 kN, became 8% higher than that of the gusset plate of 318 kN.

Table 5-1 Material properties of the frame [5.1)]

Material	Designation	F_y (MPa)	F_u (MPa)	Elongation (%)
Brace	STKR400	383	452	36
Beam flange (9 mm)	SN400B	327	456	27
Beam web (6 mm)	SN400B	376	472	29
Column	BCR295	434	518	19
Gusset plate (4.5 mm)	SS400	204	291	54

5.1.2 Modeling
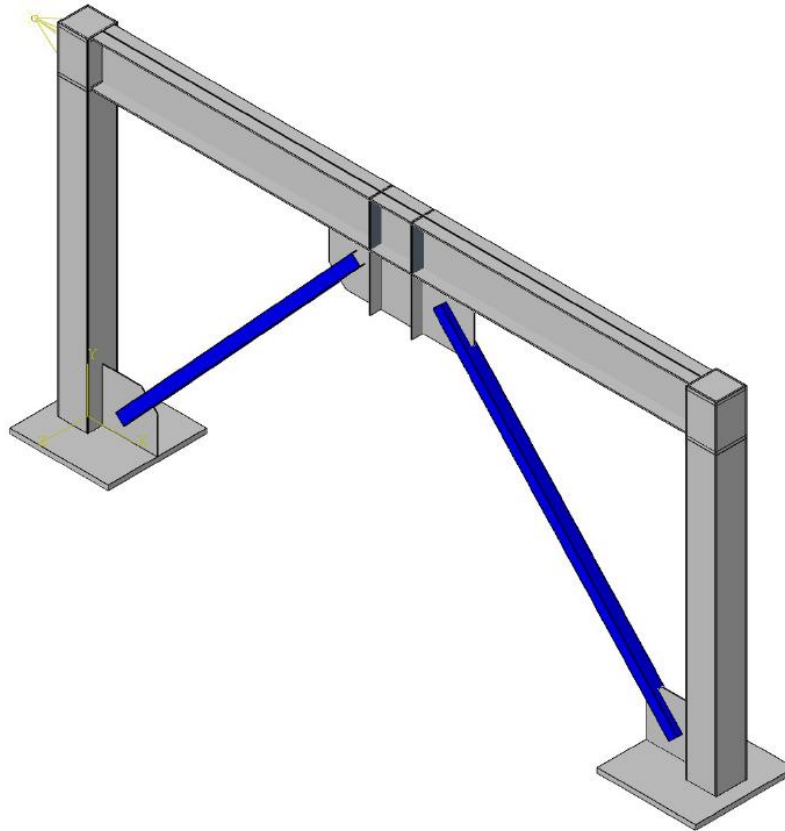
(a) 3D view of the referenced frame
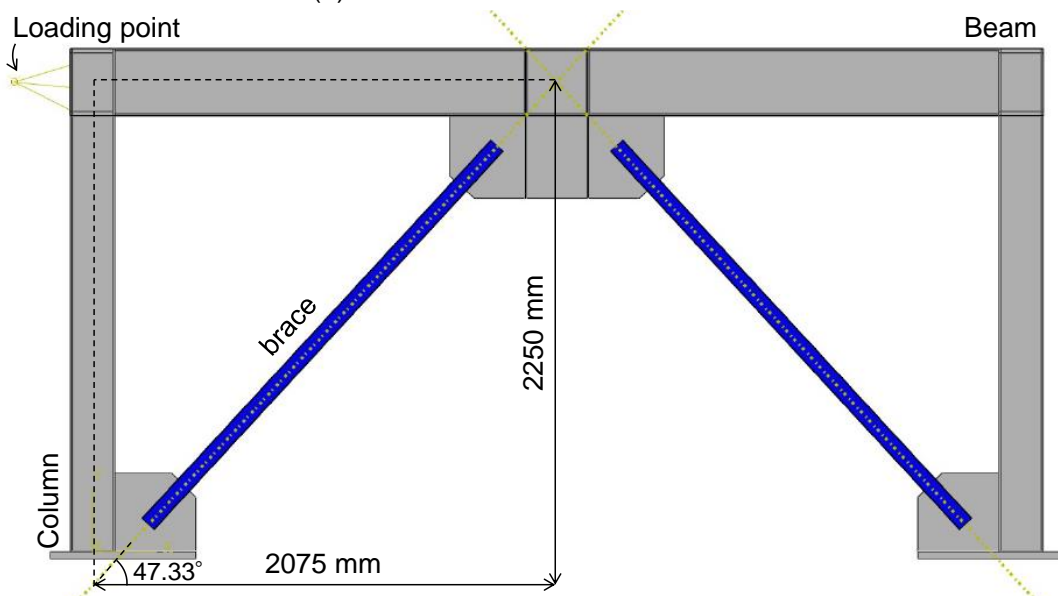
(b) Plan view of the referenced frame

Figure 5-2 Referenced frame model

ABAQUS/implicit was employed for modeling the frame. All components consisted of shell elements. The mesh size was 25 mm for braces and 60 mm for other components. As demonstrated in Figure 5-2, the dimensions of all components were constructed based on Figure 5-1. The isotropic hardenings were used for all materials. Except for SS400, the material strengths and elongations were set according to Table 5-1, and Young's modulus was 205 GPa. Tie constraints were used for all surface contacts of components. The bases were fixed in all directions, and the out-of-plane deformation of the beam was restrained. The different points between the ABAQUS model and the previous research [5.1] are shown as follows.

First, the material property of the gusset plates was modified. As presented above, the yield load of the brace was 8% higher than that of the gusset plate in the shake table test. While adopting the tested material property of gusset plates into the analysis, excessive deformations of gusset plates were observed. Therefore, the material property of gusset plates was modified to a nominal value in the analysis as 245 MPa for the yield strength and 400 MPa for the tensile strength.

Second, the model of the base beam was simplified as a base plate. It was to save computing time, and this simplification was proved not to affect the analysis results.

Third, deformation control at the loading point was employed. The referenced frame was tested by a shake table, but this study aims to investigate the structural performance of the braces under a quasi-static state as done in Chapters 2 and 3. The loading point is highlighted in Figure 5-2(b), which is 250 mm away from the side face of the left beam-column joint. It controlled the in-plane deformation of the beam by coupling constraint. Although the loading point at the mid-length of the beam was more common for the frame analysis, the loading point at the beam end was also valid to apply the lateral force to the beam, since the out-of-plane deformation of the beam was restrained. The story shear is the lateral load picked up from the loading point. The drift ratio is the ratio of the lateral deformation of the loading point to the frame height of 2250 mm.

5.1.3 Verification
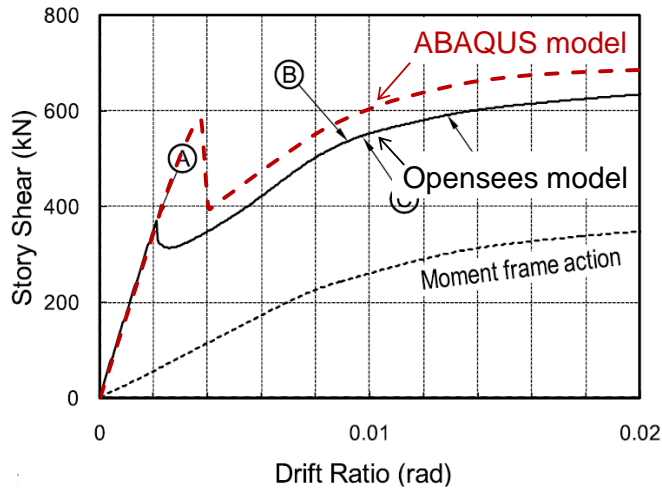
Figure 5-3 Verification of the referenced frame model under monotonic loading [5.1]

Figure 5-3 compares the analysis results obtained by the built ABAQUS model and those obtained by Opensees presented in the previous research [5.1] under monotonic loading. The maximum load values under monotonic loading are shown as well. The initial stiffness of the Opensees model was well-captured by the ABAQUS model until the buckling of the brace, where the sudden drop of the story shear load was observed. After the brace buckling, the tendency in the story shear-drift ratio curve of the ABAQUS model was nearly the same as that of Opensees one. When the drift ratio was 2.0%, both the ABAQUS model and the Opensees model reached their maximum story shear loads. The ratio of the story shear load obtained by ABAQUS to that by Opensees was 1.08.
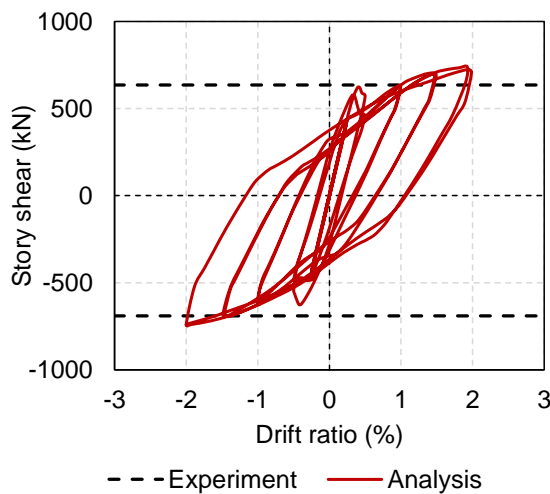
Figure 5-4 Verification of the referenced frame model under cyclic loading

Figure 5-4 compares the analysis results obtained by the built ABAQUS model under cyclic loading to the experimental results. The cyclic loadings were applied laterally at the loading point to the peak drift ratios of 0.08%, 0.1%, 0.25%, 0.5%, 1.0%, 1.5%, and 2.0%, see Figure 5-5. The horizontal dashed lines in Figure 5-4 are the maximum story shear loads obtained from the shake table test [5.1]. The positive (+) and negative (-) maximum load values obtained by ABAQUS under cyclic loading and those obtained by shake table tests are shown as well. The load ratios of the ABAQUS model to the experimental results were 1.16 on the positive side, and 1.08 on the negative side.
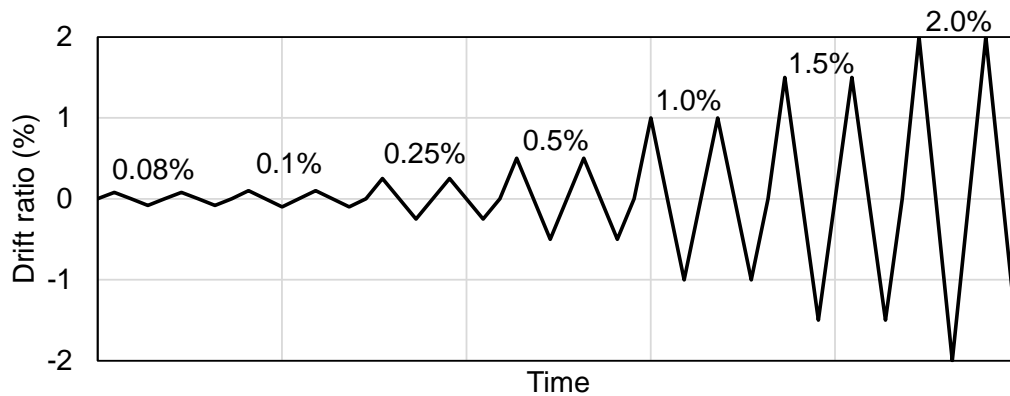
Figure 5-5 Cyclic loading protocol for the frame analysis

The errors might be contributed to the simplification of the material property, the replacement of seismic analysis by quasi-static cyclic analysis, and the differences in the software. Above all, the errors in loads were controlled within 16% both under monotonic and cyclic loadings. The accuracy of the ABAQUS frame model is confirmed, and it will be employed for the following investigations.

5.2   Outlines of the braced frame

5.2.1   Design

In the following discussions, IHCB-F40, which is the baseline model of the proposed induction-heated curved brace, and CBB, which is the conventional buckling brace, are built into the introduced frame. Note that they both have been modeled and verified in Chapter 3. To satisfy the condition that the yield load of a traditional brace is 342 kN [5.1)], geometric scaling of the cross-section is used for CBB. The scale factor works on H, W, t_w, t_f. The same scale factor is adopted for IHCB-F40 to keep its geometrical shape the same as that of CBB. The dimensions of braces are concluded in Table 5-2. The brace used for the experiment reflects the original size of the brace specimen as presented in Chapters 2 and 3, and the brace used for the frame analysis is geometrically scaled. Owing to the scale factor, the width of the IH-treated flange of IHCB-F40 changes as well.

Table 5-2 Dimensions of the braces used for frame analysis

Dimension	Brace used for experiment		Brace used for frame analysis	
	CBB	IHCB-F40	CBB	IHCB-F40
Scale factor	1.0		0.832	
H (mm)	100		83.2	
W (mm)	100		83.2	
t_w (mm)	6		4.99	
t_f (mm)	8		6.65	
A (mm²)	2104		1455	
I (mm⁴)	1334845		639047	
L_{brace} (mm)	1783		1830	
$d_{brace,0}$ (mm)		41		43.2
γW (mm)		40		33.28

Where,

$H =$ Height of the I-shaped section.

$W =$ Width of the I-shaped section.

$t_w =$ Thickness of the web of the I-shaped section.

$t_f =$ Thickness of the flange of the I-shaped section.

$A =$ Cross-sectional area.

$I =$ Cross-sectional moment of inertia around the minor axis.

$L_{brace} =$ Brace length.

$d_{brace,0} =$ Initial transverse deformation at the middle of IHCB-F40 within the brace length. It can

be calculated by $\left(R_{brace} - d_{brace,0}\right)^2 + \left(\frac{L_{brace}}{2}\right)^2 = R_{brace}^2$ as expressed in Eq. 4-1. $R_{brace} =$ 9712.8 mm.

$\gamma W =$ Width of IH-treated flange. γ is the ratio of the high-strength width to the flange width.

5.2.2 Modeling

Based on the design parameters shown in Table 5-2, the models of CBB frame and IHCB frame were built as presented in Figure 5-6 and Figure 5-7, respectively. Note that the frame is the same as that verified in Section 5.1.3 except for the gusset plates. The material property of gusset plates was modified, of which the strength was the same as that of the IH-treated flange of IHCB-F40. It was to prevent the earlier yielding of the gusset plate than the brace, which was a deficiency of the shake table test as introduced in Section 5.1.1. The cyclic loading protocol is presented in Figure 5-5.

(a) 3D view of CBB frame

(b) Top view of CBB frame (beam is hidden)
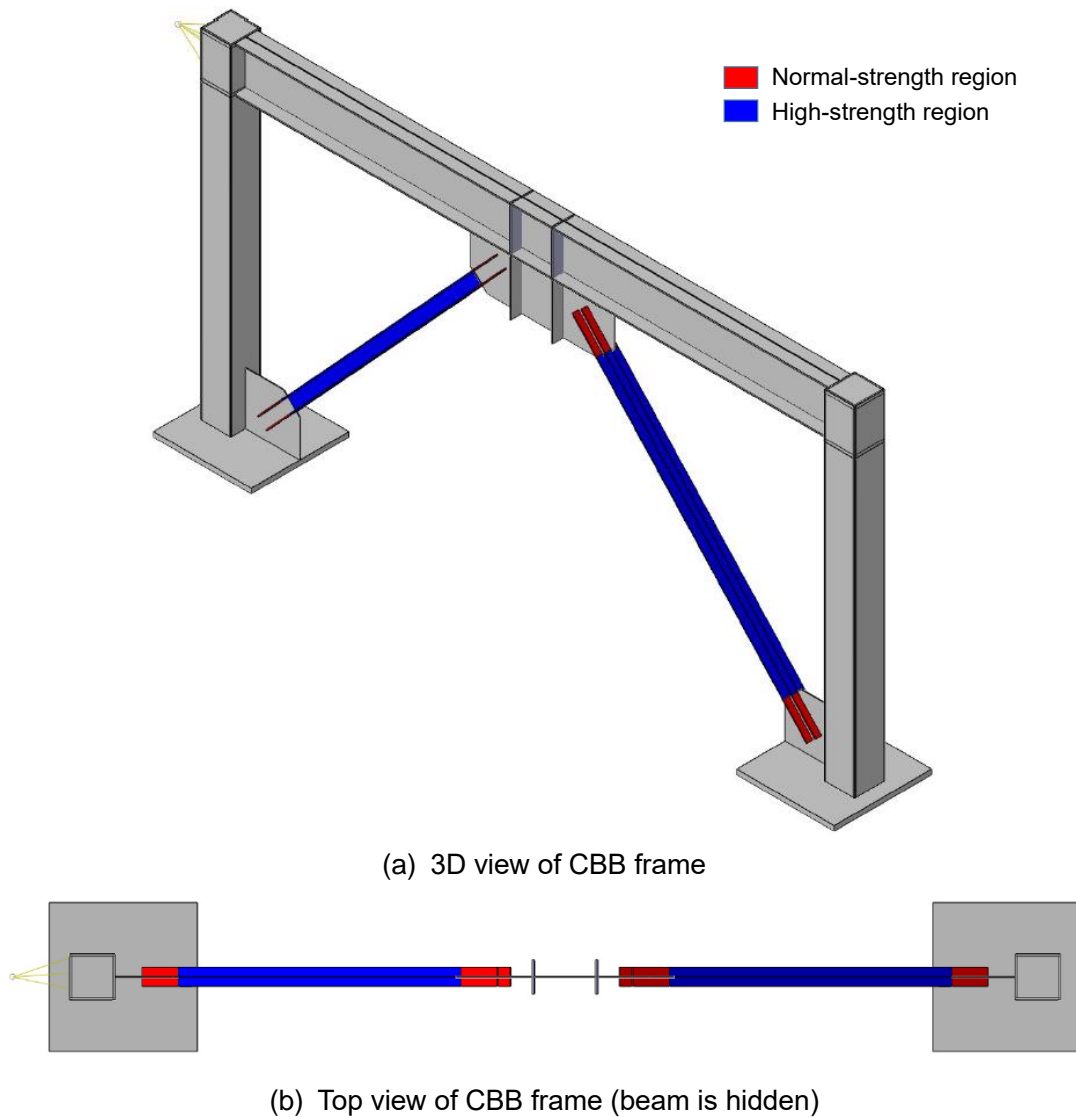
Figure 5-6 Modeling for CBB frame
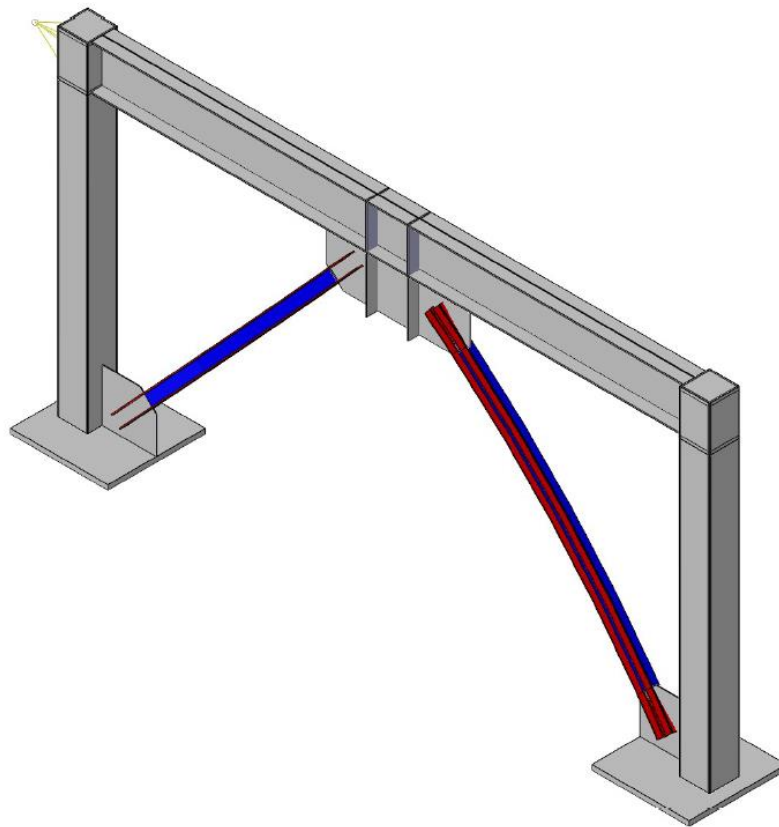
(a) 3D view of IHCB frame
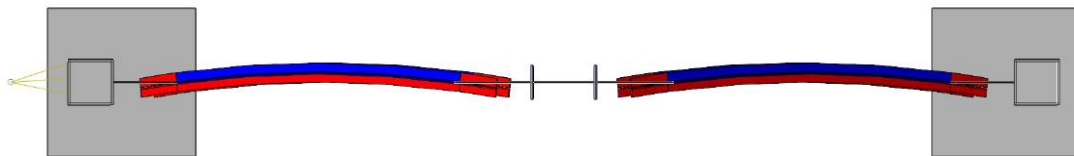
(b) Top view of IHCB frame (beam is hidden)

Figure 5-7 Modeling for IHCB frame

SS400 was used as raw material for CBB and IHCB with a yield strength of 245 MPa and tensile strength of 400 MPa. The elongation was set the same as that presented in Table 5-1 for 54%. For the high-strength region, the strength ratio of the high-strength region to the normal-strength one was set as 2 both for the yield and tensile strengths, while the elongation was set as half. Note that the brace ends for both CBB and IHCB were high-strength regions, and they were slotted for 235 mm at each side as the original brace presented in Section 5.1.1. Tie constraints were used between the slot regions of the braces and the gusset plates to simulate the welding condition. The gusset plates ensured the pin-supported condition, which allowed the out-of-plane bending of the brace around its minor axis. Although initial imperfection was employed for the analysis of CBB in Section 3.1, no initial imperfection was employed in the analyses of the braced frames since the buckling would happen naturally without any trigger.

5.3 Analysis results

5.3.1 Story shear-drift ratio relationships of frame

Figure 5-8 demonstrates the story shear-drift ratio relationships of CBB and IHCB frames with critical points as well as their skeleton curves. Table 5-3 summarizes the timing of critical behaviors and Table 5-4 concludes the load values of the braced frames. The ratios of the corresponding value of IHCB frame to that of CBB frame are shown in bracket ( ). Because the two braces in the same frame acted almost symmetrically, only the right brace is discussed in the following contents.

The definitions of each parameter are shown below.

- Drift ratio (%): the ratio of the lateral deformation of the loading point to the frame height of 2250 mm.

Frame:

- Yield load (kN): the first time when the fiber in the significant component of the frame yields, such as the beam and the column. It is judged from the contours. Note that the yielding of the gusset plate is excluded.

- Maximum load (kN): the maximum load of the braced frame.

Right brace:

- Yield load (kN): the first time when the fiber in the right brace yields under tension, which is judged from the contours.

- Maximum tensile load (kN): the maximum load of the brace under tension.

- Buckling load (kN): the load while it suddenly decreases with the increase of the drift ratio on the compressive side, which is the start point of the convex curve in the load-displacement relationship.

- Maximum compressive load (kN): the maximum load of the brace under compression.

Table 5-3 Timing of the critical behaviors of braced frame

Frame type	Time table
CBB frame	Brace: yielding → Brace: buckling → Gusset plate: yielding → Frame: yielding → Brace: Maximum tensile load → Frame: Maximum load
IHCB frame	Brace: maximum compressive load → Gusset plate: yielding → Brace: yielding → Frame: yielding → Brace: Maximum tensile load → Frame: Maximum load

* → Occur subsequently

(a) CBB frame

(b) IHCB frame

(c) Skeleton curve

Figure 5-8 Story shear-drift ratio relationships of frames

For the CBB frame, the yielding and the buckling of CBB occurred first, then the yielding of the gusset plate and the frame occurred subsequently. While, for the IHCB frame, the gusset plate yielded earlier than IHCB, and the buckling of IHCB was not observed. For both frames, the local buckling of the braces was not observed. Overall, the unsmooth cyclic behaviors seemed in the CBB frame were smoothened in the IHCB frame. Replacing CBB with IHCB lowered the stiffness of the frame at the beginning. The slope connecting the origin and the frame's yield point was 167855 kN for the CBB frame but 84307 kN for the IHCB frame, of which the ratio was about 2.0. However, their loads became close to each other after the 1.0% drift ratio, and their maximum load values were nearly the same, as shown in the skeleton curve. Therefore, it can be said that IHCB lowered the stiffness of the frame at small deformations and maintained the high load capacity at large deformations, qualitatively satisfying the development purpose of IHCB.

Table 5-4 Braced frame load capacities

Frame type	Load			
	Yield load		Maximum load	
	Value (kN)	Cycle	Value (kN)	Cycle
CBB frame	-629.5	1st of -0.5%	794.5	1st of +2.0%
IHCB frame	-421.5 (0.67)	1st of -0.5%	749.7 (0.94)	1st of +2.0%

5.3.2　Axial load-drift ratio relationships of brace

The axial loads of the braces were extracted from the braced frames to evaluate their cyclic performances. The free body cut function of ABAQUS was used as Figure 5-9 shows. The loads in three dimensions at the brace middle were output at each analysis step. Because the load in the out-of-plane direction (Z axis) was relatively low, only the resultant load in the in-plane direction (X-Y plane) was calculated as the axial load. Note that only the right brace is discussed.
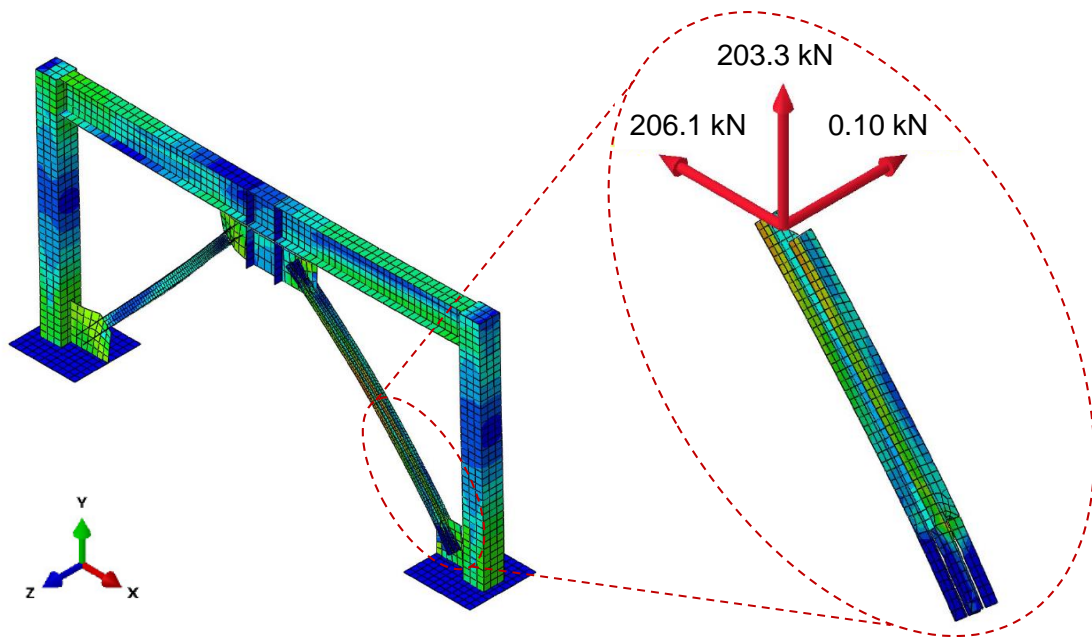
Figure 5-9 Extraction of axial load of brace (example of IHCB at the final condition)

Figure 5-10 demonstrates the axial load-drift ratio relationships of braces as well as their skeleton curves. Table 5-5 summarizes the values of the load capacities of the braces. The ratios of the corresponding value of IHCB to that of CBB are shown in bracket ( ).

Table 5-5 Brace load capacities

Brace type	Yield load		Maximum tensile load		Buckling / maximum compressive load *	
	Value (kN)	Cycle	Value (kN)	Cycle	Value (kN)	Cycle
CBB	314.6	1st of -0.25%	372.9	1st of -0.5%	-371.3	1st of +0.5%
IHCB	193.6 (0.62)	1st of -0.5%	327.9 (0.88)	1st of -1.0%	-124.2 (0.33)	1st of +0.5%

* Overall buckling was not observed on IHCB

(a) CBB

(b) IHCB

(c) Skeleton curve

Right brace: yielding
Right brace: maximum tensile
Right brace: buckling / maximum compressive
Right brace: out-of-plane bending
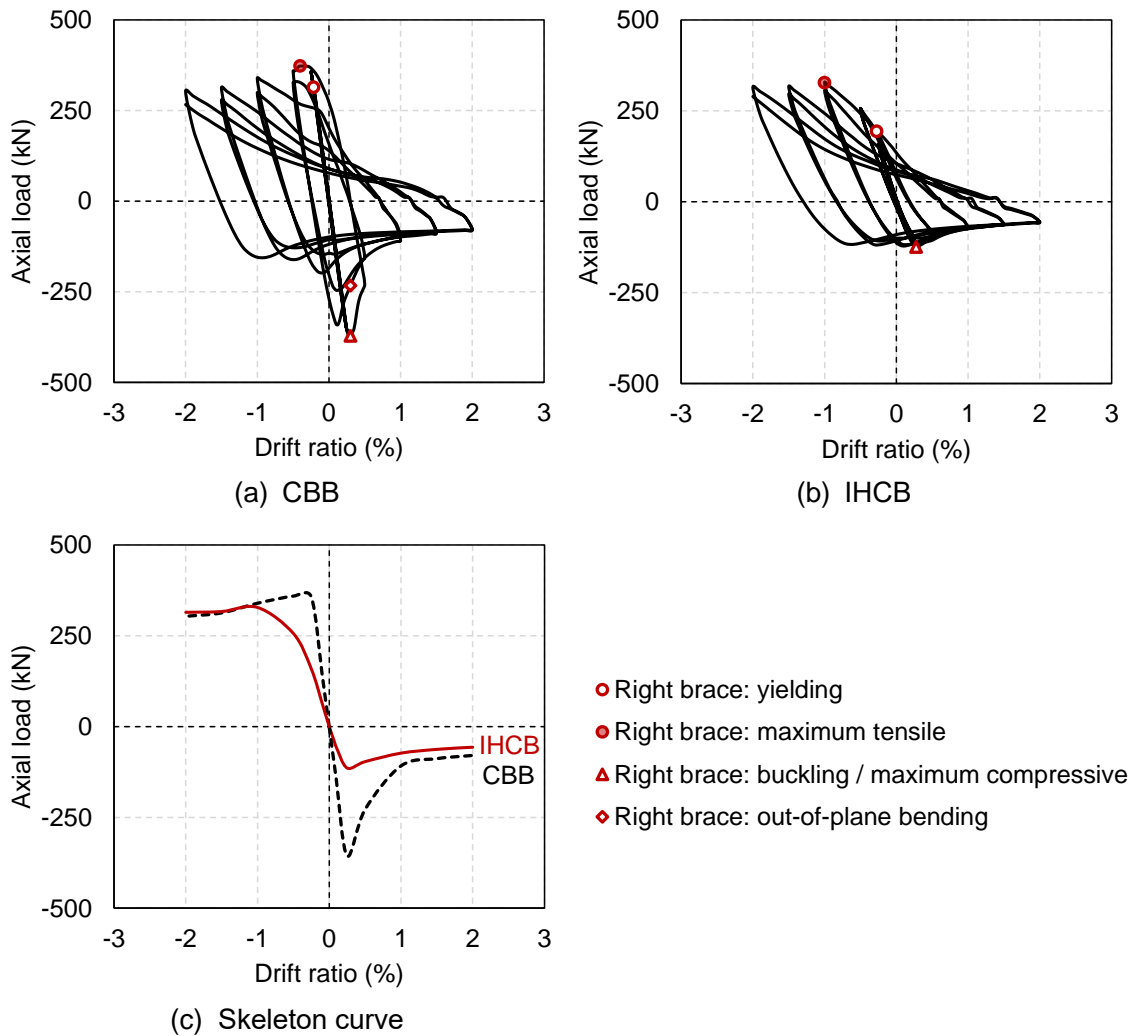
Figure 5-10 Axial load-drift ratio relationships of braces

IHCB showed a smoother axial load-drift ratio curve than CBB. The yield load of CBB was 314.6 kN, generally agreed with the designed yield load of 342.0 kN, and the error was within 10%. Although the yield load of IHCB was lower than CBB, the yield cycle was delayed to twice that of CBB. The slope connecting the origin and the brace's yield point was 148055 kN for CBB but 70396 kN for IHCB, of which the ratio was about 2.1. After the -1.0% drift ratio, the skeleton curve of IHCB was well consistent with that of CBB. Under compression, CBB buckled at the 1st cycle of +0.5% drift ratio, and drastic out-of-plane bending occurred at the 2nd cycle of +0.5% drift ratio. By comparison, IHCB avoided the overall buckling, successfully showing a stable post-buckling behavior. Therefore, it can be said that IHCB qualitatively satisfied the target performance of low initial stiffness, high post-yield stiffness, and stable compressive behavior. Note that the quantitative evaluation is not presented here, because the axial strain of the brace is hard to extract and evaluate precisely. To further understand the braced frame behaviors, their contours are described in the following discussions.

5.3.3　Yield conditions

The contours of the yield conditions of the braces and the frames are respectively shown in Figure 5-11 and Figure 5-12. To distinguish the following figures clearly, the thickness of the shell elements is invisible. The first yielded regions of CBB concentrated at the flange near the brace ends, while that of IHCB concentrated at the normal-strength flange at the outer side. These kinds of different yield behaviors explained the differences in the yield cycles and the yield loads of the braces. In terms of the frames, they yielded at the same cycles and the yielded regions were both at the beam-column joint on the left side. Therefore, it can be said that IHCB hardly affects the frame's yield behavior.

(a)　CBB (yielded at the 1st of -0.25%)　　(b)　IHCB (yielded at the 1st of -0.5%)
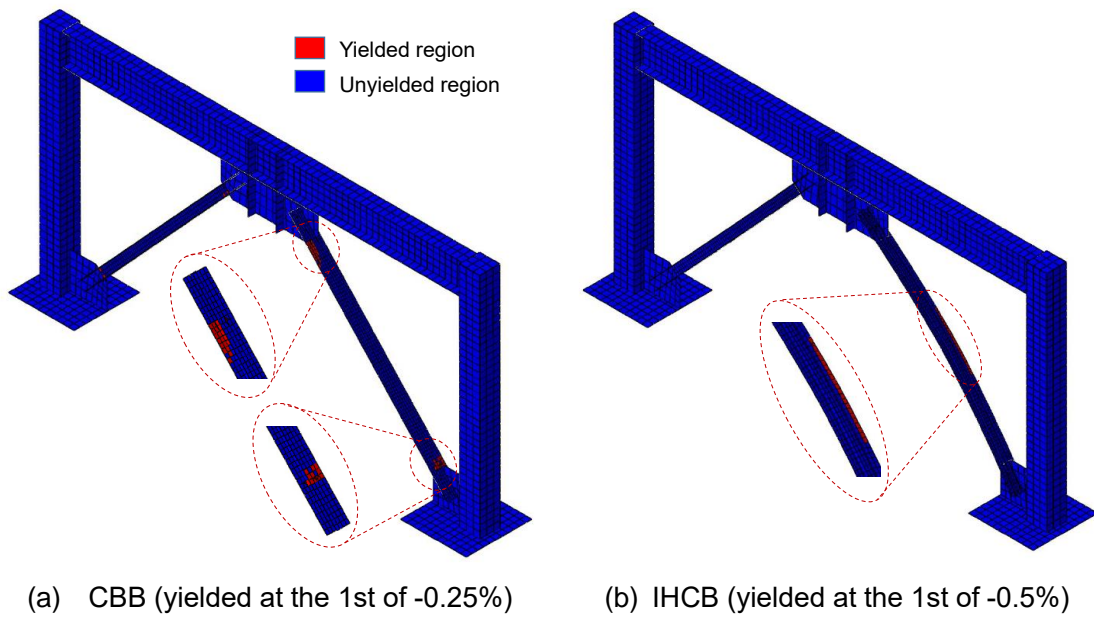
Figure 5-11 Yield cycles of braces

(a)　CBB frame (yielded at the 1st of -0.5%)　(b)　IHCB frame (yielded at the 1st of -0.5%)
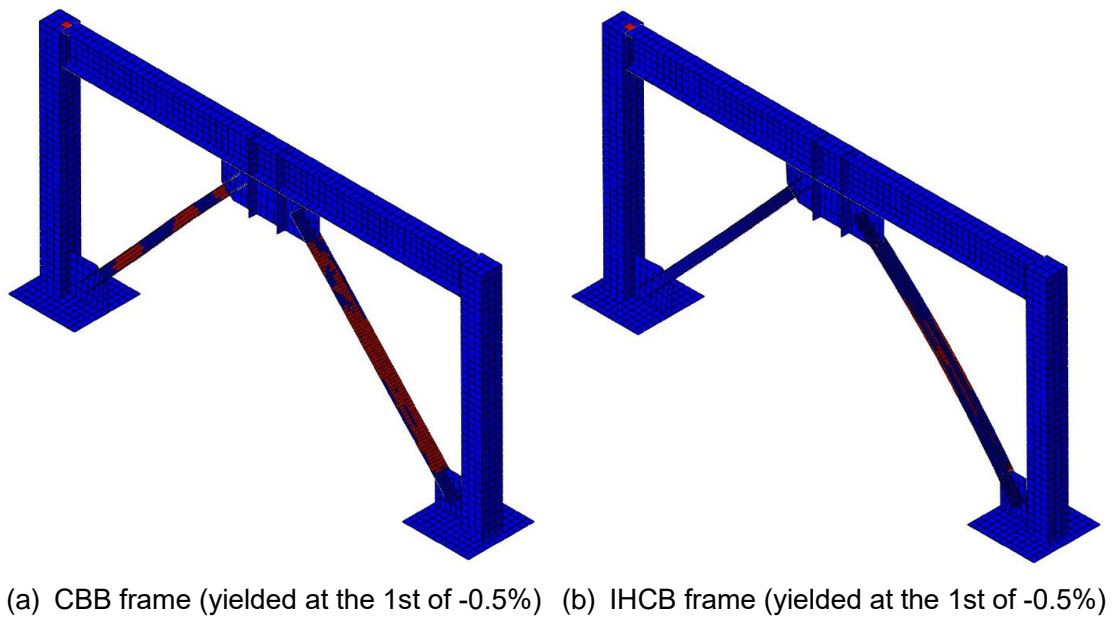
Figure 5-12 Yield cycles of braced frames

5.3.4 Buckling or bending conditions

The contour of the drastic out-of-plane bending or buckling behavior of CBB, which was observed at the 2nd cycle of +0.5% drift ratio is shown in Figure 5-13. For comparison, the contour of IHCB at the same step is shown as well. CBB bent around its minor axis in a wavy shape. The stress concentrated not only on the brace but also on the gusset plates and the left region of the beam. By contrast, IHCB uniformly bent along its initial curve shape, without causing stress concentration on the frame. Therefore, under the same drift ratio, IHCB is proved to be effective to mitigate the stress concentration on the frame.
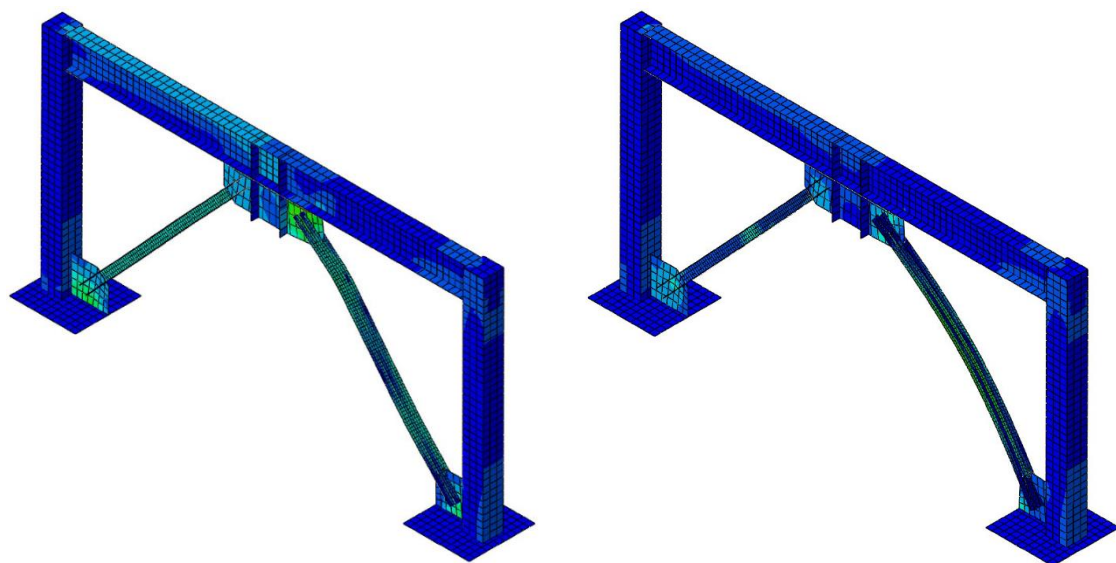
(a) CBB (at the 2nd cycle of +0.5%)   (b) IHCB (at the 2nd cycle of +0.5%)
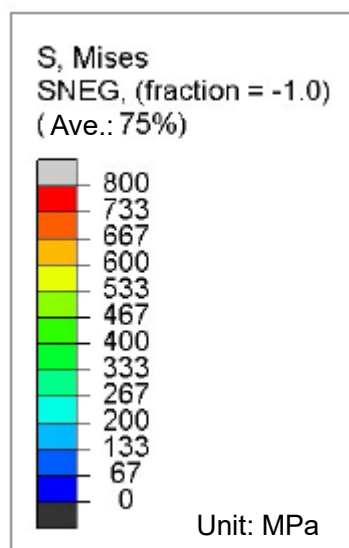
Figure 5-13 Buckling or bending conditions of braces

5.3.5 Final conditions

Figure 5-14 demonstrates the stress distributions of the braced frames at the final conditions. The stress mainly concentrated at the top and bottom parts of the columns and two ends of the beam, which were the same in both frames. The obvious difference is that the out-of-plane bending of the gusset plate at the left bottom was more significant in the CBB frame than in the IHCB frame.

(a) CBB frame   (b) IHCB frame

S, Mises
SNEG, (fraction = -1.0)
(Ave.: 75%)

800
733
667
600
533
467
400
333
267
200
133
67
0

Unit: MPa
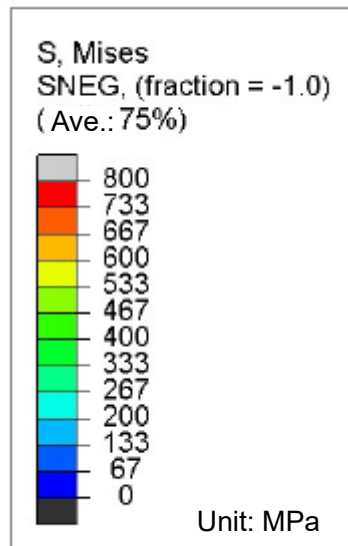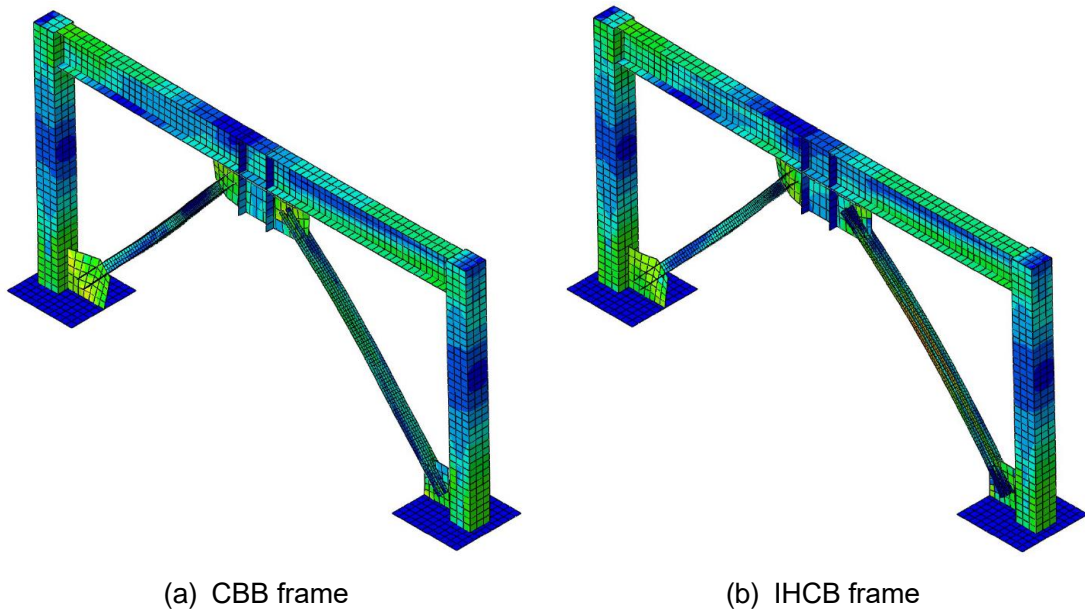
Figure 5-14 Final conditions of braced frames

To investigate the level of out-of-plane bending of the braces, top views of two braced frames at the final condition are compared in Figure 5-15. Because the out-of-plane deformations of the beam were restrained, out-of-plane deformations of the brace were noted. The deformations concentrated at the brace middle of CBB, while they were more uniformly distributed for IHCB. The maximum out-of-plane deformation of CBB was 242 mm. But, it was 188 mm for IHBRB, which was 22% smaller than that of CBB. Although IHCB had an initial curve shape, its transverse deformation was smaller than CBB at the large drift ratio. Besides, due to the initial curve shape, the bending direction of IHCB was controllable. Hence, as presented in Section 2.5.4, the concern about whether the initial curve shape would intensify the transverse deformation of a curved brace or not was resolved.

(a) CBB: 242 mm (beam is hidden)

(b) IHCB: 188 mm (beam is hidden)
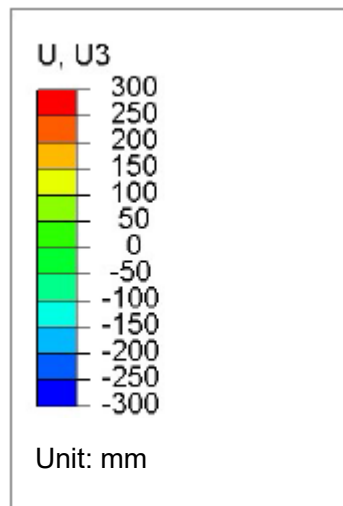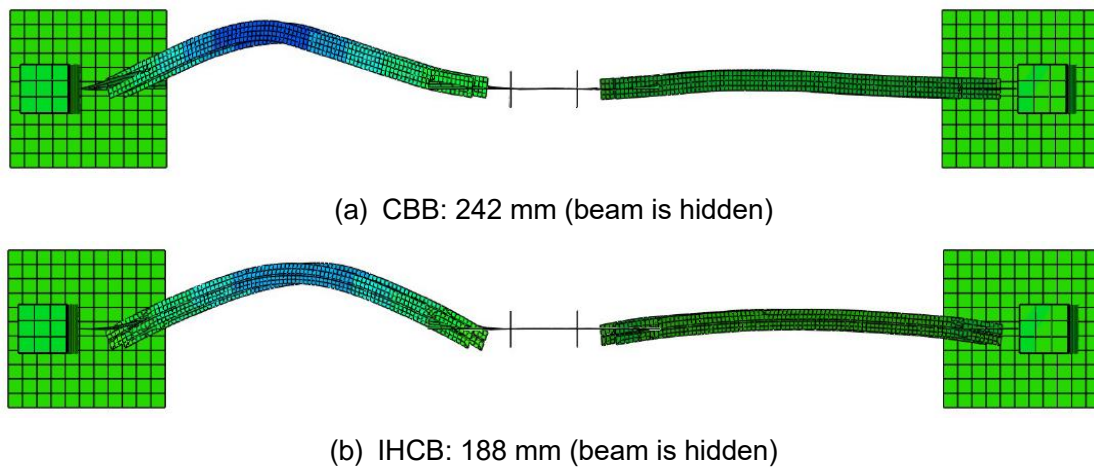
Figure 5-15 Out-of-plane deformations of braces

5.4 Conclusion

This chapter presents the numerical analysis of the frames using induction-heated curved brace (IHCB) and conventional buckling brace (CBB) conducted by ABAQUS.

Section 5.1 introduces the outlines of a frame tested by the shake table [5.1]. It was a single-story, single-span frame with chevron brace specimens. It was corresponding to 70% scale of typical buildings, representing the bottom story of a 3 to 5-story building in Japan. ABAQUS was used to reproduce the frame model, and the ABAQUS model generally captured the test data and the analysis results obtained by Opensees shown in the original research.

Section 5.2 presents the outlines of the braced frames. CBB or IHCB was attached to the aforementioned frame to investigate the brace behaviors in an identical frame. Geometric scaling of the cross-section was used for CBB to satisfy the same designed yield load of the brace in the previous research. The cross-section of IHCB was kept the same as that of CBB. The modeling details were presented.

Section 5.3 demonstrates the analysis results of the braced frames. Overall, the unsmooth cyclic behaviors seemed in the CBB frame were improved in the IHCB frame. It was because that CBB buckled under compression, while IHCB avoided the overall buckling and showed a stable compressive behavior. IHCB lowered the stiffness of the frame at small deformations and maintained the high load capacity at large deformations. It revealed that IHCB succeeded to meet the target performance of low initial stiffness, high post-yield stiffness, and stable compressive behavior. In terms of the deformation capacity, while CBB bent in the out-of-plane direction drastically, IHCB bent along its initial curve shape uniformly, which was effective to mitigate the stress concentration on the frame. Even though IHCB possessed the initial curve shape, it eventually showed a smaller out-of-plane deformation than CBB with a controllable bending direction.

It is confirmed qualitatively that IHCB is able to exert its expected performance in a frame. However, from other aspects, such as the yield cycles of the frames, the advantage of using IHCB instead of CBB is not prominent. Other analysis conditions, for example, the brace in other directions or other bracing systems, and the seismic analysis of the IHCB frame, may be necessary in the future to enrich the understanding of the proposed brace.

References

5.1) Okazaki, T., Lignos, D. G., Hikino, T., & Kajiwara, K. (2013). Dynamic Response of a Chevron Concentrically Braced Frame. Journal of Structural Engineering, 139(4), 515–525. https://doi.org/10.1061/(asce)st.1943-541x.0000679

6 Fatigue test of induction-heated steel

This chapter presents the fatigue performance of two kinds of induction-heated steel. The low cycle fatigue tests are conducted on the coupons cut out from induction-heated curved braces (IHCBs) to evaluate the fatigue performance of IH-treated material and compare the fatigue performance of the material before and after IH treatment. During these tests, cyclic hardening is observed on the untreated specimens, but cyclic softening on the IH-treated ones. Although cyclic softening is reported as a quintessential feature of highly-hardened steel [6.1], how many degrees it affects the behavior of IH-treated specimens is unclear. As one of the most-commonly-used IH-treated specimens, PT bars are investigated by high cycle fatigue tests. This chapter first introduces the low cycle fatigue of the material of IHCB, and then the high cycle fatigue of the PT bar. Last, the innovative strain control method proposed for the low cycle fatigue tests is presented.

6.1 Low cycle fatigue of I-shaped section

6.1.1 General information

The test information is summarized in Table 6-1 based on ISO standard [6.2] and previous studies on similar material in Japan [6.3], [6.4].

Table 6-1 Low cycle fatigue test information

Purpose of the test	
Aim	To investigate the fatigue performance of the material used in the proposed braces; To compare the fatigue performance of the material before and after induction heating.
Material	
Chemical composition	C: 0.13%; Si: 0.19%; Mn: 0.54%; P: 0.018%; S: 0.015%
Product	I-shaped 100×100×6×8 mm; JIS G 3101 SS400 grade (for the unheated specimen)
Heat treatment	Induction heating (for the heated specimen)
Mechanical properties	Unheated specimen E: 1.94×10^5 MPa; σ_y: 304 MPa; σ_u: 425 MPa; δ: 25.8%; ϕ: 60% Heated specimen E: 1.95×10^5 MPa; σ_y*: 678 MPa; σ_u: 952 MPa; δ: 7.8%; ϕ: 51% (*: 0.2% proof stress)

Specimen (Unit: mm)
 Cutting lines & coupon regions in the longitudinal direction Cutting lines in section A   Coupon regions in section A Normal-strength region High-strength region Cutting line Coupon region Coupon dimensions

Test methods		
Test machine	Actuator type	Hydraulic
	Force capacity	100 kN
	Controller type	Analog
	Control mode	Strain control
Load train	Grip type	Manual
Extensometer	Type	Optical displacement sensor
	Gauge length	Approximately 20 mm

Test conditions	
Axial-strain range	Unheated specimen: 0.3%-6.0%; Heated specimen: 0.5%-5.7%
Strain ratio	-1
Waveform	Triangular
Frequency	0.5 Hz

Strain rate	Unheated specimen: 0.3%-6.0% per second; Heated specimen: 0.5%-5.7% per second
First quarter-cycle	Tensile
Definition of failure	The specimen is totally separated into two parts.
Test temp.	12 °C -16 °C (manually recorded)

Note that the frequency between 0.01 Hz and 1Hz, and the strain rate ranging from 0.05% to 5% per second were recommended by ISO standard [6.2]. Additionally, it was proved that the strain rate ranging from 0.4% to 10% per second did not affect the fatigue performance [6.5]. Therefore, the frequency of 0.5 Hz, and the strain rate ranging from 0.3% to 6.0% per second were employed in this study.

6.1.2　Test data

The test data is concluded in Table 6-2.

Table 6-2 Low cycle fatigue test result

Specimen	Strain range (%)			Stress range (MPa)	Number
	Total $\Delta\varepsilon_t$ *	Plastic $\Delta\varepsilon_p$	Elastic $\Delta\varepsilon_e$	Total $\Delta\sigma_t$	N_f
Unheated	0.3**	0.04	0.25	503	31008
	0.6	0.20	0.37	676	4464
	1.0	0.68	0.35	761	1963
	2.0	1.62	0.38	875	577
	3.0	2.51	0.45	917	228
	3.6	3.23	0.38	1013	100
	5.0	4.64	0.38	1017	69
	6.0	5.44	0.51	1025	39
Heated	0.5**	0.05	0.46	898	32224
	0.8	0.37	0.43	913	3547
	1.0	0.61	0.40	1171	1513
	2.0	1.54	0.41	1448	374
	3.0	2.23	0.76	1566	123
	3.7	3.05	0.66	1352	121
	4.3	3.57	0.77	1538	32
	5.7	4.71	0.97	1758	22

* Controlled parameter

** Smaller than twice the yield strain

Where,

$\Delta\varepsilon_t$ = Total strain range. It is equal to the difference between the largest tensile and compressive strains in one cycle.

$\Delta\varepsilon_p$ = Plastic strain range. It is the plastic part extracted from the total strain range at the cycle number of $N_f/2$.

$\Delta\varepsilon_e$ = Elastic strain range. It is the elastic part extracted from the total strain range at the cycle number of $N_f/2$.

$\Delta\sigma_t$ = Total stress range. It is equal to the difference between the largest tensile and compressive stresses at the cycle number of $N_f/2$.

N_f = Number of cycles to failure.

6.1.3 Fatigue life curve

The predicted fatigue lives based on the universal slopes method and the modified universal slopes method proposed by Manson [6.6)], are shown in Eq. 6-1-Eq. 6-4.

Unheated specimen

Universal slopes: $\Delta \varepsilon_{t,uni,\text{Unheated}} = 0.9519 N_f^{-0.6} + 0.0077 N_f^{-0.12}$ Eq. 6-1

Modified universal slopes: $\Delta \varepsilon_{t,mod,\text{Unheated}} = 0.6741 N_f^{-0.56} + 0.0072 N_f^{-0.09}$ Eq. 6-2

Heated specimen

Universal slopes: $\Delta \varepsilon_{t,uni,\text{Heated}} = 0.8118 N_f^{-0.6} + 0.0171 N_f^{-0.12}$ Eq. 6-3

Modified universal slopes: $\Delta \varepsilon_{t,mod,\text{Heated}} = 0.4231 N_f^{-0.56} + 0.0140 N_f^{-0.09}$ Eq. 6-4

The fatigue test results formulized according to Manson-Coffin law [6.7)] is presented as Eq. 6-5-Eq. 6-6.

Unheated specimen

$$\Delta \varepsilon_{t,\text{Unheated}} = 1.0887 N_f^{-0.728} + 0.0059 N_f^{-0.072} \qquad \text{Eq. 6-5}$$

Heated specimen

$$\Delta \varepsilon_{t,\text{Heated}} = 0.3868 N_f^{-0.594} + 0.0112 N_f^{-0.111} \qquad \text{Eq. 6-6}$$

Figure 6-1(a) and (b) present the fatigue lives of unheated and heated specimens, respectively. For both types of specimens, the results obtained using the modified universal slopes method had better compatibility than that using the universal slopes method. However, the fatigue life obtained experimentally was shorter than the predictions in both cases. There are several plausible causes. Compared with the commonly-used bar specimen, a plate specimen is prone to cracking due to the corners in its cross-section [6.8)]. The rotation of the lower gripping apparatus in the horizontal direction might have caused torsion of the specimens. In addition, only the front and back surfaces were ground, and other surfaces were left as they were to simulate the original brace surface. Therefore, a few potential flaws on the surface might have existed.

Figure 6-1(c) compares the fatigue lives of the unheated and heated specimens. For a large strain range, the unheated specimens had a longer life than the heated specimens due to higher ductility. For a small strain range, the heated specimens had a longer life than the unheated specimens because strength dominated the behavior. Therefore, induction heating is effective to prolong the fatigue life within a small strain range.

Experimental results: ○ $\Delta\varepsilon_t$ × $\Delta\varepsilon_p$ △ $\Delta\varepsilon_e$
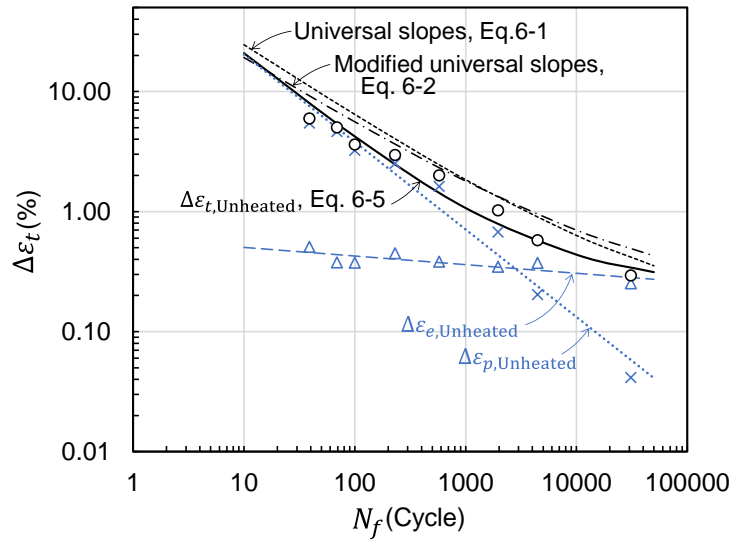
(a) Unheated specimens
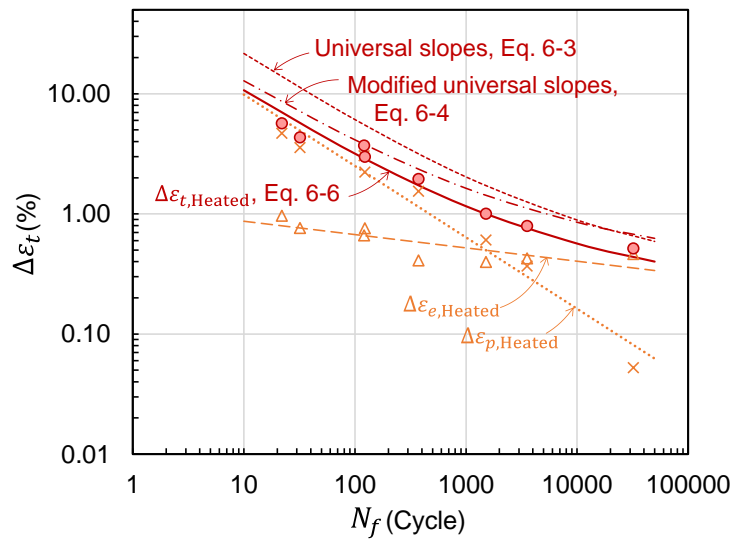
(b) Heated Specimens
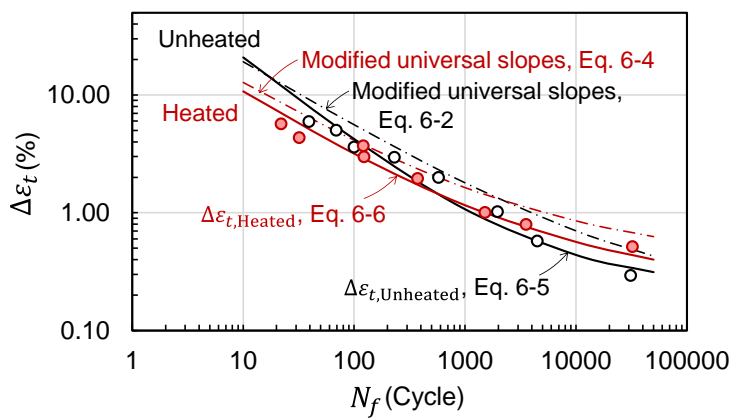
(c) Comparison between unheated and heated specimens

Figure 6-1 Fatigue lives

6.1.4 Cyclic stress-strain curve

The predicted cyclic stress-strain curves, σ_t-ε_t curve, proposed by Morrow [6.9], are demonstrated as Eq. 6-7-Eq. 6-8. Where, $\sigma_t = \Delta\sigma_t/2$, and $\varepsilon_t = \Delta\varepsilon_t/2$.

Unheated specimen

$$\varepsilon_{t,morrow,\text{Unheated}} = \frac{\sigma_t}{194000} + 0.92\left(\frac{\sigma_t}{817}\right)^{1/0.15} \qquad \text{Eq. 6-7}$$

Heated specimen

$$\varepsilon_{t,morrow,\text{Heated}} = \frac{\sigma_t}{195000} + 0.71\left(\frac{\sigma_t}{1625}\right)^{1/0.15} \qquad \text{Eq. 6-8}$$

The cyclic stress-strain curves formulized according to the Ramberg-Osgood equation for the non-linear relationship between stress and strain [6.10] are presented as Eq. 6-9-Eq. 6-10.

Unheated specimen

$$\varepsilon_{t,\text{Unheated}} = \frac{\sigma_t}{194000} + \left(\frac{\sigma_t}{884.8}\right)^{1/0.146} \qquad \text{Eq. 6-9}$$

Heated specimen

$$\varepsilon_{t,morrow,\text{Heated}} = \frac{\sigma_t}{195000} + \left(\frac{\sigma_t}{1426.4}\right)^{1/0.152} \qquad \text{Eq. 6-10}$$

Figure 6-2 depicts the cyclic stress-strain curves of the unheated and heated specimens. The circles in the figure indicate peaks of the stable state hysteresis loops, which is defined as the hysteresis loop at the cycle number of $N_f/2$. For unheated specimens, the cyclic stress-strain curve was above the static curve indicating that cyclic hardening had occurred. Morrow's equation agreed with the cyclic stress-strain curve. Conversely, for heated specimens, cyclic softening was observed. From the perspective of atomic structure, this type of quenched steel is possible to revert to what is a more stable condition under cyclic straining, which is presented as cyclic softening [6.1]. Although Morrow's equation provided a higher estimated value than that of the cyclic stress-strain curve, it was similar to that of the static stress-strain curve. Hence, Morrow's equation might not be appropriate to predict the fatigue behavior of quenched steel.

Experimental results:　　○ Unheated　　● Heated
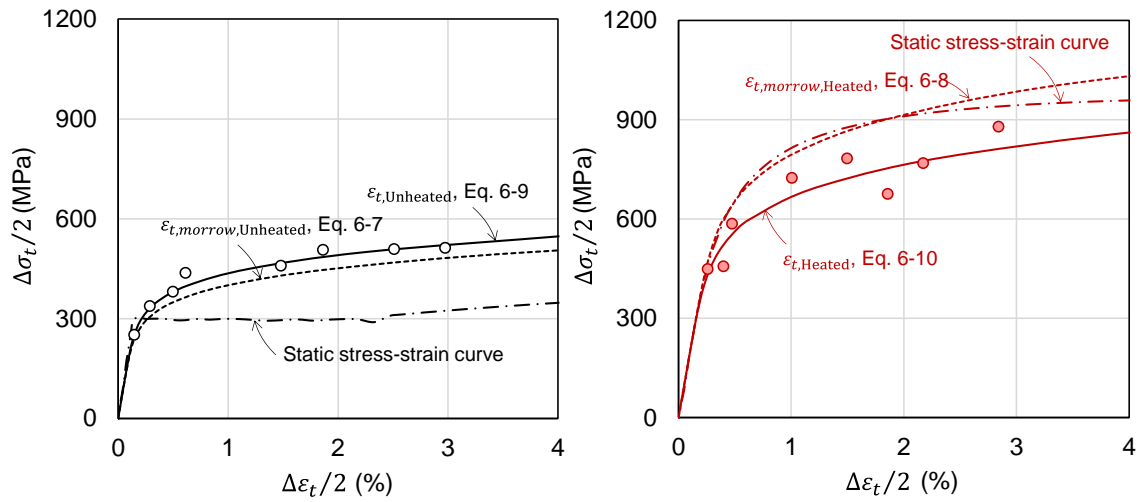
(a) Unheated specimen　　　　　　　(b) Heated specimen

Figure 6-2 Cyclic stress-strain curve

6.1.5   Fatigue performance under stroke control

As a further investigation, the stroke-controlled fatigue tests were conducted on two unheated specimens. Note that the stroke is the deformation between the upper and lower gripping tools. The variations in the total stroke range, ΔD, the deformation of the gauge length, and the total strain range with time are shown in Figure 6-3 and Figure 6-4. The range of the corresponding value at the cycle of $N_f/2$ is highlighted as well.

As presented in Figure 6-3(a) and Figure 6-4(a), the stroke was kept constant during the test, indicating that the stroke control was carried out as projected. Figure 6-3(b) and Figure 6-4(b) depict the deformation of the gauge length. The value of the gauge length was smaller than the stroke length since it excluded the elastic deformation of the loading machine and the relaxation of the gripping tool. Additionally, the mean value of the gauge length was inconstant, more precisely, it gradually moved to the compressive or tensile side. Hence, the strain drifted as well, as presented in Figure 6-3(c) and Figure 6-4(c).
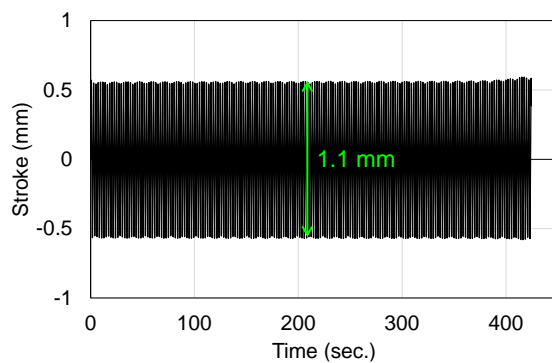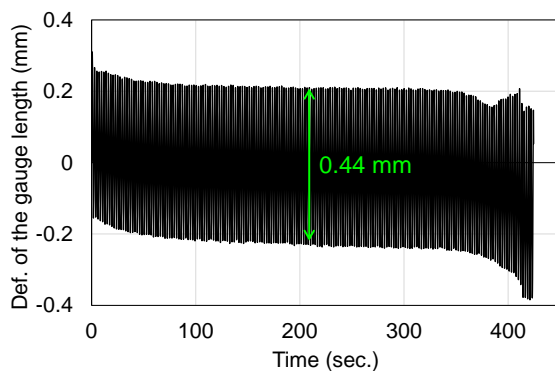
(a) Stroke-time relationship

(a) Stroke-time relationship

(b) Deformation of gauge length-time relationship
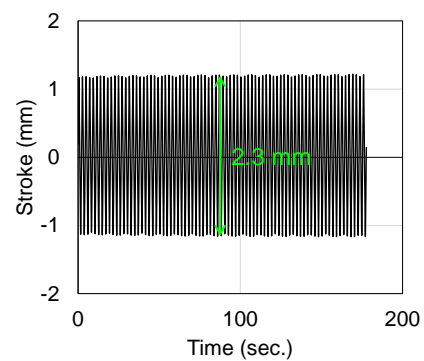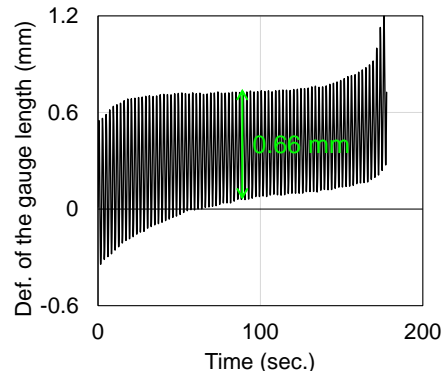
(b) Deformation of gauge length-time relationship
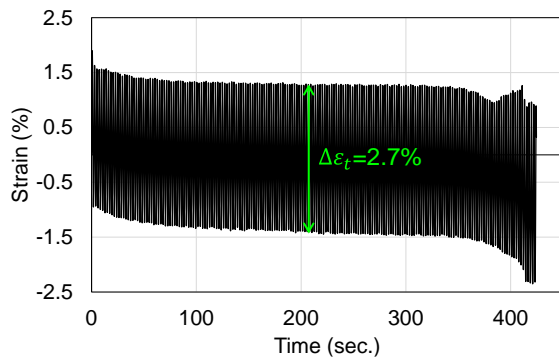
(c) Strain-time relationship

Figure 6-3 Stroke-controlled test on
unheated specimen (ΔD = 1.1 mm)
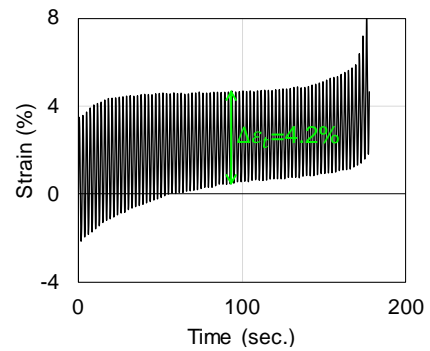
(c) Strain-time relationship

Figure 6-4 Stroke-controlled test on
unheated specimen (ΔD = 2.3 mm)

The fatigue lives of stroke-controlled test results are compared to those obtained from strain-controlled tests, see Figure 6-5. Although the test data under stroke control were limited, they surprisingly fitted into the fatigue life obtained under strain control. It can be inferred from Figure 6-3(c) and Figure 6-4(c) that although the mean strain varied with time, the total strain range was almost fixed at the level of 2.7% and 4.2%, respectively. Thus, the total strain range rather than the mean strain was dominant, or the mean strain at these levels hardly affected the low cycle fatigue performance. The stroke-controlled method may work as a nice substitute for the strain-controlled method when there are some test limitations, especially for the tests on large-scale components.

Experimental results: ○ strain control, unheated   ■ stroke control, unheated

$$\Delta\varepsilon_{t,mod,\text{Unheated}} = 0.6741 N_f^{-0.56} + 0.0072 N_f^{-0.09}$$

$$\Delta\varepsilon_{t,\text{Unheated}} = 1.0887 N_f^{-0.728} + 0.0059 N_f^{-0.072}$$
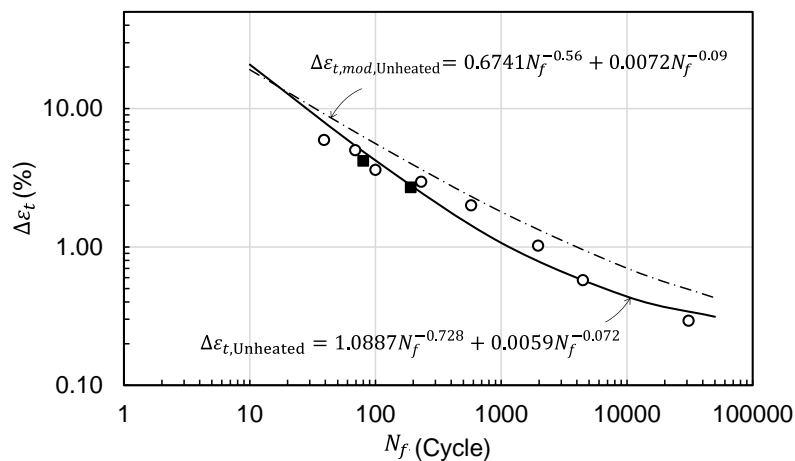
Figure 6-5 Fatigue lives (stroke control vs. strain control)

6.1.6　Fatigue performance under load control

The load-controlled fatigue tests were conducted as well. The test objects were two unheated specimens and two heated specimens. Figure 6-6 and Figure 6-7 depict the variations of the total load range, ΔP, and total strain range of the heated specimens with time. As shown in Figure 6-6(a) and Figure 6-7(a), the total load range remained unaltered with time, but as presented in Figure 6-6(b) and Figure 6-7(b), the total strain range gradually increased. Although the total strain range in Figure 6-6(b) was unsteady, the mean strain was almost 0. By contrast, the total strain range in Figure 6-7(b) shifted to the tensile side.

(a) Load-time relationship
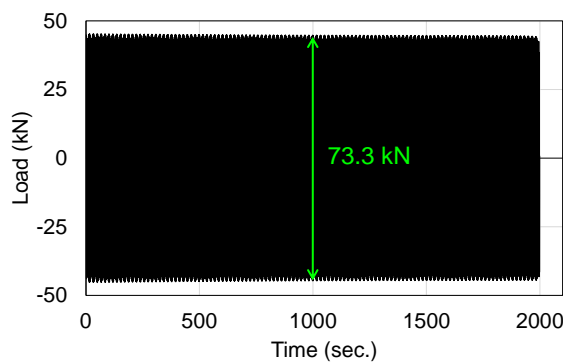
(a) Load-time relationship

(b) Strain-time relationship

Figure 6-6 Load-controlled test on heated specimen (ΔP = 73.3 kN)
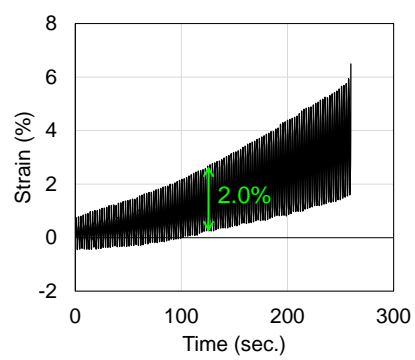
(b) Strain-time relationship

Figure 6-7 Load-controlled test on heated specimen (ΔP = 100.9 kN)

Figure 6-8 compares the fatigue life curves obtained from the strain-controlled test, of which the vertical axis was converted from $\Delta\varepsilon_t$ to $\Delta\sigma_t$, with those from the load-controlled test. For the unheated specimens, the experimental results obtained under load control agreed well with those obtained under strain control, similar to what was presented in reference [6.11]. It was because the stress amplitude was approximately equal to or smaller than the yield strength, where the elastic behavior was prevailing.

For the heated specimens, those obtained under load control had longer fatigue life. There are several reasons for this phenomenon. The calculation of the total stress range did not consider the area reduction due to the crack and ductile deformation. Thus, the true stress must be much higher. However, from Figure 6-6(b) and Figure 6-7(b), the total strain range increases with time, and it has been proved in a previous study [6.6] that increasing the total strain range from small to large extends the fatigue life. What's more, the data of heated specimens under strain control were more dispersed than those of the unheated ones. The combination of the mentioned reasons might have caused this result. Therefore, when the fatigue life is larger than approximately 10^4 cycles, what is called high cycle fatigue, the strain and load controls are undifferentiated. Whereas, in the low cycle fatigue, when the fatigue life is smaller than approximately 10^4 cycles, the precision of load-controlled test results falls.

Experimental results: ○ strain control, unheated   ● strain control, heated
         ▲ load control, unheated   ▲ load control, heated
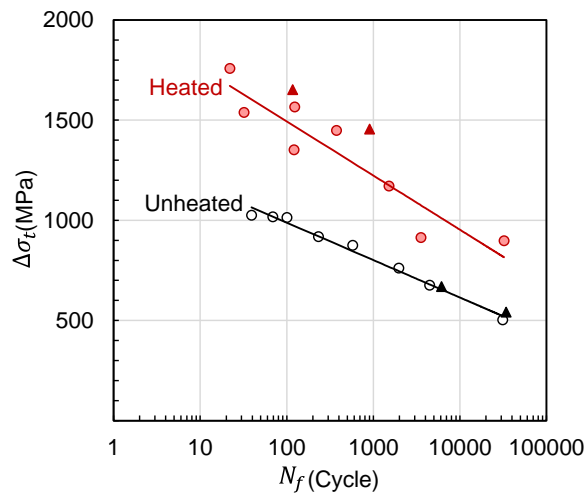
Figure 6-8 Fatigue lives (load control vs. strain control)

6.2 High cycle fatigue of PT bar

6.2.1 General information

The test information is summarized in Table 6-3 based on ISO standard [6.8].

Table 6-3 High cycle fatigue test information

Purpose of the test	
Aim	To investigate the effect of cyclic softening of PT bars under normal service conditions.
Material	
Chemical composition	C: 0.45%; Si: 1.9%; Mn: 0.63%; P: 0.01%; S: 0.002%; Cu: 0.01%
Product	JIS G 3109 SBPR 1080/1230
Heat treatment	Induction heating
Mechanical properties	E: 2.10×10^5 MPa; σ_y*: 1237 MPa; σ_u: 1326 MPa; δ: 14.1%; ϕ: 48.9% (*: 0.2% proof stress)

Specimen (Unit: mm)

Design	

Test methods		
Test machine	Actuator type	Hydraulic
	Force capacity	500 kN
	Controller type	Analog
	Control mode	Load control
Load train	Grip type	Hydraulically preloaded
Strain gauge	Type	High endurance strain gauge
Test conditions		
Stress range	Pattern A: $0.6f_{pu}$-$0.8f_{pu}$ (738 MPa – 984 MPa) Pattern B: $0.5f_{pu}$-$0.7f_{pu}$ (615 MPa – 861 MPa) (f_{pu}: nominal tensile strength of 1230 MPa)	

Waveform	Sine
Frequency	10 Hz
First quarter-cycle	Tensile
Definition of failure	The specimen is totally separated into two parts.
Test temperature	13 °C -20 °C (manually recorded)

Note that the stress range satisfied the high cycle fatigue test method on the PT bar recommended by The International Federation for Structural Concrete, fib [6.12)] as follows: 1. The maximum stress is from $0.7f_{pu}$ to $0.8f_{pu}$. 2. The stress range is about 200 MPa. Under these conditions, the number of cycles to failure N_f should be no less than 2×10^6.

6.2.2 Test data

The test data is concluded in Table 6-4. Two specimens of each pattern were tested. Because the drift of the strain was observed during the test, two kinds of strain are presented here. The initial one is the strain before the occurrence of the drift, and it should be consistent with the value of stress divided by Young's modulus. The drifted one shows the strain at the cycle which drifted most on the tensile or compressive side.

Table 6-4 High cycle fatigue test result

Pattern		Stress (MPa)			Initial strain (%)*			Drifted strain (%)**			Number
		Max.	Min.	Range	Max.	Min.	Range	Max.	Min.	Range	N_f
A	1	998	746	252	0.46	0.35	0.11	0.50	0.39	0.11	2×10^6 (Without failure)
	2	984	740	244	0.46	0.35		0.58	0.47		
B	1	860	614	246	0.40	0.29		0.35	0.24		
	2	862	615	247	0.41	0.30		0.37	0.26		

* Before the occurrence of the strain drift.

** The strain at the cycle which showed the largest drift.

6.2.3   Fatigue performance

It can be inferred from Table 6-4 that the drift of the strain occurred for all the specimens. For a comprehensive comparison, the test results of Pattern A-2 were summarized in Figure 6-9 for example. Figure 6-9(a) demonstrates the stress-strain relationship. From cycle number 10 to 10000, the strain was kept unchanged. After that, the strain gradually drifted to the tensile side and reached the maximum strain values at the last cycle of 2000000. Specifically speaking, the stress kept stable during the whole test, as shown in Figure 6-9(b), however, both the max. and the min. strains became larger with the increase of the cycle, see Figure 6-9(c). Note that the stress was always lower than the yield strength of 1237 MPa, and the stress and strain ranges maintained almost the same during the test.
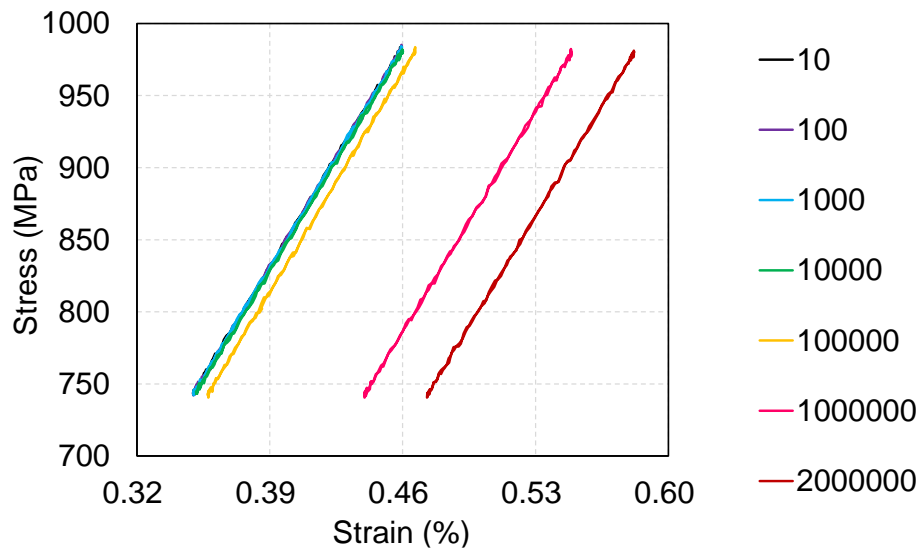
(a) Stress-strain curve
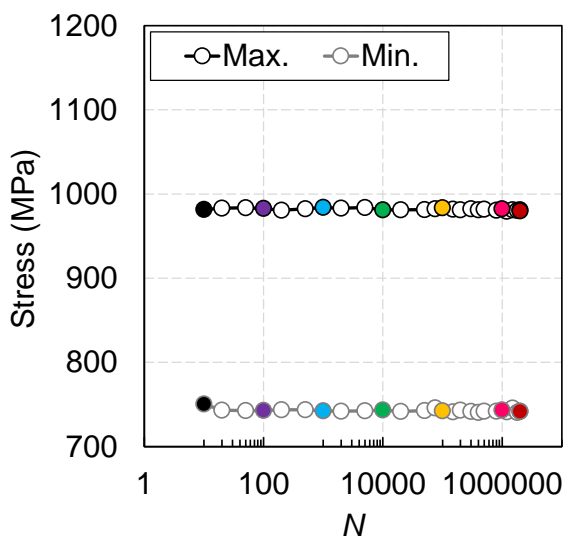
(b) Stress-N curve
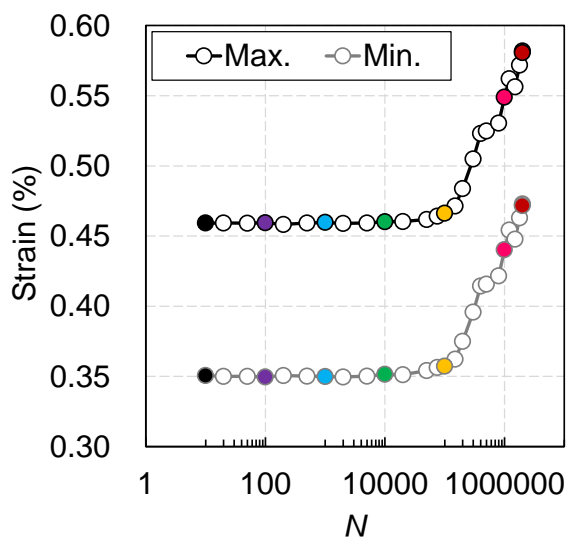
(c) Strain-N curve
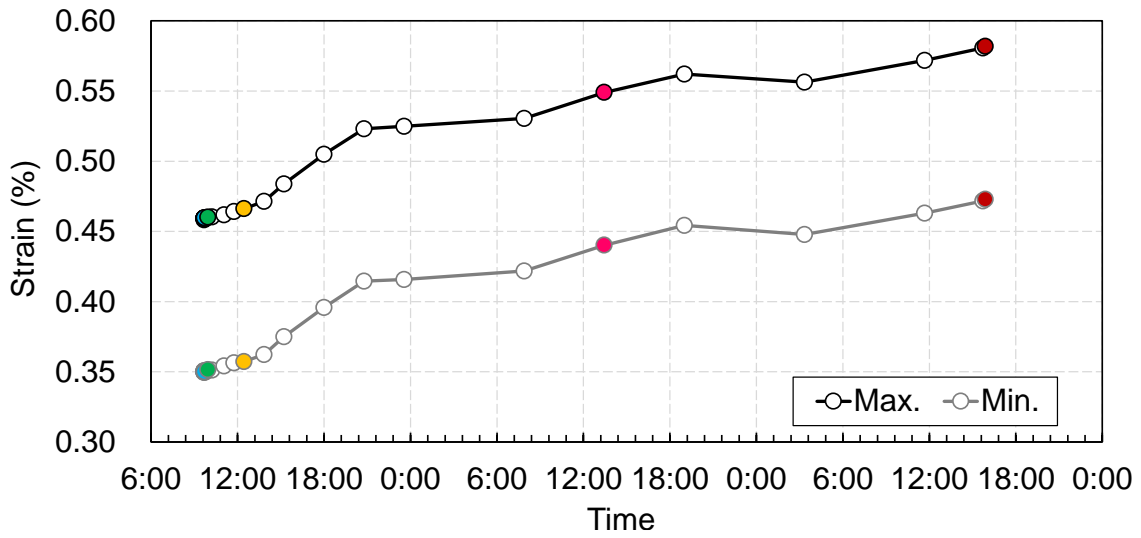
(d) Strain–time relationship

Figure 6-9 Test results (Pattern A-2)

To capture the feature, Figure 6-9(d) presents the strain-time relationship. The test was conducted for approximately 3 days in winter, and it can be inferred that the strain drift started at about 12:00 on the first day, and stopped at about 21:00. On the second day, the strain drift was observed from 8:00 to 19:00. On the third day, the strain drift was also observed at the daytime. Surprisingly, the strain rarely drifted at night and early in the morning. Hence, rather than the cyclic softening, the increase in the observed value of the strain mainly resulted from the increase in the room temperature, which was affected by the open-air temperature as well as the set temperature of the air conditioner. Note that the strain gauges were not the self-temperature compensated strain gauges. It explained the reason why patterns B-1 and 2 even showed smaller strain after the drift. Therefore, the cyclic softening behavior was not found during the fatigue test.

6.2.4 Static performance

Figure 6-10 presents the tensile test results of the two specimens. One was monotonically tensioned until it fractured, which was tested the same as those for tensile coupon tests, and it was called the one before the fatigue test. The other one underwent the high cycle fatigue of 2×10^6 cycles, and then monotonically tensioned until failure. It was called the one after the fatigue test. Although they seemed the same in general, the enlarged stress-strain relationship indicated that although the 0.2% proof stresses of them were both about 1225 MPa, the elastic limit of the one after the fatigue test decreased to approximately 1108 MPa, of which the decrease ratio was about 10%. The loss of the yield phase is one of the most common behaviors of cyclic softening. Based on such a phenomenon, the method of employing the cyclic yield strength for the safe design for structures was proposed in the previous research [6.13].
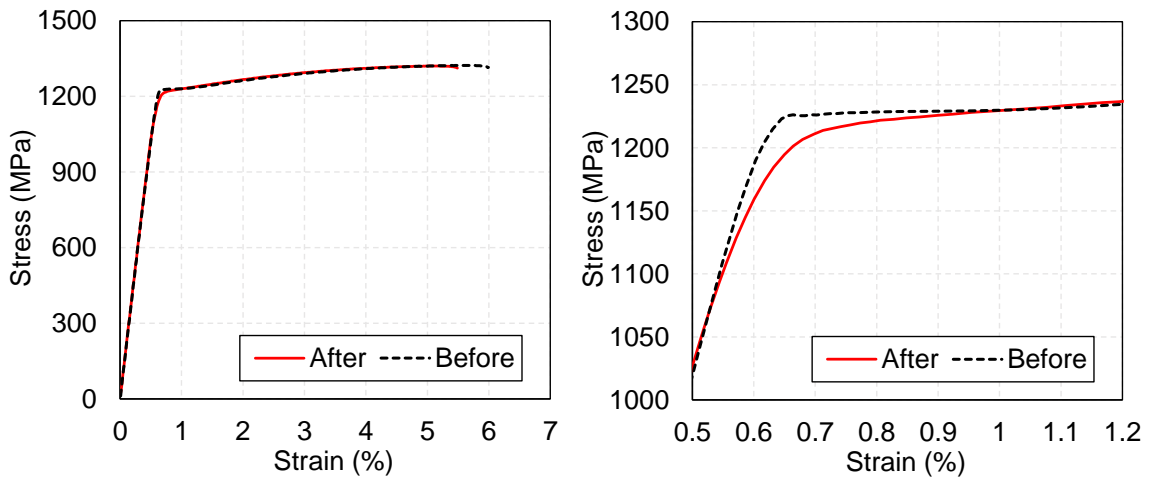
(a) Stress-strain relationship   (b) Enlarged stress-strain relationship

Figure 6-10 Tensile test results before and after the high cycle fatigue

6.3 Proposal of new measurement system

To conduct the low cycle fatigue test of the induction-heated steel as presented in Section 6.1, a new strain control method was proposed in this study. In most cases, the low cycle fatigue tests were strain-controlled and commonly achieved by conventional mechanical displacement transducers, which can convert the mechanical motion into a variable electrical current. By comparison, this study innovatively adopted a 3D scanner, called Aramis (abbreviated as AR in the figure), for the strain control of the fatigue test.

Aramis is commonly used for data processing after the test. For instance, detecting the strain on the splashed patterns through the digital image correlation (DIC) function, and measuring the displacement of the markers through the motion capture function [6.14]. However, it is rarely used for test control. In this study, the motion capture function of Aramis was used for strain control. Specifically, the cameras of Aramis tracked down the positions of two markers, and the strain calculated based on the relative deformation between the two markers was put into the machine controller in real time. Since it was a new trial, the other optical displacement sensor, OptiTrack (abbreviated as OT in the figure), was used to verify the accuracy of the test control. Additionally, the DIC analysis function of Aramis was used simultaneously to measure the strain distribution on the splashed patterns. The loading and measuring setups can be referred to in Figure 6-11.
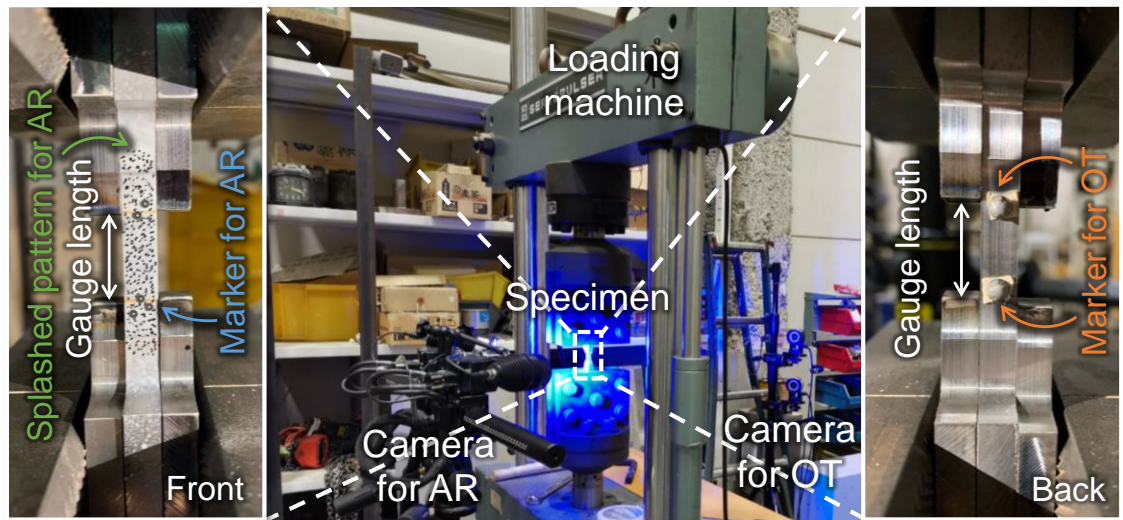
Figure 6-11 Loading and measuring setups

The signal flow is demonstrated in Figure 6-12. (1) Aramis obtained the axial strain of the specimen. (2) The axial strain was converted into voltage as an analog signal in real time. This voltage signal was transferred to the machine controller. (3) The loading was controlled according to the input. The flow (1) to (3) was the integral flow for the strain control. Although five markers were attached to the specimens for Aramis, only two markers on the orange lines shown in Figure 6-11(a) were used for loading control. The remaining three markers were used to improve the measurement accuracy, as no less than five markers were recommended. (4) The splashed pattern was simultaneously measured by Aramis. (5) OptiTrack measured the axial strain through corresponding markers for several specimens. It was to check whether the strain control went on as planned. Note that Aramis and OptiTrack did not interfere with each other. Besides, OptiTrack was not proper for the strain control of the test since there was no interface for converting the displacement of the markers into an analog signal in real time.
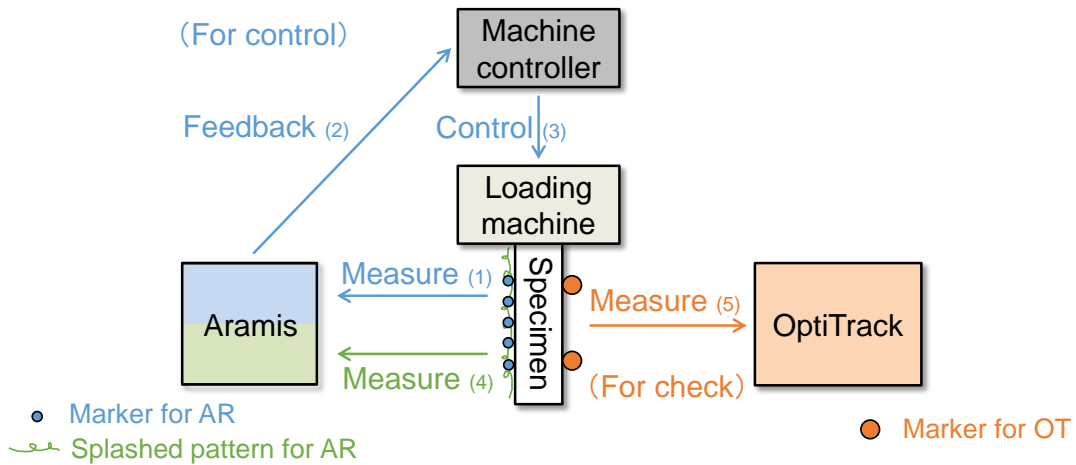
Figure 6-12 Signal flow

Figure 6-13 demonstrates the real-time monitor of Aramis. Aramis received the load data through a Bayonet Neill–Concelman (BNC) cable while measuring the axial strain. As shown in the enlarged views (1) and (2), the vertical axis of the axial strain was in the range from -1% to 1%, the load was in the range from -45 kN to 45 kN. The triangular wave remained stable during the test. The peaks of the axial strain did not match those of the load due to the time delay while calculating the axial strain. Therefore, it was modified while processing the data. The green line joining points 1 and 2 presented in enlarged view (3) was used to calculate the axial strain. Note that the DIC analysis function can be used for strain control as well, but it takes time for the data analysis [6.15].
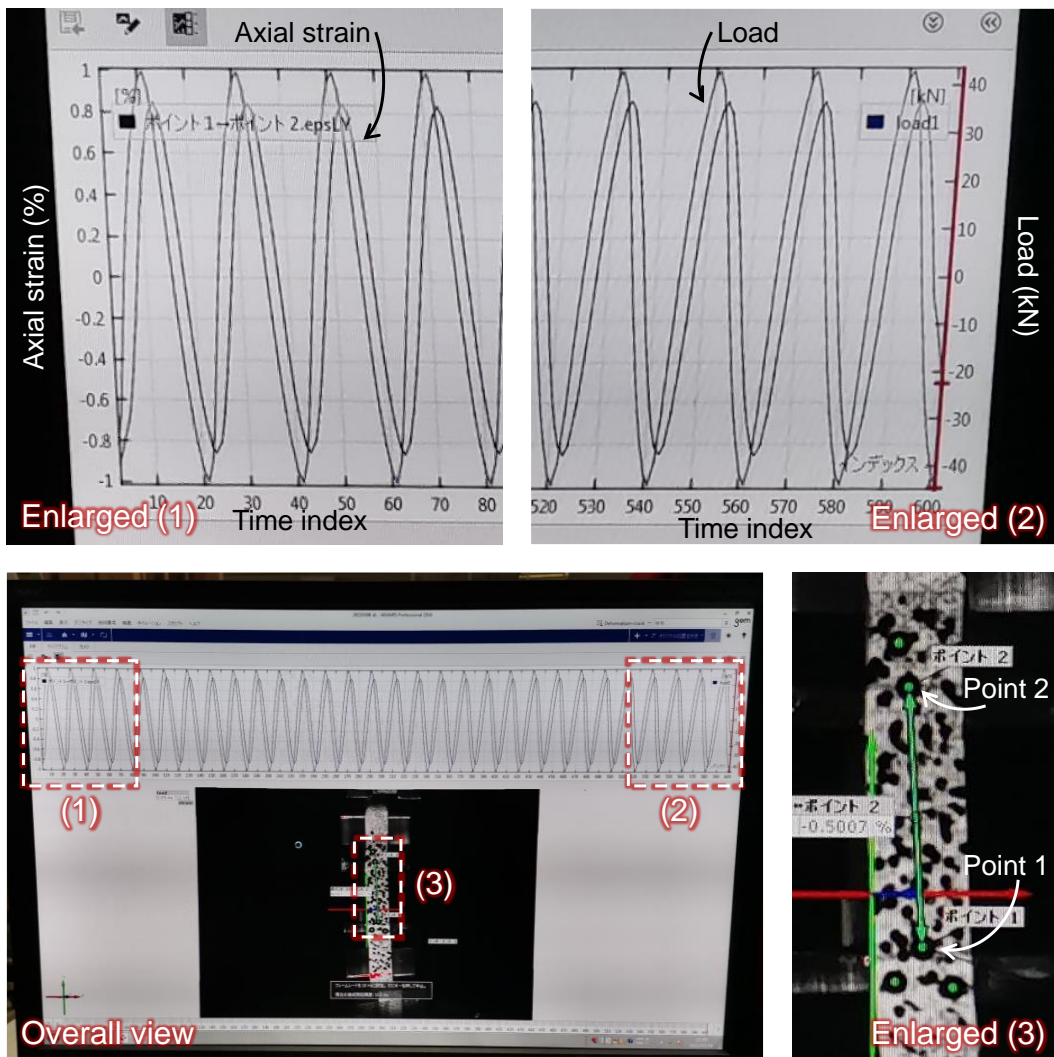
Figure 6-13 Real-time monitor of Aramis
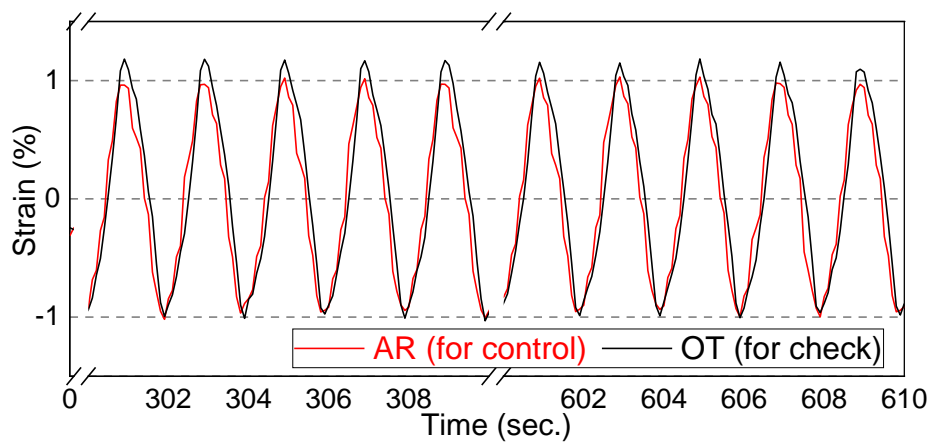
Figure 6-14 Strain-time relationship

(target total strain range of 2.0% for heated specimen)

An example of the strain-time history measured by Aramis and OptiTrack is shown in Figure 6-14. The tensile strain obtained by OptiTrack slightly exceeded that obtained by Aramis. As shown in Figure 6-15(a), the diameter of the markers used in Aramis was 0.4 mm (white center), of which the size was similar to the commonly-used punch, see Figure 6-15(b). Whereas the markers used in OptiTrack had a diameter of 4 mm. Therefore, the markers used in OptiTrack occupied a large area of the gauge length of 20 mm, which might result in a measurement error. In all, the target total strain range of 2.0% remained constant, proving that the newly-proposed axial-strain-controlled test method was achieved.
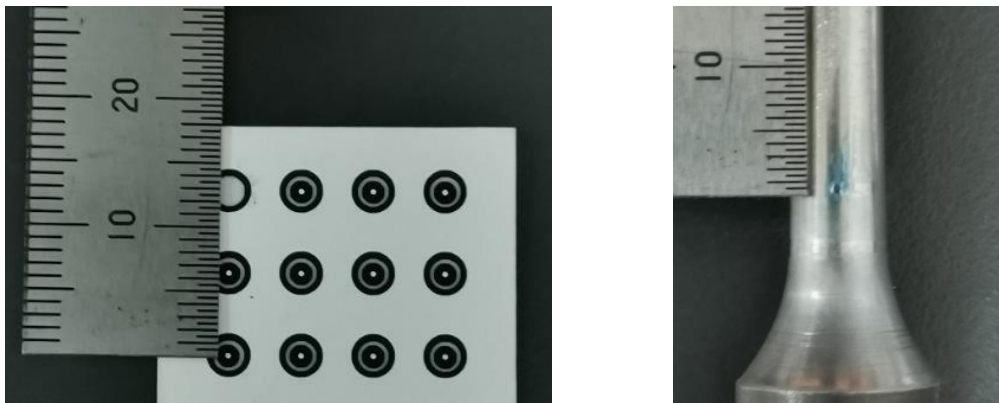
(a) Size of marker for Aramis   (b) Size of punch for standard tensile test

Figure 6-15 Comparison of the marker size and punch size (Unit: mm)

This study innovatively employs the 3D scanner, Aramis, for the strain control of the low cycle fatigue test. Table 6-5 simply concludes the advantages and disadvantages of Aramis and conventional mechanical displacement transducers.

Table 6-5 Comparison of Aramis and conventional mechanical displacement transducer

System	Advantage	Disadvantage
Aramis	Specimen dimension is nearly unlimited; Damage to the device is avoidable; Gauge length is simple to measure.	The device is sensitive to the ambient environment; High sampling speed may be inaccessible.
Mechanical displacement transducer	The requirement for the ambient environment is low; High sampling speed is accessible.	Specimen dimension is limited; The device is easy to be damaged; Measurement of the gauge length is necessary.

The detailed comparisons are written below:

Aramis's advantage:

1. Specimen dimension is nearly unlimited. The mechanical displacement transducers used for metal fatigue tests have a fixed gauge length. Take the products from Shimadzu for example, the gauge lengths of those for measuring the axial deformation are 12.5 mm, 25 mm, and 50 mm, and that for measuring the radial deformation is 10 mm. In addition, the specimen sizes, including the width, thickness, or diameter are prescribed as well. By comparison, the motion capture function of Aramis has no restriction for the specimen dimension only if the target is within the measuring range.

2. Damage to the measuring device is avoidable. When the fatigue test is controlled by a π-shape displacement transducer, it should be stopped before obvious strength reduction occurs, to avoid the overstretch of the device. When it is controlled by a strain gauge, re-attaching of the gauges is needed due to its invalidation after several cycles. By contrast, the non-contact measurement way of Aramis prevents it from being damaged.

3. Measurement of the gauge length becomes simple. In the case of a conventional mechanical displacement transducer, the gauge length should be precisely set on the specimen, such as 50 mm. When Aramis is employed, it is unnecessary to mark the gauge length on the specimen accurately for it is measurable.

Aramis's disadvantage:

1. The device is sensitive to the ambient environment. The change of light and temperature after calibration, and the sudden occurrence of noise, influence the measuring accuracy. Thus, it is vital to keep the ambient environment unchanged during the test, or it is better to redo the calibration if the environment varies.

2. High sampling speed may be inaccessible. The maximum sampling speed depends on the exposure time of the cameras, which is greatly affected by the ambient light. In this study, the sampling speed was 20 Hz, representing that 40 data were recorded every cycle. But for the test which needs a much higher sampling speed, Aramis might be unbefitting.

6.4   Conclusion

This chapter introduces the low cycle fatigue performance of the induction-heated steel cut out from induction-heated curved braces (IHCBs) and the high cycle fatigue performance of the PT bars. The newly-proposed strain control method for the low cycle fatigue test is introduced as well.

Section 6.1 introduces the low cycle fatigue of the unheated and heated specimens cut out from IHCBs. The fatigue lives of the unheated and heated specimens were formulized by the Manson-Coffin law and were generally captured by the universal and modified universal slopes methods proposed by Manson. However, the experimental results revealed that both types of specimens had a shorter life compared with that of the value obtained by Manson's equations. The unheated specimens had a longer life when the strain range was large owing to higher ductility. While the strain range was small, the heated specimens had a longer life contrarily mainly due to higher strength. The cyclic stress-strain curves of the unheated and heated specimens were expressed according to the Ramberg-Osgood law, and compared to the prediction equation proposed by Morrow. It indicated that Morrow's equation might be unsuitable to predict the cyclic stress-strain curve of the heated specimen. Additional fatigue tests proved that the stroke control might work as a simple alternative to strain control, but the load control was improper for the low cycle fatigue test. Since the research comparing the fatigue performance of the steel before and after heat treatment was rare, the test results obtained in this study might be helpful for future research.

Section 6.2 indicates the high cycle fatigue of PT bars. Due to the cyclic softening found in heated specimens presented in Section 6.1, the question of the cyclic softening of the PT bar under normal service conditions was raised. To sum up, by excluding the effect of temperature, no obvious cyclic softening was observed during the fatigue tests, but the ones that underwent fatigue tests showed a nearly 10%-lower elastic limit during the tensile test.

Section 6.3 introduces the innovative method for the strain control of the low cycle fatigue test which employed the motion capture function of a 3D scanner called Aramis. The strain was controlled by the relative deformation of two markers which were tracked down by the cameras of Aramis, and the strain value was transported to the machine controller in real time. In addition, its accuracy was verified by another motion capture system. Compared to the conventional mechanical displacement transducer, the proposed system reduced the limitations on the specimen dimension and gauge length, and the risk of being damaged. However, the requirements for the ambient environment and the sampling speed were stringent.

Part of the content is published in reference [6.16)].

References

6.1)	Manson, S. S. (1966). Thermal Stress and Low-cycle Fatigue. McGraw-Hill Education.

6.2)	164/Sc 5, I. (2007). ISO 12106:2003, Metallic materials - Fatigue testing - Axial-strain-controlled method. Multiple. Distributed through American National Standards Institute (ANSI).

6.3)	棚橋諒，横尾義貫，中村恒善，久保田俊彦，山本浅雄. (1969). H 型鋼フランジの引張圧縮塑性疲労. 日本建築学会大会学術講演梗概集構造系，1003-1004，8 月，北海道.

6.4)	花井正実，黒羽啓明，吉村浩二，藤田文雄. (1971). 鋼素材の低サイクル疲労挙動に関する実験的研究. 日本建築学会論文報告集，184，29-37.

6.5)	小野徹郎，加古康也，佐藤篤司，岩田衛. (2000). 金属系素材の低サイクル疲労特性に関する研究. 日本建築学会構造系論文集，532，193-199.

6.6)	Manson, S. S. (1965). Fatigue: A complex subject - Some simple approximations. Experimental Mechanics, 5(4), 193-226. https://doi.org/10.1007/bf02321056

6.7)	Manson, S. S. & United States. National Advisory Committee for Aeronautics. (1953). Behavior of Materials under Conditions of Thermal Stress. National Advisory Committee for Aeronautics.

6.8)	164/Sc 5, I. (2007a). ISO 1099:2006, Metallic materials - Fatigue testing - Axial force-controlled method. Multiple. Distributed through American National Standards Institute (ANSI).

6.9)	Morrow, J. D., ASTM International, & American Society for Testing and Materials. (1965). Cyclic Plastic Strain Energy and Fatigue of Metals. ASTM International.

6.10)	Ramberg, W., Osgood, W. R., & United States. National Advisory Committee for Aeronautics. (1943). Description of Stress-strain Curves by Three Parameters. National Advisory Committee for Aeronautics.

6.11)	Ahlström, J., & Karlsson, B. (2005). Fatigue behaviour of rail steel - a comparison between strain and stress controlled loading. Wear, 258(7–8), 1187–1193. https://doi.org/10.1016/j.wear.2004.03.030

6.12)	fib - federation internationale du beton. (2013). fib Model Code for Concrete Structures 2010 (1st ed.). Ernst & Sohn.

6.13)	Gorash, Y., & MacKenzie, D. (2014). Cyclic yield strength in definition of design limits for fatigue and creep. PAMM, 14(1), 365–366. https://doi.org/10.1002/pamm.201410170

6.14)	ARAMIS 3D camera systems: High-end industrial applications. (n.d.). Aramis. Retrieved June 30, 2022, from https://www.gom.com/en/products/3d-testing/aramis-3d-camera

6.15)	Lusiak, T., & Knec, M. (2018). Use of ARAMIS for Fatigue Process Control in the Accelerated Test for Composites. Transportation Research Procedia, 35, 250-258. https://doi.org/10.1016/j.trpro.2018.12.023

6.16) Liu, Y., Iwata, K., Sanda, S., & Nishiyama, M. (2022). Utilization of motion capture systems for low cycle fatigue tests on induction-hardened steel. Journal of Constructional Steel Research, 190, 107166. https://doi.org/10.1016/j.jcsr.2022.107166

7 Conclusions

This project aims to make flexible use of the partial strengthening technology provided by induction heating (IH) treatment in the civil and architectural engineering fields. In this thesis, the spotlight was on the induction-heated curved brace (IHCB). The fatigue performance of the material itself was investigated as well. The conclusions of this thesis are first presented, then, the limitations and the tasks that need solving are explained.

7.1 Conclusion

The conclusions of this thesis are as follows.

Chapter 1 introduces the background, research contents, and research objectives of this study. IH treatment is effective to raise the steel material strength at the selected region, and the development of IH technology recently makes it available for partial strengthening on large-scale structural steel components. This study flexibly employs the IH technology to develop a new kind of brace, an induction-heated curved brace (IHCB). IHCB is parallel treated by IH technology along the brace length, thus, the untreated normal-strength region and the IH-treated high-strength region are coexisting in the same cross-section. Besides, this uneven IH treatment bends the brace as an arc due to the shrinkage of the high-strength region. The strength difference can trigger the two-stage yielding behavior, thereby, modifying the post-yield behavior. The initial curve shape, which is regarded as a disadvantage of the heat treatment formerly, is surprisingly turned into an advantage in this study to improve the compressive stability and delay the first yielding behavior. IHCB is proposed to overcome the weakness of the conventional buckling brace (CBB) whose compressive behavior is unstable and the post-yield stiffness is low.

Chapter 2 presents the novel experimental study on IHCBs. Three types of IHCBs were fabricated. IH treatment effectively raised the yield and tensile strengths of the material to approximately 2.2 times at the flange and 2.6 times at the web. It also triggered the curve shape of IHCB, and the curvedness, which was the ratio of the initial transverse deformation to the specimen length was 2.2%-2.6%. One CBB and three IHCBs were tested cyclically. The test results demonstrated that the IHCB series showed approximately 58% lower initial stiffnesses but two times larger yield cycles and 13-18 times higher post-yield stiffness compared to those of CBB. The buckling behavior seemed in CBB was replaced by overall smooth flexural behavior for IHCBs, and their post-buckling loads were as high as 87%-91% of their maximum compressive loads. Besides, the transverse deformations and local strains of the IHCB series were more uniformly distributed along the brace length rather than locally concentrated at the brace middle as CBB. The test results revealed that IHCBs satisfied their target

performances, including low initial stiffness, high post-yield stiffness, stable compressive behavior, and sufficient load capacity at the brace end. Therefore, the IHCB series is able to remain elastic to a larger axial strain, which lowers the load capacity demands for the frame at the small story drift ratio of about 1/200. Additionally, IHCB can provide relatively large post-yield stiffness, indicating that they can continue supporting the frame at the large story drift ratio of about 1/100. Besides, stable compressive behavior is achieved, which reduces the damage brought by buckling and simplifies the design conditions.

Chapter 3 demonstrates the numerical analytical study of IHCBs. ABAQUS/implicit was used to build the IHCB series and CBB models, and the model accuracy was confirmed by comparing the numerical analysis results to the experimental results. The investigation into the effect of curve shape indicated that the curve shape alone mainly acted on smoothing the load-axial strain relationship and removing the sharp turning points, specifically, lowering the initial stiffness and stabilizing the compressive behavior. The partial strengthening alone mainly worked on increasing the value and delaying the occurrence of critical loads. It triggered the multistage yielding behavior under tension. Both the curve shape and partial strengthening worked on the increase of the post-yield stiffness, improvement of the buckling load or buckling behavior, and improvement of the post-buckling load. To meet the target performance of IHCB, the curvedness should be controlled within the range from 2.3% to 2.7%, and the strength ratio of the high-strength region to the normal-strength one should be within the range from 2.2 to 3.5.

Chapter 4 proposes the design formula of IHCBs. The curve shape was assumed as a sine curve for the calculation of critical load and an arc curve for the calculation of stiffness. The equations for the initial stiffness, yield load, post-yield stiffness, maximum tensile load, and post-buckling strength were proposed based on their material properties, deformations, and IH-treated patterns. Note that the calculation of the post-buckling strength was referred to as the P-M_{pn} curve presented in Appendix 1. The design formulas were proven effective to evaluate the behaviors of CBB and the IHCB series. The deviations of most of the evaluation index were within 20%.

Chapter 5 presents the numerical analysis of the frames using IHCBs. A single-story, single-span frame with chevron brace specimens from previous research was reproduced by ABAQUS/implicit. CBB and IHCB with the same dimensions were attached to the frame to investigate the brace behaviors. The analysis revealed that the unsmooth cyclic behaviors seemed in the CBB frame were improved in the IHCB frame. It was because that CBB buckled under compression, while IHCB avoided the overall buckling and showed a stable compressive behavior. IHCB lowered the stiffness of the frame at small deformations and maintained the high load capacity at large deformations, indicating that IHCB was

able to exert its expected performance in a frame. Additionally, when CBB bent in the out-of-plane direction drastically, IHCB bent along its initial curve shape uniformly, which mitigated the stress concentration on the frame. Even though IHCB possessed the initial curve shape, it eventually showed a smaller out-of-plane deformation than CBB with a controllable bending direction.

Chapter 6 demonstrates the fatigue performance of induction-heated steel. For the low cycle fatigue tests, the strain control by the motion capture function of a 3D scanner called Aramis was innovatively proposed, instead of the common control method by conventional mechanical displacement transducer. The accuracy of this system was verified by another motion capture system. The fatigue lives of the unheated and heated specimens cut out from IHCBs were formulized by the Manson-Coffin law and were generally captured by the universal and modified universal slopes methods proposed by Manson. The unheated specimens had a longer life when the strain range was large, and the heated specimens had a longer life contrarily when the strain range was small. The cyclic stress-strain curves of the unheated and heated specimens were expressed according to the Ramberg-Osgood law. They pointed out that the unheated specimens showed cyclic hardening, while the heated ones showed cyclic softening. For the high cycle fatigue tests of PT bars, no obvious cyclic softening was observed during the fatigue tests. However, the specimens that underwent fatigue tests showed a nearly 10%-lower elastic limit in the tensile test.

7.2   Future challenges and other works

The limitations of this thesis are as follows.

- As presented in Chapter 2, due to the lack of knowledge and experience, the curvature of the induction-heated brace specimen with an I-shaped section is yet unpredictable. Besides, due to the limitation in the carbon content of the structural steel SS400, and the restraint in the devices, the strength and the range of IH-treated regions are hard to control. Therefore, further investigations not only in architectural engineering but also in material science are necessary for the improvement of induction-heated braces in the future.

- As presented in Chapter 5, only one bracing system was employed for the frames using IHCBs. Other analysis conditions, for example, the brace in other directions or other bracing systems, and the seismic analysis of the IHCB frame, may be necessary in the future to enrich the understanding of IHCB in a frame and evaluate IHCB's behavior quantitatively.

- The material fatigue test described in Chapter 6 was meaningful to accumulate the fatigue data of the induction-heated specimens. However, the data were not sufficient enough to build the relationships between the material fatigue and the specimen fatigue performances. Therefore, predicting the fatigue performance of the seismic component based on material fatigue is still a challenge that needed to be solved in the future.

Nevertheless, this series of experiments and analyses brings a new perspective of bonding two different disciplines, to be specific, applying the IH technology of material science to the development of the seismic component of architectural engineering. There is no denying that this kind of discipline integration opens more possibilities for the development of safe and high-performance building structures.
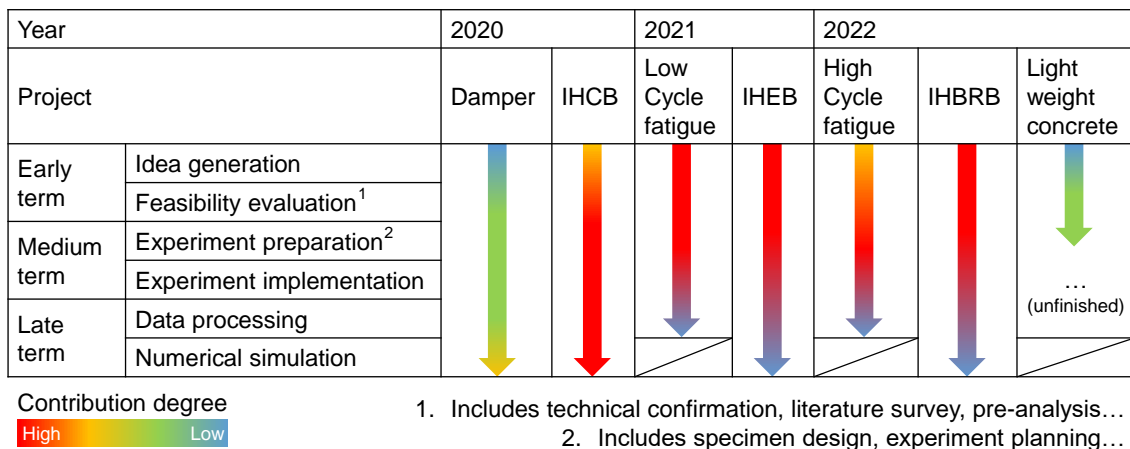
Figure 7-1 My research contents during the doctoral course

This thesis mainly presented the study on IHCB and the fatigue tests, other research contents that I participated in during the doctoral course are summarized in Figure 7-1. My research contents about damper can be referred to as B.3 and B.4, IHEB is referred to as B.7, and IHBRB is referred to as B.5 and B.6 in "Research paper and award".

Appendix 1. $P\text{-}M_{pn}$ curve

The $P\text{-}M_{pn}$ curves of CBB, IHCB-F40, and IHCB-2F60 are shown in Appendix figure 1. These curves are obtained analytically as follows. For a given axial load P, the unique solution of the location of the neutral axis x_n is calculated based on the equilibrium of forces. Then, the full plastic moment around the minor axis M_{pn} is obtained. Note that the curve of IHCB-F40 is not symmetric around the coordinate axis due to its asymmetric IH treatment at the cross-section. The values of P, M_{pn}, and x_n, are listed in Appendix table 1. Note that x_n is the distance between the neutral axis and the tensile edge.

(a) CBB

(b) IHCB-F40
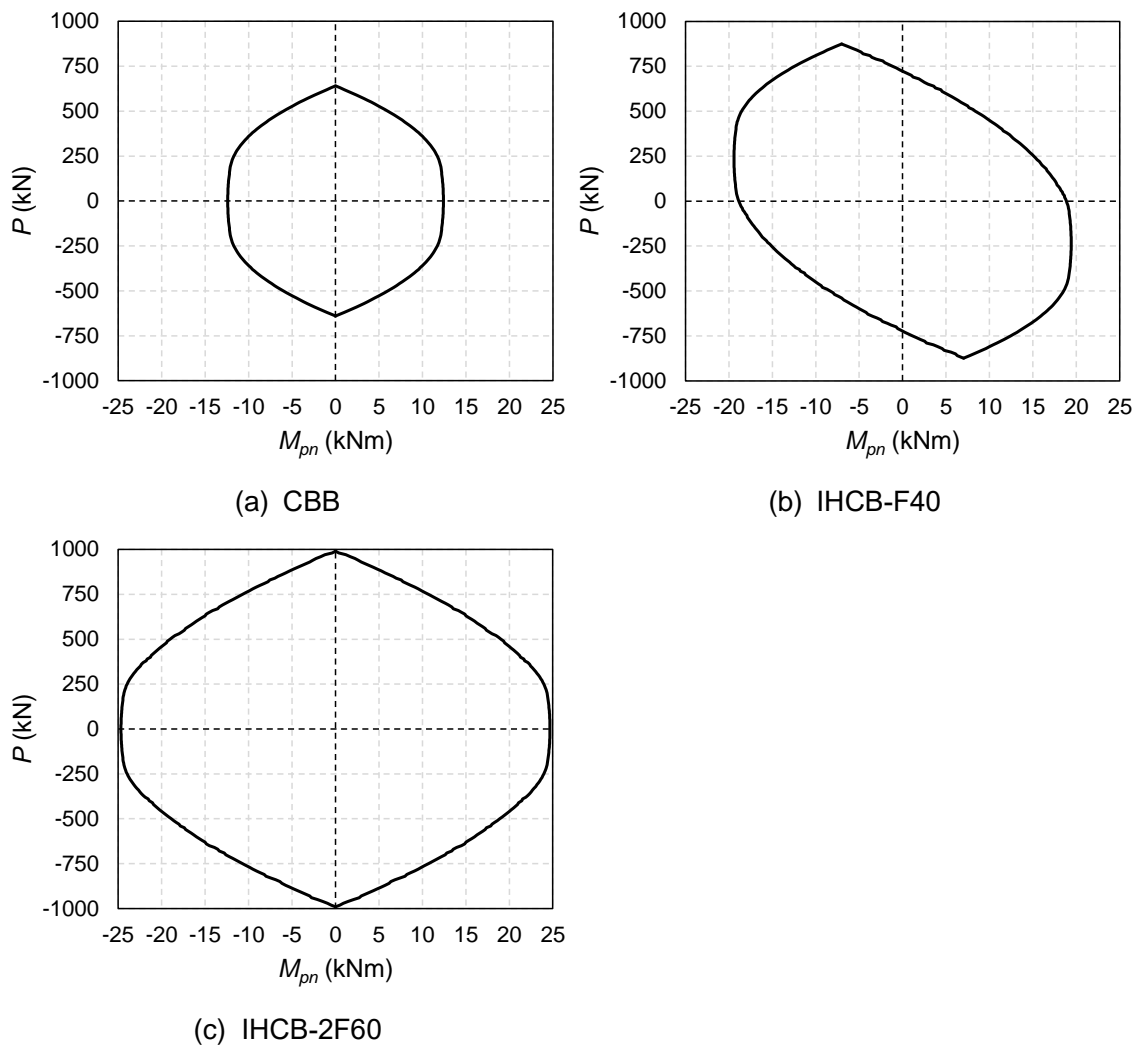
(c) IHCB-2F60

Appendix figure 1 $P\text{-}M_{pn}$ curve

Appendix table 1 Lists of P, M_{pn}, and x_n

CBB			IHCB-F40			IHCB-2F60		
P	M_{pn}	x_n	P	M_{pn}	x_n	P	M_{pn}	x_n
(kN)	(kNm)	(mm)	(kN)	(kNm)	(mm)	(kN)	(kNm)	(mm)
640.46	0.00	100.00	874.24	-7.01	100.00	991.13	0.00	100.00
640	0.02	99.95	870	-6.80	99.87	990	0.00	100.00
630	0.52	98.93	860	-6.31	99.44	980	0.39	99.50
620	1.00	97.90	850	-5.81	99.00	970	1.20	99.00
610	1.47	96.87	840	-5.29	98.50	960	1.72	98.50
600	1.94	95.85	830	-4.77	98.00	950	2.24	98.00
590	2.39	94.82	820	-4.54	97.50	940	2.61	97.50
580	2.83	93.79	810	-3.76	97.00	930	2.97	97.02
570	3.27	92.77	800	-3.53	96.50	920	3.44	96.60
560	3.69	91.74	790	-3.03	96.00	910	3.90	96.17
550	4.10	90.71	780	-2.28	95.50	900	4.36	95.74
540	4.50	89.69	770	-2.06	95.00	890	4.82	95.32
530	4.90	88.66	760	-1.61	94.57	880	5.27	94.89
520	5.28	87.63	750	-1.16	94.15	870	5.71	94.47
510	5.65	86.61	740	-0.72	93.72	860	6.17	94.00
500	6.01	85.58	730	-0.29	93.29	850	6.64	93.50
490	6.36	84.55	720	0.14	92.87	840	6.98	93.00
480	6.70	83.53	710	0.57	92.44	830	7.56	92.50
470	7.03	82.50	700	0.99	92.00	820	7.76	92.00
460	7.35	81.47	690	1.20	91.50	810	8.21	91.50
450	7.66	80.45	680	1.88	91.00	800	8.65	91.00
440	7.96	79.42	670	2.20	90.50	790	9.09	90.50
430	8.25	78.39	660	2.51	90.00	780	9.52	90.03
420	8.53	77.37	650	2.94	89.50	770	9.91	89.60
410	8.80	76.34	640	3.59	89.00	760	10.31	89.17
400	9.05	75.31	630	3.78	88.50	750	10.70	88.75
390	9.30	74.29	620	4.41	88.00	740	11.08	88.32
380	9.54	73.26	610	4.57	87.57	730	11.46	87.89
370	9.77	72.23	600	4.94	87.15	720	11.84	87.47
360	9.98	71.21	590	5.31	86.72	710	12.23	87.00
350	10.19	70.18	580	5.68	86.29	700	12.62	86.50
340	10.39	69.15	570	6.04	85.87	690	13.01	86.00
330	10.57	68.13	560	6.39	85.44	680	13.39	85.50
320	10.75	67.10	550	6.75	85.00	670	13.56	85.00
310	10.92	66.07	540	7.12	84.50	660	14.13	84.50
300	11.07	65.05	530	7.49	84.00	650	14.50	84.00
290	11.22	64.02	520	7.65	83.50	640	14.86	83.50
280	11.35	63.00	510	8.11	83.00	630	15.01	83.03
270	11.48	61.97	500	8.36	82.50	620	15.34	82.60
260	11.59	60.94	490	8.71	82.00	610	15.67	82.17

CBB			IHCB-F40			IHCB-2F60		
P	M_{pn}	x_n	P	M_{pn}	x_n	P	M_{pn}	x_n
(kN)	(kNm)	(mm)	(kN)	(kNm)	(mm)	(kN)	(kNm)	(mm)
250	11.70	59.92	480	9.05	81.50	600	15.99	81.75
240	11.79	58.89	470	9.39	81.00	590	16.30	81.32
230	11.87	57.86	460	9.69	80.57	580	16.61	80.89
220	11.95	56.84	450	10.00	80.15	570	16.92	80.47
210	12.01	55.81	440	10.30	79.72	560	17.23	80.00
200	12.06	54.78	430	10.59	79.29	550	17.38	79.50
190	12.11	53.76	420	10.88	78.87	540	17.69	79.00
180	12.14	52.96	410	11.17	78.44	530	18.00	78.50
170	12.16	52.79	400	11.45	78.00	520	18.47	78.00
160	12.19	52.63	390	11.59	77.50	510	18.76	77.50
150	12.21	52.46	380	11.96	77.00	500	19.05	77.00
140	12.24	52.30	370	12.33	76.50	490	19.34	76.50
130	12.26	52.14	360	12.53	76.00	480	19.46	76.03
120	12.29	51.97	350	12.73	75.50	470	19.72	75.60
110	12.30	51.81	340	13.00	75.00	460	19.97	75.17
100	12.32	51.64	330	13.27	74.50	450	20.22	74.75
90	12.33	51.48	320	13.53	74.00	440	20.47	74.32
80	12.35	51.31	310	13.77	73.57	430	20.71	73.89
70	12.36	51.15	300	14.00	73.15	420	20.95	73.47
60	12.38	50.99	290	14.23	72.72	410	21.19	73.00
50	12.38	50.82	280	14.46	72.30	400	21.30	72.50
40	12.39	50.66	270	14.68	71.87	390	21.66	72.00
30	12.39	50.49	260	14.90	71.44	380	21.77	71.50
20	12.40	50.33	250	15.11	71.00	370	22.12	71.00
10	12.40	50.16	240	15.33	70.50	360	22.34	70.50
0	12.41	50.00	230	15.49	70.00	350	22.44	70.00
-10	12.40	49.84	220	15.76	69.50	340	22.66	69.15
-20	12.40	49.67	210	15.91	69.00	330	22.85	68.13
-30	12.39	49.51	200	16.05	68.50	320	23.02	67.10
-40	12.39	49.34	190	16.30	68.00	310	23.19	66.07
-50	12.38	49.18	180	16.54	67.50	300	23.35	65.05
-60	12.38	49.01	170	16.63	67.00	290	23.49	64.02
-70	12.36	48.85	160	16.80	66.58	280	23.63	63.00
-80	12.35	48.69	150	16.96	66.15	270	23.75	61.97
-90	12.33	48.52	140	17.12	65.72	260	23.87	60.94
-100	12.32	48.36	130	17.27	65.30	250	23.97	59.92
-110	12.30	48.19	120	17.42	64.87	240	24.06	58.89
-120	12.29	48.03	110	17.57	64.44	230	24.15	57.86
-130	12.26	47.86	100	17.71	64.00	220	24.22	56.84
-140	12.24	47.70	90	17.78	63.50	210	24.28	55.81
-150	12.21	47.54	80	18.00	63.00	200	24.34	54.78
-160	12.19	47.37	70	18.14	62.50	190	24.38	53.76

CBB			IHCB-F40			IHCB-2F60		
P	M_{pn}	x_n	P	M_{pn}	x_n	P	M_{pn}	x_n
(kN)	(kNm)	(mm)	(kN)	(kNm)	(mm)	(kN)	(kNm)	(mm)
-170	12.16	47.21	60	18.23	62.00	180	24.41	52.96
-180	12.14	47.04	50	18.39	61.50	170	24.44	52.79
-190	12.11	46.24	40	18.44	61.00	160	24.47	52.63
-200	12.06	45.22	30	18.62	60.50	150	24.49	52.46
-210	12.01	44.19	20	18.67	60.00	140	24.52	52.30
-220	11.95	43.16	10	18.77	59.28	130	24.54	52.14
-230	11.87	42.14	0	18.86	58.25	120	24.56	51.97
-240	11.79	41.11	-10	18.93	57.22	110	24.58	51.81
-250	11.70	40.08	-20	19.00	56.20	100	24.60	51.64
-260	11.59	39.06	-30	19.06	55.17	90	24.61	51.48
-270	11.48	38.03	-40	19.11	54.14	80	24.63	51.31
-280	11.35	37.00	-50	19.14	53.12	70	24.64	51.15
-290	11.22	35.98	-60	19.17	52.85	60	24.65	50.99
-300	11.07	34.95	-70	19.20	52.69	50	24.66	50.82
-310	10.92	33.93	-80	19.22	52.53	40	24.66	50.66
-320	10.75	32.90	-90	19.25	52.36	30	24.67	50.49
-330	10.57	31.87	-100	19.27	52.20	20	24.67	50.33
-340	10.39	30.85	-110	19.29	52.03	10	24.68	50.16
-350	10.19	29.82	-120	19.31	51.87	0	24.68	50.00
-360	9.98	28.79	-130	19.33	51.70	-10	24.68	49.84
-370	9.77	27.77	-140	19.35	51.54	-20	24.67	49.67
-380	9.54	26.74	-150	19.36	51.38	-30	24.67	49.51
-390	9.30	25.71	-160	19.37	51.21	-40	24.66	49.34
-400	9.05	24.69	-170	19.39	51.05	-50	24.66	49.18
-410	8.80	23.66	-180	19.39	50.88	-60	24.65	49.01
-420	8.53	22.63	-190	19.40	50.72	-70	24.64	48.85
-430	8.25	21.61	-200	19.41	50.55	-80	24.63	48.69
-440	7.96	20.58	-210	19.41	50.39	-90	24.61	48.52
-450	7.66	19.55	-220	19.42	50.23	-100	24.60	48.36
-460	7.35	18.53	-230	19.42	50.06	-110	24.58	48.19
-470	7.03	17.50	-240	19.42	49.90	-120	24.56	48.03
-480	6.70	16.47	-250	19.42	49.73	-130	24.54	47.86
-490	6.36	15.45	-260	19.41	49.57	-140	24.52	47.70
-500	6.01	14.42	-270	19.41	49.41	-150	24.49	47.54
-510	5.65	13.39	-280	19.40	49.24	-160	24.47	47.37
-520	5.28	12.37	-290	19.39	49.08	-170	24.44	47.21
-530	4.90	11.34	-300	19.38	48.91	-180	24.41	47.04
-540	4.50	10.31	-310	19.37	48.75	-190	24.38	46.24
-550	4.10	9.29	-320	19.36	48.58	-200	24.34	45.22
-560	3.69	8.26	-330	19.34	48.42	-210	24.28	44.19
-570	3.27	7.23	-340	19.32	48.26	-220	24.22	43.16
-580	2.83	6.21	-350	19.31	48.09	-230	24.15	42.14

CBB			IHCB-F40			IHCB-2F60		
P	M_{pn}	x_n	P	M_{pn}	x_n	P	M_{pn}	x_n
(kN)	(kNm)	(mm)	(kN)	(kNm)	(mm)	(kN)	(kNm)	(mm)
-590	2.39	5.18	-360	19.29	47.93	-240	24.06	41.11
-600	1.94	4.15	-370	19.27	47.76	-250	23.97	40.08
-610	1.47	3.13	-380	19.24	47.60	-260	23.87	39.06
-620	1.00	2.10	-390	19.22	47.43	-270	23.75	38.03
-630	0.52	1.07	-400	19.19	47.27	-280	23.63	37.00
-640	0.02	0.05	-410	19.16	47.11	-290	23.49	35.98
-640.46	0.00	0.00	-420	19.13	46.63	-300	23.35	34.95
			-430	19.10	45.61	-310	23.19	33.93
			-440	19.05	44.58	-320	23.02	32.90
			-450	18.99	43.55	-330	22.85	31.87
			-460	18.92	42.53	-340	22.66	30.85
			-470	18.84	41.50	-350	22.50	30.00
			-480	18.75	40.47	-360	22.34	29.50
			-490	18.65	39.45	-370	22.12	29.00
			-500	18.54	38.42	-380	21.90	28.50
			-510	18.42	37.39	-390	21.54	28.00
			-520	18.28	36.37	-400	21.43	27.50
			-530	18.14	35.34	-410	21.05	27.00
			-540	17.99	34.31	-420	20.95	26.53
			-550	17.83	33.29	-430	20.71	26.11
			-560	17.66	32.26	-440	20.47	25.68
			-570	17.47	31.23	-450	20.22	25.25
			-580	17.28	30.21	-460	19.97	24.83
			-590	17.08	29.18	-470	19.72	24.40
			-600	16.86	28.15	-480	19.46	23.97
			-610	16.64	27.13	-490	19.18	23.50
			-620	16.41	26.10	-500	18.90	23.00
			-630	16.16	25.07	-510	18.60	22.50
			-640	15.91	24.05	-520	18.30	22.00
			-650	15.64	23.02	-530	18.00	21.50
			-660	15.37	21.99	-540	17.86	21.00
			-670	15.08	20.97	-550	17.38	20.50
			-680	14.79	19.94	-560	17.23	20.00
			-690	14.48	18.91	-570	16.92	19.53
			-700	14.17	17.89	-580	16.61	19.11
			-710	13.84	16.86	-590	16.30	18.68
			-720	13.50	15.83	-600	15.99	18.25
			-730	13.16	14.81	-610	15.67	17.83
			-740	12.80	13.78	-620	15.34	17.40
			-750	12.43	12.75	-630	15.01	16.97
			-760	12.06	11.73	-640	14.86	16.50
			-770	11.67	10.70	-650	14.50	16.00

CBB			IHCB-F40			IHCB-2F60		
P	M_{pn}	x_n	P	M_{pn}	x_n	P	M_{pn}	x_n
(kN)	(kNm)	(mm)	(kN)	(kNm)	(mm)	(kN)	(kNm)	(mm)
			-780	11.27	9.67	-660	13.93	15.50
			-790	10.86	8.65	-670	13.56	15.00
			-800	10.44	7.62	-680	13.39	14.50
			-810	10.01	6.59	-690	12.79	14.00
			-820	9.57	5.57	-700	12.62	13.50
			-830	9.12	4.54	-710	12.23	13.00
			-840	8.67	3.51	-720	11.84	12.53
			-850	8.20	2.49	-730	11.46	12.11
			-860	7.71	1.46	-740	11.08	11.68
			-870	7.22	0.43	-750	10.70	11.25
			-874.24	7.01	0.00	-760	10.31	10.83
						-770	9.91	10.40
						-780	9.52	9.97
						-790	9.09	9.50
						-800	8.65	9.00
						-810	8.21	8.50
						-820	8.01	8.00
						-830	7.43	7.50
						-840	6.85	7.00
						-850	6.38	6.50
						-860	6.17	6.00
						-870	5.71	5.53
						-880	5.27	5.11
						-890	4.82	4.68
						-900	4.36	4.26
						-910	3.90	3.83
						-920	3.44	3.40
						-930	2.97	2.98
						-940	2.75	2.50
						-950	2.10	2.00
						-960	1.44	1.50
						-970	0.92	1.00
						-980	0.53	0.50
						-990	0.00	0.00
						-991.13	0.00	0.00